UNIVERSITÀ DEGLI STUDI DI PADOVA
DIPARTIMENTO DI FISICA ED ASTRONOMIA
SCUOLA DI DOTTORATO DI RICERCA IN FISICA
CICLO XXV

The TeV AGN Portfolio: extending Fermi LAT analysis into the CTA realm

THESIS PRESENTED BY

Sara BUSON

SUPERVISORS

Denis BASTIERI
Grzegorz MADEJSKI

DIRECTOR OF THE DOCTORAL SCHOOL

Andrea VITTURI

To my grandmothers,
Zita and Giorgina,
and to my family
for so much love

ABSTRACT

The extragalactic γ-ray sky is completely dominated by active galaxies, where by *active* we mean that a significant fraction of the emitted energy is not due to the standard components of a galaxy: stars, gases and interstellar dust. Every detected active galaxy seems to be powered by a compact region at their center; explaining why active galaxies are often referred as Active Galactic Nuclei (AGNs). About 1% of all galaxies are AGNs, believed to be fueled by the accretion onto a supermassive black hole, the *central engine* of the active galaxy. In addition, about 10% of AGNs display powerful jets of particles and radiation.

The current model of AGNs is highly anisotropic and many of the observational characteristics of AGNs can be attributed to the way we are observing it and, in particular, to the orientation of the relativistic jets with respect to the observer. Among AGNs, blazars, which host a jet oriented at a small angle to the line of sight, are of particular interest for γ-ray astrophysics. The emission from these objects is dominated by relativistic beaming effects, which dramatically boosts the observed photon energies and luminosity, the reason why we expect that the observation of blazars at γ-ray energies should be the most fruitful.

To confirm our guess, after the launch of the *Fermi Gamma-ray Space Telescope*, bearing on-board the Large Area Telescope (LAT), which provides virtually continuous observation of blazars between 20 MeV and 300 GeV, many new discoveries refined the current modeling of blazars, by providing useful insights into jets and other AGN features. On the other hand, at the same energies, other observations found puzzling results, bewildering astronomers and astrophysicists.

In addition to the LAT, Imaging Atmospheric Cherenkov (IAC) telescopes (namely MAGIC, HESS and VERITAS) provided a good coverage at even higher energies (typically above 30 GeV) and the benefit of simultaneous observations was apparent just after the first broadband paper about PKS 2155−304 (Aharonian et al., 2009a).

More insights should be gained when the Cherenkov Telescope Array (CTA) will become operational, as it will cover an extended energy window with respect to operating IAC telescopes and will reduce the sensitivity threshold. In addition, CTA will have a huge energy overlap with the LAT, allowing for the first time a reliable way to correlate data obtained by the two detectors.

In this Thesis, we present in-depth studies of LAT γ-ray observations of blazars, complemented by multifrequencies observations which are an essential tool to model their behavior.

On one hand, we will discuss the characterization of a TeV blazars sample that were simultaneously observed both by *Fermi* and MAGIC instruments. The joint observations and the ideal coverage provided by the synergy of the two instruments naturally motivates the extrapolation of *Fermi* spectra to MAGIC energies, with the aim, in the near future, to extend this effort to CTA realm.

On the other hand, we will discuss a flux-limited sample of bright blazars detected by *Fermi* in the first 3.5 years of operations. These objects, displaying extreme outbursts, make up less than 10% of the sources detected by *Fermi* in its second source catalog. We discuss the characteristics of the sample with respect to the entire catalog of AGNs detected by *Fermi* and adding some considerations with respect to previous γ-ray observation carried out by EGRET. At the end of this work, we will then focus on one of these objects, that met particular attention for being a gravitationally lensed system, PKS 1830$-$211.

SOMMARIO

Il cielo extragalattico nei raggi gamma è completamente dominato da galassie attive, dove per attive si intende che una significante parte di energia emessa non è generata dalle usuali componenti delle galassie: stelle, gas e polveri interstellare. Ogni galassia attiva è una sorgente altamente energetica, variabile e molto compatta associata a un buco nero supermassiccio che si trova al centro del sistema. In questi oggetti è il nucleo, il cosiddetto motore centrale, ad essere la fonte di energia, da qui deriva il nome di Nucleo Galattico Attivo (AGN). Soltanto circa l'uno per cento delle galassie conosciute sono AGN e di queste, circa il dieci per cento degli AGN sono caratterizzati da un potente getto composto da radiazione e materia.

Data la forte anisotropia di questi oggetti molte delle loro proprietà osservative sono dovute al punto di vista, in particolar modo dall'orientazione del getto rispetto all'osservatore. Nel modello unificato degli AGN, i blazar hanno un ruolo centrale per l'Astrofisica dei raggi γ, interpretati come galassie attive osservate in direzione del getto relativistico. La loro emissione risulta dominata da effetti relativistici che accelerano i fotoni osservati ad energie estreme. Questo ha indotto a credere che tali oggetti potessero essere importanti sorgenti di raggi γ.

A conferma di cio, il Large Area Telescope (LAT), lanciato in orbita a bordo del satellite *Fermi Gamma-ray Space Telescope*, che opera nell'intervallo di energie $20\,\mathrm{MeV} - 300\,\mathrm{GeV}$, ha permesso di raffinare il modello descrittivo dei blazar portando ad una maggiore comprensione dei meccanismi che ne sono alla base. Allo stesso tempo, i risultati ottenuti grazie al LAT hanno portato anche scoperte del tutto inaspettate, così da rimettere in discussione alcuni fondamenti del modello degli AGN.

Gli strumenti in grado di studiare energie ancora più elevate di quelle monitorate dal LAT (generalmente sopra i $100\,\mathrm{GeV}$), sono i telescopi Imaging Atmospheric Cherenkov (IAC, in particolare MAGIC, HESS and VERITAS). Il beneficio che può derivare dalla sinergia di questi strumenti con il LAT è stato evidente sin dalla prima pubblicazione riguardante la sorgente PKS 2155−304 (Aharonian et al., 2009a).

Per di più, notevoli progressi saranno raggiunti quando Cherenkov Telescope Array (CTA) diverrà operativo. Questo strumento infatti sarà in grado di studiare un intervallo di energie più esteso rispetto ai precendeti esperimenti IAC, osservando per la prima volta alcune bande di frequenze e in particolare con una sensibilità maggiore. Inoltre CTA osserverà in parte lo stesso spettro di frequenze del LAT

permettendo per la prima volta osservazioni simultanee tra le due tipologie di strumenti.

Questa Tesi presenta uno studio approfondito di osservazioni di blazar nella banda γ effettuate con il LAT accompagnate da dati multifrequenza, strumento indispensabile per lo studio di questi oggetti. Nella prima parte verranno discusse osservazioni simultanee di blazar osservati ad energie del TeV, simultaneamente dal LAT e da MAGIC. La sinergia di questi due strumenti infatti permette di osservare l'emissione γ dei blazar senza soluzione di continuità, cosa che in futuro si prevede di estendere a CTA.

Nella seconda parte della Tesi verranno discussioni dei blazar estremamente luminosi osservati da *Fermi* nei primi 3.5 anni di operazioni in uno stato di alta emissione (flare). Questi oggetti, caratterizzati da estreme condizioni, costituiscono meno del 10% di tutte le sorgenti rilevate da *Fermi*, incluse nel secondo catalogo. Le carattestiche generali di questi oggetti verranno presentate e confrontate con quelle delle sorgenti del secondo catalogo *Fermi*. Inotre verranno anche discusse in luce delle precedenti osservazioni condotte da EGRET nella banda γ. Infine, l'attenzione verrà focalizzata su uno di questi oggetti, PKS 1830+211 , di particolare interesse dato che si tratta di un sistema soggetto all'effetto di lente gravitazionale.

CONTENTS

INTRODUCTION

Cosmic sources of γ rays are sites of relativistic particle acceleration which reflect extreme physical conditions. Since the Universe is mostly transparent to this radiation up to high redshift, high energy photons turn out to be the ideal messengers to probe the astrophysical settings originating the most powerful phenomena.

Due to the opaqueness of our atmosphere to γ rays, space borne instruments are the best way to study soft γ rays ($< 100\,\mathrm{GeV}$), whose flux is large enough to be detected by a reasonably small payload. In this field, after the pioneering observation by NASA's SAS-2 (Small Astronomy Satellite: 1972-73) and ESA's Cos-B (1975-82), most was due to the observations by EGRET (Energetic Gamma Ray Experiment Telescope), on board CGRO, the *Compton Gamma-Ray Observatory*, that provided the first complete survey of the γ-ray sky subsequently followed by the AGILE satellite and the *Fermi Gamma-ray Space Telescope*.

At higher energies ($> 100\,\mathrm{GeV}$), it has to be considered that the flux of γ rays is much smaller (decreasing roughly by two decades for every decade in energy), and detection on-board satellite, with their limited effective area is not viable any more. Nevertheless, primary γ rays produce extended air showers that can be detected by ground-based instruments able to reconstruct the characteristics of the primary particle initiating the shower. In particular, most of secondary particles are ultrarelativistic, and can be detected by their yield in Cherenkov light. In 1989, this technique reached a firm experimental footing with Whipple's $10\,\mathrm{m}\,\varnothing$ telescope (Weekes et al., 1989), that set the beginning of the so-called imaging technique or IACT (Imaging Atmospheric Cherenkov Technique) by detecting a steady γ-ray emission from the Crab Nebula. Starting with the commissioning of H.E.S.S. in 2003, the new generation of IACTs (H.E.S.S., MAGIC and VERITAS[1]) (Hinton, 2004; Albert et al., 2008b; Holder et al., 2006) demonstrated to have reached a significant maturity.

Since the identification of the first TeV sources, significant improvements in instrumentation helped in the exploration of the γ-ray sky both by satellite experiments and by ground based detectors. As a consequence, the rapidly developing field of MeV-TeV γ-ray astrophysics has entered a golden age producing many exciting results: on the one hand enlarging the list of known γ-ray emitters, on the other hand continuing to expand the range of astrophysical questions which can be answered.

1 The acronyms standing for imaging atmospheric Cherenkov telescope, High Energy Stereoscopic System, Major Atmospheric Gamma Imaging Cherenkov and Very Energetic Radiation Imaging Telescope Array System, respectively.

The goals of this field are wide-ranging, but the main common interest is to reveal the conditions and mechanisms that are responsible for the detected emission and the underlying particle acceleration processes. In fact, the high energy sky hosts only non-thermal sources, therefore providing a direct view of galactic and extragalactic sites where highly relativistic particles are produced and interact.

Since the beginning of γ-ray astronomy, it had been suggested that extragalactic sources could be a significant component of the high-energy sky and decisive evidences were provided by EGRET, that revealed a series of bright, variable sources positionally consistent with prominent blazars. This finding has been firmly established by the *Fermi* satellite, that after its second year of survey already detected more than 600 sources associated with blazars.

Blazars are Active Galactic Nuclei that typically encompass the following characteristics: radio-loud, with flat radio spectrum; significant polarization in optical and/or radio and a significant variability. Blazars are seen across the entire electromagnetic spectrum, with a characteristic two-peak Spectral Energy Distribution (SED). Most VHE γ-ray emitters are X-ray bright BL Lac sources, while only three flat spectrum radio quasar (FSRQ) were showed to to emit VHE γ-rays.

This Thesis is aiming at obtaining more insights of blazars as can be provided from both the observational and the theoretical side. It represents the outcome of the work I carried out as a member of the *Fermi* LAT collaboration and it is mainly a fruit of a wide multiwavelength framework in which I developed my research activities in the past three years.

The first three Chapters highlight the basics to understand the results presented in the Thesis. Experienced readers in the field could skip them and go directly to the second part of the Thesis.

Chapter 1 gives a general introduction combined with main observational properties and interpretations of AGNs with a particular emphasis on the subclass of objects on which this Thesis is focusing: the blazars.

Chapter 2 reports the very basic ingredients of blazar acceleration and radiation mechanisms, namely Fermi acceleration and in particular synchrotron and inverse Compton radiative processes. In addition, it illustrates the blazar emission models.

Chapter 3 is the last introductory section and provides an overview about *Fermi* LAT data analysis, which presents the γ-ray data and the analysis methods discussed in the following Chapters.

In the second part of the Thesis, I discuss the outcomes of the analysis of γ-ray *Fermi* data, together with other multifrequency data, for specific objects.

Chapter 4 is focused on a sample of TeV blazars, in order to investigate the phenomenology and relationship among their multi-

wavelength properties. In this Chapter, you can find the analysis from the LAT side, and the results of the multiwavelength campaigns for newly announced TeV emitters (i.e. B3 2247+304, 1ES 1215+303, 1ES 1727+502) and for well known VHE blazars (i.e. PG 1553+113, 1ES 0806+524, PKS 1510−089).

Chapter 5 discusses the most extreme flaring sources that have been highlighted by the *Fermi* Flare Advocate framework in the first 3.5 years of *Fermi* operations. Their general properties are presented along with a comparison with the whole sample of sources detected by *Fermi* (source catalogs). One of these sources, PKS 1830+211, is the central topic of Chapter 6, a bright γ-ray gravitationally lensed FSRQ. The study explores the γ-ray spectral and temporal properties of PKS 1830+211 as observed by the *Fermi* LAT, with particular attention to the three main outburst that occurred in 2010 and 2011. In addition, it provides a critical assessment of the 4 σ evidence of a time delay caused by macrolensing previously claimed. Finally, Chapter 7 summarizes the results and synthetically discusses a few developments and perspectives.

In the work that I present here, I took care of the entire *Fermi* data analysis. In addition, my personal contribution on the results of this Thesis spawns both the theoretical interpretations of the results and to the reduction phases. The original scientific results have been published or will be included in upcoming publications in international journals (e.g. Astronomy & Astrophysics and the Astrophysical Journal) and have been presented in several national and international conference.

1

AGN PROPERTIES AND OBSERVATIONAL BLAZAR SIGNATURES

AGNs have been observed and studied extensively over the whole electromagnetic spectrum in the past 50 years and, despite the increasing knowledge about their individual and collective properties, a complete understanding of the emission mechanisms at work in these extreme objects is still far enough away.

1.1 THE AGN PARADIGM

Active Galactic Nuclei represent only a few percent of galaxies, including all those objects whose main emission cannot be considered of stellar origin, but since the discovery of the first prototype by Seyfert in 1943, the number of these extragalactic sources has increased tremendously revealing a complex and challenging scenario. The picture reveals now a wide diversification in several classes but all with the same basic characteristics, among all, a peculiar non-thermal emission engine.

Hoyle and Fowler (1963) for the first time suggested that the energy source of an AGN was gravitational driven and could arise from in-fall of matter onto an highly collapsed object or black hole. Since then, huge progress in this direction have been made and nowadays the essential features of the most commonly believed unified scenario are sketched in Figure 1.1 Urry and Padovani (e.g. 1995). It consists of a rotating super massive black hole ($M \simeq 10^6 - 10^9 M_\odot$) playing the role of the central object, which can have a Schwarzschild radius of the order of 10^{-7} to 10^{-3} pc. The black hole is attracting material: the nearer matter is pulled inward by the gravitational potential and forms an accretion disk according to the conservation of the angular momentum. The accretion disk is probably made of an optically-thick thermal plasma and is subject to dynamical instabilities and dissipative processes that convert part of the bulk matter motion into internal energy (heat). The radiation thus results from the conversion of potential energy into thermal. The accretion disk is believed to be radiation-dominated in the inner region, with a thickness proportional to the adimensional mass accretion rate, whereas further from the hole the disk is supported by gas pressure. The unstable accretion disk, difficult to be observed separately from the black hole, is likely to be embedded in a very active corona and can extend to several hundred of thousand Schwarzschild radii. The outer part of the accretion disk, beyond $\simeq 0.1$ pc, may contain dusty molecular gas which can re-

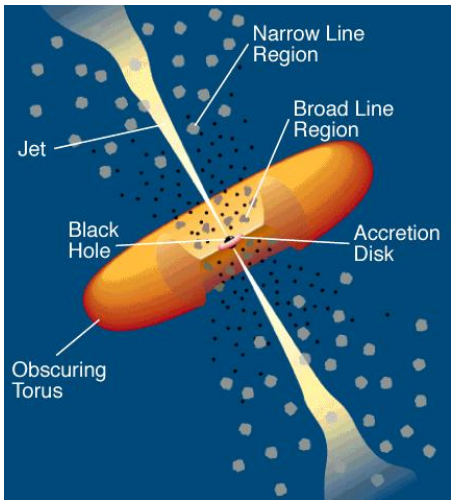

Figure 1.1 Outline of the Unified Model for a radio-loud AGN (not to scale) adapted from Urry and Padovani (1995). The black hole with a mass $\geq 10^6 M_\odot$ is located in the center of the system and it has a radius in the range of 10^{-7} to 10^{-3} pc (~ 1 AU). Surrounding it, there is the accretion disk which produces radiation through the conversion of potential into thermal energy. Above the disk there are orbiting clouds of gas. The clouds closer to the black hole (at a distance of $\sim 3 - 100 \times 10^{-5}$ pc) represented by dark spots, are referred as the BLR, while the farthest clouds (located at ~ 1 up to few 10^3 pc) are the light blobs and correspond to the NLR (see text for more details). Either the clouds or (probably) the accretion disk are responsible for the emission lines often observed in AGNs. The dust torus *or warped disk* obscures the central region from transverse line of sight and extends from ~ 0.1 pc. In the picture, a sketch of the radio jets that stem out from the region close to the black hole and can extend as far as 0.1 to several times 100 kpc.

radiate incident UV flux from the inner parts of the disk as infrared radiation.

Around this central structure, gas clouds are gravitationally attracted by the black hole. These clouds, ionized by the radiation from the accretion disk, generate the observed strong emission lines via photoionization and collisional excitation processes.

Clouds located closer to the central engine, in the so-called Broad Line Region (BLR), move faster (displaying high velocity dispersion FWHM $> 1000 - 2000\,\mathrm{km\,s^{-1}}$ and up to $\sim 10000\,\mathrm{km\,s^{-1}}$) and are dense ($\sim 10^8 - 10^{12}\,\mathrm{cm^{-3}}$) so they are responsible for the characteristic broad lines. Among the latter, the most noticeable are the permitted Hydrogen ones from Balmer and Lyman series and transition of Magnesium and Carbon ions.

Clouds far from the black hole (up to few kpc), in the Narrow Line Region (NLR), have lower densities ($n \sim 10^3 - 10^6\,\mathrm{cm^{-3}}$) and

smaller velocities with a typical FWHM $< 1000 - 2000\,\mathrm{km\,s^{-1}}$, thus generating narrow emission lines, both permitted and forbidden, the strongest of which are transitions of ionized Oxygen and Neon.

On the other hand, the lack of the detection of these features in some AGN leads us to the believe that a thick, dusty structure (torus or warped disk) surrounds the central regions; the torus is probably formed by dust molecules, that can obscure the central zone.

Since all the space around the black hole is warped by its gravitational potential and spin, the release of energy is highly anisotropic, mainly collimated along the axis direction. In some cases (radio-loud objects), strong jets of relativistic plasma (most likely electrons and positrons or electrons and protons) originate perpendicularly to the plane of the accretion disk. The magnetic field collimates and accelerates the particles from regions close to the black hole until $\sim 100\,\mathrm{kpc}$, forming "hot spots", also called *radio lobes* with reference to the fact that in these regions the energy is released mainly at radio frequencies, and are probably characterized by strong shocks where particle acceleration and magnetic field amplification take place. Often, when looking into the jet, there are regions appearing to move away from the center faster than the speed of light (superluminal motion). This can be easily explained by a perspective effect due to the transformation properties of angles in special relativity.

The radiation produced in the jet is of non-thermal origin, most likely produced by the interaction of an accelerated leptonic plasma with a magnetic field radiating via synchrotron and inverse Compton mechanisms (IC, more details in § 2.1). Nonetheless, the jet production mechanism and the jet composition itself on very small scales are still not known, as observations cannot distinguish among the various theoretical models proposed (more details in § 2.3).

The radiation observed from AGNs extends through the whole observable electromagnetic spectrum, thanks to the contribution of several components. The expected spectrum of the accretion disk extends from optical to soft X-ray frequencies and peaks in the optical-ultraviolet band. This radiation excites cloud material giving rise to emission lines while, when absorbed by the dusty torus, it is re-radiated predominantly in the infrared. The hard X-ray continuum is probably due to the corona of hot electrons which, surrounding the black hole, can scatter photons via the inverse Compton process up to keV energies. Notably, the jet emission is detectable in all wavebands, though it dominates at radio and γ-ray frequencies.

1.2 AGN CLASSIFICATION

AGN terminology is often confusing, as the distinctions among different types of AGNs sometimes reflect historical differences in how

objects were discovered or initially classified, rather than actual physical differences.

A historical important division has been made considering the optical-UV properties and the orientation of the accretion disk axis w.r.t. to the observer (Urry and Padovani, 1995). AGN are then divided into:

- Looking close to the plane we have *Type 2 AGNs*, characterized by a weak continuum emission and the presence of narrow emission lines. In these objects the non detection of broad lines is thought to be due to the low dispersion velocity or to orientation effects (an obscuring torus in the line of sight). Among this class, there are Narrow Line Radio Galaxies (NLRG, radio-loud), that show different levels of jet collimation and morphology, Seyfert 2 galaxies and infrared excess galaxies (radio-quiet, low luminosity and high luminosity, respectively).

- Looking close to the disk axis we have *Type 1 AGNs*, featuring a bright continuum and large Doppler-broadened emission lines. This class comprises Seyfert 1 Galaxies, Quasi Stellar Objects (QSOs, radio-quiet), Broad Line Radio Galaxies (BLRG), Flat Spectrum Radio Quasar and Steep Spectrum Radio Quasar (radio-loud, FSRQ and SSRQ, respectively). The difference between the latter two being the value of the radio spectral index ($F_\nu \propto \nu^{-\alpha}$) relative to the separation value $\alpha = 0.5$.

This scheme was based mainly on the general observational properties of AGNs. Nowadays, with the wider knowledge acquired, we can attempt to relate these general properties to the underlying physical processes (Abdo et al., 2010m). The radiation emitted by an AGN is usually produced by one (or both) of the following two physical processes:

- thermal radiation attributed to in-falling matter strongly heated in the inner parts of the accretion disk close to the black hole

- non-thermal radiation due to the presence of a jet of relativistic material (see Chapter 2).

Given that the first process contributes mostly in the optical, UV and X-ray bands, whereas the second one can dominate the entire electromagnetic spectrum, this model has been proposed as a physical classification scheme combining the widely accepted AGN standard paradigm (Urry and Padovani, 1995) and the well-known radiation emission processes. AGNs can therefore be subdivided as follows.

- *Thermal/Disk Dominated AGNs*
  AGNs for which the output power is dominated by thermal radiation (in the optical/X-ray band), can be classified as Thermal (or disk) dominated. These objects should correspond to Type

2 AGN in the precedent scheme. They are usually called QSOs or Seyfert 2 galaxies which do not display significant nuclear radio emission compared to the observed emission in the optical or X-ray band. They correspond to the usual type of sources known as radio quiet objects and they constitute the large majority (∼90%) of AGNs.

- *Non-Thermal/Jet dominated AGNs*
  AGNs where the non-thermal processes prevail at all frequencies can be classified as Non-Thermal (or jet) dominated. These sources would correspond instead to Type 1 AGNs. The class of Non-Thermal/Jet Powered AGNs, are usually referred to as radio loud AGNs. These can be subdivided into blazars and non-aligned non-thermal dominated AGNs depending on the orientation of their jets w.r.t. the line of sight.

Following the guidelines of the classification based on the radio/optical flux ratio, the conventional separation of AGNs in *radio-quiet* and *radio-loud* objects depends on whether they have a radio (5 GHz) - optical (B band) flux ratio ($R = F_{5\,\mathrm{GHz}}/F_B$) lower or higher than 10, respectively (Kellermann et al., 1989). Since in AGNs, HE-VHE emission has been found only in radio loud ones, for the purposes of this Thesis we will refer mainly to Jet-dominated ones and focus on this subclass of objects.

1.3 RADIO-LOUD AGNS

In radio-loud objects the luminosity is dominated by the contribution from the powerful relativistic jet and the related lobes (at least at radio frequencies). As first argued by Rees (1966), the plasma within the jets of radio-loud AGNs moves at relativistic speed and so it transports efficiently the energy from the vicinity of the super massive black hole to the distant lobes. This has strong implications on the observational properties of the object, as the observer will be biased depending upon the angle under which he is observing the objects. In particular, according to the unified model, we can divide the radio loud AGNs in the following three main categories:

Blazars: when jet and line of sight form a small angle, the observed emission is extremely variable and completely dominated by the contribution of the jet. The emission line features may be intrinsically absent or simply swamped by the additional variable components. Blazars are in their turn divided into two main subclasses: Flat Spectrum Radio Quasars (FSRQ) and BL Lac objects (BL Lacs). More details will be given in the following section.

Non-aligned Non-Thermal dominated AGN. These sources are radio loud AGN with jets pointed at large or intermediate ($\sim 15 - 40^\circ$ Urry and Padovani, 1995) angles w.r.t. the observer. For this

reason, they are sometimes called non-aligned, misaligned or mispointed blazars. This category includes:

- *Radio Galaxies*: their jets lie at a very large ($> 30°$) angle w.r.t. the line of sight and are generally considered misaligned blazars. Central structures of the system are obscured by the large torus that reprocesses the light coming from the inner disk and the BLR. In turn, the broad emission lines are not seen in these sources because at such large angles they are hidden by the torus. Often they display an extended, double-sided radio jets/lobes pointing in opposite directions in the plane of the sky w.r.t. the central nucleus. Their nuclear emission resembles that of blazars, but it is not amplified. As a consequence, it is usually fainter than the extended emission, especially at low radio frequencies.
- *SSRQ*: in these objects the orientation of the jet in these sources is thought to be intermediate between that of blazars and radio galaxies (Urry and Padovani, 1995), they are characterized by broad emission lines.

1.4 BLAZAR CHARACTERISTICS

Blazars are the most extreme class of AGNs, characterized by the emission of strong non-thermal radiation across the entire electromagnetic spectrum, from radio to very high γ-ray energies. Once considered a relatively rare sub-class of radio loud AGNs, nowadays blazars have been discovered using radio, μ-wave, X-ray or γ-ray bands. Recent results from the *Wilkinson Microwave Anisotropy Probe* (WMAP), Planck and *Fermi* missions have shown that blazars are the most common type of extragalactic sources found at microwave and γ-ray energies. Worth to notice, for example, that out of the 1873 sources listed in the 2-year LAT source catalog (2FGL, Nolan et al., 2012), $\sim$ 44% are reliably associated with AGNs (and an additional $\sim$ 14% are tentative AGN associations) and the overwhelming majority of them are blazars.

Typical observational properties of blazars include irregular, core-dominated flat or inverted radio spectrum, strong and rapid variability, apparent superluminal motion of the jet at VLBI scales (see § 1.4.2), flat or inverted radio spectrum, high and variable polarization at radio and optical frequencies. These features are interpreted as the result of the emission of electromagnetic radiation from a relativistic jet that is viewed closely aligned to the line of sight, thus causing strong relativistic amplification (Blandford and Rees, 1978).

If on the one hand all blazars share the same properties, on the other hand they also display diversity. As noted in the previous section, we distinguish between two types of blazar, basing this separation mainly upon their appearance in the optical band.

FSRQs are characterized by optical spectra with strong, broad emission lines while **BL Lacs** have an optical spectrum which at most shows weak emission lines, sometimes displays absorption features, and in some case can be completely featureless.

Historically, the two classes have been separated looking at the rest-frame equivalent width of 5 Å. A blazar is therefore defined as a BL Lac object when the equivalent width of the strongest optical emission line is < 5 Å, with the additional requirement that the wavelength coverage of the spectrum must satisfy $(\lambda_{max} - \lambda_{min}/\lambda_{max}) > 1.7$. The latter requirement to ensure that, if present, at least one strong emission line would have been detected, in order to be safe against biasing the classification for AGNs at different redshifts where the emission lines could be redshifted out of the relevant wavelength range. Moreover, in order to ensure that the radiation is predominantly non-thermal, the optical spectrum has to show a Ca II H/K break ratio[1] lower than 0.4. For sources exhibiting BL Lac or FSRQ characteristics at different times, the criterion often adopted is that if the optical spectrum conforms to BL Lac properties at any time, then it is classified as a BL object.

We refer to objects that share many of the properties of blazars, but do not have optical spectra of sufficient quality to establish their subclass, as Blazars of the Unknown type (or BZU, Massaro et al., 2009).

A currently interesting possibility is that the presence or absence of the jet could be strictly related to the mass accretion rate in Eddington unit, in particular to the accretion regime of the considered source (e.g. Maraschi and Tavecchio, 2003). Accordingly, the division between BL Lacs and FSRQs could be readily interpreted as the change in the accretion regime of the disk, becoming radiatively inefficient below a critical disk luminosity. If the accretion rate is less than $\sim 0.1\%$, jets can form easily, since the accretion is "hot" (probably advection-dominated). Jet particles preserve their energy, propagating in a clean ambient, since the disk accretes inefficiently. These are BL Lacs (HBLs when seen on-axis) and FR-I radio galaxies when seen off-axis. Then when the accretion rate is $0.1 - 20\%$, the disk is essentially flat and thin, and it radiates roughly like a black body. Those are generally Seyfert 1 and Seyfert 2 galaxies. Finally, in this view for objects in which the accretion is efficient and can reach very high values, the central region is full of photons emitted by the disk, so that the high radiation pressure favor the jets formation. Moreover, the BLRs are heated up by these photons. In such conditions, the jet propagates in a crowded medium, with the result that its power is strongly reduced by the interactions with the ambient photons. These are radio-loud quasars (and possibly FR-II galaxies) when seen away from the jet, and FSRQs when seen close to the jet axis.

1 the Ca II break arises from old stars in elliptical galaxies.

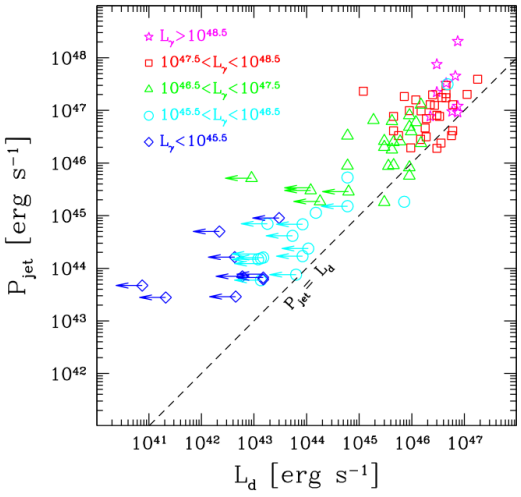

Figure 1.2 The total jet power P_{jet} as a function of the accretion disk luminosity L_d, from (Ghisellini et al., 2009)

In this context, the blazar unification finds a physical justification: BL Lacs and FSRQs could be objects with similar masses, but with different accretion efficiencies, coupled, ultimately, to the radiation efficiency of the accretion disk. An important result related to such scenario is provided by the study of *Fermi* sources shown in Figure 1.2. The plot represents the total jet power as a function of the disk luminosity (directly observed in FSRQ, upper limit in BL Lac objects). A clear correlation is found between the two parameters, which scale linearly. This is in agreement with the predictions of the Blandford-Znajek effect (see § 1.5.3), as discussed in (Ghisellini et al., 2009). Further considerations on the FSRQs-BL Lacs dichotomy will be addressed in § 1.6.1.

1.4.1 *Time Variability*

The broadband emission from all AGNs is highly variable, but the most extreme flux variability, i.e., largest magnitude and shortest timescale, is observed only in blazars. Extreme variability is actually one of the most distinctive features of these objects.

The timescales range from years down to minutes, with the longer ones being observed from radio to visible, while in X-rays and γ-rays typical flux variations are on the scale of hours, with the TeV flares being the most dramatic ones, with flux doubling time as short as few minutes. As a matter of fact, the very rapid TeV flare of Mrk 501 detected by MAGIC during 2005 (Albert et al., 2007b) and that of PKS 2155–304 observed by H.E.S.S. during 2006 (Aharonian et al., 2007) (both on the scale of few minutes), indicate variability timescales much shorter than the inferred light crossing times at the black hole

horizon, setting stringent requirements on the bulk Lorentz factor of $\sim 50 - 100$. This value of the Lorentz factor is clearly in excess of the jet Lorentz factor $\Gamma_{\rm jet} \sim 10$ measured for these two sources (Giroletti et al., 2004). Even accounting for the effects of relativistic beaming such shorter timescales are challenging conventional emitting models.

1.4.2 *Superluminal Motion*

Several observational evidences, obtained mainly with Very Large Baseline Interferometry (VLBI) observations of blazar radio jets, show that AGNs feature very compact components, moving apart with apparent transverse speeds greater than the velocity of light (see e.g. Figure 1.4 Marscher et al., 2008). The phenomenon can be explained in terms of an emitting region with a relativistic bulk velocity subtending small angles w.r.t. the observer line of sight and considering small inhomogeneities (blob) that move alongside with the jet (Rees, 1966). Here we will refer to Figure 1.3 and consider the simplest scenario of superluminal monition which is provided by a two source (blob) model.

Let us suppose that initially we have two sources at point B at time t_1, which are detected by an observer at point A at time t_1'. At time $t_2 = t_1 + \delta t$, one blob has moved a distance $v\delta t$ from the other.

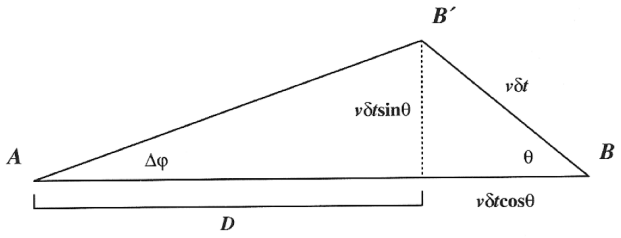

Figure 1.3 Geometric sketch of superluminal motion. This phenomenon is due to relativistic beaming explained by considering small inhomogeneities that move alongside with the jet, the latter pointing at small offset angles with respect to our line of sight.

The observer detects an initial signal at time t_1' (when the blobs are both in the same position): in this case, their signal will have traveled the distance $D + v\delta t \cos\theta$. Later, at time t_2', the observer records again information about the light-travel time between him and the two sources: one is still at the distance AB but now the other is approximately at a distance D. The angular separation between the two blobs at time t_2' is

$$\Delta\phi = \frac{v\delta t \sin\theta}{D}$$

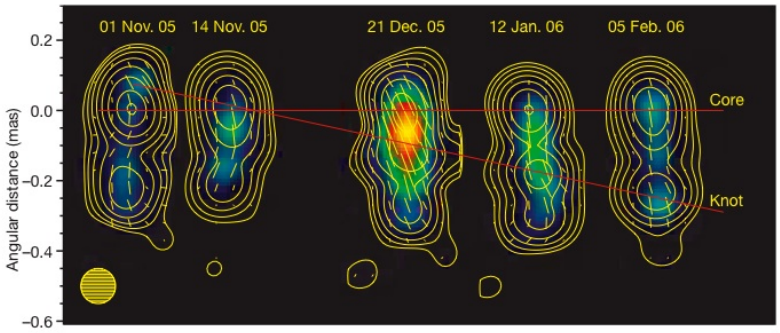

Figure 1.4 VLBA observations at 7 mm (43 GHz) of BL Lac (Marscher et al., 2008).

If Δt indicates the time that the observer measures between the two detections, it can be easily calculated by noting that:

$$t_1' = t_1 + \frac{D + v\delta t \cos\theta}{c} \quad \text{and} \quad t_2' = t_2 + \frac{D}{c}$$

Thus, the time elapsed between the two observations is

$$\Delta t = t_2' - t_1' = t_2 - t_1 - \frac{v\delta t \cos\theta}{c} = \delta t\,(1 - \beta\cos\theta)$$

where $\beta = v/c$ in the usual convention. We can finally compute the transverse velocity

$$\beta_T = \frac{v_T}{c} = \frac{D}{c}\frac{\Delta\phi}{\Delta t} = \frac{v\sin\theta}{c(1-\beta\cos\theta)} = \frac{\beta\sin\theta}{1-\beta\cos\theta} \tag{1}$$

It is interesting to find for which angle β_T is maximized; to express β_T as a function of the angle to the line of sight θ, we differentiate eq. 1 w.r.t. θ and set the result equal to zero:

$$\frac{\partial\beta_T}{\partial\theta} = \frac{\beta\cos\theta}{1-\beta\cos\theta} - \frac{(\beta\sin\theta)(\beta\sin\theta)}{(1-\beta\cos\theta)^2} = 0$$

and then this yields $\theta_{\max} = \cos^{-1}\beta$. By inserting this in eq. 1 and noting that

$$\sin(\cos^{-1}\beta) = (1-\beta^2)^{\frac{1}{2}}$$

the maximum value of β_T can be obtained as function of the Lorentz factor, $\gamma = 1/(1-\beta^2)^{-\frac{1}{2}}$

$$\beta_{\mathrm{T}}^{\max} = \frac{\beta(1-\beta^2)^{\frac{1}{2}}}{(1-\beta^2)} = \beta\gamma \tag{2}$$

It is worth notice that for $\beta \to 1$, $\beta_{\mathrm{T}}^{\max} \to \gamma$, and thus, in the case of relativistic motion close to the line of sight (i.e. $\theta \approx \cos^{-1}\beta$), the observer detects transverse separation velocities apparently greater than c.

1.5 FUELING OF AGNS

One of the main characteristics of AGNs is that they produce extreme luminosities, typically in the range $10^{42} - 10^{48}\,\mathrm{erg\,s^{-1}}$, in a comparable small volume ($< 1\,\mathrm{pc}^3$). Although it is evident that an active galaxy has a major bearing upon its nuclear activity, the origin of this extra power is still matter of a wide debate. The two main mechanisms that are considered to be responsible for blazars properties are:

- *Accretion* of material around the central hole: gravitational energy is extracted and partially converted into radiation;
- *Ejection* of material from the vicinity of the central object, through jets which accelerate material up to ultra-relativistic energies.

The ejection mechanism is deeply coupled with accretion. As will be discussed in the next paragraph, the resulting energy is thought to be rotational energy of the accretion of matter in addition to that of the black hole.

1.5.1 *Accretion Disks and Jets*

The accretion mechanism is an extremely efficient process that fuels compact galactic objects, namely white dwarfs, neutron stars, black holes with masses lower than $100\,M_\odot$ and AGNs as well. Generally it is explained considering an object which is gravitationally attracted by a much more massive body: When the former hits the surface of the latter, at a radius R, its potential energy can be available eventually as thermal radiation. The efficiency of this process (indicated by the parameter η) is proportional to the compactness of the hitting object. Indeed, the value of η is very high for neutron stars (by comparison, it is much higher than that of nuclear fusion). Therefore, when considering AGNs, it would be obvious to assume that the higher values are reached in presence of the massive black holes.

Nevertheless, since black holes do not have a surface, the accretion mechanism must be induced by the presence of an accretion disk of gas rotating around the central black hole. Moreover, it is not possible for matter to rotate beyond the so called "last stable orbit", thus the efficiency for this process would not be higher than what found for a neutron star. However, considering spinning black holes, the last stable orbits is shifted to smaller radii, allowing an efficiency up to $\eta \simeq 10\%$.

The dynamics of particles in the disk depends strongly on the nature of the central object: the huge mass of the black hole, in fact, deforms the time-space structure of the surrounding environment, and a general relativistic approach is necessary to describe the system. A

correct framework involves black holes with no charge but with angular momentum, namely the *Kerr black holes*. Detailed calculations show that accretion from a black hole can be an efficient mechanism only if the particles move in stable orbits. Then, the particles, constrained to move on circular orbits by viscose torques[2], will loose angular momentum transforming their rotational energy into radiative energy. As we will see in § 1.5.2, associated with quasi-spherical accretion there is an important fiducial number which governs the process, i.e. the *Eddington luminosity*.

Strictly related to accretion disks are the jets. It is commonly believed, in fact, that the two structures are symbiotically connected, despite the precise mechanism of interconnection is not fully understood, yet. The jets are probably generated in the inner region of the disk, near the last stable orbit, where gas pressure, radiation pressure and gravitational forces become comparable. Relativistic jets extract energy and angular momentum from the central engine (i.e. the inner part of the disk and the central black hole) driving a substantial amount of them far away, to the ambient medium (e.g. kpc scale, as seen in the case of Centaurus A, but sometimes also Mpc). They are composed of ionized material, most likely electrons, and probably protons and the products of their interactions, in relativistic motion and immersed in a strong magnetic field.

The origin of relativistic jets together with their main characteristics, e.g. their strict collimation, is still an open problem in astrophysics. Two accredited theories were proposed by Blandford and Payne (1982) and Blandford and Znajek (1977), in both of them a crucial role is played by the magnetic field, but while the former scenario considers the ejecting of an outflow from a magnetized disk, the latter describes the extraction of rotational energy from a spinning black hole through magnetic interactions with a surrounding plasma. Another major problem of jet formation is that it needs a Poynting flux dominated energy transport by a strongly magnetized plasma, whereas pc scale observations seem to point to particle dominated plasma (Celotti and Fabian, 1993).

Theory and observations can be reconciled assuming that initially the jet formation is by a magnetic dominated outflow, later converted to a particle dominated jet.

In the following sections we will give the main insights of the Blandford-Znajek mechanism, the most popular mechanism about the origin of the radiation channeled into jets (see § 1.5.3). The acceleration issue instead will be discussed inside the framework of the first and second order Fermi acceleration (see § 2.1).

2 The viscosity is generally thought to arise from differential rotation of the disk annuli.

1.5.2 *The Eddington limit*

As discussed, the accretion mechanism can be extremely efficient, nevertheless it is characterized by a maximum luminosity above which the AGN accretion is halted. This upper threshold is reached when the outward force exerted by the radiation pressure exceeds the inward gravitational force driving the accretion and is usually referred as the Eddington luminosity (L_{Edd}) of the object. The value can be easily derived through a simple treatment, following the approach of Frank et al. (1992). Assuming a steady, spherically-symmetric accretion and taking ionized hydrogen as accreting material, the photons-matter interactions can be treated as a simple Thomson scattering. Moreover, the proton contributions can be neglected because the photon-proton scattering cross-section is a factor $(m_e/m_p)^2 \sim 2.5 \times 10^{-7}$ smaller than the photon-electron one. The pressure force exerted on each electron is:

$$F_p = \sigma_T \frac{S}{c} \tag{3}$$

where S is the radiant energy flux (erg s^{-1} cm^{-2}, and $\sigma_T = 6.7 \times 10^{-25}$cm^2 is the Thomson cross-section. The electrostatic force between electrons and protons acts as a drag force: while they move, electrons carry protons with them. The gravitational force on each electron-proton pair is:

$$F_g = \frac{GM(m_e + m_p)}{r^2} \simeq \frac{GMm_p}{r^2} \tag{4}$$

The net force inward on each pair is, then:

$$F = \frac{GM(m_p)}{r^2} - \sigma_T \frac{S}{c} = GM(m_p) - \frac{L\sigma_T}{4\pi c} \times r^{-2} \tag{5}$$

where $L = 4\pi r^2 S$ is the total luminosity. The Eddington luminosity is thus defined as:

$$L_{Edd} = \frac{4\pi GMm_p c}{\sigma_T} \simeq 1.26 \times 10^{38} \frac{M}{M_\odot} \text{ erg s}^{-2} \tag{6}$$

To ensure efficiency through the accretion mechanism, then the total luminosity cannot overcome the Eddington luminosity. Following few more simple considerations we can extract other basic physical information of the accreting object, e.g. knowing its luminosity we can infer an upper limit on its mass. The last equation actually can be used to evaluate the Eddington mass $M_{\rm Edd}$, that in appropriate units could be expressed as:

$$L_{\rm Edd} = 8 \times 10^5 L_{44} M_\odot \tag{7}$$

Historically, this provided the first evidences of the existence of supermassive objects in the core of AGNs. It must be noticed, however, that the assumption of spherical symmetric accretion in this case is no longer valid.

In real objects, the dynamics of the accretion flow strongly depends on the efficiency of the radiative process, and, ultimately, on the rate of mass accretion. If L is the luminosity of the object, and $\dot{M}$ the mass accretion rate, then we can define the accretion efficiency, η, as:

$$L_{acc} = \eta \dot{M} c^2 \tag{8}$$

which is usually closely tied to $\dot{M}$. In blazars, accretion occurs at sub-Eddington rates, and we distinguish between:

- *Efficient accretion* ($\dot{M} > 0.01\dot{M}_{\rm Edd}$): in this condition, usually accretion occurs through (optically thick) geometrically thin disks, called accretion disks. The efficiency is quite high, at the level of $\eta \sim 0.1$, hence also the luminosity is high. It is commonly believed that FSRQs belong to this class of objects.
- *Inefficient accretion* ($\dot{M} < 0.01\dot{M}_{\rm Edd}$) typical of objects accreting trough ADAFs (Advection Dominated Accretion Flows), corresponding to optically thin disks (Abramowicz et al., 1998). Is the case of objects such as BL Lacs, characterized by very low efficiency ($\eta \ll 0.01$), and low luminosity.

1.5.3 *The Blandford-Znajek mechanism*

The most reliable scenario to explain the origin of the power fueled into the jets in AGNs is the Blandford-Znajek (BZ) mechanism (Blandford and Znajek, 1977). In their work, the authors hypothesize that energy and angular momentum can be extracted electromagnetically from a black hole and its surrounding disk.

Following the simplified formulation proposed by MacDonald and Thorne (1982), the idea at the basis of the BZ mechanism can easily be explained as follows. Let us consider a system composed by a rotating black hole of velocity Ω_H, mathematically described by the Kerr metric, surrounded by a thin accretion disk (region D) dipped in a magnetosphere filled with plasma (region FF in Figure 1.5), which extends far away from the hole.

For a stationary and axisymmetric system, the flow of electromagnetic angular momentum and redshifted energy in the magnetosphere is described by the poloidal parts of the flux vectors; moreover, the poloidal magnetic field lines are parabolic in the region FF. If the disk and the magnetosphere are degenerate ($\mathbf{E} \cdot \mathbf{B} = 0$), the magnetic field lines result frozen into the disk plasma, and rotate at the plasma local angular velocity Ω_F.

Assuming that the magnetosphere is force-free[3], there are free charges from the disk and in the region close to the black hole (pairs produc-

3 This special case arises when the plasma pressure is so small, relative to the magnetic pressure, that the plasma pressure may be ignored, and so only the magnetic pressure is considered. The name "force-free" comes from being able to neglect the force from the plasma.

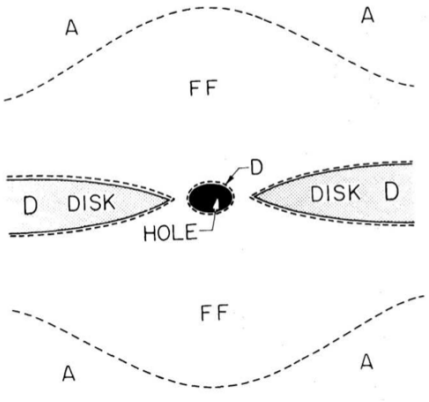

Figure 1.5 The Blandford-Znajek mechanism: a rotating black hole surrounded by a degenerate accretion disk (region D), dipped in a force free magnetosphere (region FF), which, far out is no longer free nor degenerate (region A)

tion from vacuum). An electric current flows on poloidal magnetic field surfaces; hence, fluxes of angular momentum and redshifted energy flow without any loss along the poloidal magnetic field lines.

Far outward, in the external region A, the magnetosphere is no longer force-free nor degenerate and particles are forced to move at speed lower then the field lines. A drag effect slows down the field lines (in radial motion). This causes a difference between the angular velocity of the disk Ω_D and that of poloidal field lines Ω_F . Accounting also for the boundary conditions at the horizon, angular momentum extraction from the disk and black hole energy takes place, and a collimated jet forms (BZ effect). The total power produced in the jet is:

$$P_{BZ} \simeq \frac{1}{128} B_0^2 r_g^2 a^2 c \tag{9}$$

where r_g is the gravitational radius and $a = j/j_{\max}$ is the adimensional angular momentum of the black hole ($a = 1$ for a maximally rotating object). Following Maraschi and Tavecchio (2003), it can be shown that, in the extreme approximation of a spherical free fall accretion, with $P_{acc} = \dot{M}c^2$:

$$P_{BZ} \simeq \frac{1}{64} a^2 P_{acc} = \frac{1}{64} a^2 \dot{M} c^2 \tag{10}$$

Therefore, even when the jet is produced at the expense of the black hole rotational energy, the generated power is closely linked to the accretion rate, and consequently to the disk luminosity.

1.6 SPECTRAL ENERGY DISTRIBUTIONS

As explained previously, blazar classification depends on the particular features in the optical band, where the main contributions come from the non-thermal jet component, the thermal radiation originated from the accretion onto the supermassive black hole and from the broad line region, and the radiation from the host galaxy, generally a giant elliptical one. In Figure 1.6 these three components are repre-

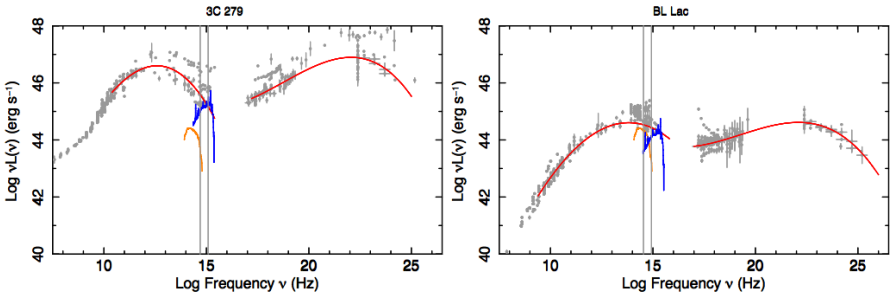

Figure 1.6 The SEDs of two representative blazars: 3C 279 (FSRQ) and BL Lacertae (BL Lac). Gray points are observational data. The three main components of blazars SEDs are indicated with the color lines. Non-thermal radiation from the jet (red), emission from the disk and from the broad line region (blue), and light from the host galaxy (orange). Disk and BLR contribution are represented by the composite QSO optical spectrum of Vanden Berk et al. (2001) while the host galaxy light is represented by the giant elliptical template of Mannucci et al. (2001) and Nilsson et al. (2003). The two vertical lines indicate the optical observing window (3800–8000 Å).

sented as red, blue and orange lines, overlaid to the spectral energy distribution (SED) of two well-known blazars (from Giommi et al., 2012b). The strong non-thermal radiation is the only one to be detected over the entire electromagnetic spectrum and represents the signature of a blazar. The SED displays two broad peaks, widely interpreted as due to synchrotron (low frequency peak) and inverse Compton (high frequency peak) mechanisms. However, as proposed in Mannheim (1993), the high energy peak could also be the result of hadronic processes (see § 2.3).

Blazars can be classified according to their broadband SED when there is sufficient multiwavelength coverage to reconstruct a spectrum from the radio through the optical and X-ray bands. Since the peak of the synchrotron hump can occur at different frequencies, ranging from about $\sim 10^{12.5}$ Hz to over 10^{18} Hz and reflecting the maximum energy at which particles can be accelerated (e.g. Giommi et al., 2012b), we distinguish between:

- Low Synchrotron Peaked sources (LSP), when ν^S_{peak} is lower than 10^{14} Hz in their rest frame. These are also referred to as *red blazars* and are mainly radio selected BL Lac objects. They have the low energy peak in the IR/optical band while their high energy component is located at hard-X/soft-γ rays and typically dominates the luminosity;
- High Synchrotron Peaked sources (HSP), whenever $\nu^S_{peak} > 10^{15}$ Hz. These are also called blue blazars and are above all X-ray selected BL Lac objects. The peak of the synchrotron component is generally located in the UV/soft-X-ray region and the high and low energy components show similar luminosities;
- Intermediate Synchrotron Peaked sources (ISP), in these objects 10^{14} Hz $< \nu^S_{peak} < 10^{15}$ Hz. Their luminosities and synchrotron peak frequencies are intermediate between the above sub-classes and their high energy hump usually peaks at MeV-GeV energies.

Essentially, all FSRQs are LSP blazars, whereas BL Lac objects sample the LSP, ISP, and HSP range. This definition extends the original division of BL Lacs into LBL and HBL sources first introduced by Padovani and Giommi (1995)

1.6.1 *The Blazar Sequence*

As long as a deeper comprehension of blazar physics has been acquired, several attempts have been made in finding few basic parameters able to completely describe the observational properties of blazars. In particular, Fossati et al. (1998) combined several blazar surveys and derived peculiar relations between the SED parameters of the sources of their samples. They studied FSRQs and BL Lacs discovered in shallow radio surveys (2 and 1 Jy samples) and BL Lacs found in the X-ray flux-limited Einstein Slew Survey ($f_X \gtrsim 10^{-12}$ erg cm^2 s^1). They noted a strong anti-correlation between the luminosity at the synchrotron peak, $L^S_{\rm peak}$, and the frequency of this peak, $\nu^S_{\rm peak}$. They also stressed anti-correlations between the 5 GHz luminosity $\nu L_\nu(5\,\mathrm{GHz})$ and $\nu^S_{\rm peak}$; the γ-ray luminosity L_γ and $\nu^S_{\rm peak}$; and the γ-ray dominance (the ratio of the EGRET γ-ray luminosity to the synchrotron peak luminosity) and $\nu^S_{\rm peak}$ (see Figure 1.8). These correlations were claimed as evidence for the existence of a "blazar sequence". One of their main result is sketched in Figure 1.7 and is based on the correlation shown in the $\log(\nu^S_{\rm peak}) - \log(\nu L_\nu(5\,\mathrm{GHz}))$ plane. The first peak of the SED occurs in different frequency ranges for different luminosity classes: blazars with greater bolometric luminosity have smaller peak frequencies and "redder" SEDs, while blazars of lower bolometric luminosity have higher peak frequencies

and then are "bluer". Moreover, the higher energy peak component correlates positively with the peak frequency of the lower energy one and the luminosity ratio of the high to the low frequency components increases with bolometric luminosity.

These correlations have been further supported by theoretical explanation (see e.g. Ghisellini et al., 1998) and have been explained in the context of the blazar sequence, a well defined trend from luminous, low peaked sources with strong broad emission lines to less luminous, high peaked sources with weak or nonexistent broad emission lines. Subsequent observations of high redshift blazars ($z > 1$, Fabian et al., 2001a,b), and of low power BL Lac objects (Costamante et al., 2001) have extended the blazar sequence at both ends, resulting in agreement with the original trend.

Since the $L^S_{\rm peak} - \nu^S_{\rm peak}$ relation has been found, the blazar sequence has been matter of strong debate and criticisms. If on the one hand several studies support it (Chen et al., 2011), works in other samples did not find evidences of the systematic trend (see e.g. Padovani et al., 2003; Nieppola et al., 2006a).

The detection of a large number of blazars with the *Fermi* satellite (more than 100 objects already in the first three months of observations, Abdo et al., 2009a) provided the unique opportunity to further test this theory in a new energy range. Claims in favor of the sequence have been advanced soon after the released of *Fermi* catalogs (e.g. Ghisellini et al., 2009), supported several evidences, among the others the clear clustering of FSRQs and BL Lacs in two different regions of the $\alpha_\gamma - L_\gamma$ distribution as shown in Figure 1.9. As suggested, this plot could represent the γ-ray selected version of the blazar se-

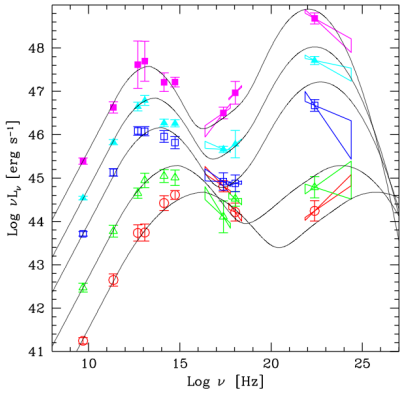

Figure 1.7 The blazar sequence concept of Fossati et al. (1998). The blazar SEDs display a multiwavelength pattern in which FSRQs (toward the top) have higher luminosity and peaks at lower energy, while ISP and HSP have lower luminosity but peaks at higher energy. Thin solid lines are the spectra constructed following analytic approximations.

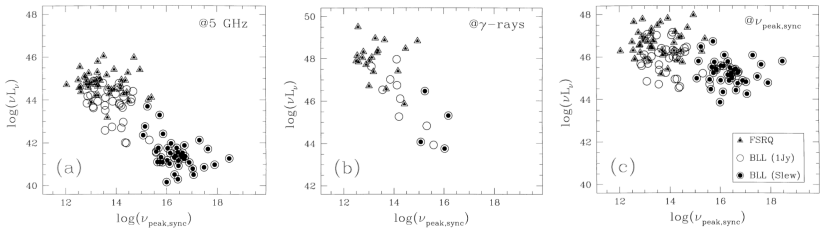

Figure 1.8 Correlations found by Fossati et al. (1998): the peak frequency of the synchrotron component, ν^S_{peak} is plotted against (a) the radio luminosity $L_\nu(5GHz)$, (b) the γ-ray luminosity L_γ, and (c) the fitted peak luminosity of the synchrotron component, L^S_{peak}.

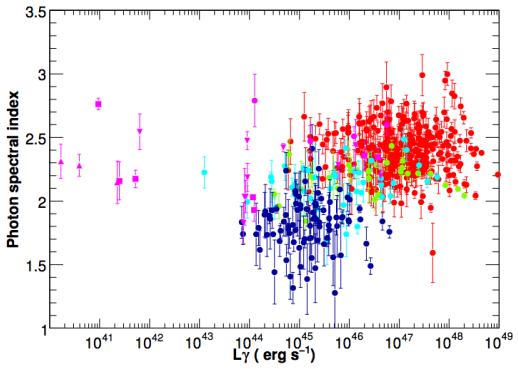

Figure 1.9 Photon index versus γ-ray luminosity derived for the 2LAC sources (Ackermann et al., 2011). Red: FSRQs, green: LSP , light blue: ISP, dark blue: HSP, magenta: non-blazar AGNs (circles: NLS1s, squares: misaligned AGNs, up triangles: starbursts, down triangles: other AGNs).

quence: low power BL Lac objects peak at higher energies, they have smaller γ luminosity and flatter index. FSRQs, instead, peak at lower frequencies, and the peak of their high energy emission (dominating their power output) is below 100 MeV. Despite this, it is important to bear in mind important caveats when interpreting this correlation. For instance, more than half of the BL Lacs lack measured redshifts. Moreover, until the nature of the unassociated sources in the 2LAC, and underlying biases introduced by using different source catalogs (Padovani et al., 2003; Giommi et al., 2012a) are resolved, conclusions about the blazar sequence remain tentative. In addition, it is also worthwhile to mention that the correlation visible for blazars in Figure 1.9 is very weak if FSRQs and BL Lacs are considered separately.

Several major predictions of the blazar sequence that can also be intended as tests for its existence have been indicated by Padovani (2007):

- the anti-correlation will be enhanced in more complete samples;

- since low luminosity objects are almost always more plentiful than high luminosity objects, HSP should be more plentiful than LSP;

- the lack of outliers, i.e., objects that are low peaked and faint, or high peaked and bright.

If any of these predictions are contradicted, then the blazar sequence itself would be invalidated.

Ghisellini and Tavecchio (2008) pointed out that since blazars are anisotropic emitters, the lower left of the $L^S_{\rm peak} - \nu^S_{\rm peak}$ diagram (i.e., sources that have low peaked, faint synchrotron components) should be filled in by sources which are viewed increasingly off-axis. In agreement with this prediction, lower luminosity low-peaked sources have been detected with more sensitive instruments (Meyer et al., 2011; Giommi et al., 2012b). But the lack of sources in the upper right region of the $L^S_{\rm peak} - \nu^S_{\rm peak}$ plot (i.e., sources that have high peaked, bright synchrotron components) could be the result of a selection effect. Since a large fraction of BL Lac objects have featureless optical spectra, their redshifts, and in turn their luminosities, are impossible to determine. These sources could be good candidate to populate the upper right regions, as they could be extremely luminous, distant BL Lacs.

A study that supports the latter idea has been made by means of simulations based on a consistent physical and observational approach. Giommi et al. (2012a) have shown that several (simulated) sources might end up in the high right part of the plane of Fig. 1.10 (a), the prohibited, empty region of the blazar sequence (according with the results of Fossati et al., 1998). These outliers would correspond to most of the radio and X-ray peak selected objects with unknown redshift (red and green filled points in Figure 1.10 a) but with high luminosity and high ν^S_{peak}.

At the same time, Rau et al. (2012) have provided reliable photometric redshifts for eight BL Lacs at $z > 1.3$, and four of these do indeed seem to have $\nu^S_{\rm peak} \gtrsim 10^{15}\,|mathrmHz$ and $L^S_{\rm peak} \gtrsim 10^{46}\,{\rm erg\,s^{-1}}$. Moreover, Padovani et al. (2012) show that the newly discovered HSPs populate the region of parameter space mostly filled by sources with unknown redshift. These are the red points in Fig. 1.10 (b) were it is plotted the bolometric power, namely the sum of the synchrotron and inverse Compton peak powers, for blazars in the Giommi et al. (2012b) sample (selected in the radio, X-ray and γ-ray bands), against ν^S_{peak}. Since these sources lie in the region where there are sources with unknown redshift (basically the ones with totally featureless optical spectra) they argue that these objects are most likely FSRQs that have their emission lines swamped by the non-thermal continuum.

These four high power HSPs and especially the discovery of more sources with these properties indeed would challenge the blazar sequence scenario opening a new perspective not only in the context of

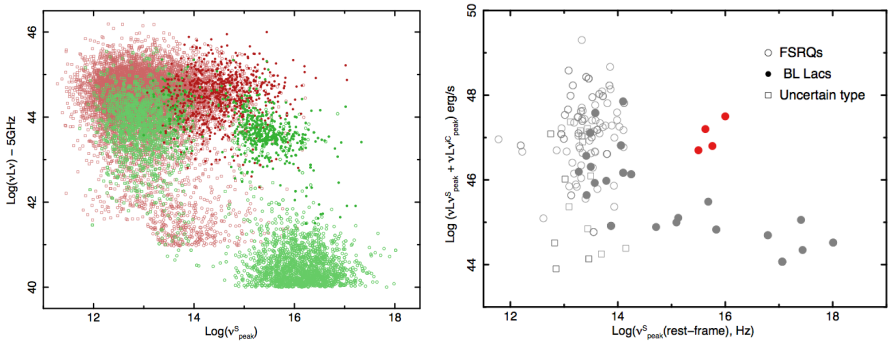

(a) (b)

Figure 1.10 (a): $\log(\nu) - \log(\nu L_\nu)$ plane filled with the simulated objects from the radio flux density limited (red symbols) and X-ray flux limited (green symbols) simulated samples in Giommi et al. (2012a): FSRQs are open squares and BL Lacs are circles. Filled circles represent BL Lacs with very weak lines (EW < 2Å) or totally featureless for which, in a real survey the redshift would most probably not be measured. As they occupy the top right part of the diagram, they are almost all high luminosity HSP sources, "prohibited" in the blazar sequence scenario. (b): bolometric power (see text for details) of the flux-limited samples of blazars of Giommi et al. (2012b) plotted against ν^S_{peak}. The four peak objects (red filled points) discovered by Padovani et al. (2012), are clearly located in a region of the diagram that should be empty according with the blazar sequence.

blazars but also in other fundamental topics (see Padovani et al., 2012, for more details). On the other hand, the confirmation that these blue FSRQs are rare, would strengthen the blazar sequence as have been suggested by Meyer et al. (2012) and Ghisellini et al. (2012). Indeed, the determination of the redshifts of many BL Lacs in the future will most probably be crucial in shedding light into this open debate.

2

ACCELERATION AND EMISSION MECHANISMS

As explained in the previous Chapter, blazars are extremely challenging objects and indeed, the most direct diagnostics for their settings come from the radiation that we observe. This is the final result of a variety of mechanisms that need to be understood in order to explain the features of blazar emission. For instance, by inferring properties of the radiating particle distributions we can then use these particle distributions to deduce the acceleration processes. In turn, acceleration mechanism provide essential clues to the central engine, the conversion of the gravitational energy into the process that energizes the particles. Intense theoretical efforts have been spent in the last decades to provide an exhaustive framework. In the following sections we will complete our view throughout blazars presenting their basic physical processes.

2.1 ACCELERATION MECHANISMS

Since the discovery of cosmic rays, huge efforts were made to investigate the acceleration processes working in the extreme conditions of blazars. Noteworthy, the first remarkable step was made by the Italian physicist Fermi (1949). In his original idea, he assumed that collisions with interstellar clouds would be the main source of energy for the particles. However, this process is very inefficient and it cannot explain the "universal" spectral index[1] observed in different astrophysical environments.

Afterwards, this idea has been elaborated producing a more general and complex framework. Nowadays, to accelerate particle to relativistic energies, the first and second order Fermi acceleration mechanisms are taken into account as possible mechanisms, together with the diffusive shock acceleration scenario (Blandford and Eichler, 1987) where a particle that crosses the shock front gains energy via a first order process resulting with a power law spectrum.

Even if this scenario has been successfully applied to the observed cosmic ray energy spectra, there are still astrophysical cases in which the acceleration processes can results in an electron distribution deviating from a power law. Actually, it has been shown that if the acceleration probability is energy dependent, the power-law turn into a curved distribution with a log-parabolic shape (e.g. Massaro et al., 2004). Moreover, it has to be taken into account the role of stochastic

1 Actually the energy spectrum of many non-thermal sources is well described by the formula $dN(E) \propto E^{-\gamma} dE$ with the spectral index γ ranging between 2 and 3.

acceleration that results from second order mechanism. Historically, the importance of the second order process has been neglected to explain the acceleration in astrophysical jets due the quadratic dependence in the relative energy gain w.r.t. the velocities ratio. Nevertheless, Schlickeiser et al. (1993) demonstrated that the second order process is never negligible behind the shock and Jones (1994) stressed that for non relativistic shocks, first or second order process are not so different in terms of efficiency. More recently, Nodes et al. (2004) have shown that relativistic particle acceleration can result from a three-dimensional turbulent electromagnetic field configuration and Virtanen and Vainio (2005) showed that the second order efficiency can be comparable with the first one.

We can therefore assume that in blazar jets both processes can compete, determining the resulting particle distribution which may show the signature of a non negligible contribution by stochastic acceleration. In particular, the original "universal" picture has now been challenged by recent studies, e.g. in γ-rays, where we are observing several more sources which display a non power law energy spectrum (see e.g. the Second *Fermi* Catalog of AGN, 2LAC; Ackermann et al., 2011). We will dedicate the rest of the section to introduce the first and second order Fermi acceleration.

2.1.1 *First order Fermi acceleration*

Let us assume a shock developed in a plasma with a velocity $U \gg c_s$, where c_s is the sound speed in the medium. In the shock rest frame the fluid flows upstream with velocity $u_1 = |U|$, and downstream with velocity u_2. The compression ratio $r = u_1/u_2$ is the ratio between the two velocities.

Magnetic disturbances are present in the plasma and as long as the associated electric fields are neglected, the only result of the interaction of charged particle with random magnetic field is the pitch angle scattering[2].

A particle crossing the shock front from upstream to downstream, due to the pitch angle scattering, comes back to the upstream region and then crosses again the shock front. The gain of energy in a round loop crossing, for a non relativistic oblique shock is

$$\frac{< \Delta p_I >}{p} = \frac{4}{3} \frac{u_1 - u_2}{v \cos \Theta_1} \tag{11}$$

where v is the velocity of the particle and Θ_1 is the upstream angle between the shock normal and the magnetic field (Jones, 1994). In this case the effective speed of the particle is reduced to $v \cos \Theta_1$.

The particle residence time in the vicinity of the shock is determined by the downstream spatial diffusion coefficient D through

2 the *pitch angle* is the angle between field and velocity.

$t_r = 2D/u_2$. This coefficient depends on the pitch angle frequency ($\nu_\alpha = \langle \Delta\alpha^2 \rangle / \Delta t$), and on the shock obliquity. Then, it can be defined as a combination of parallel and perpendicular terms:

$$D_\parallel = \frac{v^2}{\nu_\alpha} \tag{12}$$

$$D_\perp = \frac{r_L^2 \nu_\alpha}{4} \tag{13}$$

$$D_{\text{eff}} = D_\parallel \cos^2 \Theta_2 + D_\perp \sin^2 \Theta_2 \tag{14}$$

were $r_L = p/eB$ is the Larmor radius of the particle. Given that $v \cos\Theta \gg u$, the probability of the particle to be re-accelerated is:

$$P = \left(\frac{1 - u/v}{1 + u/v} \right)^2 \simeq 1 - \frac{4u_2}{v \cos\Theta} \tag{15}$$

For a relativistic particle ($v \simeq c$) the crossing frequency is $\nu_{cr} = 1/(\eta t_{cr})$ and the re-acceleration probability will be $P = 1 - 4u_2/c$, very close to that for non-relativistic shock. The particle spectral index in this case will be (Ostrowski and Schlickeiser, 1993):

$$\alpha = \log P / \log \left(1 + \frac{\langle \Delta p \rangle}{p} \right) = \frac{3r}{1 - r} \tag{16}$$

The acceleration rate will be given (with a factor of the order of unity) by

$$\frac{\langle \Delta p_{\text{I}} \rangle}{p \Delta t} \sim \frac{4}{3} \frac{u_1 - u_2}{v} v_{cr} = \frac{r - 1}{3 t_{cr}} \tag{17}$$

and the corresponding acceleration time scale for first order can be deduced as:

$$t_{\text{acc}}^{\text{I}} = \frac{3 t_{cr}}{r - 1} \sim \left(\frac{c}{u_2} \right) v_\alpha^{-1} \tag{18}$$

In the diffusive shock acceleration scenario (Blandford and Eichler, 1987) the particle crosses the shock front several times gaining energy via a first order process. When the particle is diffused from downstream to upstream the shock, it crosses the shock many times. The diffusion may results in the particle interacting with the disturbances in the magnetic field of the plasma. The probability that the particle is accelerated depends on a competition between acceleration and escape. In this scenario, the resulting energy spectra of the particle distribution will follow a power-law distribution.

2.1.2 *Second order Fermi acceleration*

A plasma subject to random magnetic fields produces pitch angle scattering with a frequency ν_α and energy changes as well. Actually, the most easily excitable magnetic perturbations are the Alfvén waves and they propagate along the magnetic field with a phase velocity V_A,

developing an electric component smaller than the magnetic one by a factor V_A/v. For relativistic particles, the particle momentum variation between two scatterings will be $\Delta p \simeq (V_A/c)p$. The number of scatterings per cycle near the shock will be $n_{scat} \simeq c/u_1 + c/u_2$ (Ostrowski and Schlickeiser, 1993). The relative mean momentum change per cycle is approximately:

$$\langle \frac{\Delta p_{\rm II}}{p} \rangle \simeq n_{\rm scat} \left(\frac{V_A}{c} \right)^2 \tag{19}$$

The acceleration produced is the "second order" as the relative momentum gain will be proportional to the second power of the velocity ratio (Fermi, 1949). The rate of momentum gain will be the relative momentum gain times the collision frequency:

$$\langle \frac{\Delta p_{\rm II}}{\Delta t p} \rangle \simeq n_{\rm scat} \left(\frac{V_A}{c} \right)^2 \nu_\alpha \tag{20}$$

from which follow the second order acceleration time scale:

$$t_{\rm acc}^{\rm II} \simeq n_{\rm scat} \left(\frac{V_A}{c} \right)^2 \nu_\alpha^{-1} \tag{21}$$

2.2 RADIATION MECHANISMS

In the following section we will give a short review of the most important emission processes acting in the blazar jet, namely synchrotron radiation and Inverse Compton emission. This description is mainly based on Rybicki and Lightman (1979).

2.2.1 *Relativistic beaming*

Relativistic beaming is the process by which relativistic effects modify the apparent luminosity of emitting matter that is moving at speeds close to the speed of light. This process plays a key role in blazars when line of sight of the observer and jet form a small angle and the emitting particles move towards the observer. The main features of the observed spectrum are, namely:
1. Due to the relativistic velocities of the emitting particles, the spectrum collimates into a cone of angle $\sin\theta = 1/\gamma$
2. The observed time interval is different w.r.t. the time interval of emission:

$$\Delta t_{obs} = \Gamma(1 - \beta\cos\theta)\Delta t_{em} \equiv \frac{\Delta t_{em}}{\delta} \tag{22}$$

where δ is the so called Doppler factor. In the case of blazars typical values of Doppler factor are of the order of some tens. If the jet emission is variable, the timescale is then reduced by this effect. In particular, from estimations of the variability of a source it is possible

to infer upper limits on the size of the emitting region.
3. The Doppler effect involves also the frequencies of the photons, that are blue-shifted if the motion is toward the observer. The relation between the observed and emitted frequencies is: $\nu_{obs} = \delta\nu_{em}$ This means that the flux observed in blazars is shifted at higher energies.
4. Another important feature to take into account in presence of relativistic beaming is that the luminosity is highly overestimated. It is demonstrated that the relation between the observed and emitted luminosity is: $mathrmL_{obs} = \delta^p mathrmL_{em}$ where p is a parameter > 1 depending on the jet and emission features (for example, it is 4 for a uniform sphere).

2.2.2 *Synchrotron Emission*

Relativistic particles, centripetally accelerated in a magnetic field, will radiate their energy via synchrotron emission process. Many reviews and books treat this emission mechanism in detail, e.g. Blumenthal and Gould (1970), Rybicki and Lightman (1979), Longair (2010) and references therein. Here we collect the basic formulae used.

Synchrotron emission from a single electron

Consider a particle of mass m and charge e in motion in an uniform magnetic field. Referring to Fig. 2.1, the particle is following the relativistic equations:

$$\frac{d}{dt}(\gamma m\mathbf{v}) = \frac{e}{c}\mathbf{v}\times\mathbf{B} \tag{23}$$

$$\frac{d}{dt}(\gamma mc^2) = e\mathbf{v}\cdot\mathbf{E} \tag{24}$$

The last equation implies that, for small radiated power, γ can be considered as a constant: it follows

$$m\gamma\frac{d\mathbf{v}}{dt} = \frac{e}{c}\mathbf{v}\times\mathbf{B} \tag{25}$$

Separating the velocity components along the line of the magnetic field, $\mathbf{v}_\parallel$, and in a plane orthogonal to the $\mathbf{B}$ direction, $\mathbf{v}_\perp$ and indicating with θ_p the pitch angle between the velocity direction and the magnetic field line, Eq. 25 can be written as:

$$\frac{d\mathbf{v}_\parallel}{dt} = 0, \qquad \frac{d\mathbf{v}_\perp}{dt} = \frac{e}{\gamma mc}\times\mathbf{B} \tag{26}$$

It follows that $\mathbf{v}_\parallel$ is constant, and since $|\mathbf{v}|$ is constant also $|\mathbf{v}_\perp|$ = costant. The solution to this equation is a helical motion of the electron around the field line. The frequency of rotation is

$$\nu_B = \frac{e\mathbf{B}}{2\pi\gamma mc} = \frac{\nu_L}{\gamma}, \qquad \text{with} \quad \nu_L = \frac{e\mathbf{B}}{2\pi mc} \tag{27}$$

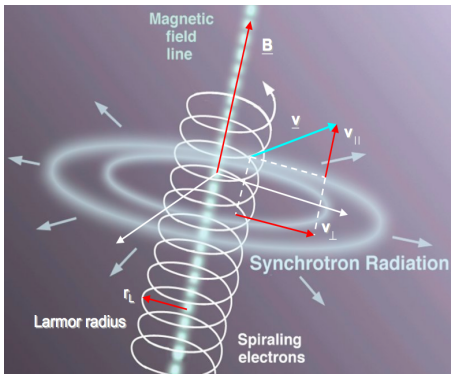

Figure 2.1 Helical motion of an electron in a uniform magnetic field

where ν_L is the *Larmor frequency*. A direct formula to evaluate the latter in CGS units is given by

$$\nu_L = 2.80 \times 10^6 B(\mathrm{G}) \, \sin\theta_p \, \mathrm{Hz} \tag{28}$$

The motion in the plane perpendicular to the magnetic field line is circular with Larmor radius r_L:

$$r_L = \frac{mc^2}{eB} \, \gamma \, \beta \sin\theta_p = 1.71 \times 10^3 \gamma B^{-1}(\mathrm{G}) \sin\theta_p \, \mathrm{cm} \tag{29}$$

The acceleration is perpendicular to the velocity and, from the Larmor formula, the total emitted power is

$$P = \frac{dE}{dt} = \frac{2}{3} r_e^2 c \beta^2 \gamma^2 B^2 \, \sin^2 \, \theta_p = 2\sigma_T c \beta^2 \gamma^2 \frac{B^2}{8\pi} \sin^2 \, \theta_p \tag{30}$$

that in CGS units gives

$$P = 1.59 \times 10^{-15} \beta^2 \gamma^2 B^2(\mathrm{G}) \sin^2\theta_p \, \mathrm{erg\,s^{-1}} \tag{31}$$

For an isotropic distribution of velocities it is necessary to average this value over all pitch angles; then this will given

$$\langle P \rangle = \frac{4}{3} \sigma_T c \beta^2 \gamma^2 u_B = 1.06 \times 10^{-15} \beta^2 \gamma^2 B^2(G) \, \mathrm{erg\,s^{-1}} \tag{32}$$

where $\mu_B = \frac{B^2}{8\pi}$ is the energy density of the magnetic field.

Due to beaming effects, the resulting spectrum will appear to be concentrated in a narrow cone centered on the particle's velocity. Thus the observer will see a pulse of radiation confined in a time interval smaller than the gyration period and the spectrum will spread on a much larger range of frequencies than one order of ν_B. Detailed calculations allow to write the synchrotron spectrum for the single ultrarelativistic electron ($\beta \sim 1$) as

$$\frac{dP}{d\nu} = c_0 \mathcal{F}_S(\frac{\nu}{\nu_s}) \tag{33}$$

where

$$[l]c_0 = \frac{\sqrt{3}e^3 B \sin\theta_p}{mc^2} = 2.34 \times 10^{-22} B(\mathrm{G}) \sin\theta_p \,\mathrm{erg\,s^{-1}\,Hz^{-1}} \quad (34)$$

$$\nu_c = \frac{3}{2}\gamma^2 \nu_L \sin\theta_p = 4.20 \times 10^6 \gamma^2 B(\mathrm{G}) \sin\theta_p \,\mathrm{Hz} \quad (35)$$

The latter is the synchrotron critical frequency, and the *synchrotron kernel* $\mathcal{F}_S(\frac{\nu}{\nu_c})$ can be defined by the relation

$$\mathcal{F}_S(\frac{\nu}{\nu_c}) = \mathcal{F}_S(\chi) = \chi \int_\chi^\infty K_{\frac{5}{3}}(\eta) d\eta \quad (36)$$

where $K_{\frac{5}{3}}$ is the modified Bessel function of $5/3$ order

$$K_n(\eta) = \frac{\delta(n + \frac{1}{2}(2\eta)^n}{\sqrt{\pi}} \int_0^\infty \frac{\cos y}{(y^2 + \eta^2)^{n+\frac{1}{2}}} \quad (37)$$

The maximum of the single electron spectrum correspond to the frequency ν_m, given by the relation

$$\nu_m \simeq 0.29\, \nu_c = 1.22 \times 10^6 \gamma^2 B(G) \sin\theta_p \mathrm{Hz} \quad (38)$$

the total emitted power for a single electron is obtained integrating equation 33 over the frequencies

$$P_S = \int \frac{dP}{d\nu} d\nu = 2\sigma_c \beta^2 \gamma^2 u_B \quad (39)$$

For each emission process it is possible to define a cooling time as:

$$t_{\mathrm{cool}} = \frac{\gamma mc^2}{P} \quad (40)$$

Synchrotron emission from an electron distribution

We consider the case of the synchrotron emission from an electron population with a distribution $N(\gamma)$ representing the number density of electrons per unit of volume and energy. The value of γ_{min} and γ_{max} define the electrons energy range. Under the assumption that the electrons are uniformly distributed in the space and that the velocities are isotropically distributed, the emission coefficient is given by:

$$j_\nu^S(\nu) = \frac{1}{4\pi} \int_{\gamma_{\mathrm{min}}}^{\gamma_{\mathrm{max}}} \int \frac{dP}{d\nu} N(\gamma) d\nu \quad (41)$$

Synchrotron Self Absorption

When considering the synchrotron emission, it must be taken into account also the photon-electron interactions in the magnetic field. The results of this is the absorption of the photon which will give up its energy to the particle. Another process that can occur is the stimulated

emission or negative absorption, in which a charge is induced to emit more strongly into a direction and at a frequency where photons are already present. These processes can be interrelated by means of the Einsteins coefficients, generalized to continuum states. For a detailed calculations we remind to Rybicki and Lightman (1979).

2.2.3 *Inverse Compton Emission*

The Compton scattering refers to the general interaction between photons and particles. In the following, we will focus on the electron case, relevant in high energy astrophysical processes. For low photon energies, $h\nu \ll mc^2$, the scattering of radiation from free charges can be treated according to the classical Thomson scattering, in which the incident photons are approximated as a continuous electromagnetic wave. In this case, the energy of scattered photons is conserved and the scattering is called elastic. Quantum effects about the interaction between electrons and photons appear in two ways: first, through the kinematics of the scattering mechanism and then, through the change of the cross section. In the astrophysical framework, the so called inverse Compton scattering occurs when in the scattering, scattered photons gain energy from electrons.

Scattering From a Single Electron in the Electron Rest Frame

Let ϵ'_i and ϵ'_f be the energies of the photons before and after the collision respectively in the electron rest frame. Both energies are expressed in unit of $m_e c^2$ by

$$\epsilon' = \frac{h\nu'}{m_e c^2} \tag{42}$$

From Compton kinematics it follows:

$$\epsilon'_f = \frac{\epsilon'_i}{1 + \epsilon'_i(1 + \cos(\lambda))} \tag{43}$$

where $\cos(\lambda)$ is the scattering angle. Two approximations depending on the value of ϵ' can be deduced:

- ($\epsilon'_i \ll 1$) (Thomson limit), there is no change in the scattered photon energy $\epsilon'_f \simeq \epsilon'_i$;
- $\epsilon'_i \gg 1$) two cases are derived: for small angles θ (forward diffusion) we have $\epsilon'_f \simeq \epsilon'_i$; while for large angles the value of ϵ'_f is of the order of the unity.

The differential scattering cross section is given by the Klein Nishina formula. For non polarized incident radiation it is:

$$\frac{d\sigma_{KN}}{d\Omega} = \frac{3}{16\pi}\sigma_T \frac{1}{[1 + \epsilon'_i(1-\lambda)]^2}\left[\frac{\epsilon'^2_i}{(1-\lambda)} + \epsilon'_i(1-\lambda) + 1 + \lambda^2\right] \tag{44}$$

where σ_T is the Thomson cross section. For low values of photon energy Eq. 44 become the classical Thomson scattering:

$$\frac{d\sigma_{KN}}{d\Omega} = \frac{3}{16\pi}\sigma_T(1-\lambda)^2 \tag{45}$$

When the Compton scattering is viewed in the frame where electrons are relativistic $\gamma \gg 1$ (laboratory frame) it is generally referred as *inverse Compton scattering*. When electrons are ultrarelativistic the rule for angle transformations implies that the collision in the electron rest frame are almost head-on (see Fig. 2). Under this approximation it follows that the energy of the scattered photon in the laboratory frame will be given by:

$$\epsilon_f = \gamma^2\epsilon_i\frac{(1-\beta\cos\theta)[1+\beta\cos(\phi'+\theta')]}{1+\gamma\epsilon(1-\beta\cos\phi)(1-\beta\cos\theta')} \tag{46}$$

The minimum and maximun values for the final photon energy are

$$\epsilon_1 \leq \epsilon_f \leq \frac{4\epsilon_i\gamma^2}{1+4\gamma\epsilon_i} \tag{47}$$

It is possible to distinguish the maximum energy gained by inverse Compton scattering in the Thomson and Klein Nishina regime, respectively:

$$\begin{cases} \epsilon_{f,max} \simeq 4\epsilon_i\gamma^2, & (4\epsilon_i\gamma \ll 1) \\ \epsilon_{f,max} \simeq \gamma, & (4\epsilon_i\gamma \gg 1) \end{cases} \tag{48}$$

Inverse Compton spectrum

The spectrum emitted by an arbitrary electron distribution, $N(\gamma)$, upscattering an arbitrary photon distribution $(J_\nu(\nu_i))$, can be derived following the approach of Blumenthal and Gould (1970). This derivation is accurate for highly energetic electrons ($\gamma \gg 1$), and for isotropic electrons and photons distributions. The emission coefficient is given by:

$$\int d\gamma N(\gamma) f(\nu_i, \nu_f, \gamma) \tag{49}$$

where $f(\nu_i, \nu_f, \gamma)$ is the Compton kernel of Jones (1968) given by

$$f(\nu_i,\nu_f,\gamma) = \frac{K}{\nu_i\gamma^2}[2q\ln q + (1+2q)(1-q) + \frac{(4\epsilon_i\gamma q)^2}{2(1+4\epsilon_i\gamma q)}(1+q)] \tag{50}$$

where

$$\begin{aligned} K &= \tfrac{3ch\sigma_T}{16\pi} \\ q &= \tfrac{\epsilon_f}{4\epsilon_i\gamma(\gamma-\epsilon_i)} \end{aligned} \tag{51}$$

For a given ϵ_i the kinematic constraint of Eq. 47 gives the integration range for Eq. 49.

2.3 EMISSION MODELS

As shown in many models, the first spectral component of blazars is synchrotron emission from a population of relativistic electrons in the jet. The origin of the high-energy component is more debated. Indeed, the discovery of high energy γ-rays from over 60 AGNs with the EGRET instrument on the Compton Observatory, showed that the non-thermal γ rays production is an important dissipation mechanism of jet energy generated by black-hole accretion. Historically, two emission models were proposed to explain the GeV-TeV emission from blazars: namely leptonic and hadronic models.

In the case of the most popular *leptonic models*, the same population of non thermal electrons (and possibly positrons) responsible for the radio to X-ray SED could also be responsible for γ-ray emission, through Compton upscattering of the synchrotron photons off their own parent electrons: the synchrotron self-Compton (SSC) process (e.g. Böttcher et al., 2002). Alternatively, electrons scatter external photons that originate outside the jet (external Compton, EC models). In BL Lac objects the lack of strong emission lines suggests a minor role of ambient photons and hence supports the SSC models; on the other hand FSRQs are often better modeled with EC.

In *hadronic models*, the high energy radiation is produced by hadronic interactions of the highly relativistic baryonic outflow with the ambient medium, and/or by interactions of ultra high energy protons with synchrotron photons produced by electrons (Mannheim and Biermann, 1992), with the jet magnetic field (Aharonian, 2000), or with both (Dermer and Schlickeiser, 1993).

In this Section we will briefly describe the two emission scenarios, with particular attention (see § 2.3.3) to the main model that we will use for SED fit in Chapter 4. We stress that at present, the measured SEDs of blazars can be successfully explained in first approximation by the leptonic origin scenario. Instead, no observational results have yet confirmed the hadronic origin scenario.

2.3.1 *Hadronic Models*

Proton synchrotron and photohadronic models for blazars have been proposed. Radio observations support the idea that relativistic protons are present in AGN jets. However, to explain the observed AGN luminosities, very large proton velocities are necessary. This fact, together with the very short variability observed in some blazars, unlikely to happen in relatively slow hadronic processes, disfavor the hadronic emission mechanism with respect to the leptonic one.

In hadronic models the protonic component would contribute to the high energy bump, while primary electron synchrotron radiation is still usually invoked to make the non-thermal radio/optical/X-ray

synchrotron blazar emission. The three main processes able to convert the energy of relativistic protons into high energy radiation are:

1. direct synchrotron radiation of protons,
2. photo-meson production ($p + \gamma \rightarrow p + k\pi$)
3. nuclear collisions ($p + p \rightarrow \pi + X$).

The first two processes are known to be quite inefficient, and they can be important in AGN jets only for proton energies $\gtrsim 10^8 - 10^10$ GeV. Actually, at such high energies the time scales of the proton energy losses can become comparable to or shorter than the propagation time scale observed in AGN jets. For energetic protons, the energy losses are dominated by photo-meson production, and proton-induced cascade can induce γ rays production (see e.g. Mannheim, 1993). The radiation target of photo-meson output is dominated by near/mid-IR radiation. In blazars environment, this radiation is provided by hot dust at distances of $\sim 1 - 10$ pc from the central engine and/or by the synchrotron radiation due to relativistic electrons in the jet.

The main product of the photo-meson processes are pions. The pions carry about $\frac{1}{3}$ of the proton energy and convert it into photons, neutrinos, and in turn, to electrons and positrons by means of muons. The photons injected by neutral pions are immediately absorbed by soft photons in the pair production process. Most of this energetic radiation can produce two more generations of photons and pairs.

The final result of the synchrotron supported pair cascade is the high energy component, which will be characterized by a cutoff since it will undergo $\gamma\gamma$ pair production processes. The maximum energy for such photons will therefore be ~ 30 GeV in FSRQs, as determined by external UV radiation, and ~ 1 TeV in BL Lac objects, as deduced by infrared radiation of dust.

Considering now the third mechanism, it assumes that the proton energy losses are dominated by collisions with the ambient gas and requires less extreme proton energies. Alike the other processes, the final products will be relativistic electrons/positrons, photons and neutrinos. The process can be efficient only if the column density of the target is $n_H \geq 10^{26}$ cm^2. The proposed targets are, for example, funnels formed around the black hole by a geometrically thick disk or interactions of jet with cloud and/or stellar winds (see e.g. Bednarek, 1993; Dar and Laor, 1997, respectively). The disadvantage of this model is that relativistic protons may easily suffer deflections by magnetic fields before colliding with the nuclei, hence resulting in a lack of collimation of the radiation.

2.3.2 *Leptonic Models: SSC and EC Scenario*

Leptonic models consider the inverse Compton scattering of soft photons by the same electrons responsible for the synchrotron emission. Different sources of soft photons have been considered and, depending on the population of soft photons dominating the IC process, two different models are generally discussed: the synchrotron self Compton (SSC) and the external Compton (EC) models. Probably the two mechanisms are present simultaneously in blazars. For example, one of the results of the 2LAC catalog (Ackermann et al., 2011) is that the mean fractional variability of FSRQs is greater than the one of BL Lac objects. This suggests that the two categories may intrinsically be different: higher energy, rapidly cooling electrons make the GeV emission in FSRQs through external Compton scattering processes, whereas lower energy, slowly cooling electrons make the GeV emission in BL Lac objects due to SSC processes.

Usually the SEDs of BL Lac objects are successfully modeled with synchrotron and SSC components from broken power-law electron distributions with low energy cutoffs. Concerning FSRQs the picture is still foggy. The strong thermal features often observed in FSRQs at optical/UV frequencies suggest that their environment is rich of soft photons produced by the accretion disk and/or reprocessed by the BLR. This implies that the energy density of the external soft radiation is much higher than the one of the synchrotron radiation. Therefore, traditionally, it has been thought that the most important process for γ rays production may be EC, with the γ-ray production located close to the central black hole, where the external photons can serve as seed photons for IC scattering.

But this picture was challenged already in the EGRET era, by the observations of connection between radio outburst and γ-ray flares (e.g. Lindfors et al., 2006) and, in addition, by observations of presumably co-spatial radio-VHE emissions. Actually, at least as observed in some sources, the γ-ray detections are coincident with zero-separation epochs of new knots emerging from the 43 GHz VLBA core (see e.g. the case of AO 0235+164, Marscher and Jorstad, 2010), thus supporting the idea that VHE γ rays could be emitted in these knots, tens of parsecs from the central core. Indeed whether in FSRQs the γ rays are originated inside BLR or further out remain still a challenging topic.

Synchrotron Self Compton Emission

Conventional scenarios differ on the origin of the soft target photons that undergo IC process. Simple SSC models assume that energetic photons observed in blazars are produced by IC scattering of synchrotron photons with the same electronic population emitting them. If the magnetic field, electron density, and particle energy decrease outward along the jet, the highest energy synchrotron emission orig-

inates primarily from the innermost region, while longer wavelength emission comes from farther, extended regions. Therefore, the Compton component is presumably produced by scattering of ambient UV or X-ray photons by the same electrons that are radiating the synchrotron photons.

Additionally, in the single-zone homogeneous SSC model, the radiation is considered to be produced in a homogeneous emitting region by a single electron population. In this scenario, synchrotron and IC emissions are strongly linked, allowing to derive robust constraints on the basic physical quantities of the jet and often, the additional knowledge of the location of the two peaks and their fluxes, together with the variability timescale, suffices to derive unambiguously all relevant physical parameters. In § 2.3.3 we will describe the mechanism, originally introduced by Tavecchio et al. (1998), which is also the primary model that will be applied to derive basic physical constrains for the sources that will be studied in Chapter 4. More elaborated models for the observed emission have been proposed, such as SSC models with multiple emission zones (Graff et al., 2008).

External Compton Radiation

In the external Compton scenario it is assumed that soft photons produced in the central region of the AGN, probably by the accretion disk or reprocessed by the gas in the BLR, dominate over the synchrotron photons. Originally proposed by Dermer and Schlickeiser (1993); Boettcher (2010), the model considered the direct UV emission from the accretion disk as the principal source of soft photons. However, as pointed out by Sikora et al. (1994), the de-beaming suffered by the radiation directly coming from the disk in the reference frame of the jet, induces a strong depression of this contribution. Despite this, it has to be considered that the primary disk radiation reflected or reprocessed by the gas of the BLR and beamed in the jet frame can provide an important contribution to the emission: this radiation can be considered isotropic in the BLR rest frame and is strongly amplified in the rest frame of the emitting source. In addition, Błażejowski et al. (2000) pointed out that IC scattering of the thermal near-IR radiation emitted by the dust of the torus could provide the dominant contribution to the high energy emission, especially in the energy band 10 keV – 100 MeV.

With respect to the leptonic models (see details in next paragraph), this scenario requires two more ingredients: the energy and the density at peak of the external photons as seen by the moving blob. On the other hand, the model contains two additional degrees of freedom and the evaluation of the parameters could become degenerate. Moreover, the picture is complicated by the fact that these new quantities are related to the corresponding quantities in the observer frame through the bulk Lorentz factor Γ and depend on the geometry of the

system (Dermer and Schlickeiser, 2002). This causes an additional dependence of Γ in the EC spectra.

2.3.3 *Relating SSC and IC Spectral Parameters to Observed Quantities*

It is commonly accepted that the emission from the jets is generated by blobs of electrically charged material accelerated to ultra relativistic velocities by relativistic shock waves. If observed at large angles, in fact, as in the case of radio galaxies, the emission from the jets is dominated by a non-thermal component. This is unanimously attributed to synchrotron radiation, emitted by ultra relativistic electrons interacting with the randomly oriented magnetic field that is present inside the jet and peaking at radio frequencies. The detection of this emission was the first evidence of the ultra relativistic nature of the emitting particles. A further evidence came from the detection of regions in apparent superluminal motion in some AGNs.

The modeling that will be considered in our analysis refers to Tavecchio et al. (1998) and Maraschi and Tavecchio (2003), and can be explained in the framework of the simplest homogeneous SSC model. This model suggests that synchrotron radiation is produced in a single zone of the jet moving relativistically at small angle w.r.t. the observer's line of sight. Photons up to X-ray energies are produced by relativistic electrons through the synchrotron process and are subsequently inverse-Compton scattered by the same electrons to energies in the γ-ray band. We can think of it as a blob of radius R, containing relativistic electrons immersed in a tangled magnetic field. The resulting radiation will be strongly subject to relativistic effects. We can assume that the emitters move toward the observer with Doppler factor $\delta = [\Gamma(1 - \beta\cos\theta)]^{-1}$, where Γ is the bulk Lorentz factor and $\beta = v/c$.

Below and above both peaks, in the $\nu - \nu F_\nu$ representation, the photon distribution can be usually well described with increasing and decreasing power laws (of indices α_1 and α_2). Hence, given the fact that the observed spectral shape requires steepening of the relativistic electron spectrum with the increasing energy, the primary electron spectrum can be approximated with a broken power law that can be described as follow:

$$N(\gamma) = \begin{cases} K\gamma^{-n_1}, & \text{if } \gamma < \gamma_b \\ K\gamma_b^{n_2-n_1}\gamma^{-n_2}, & \text{if } \gamma > \gamma_b \end{cases} \tag{52}$$

The indexes n_1 and n_2 are greater and smaller than 3, below and above the break energy ($\gamma_b m_e c^2$), respectively, reflecting the Lorentz factor of the electrons at the break. In these assumptions, the model is totally constrained by means of 7 parameters: the magnetic field intensity B, the size of the emitting region R, the Doppler factor δ, the slopes n_1 and n_2, the Lorentz factor of the electrons at the break

γ_b and the electron density parameter K. The peak synchrotron power is emitted by electrons with the break energy $E_b = \gamma_b m_e c^2$.

The above parameters are needed to physically constrain blazars mechanisms and can be inferred by the determination of observable quantities in the SEDs, namely, the indices α_1 and α_2, the frequencies of the synchrotron and inverse Compton peaks ν_S and ν_C, and the peak luminosities $L_S(\nu_S)$ and $L_C(\nu_C)$. The last necessary ingredient is the minimum timescale of variation, $t_{\rm var}$, which can be directly connected to the source dimension, and hence the parameter R. Through the causality relation actually we have $R \leq c\delta t_{\rm var}(1+z)^{-1}$, where z is the redshift of the source. In turn, calculating the size of the emitting region allows to evaluate at which distance from the central black hole the jet originates.

As we will see in Chapter 4, such model reproduces reasonably well the data in most cases although we have to note that one-zone models cannot reproduce the spectrum at the lowest frequencies, since the emission is self-absorbed below the millimeter band. It is generally assumed that this part of the SED is due to outer regions of the jet that is not important for the modeling of the high-energy emission.

3

THE *FERMI* LARGE AREA TELESCOPE: INSTRUMENT OVERVIEW, DATA AND ANALYSIS

The Large Area Telescope (LAT) is the primary instrument on board the *Fermi Gamma-ray Space Telescope* (*Fermi*)[1]. The LAT is an imaging telescope detecting photons from 20 MeV to more than 300 GeV. The second instrument on board *Fermi* is the γ-ray burst monitor (GBM), dedicated to the study of transient phenomena in the 8 keV to 40 MeV energy range.

This chapter we will introduce the reader to LAT data and their analysis. In paragraph 3.1 we will give a brief overview of the detector and data taking, then we will present the analysis chain which assigns to each event the best estimate of energy and arrival direction and reduces the backgrounds by about six order of magnitudes.

An essential task for the interpretation of data is the understanding of the instrument performance, which is modeled using both Monte Carlo simulations and in-flight data. We will briefly describe the LAT performance and how it is modeled through Instrument Response Functions (IRFs). We will then introduce the reader to the statistical technique mainly used to analyze LAT data, the likelihood analysis based on Poisson statistics, and to the high-level analysis environment developed by the LAT team.

Finally, in paragraph 3.5 we will discuss the strong γ-ray background that need to be taken into account when using LAT data, namely the Galactic Diffuse and the Extragalactic Diffuse components.

This chapter aims to provide the reader with a comprehensive introduction about LAT data and their analysis. The work developed for the purposes of this thesis will be presented in Chapter 4 and Chapter 5.

3.1 LAT ORBITAL ENVIRONMENT, INSTRUMENT, DATA ANALYSIS

3.1.1 *The Fermi LAT on orbit*

The *Gamma ray Large Area Space Telescope* (GLAST) has been successfully launched on 11 June, 2008 and then renamed the *Fermi Gamma Ray Space Telescope*. After a commissioning phase the LAT began its

1 http://fermi.gsfc.nasa.gov/

nominal Science operations on August 13, 2008[2]. The observatory is on a circular orbit around the Earth, at $\sim$ 565 km with an inclination of 25.6° with respect to the Equator so that the Earth magnetosphere will partially shield the instrument from cosmic rays. The primary observing mode for *Fermi* is the scanning mode, where the LAT monitors the whole sky every two orbits ($\sim$ 3 hours). For this purpose the spacecraft rocks north and south about the orbital plane on alternate orbits. Namely the LAT boresight is offset from the zenith with respect to both the north and south orbital poles by a characteristic rocking angle (35°)[3]. The orbit of *Fermi* has a precession period of $\sim$ 53.5 days. Calibration runs, which may involve or not pointings, are also periodically performed.

The LAT (Atwood et al., 2009) is an imaging, wide-field-of-view, γ-ray telescope, detecting photons from 20 MeV to more than 300 GeV. The instrument is a pair-tracking telescope, composed by a 4×4 array of towers. The latter are inserted in an aluminium grid, the structural backbone of the instrument, which also conducts heat away to the radiators. A segmented anticoincidence detector (ACD) covers the tracker array. In each tower a converter-tracker module is located on top of the corresponding calorimeter module while on the bottom the Tower Electronics Modules (TEM) are placed with a programmable trigger and Data Acquisition System (DAQ). A foam thermal blanket surrounds everything, providing a light-tight cover and preventing damage by micrometeor hits. Figure 3.1 provides a schematic illustration of the LAT.

High-energy γ rays interact with matter mainly through production of $e^+ - e^-$ pairs. Each LAT converter-tracker module (Atwood et al., 2007) contains high-Z material (tungsten), which facilitates the conversion into pairs (being the conversion probability proportional to Z^2), and silicon microstrip detectors, which detect the passage of crossing radiation and requires no consumables and limited operational power.

For the backbone structure of the planes carbon has been chosen because of its large radiation length, high modulus (stiffness) to density ratio, good thermal conductivity and thermal stability. The sensitive tracker apparatus consists of 18 (x, y) tracking planes of similar construction, each with two layers (x and y) of single-sided silicon strip detectors and, depending on its position, a tungsten (W) foil of variable thickness. The first 12 planes are interleaved with the tungsten

2 The LAT was operated in the standard Science operation mode almost continuously since 4 August, 2008.

3 The rocking angle used to be 35° at the beginning of the mission, and later, on 2009 September 3, it was increased to 50° to improve the battery performance and extend their lifetime, being its cooling more efficient when the bottom of the spacecraft points away from the Earth. As a result of this change, the amount of the Earth limb that is subtended by the FoV of the LAT during survey-mode observations increased substantially. The most noticeable consequence is a much larger contribution to the LAT data volume from atmospheric γ rays.

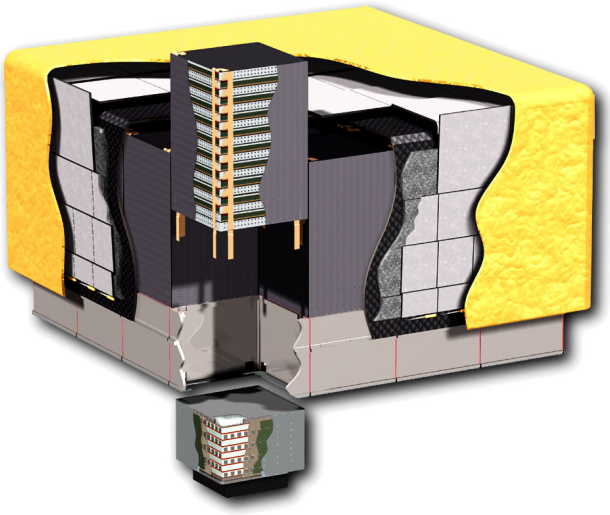

Figure 3.1 Schematic view of the LAT (Atwood et al., 2009): a tower is cut-away showing the tracker and calorimeter module. The real telescope dimensions are 1.8 m×1.8 m×0.72 m.

foils with a thickness of 0.03 radiation lengths (*thin* or *front* section) to maximize the angular resolution at low energies while limiting the Coulomb scattering. The following 4 with a thickness of 0.18 radiation lengths (*thick* or *back* section) to maximize the conversion probability at high energies, thus maximizing the effective area. Finally, the last two planes have no converter foils in order to ensure an accurate measurement of the entering point in the calorimeter[4] The total tracker depth is about 1.5 radiation lengths.

The aspect ratio of the tracker (height/width) is 0.4, allowing a large field of view (FoV) of 2.4 sr and guaranteeing that nearly all converted events will go through the calorimeter. The tracker contributes to the first-level trigger for the LAT. This important new feature w.r.t. to the previous γ-ray instruments is possible because of the choice of silicon-strip detectors, which do not require an external trigger. Each detector layer generates a logical signal OR of all of its 1536 channels, and the coincidence of successive layers (typically 3 x – y planes) provides a trigger request that will be used by subsequent subsystems. The read-out electronics are fully described in Baldini et al. (2006). Noteworthy, all of the LAT instrument subsystems utilize technologies that do not use consumables, such as the gas of tracking spark chambers in previous high-energy γ-ray telescopes.

Inside the tower is positioned a calorimeter module of 96 CsI crystals doped with Thallium. These are arranged in an eight-layer hodoscopic configuration so that each layer is aligned 90° with respect

4 The basic tracker trigger primitive is 3-in-a-row and conversion in the last two layers would yield no additional LAT events.

to the previous one, forming an x–y array. A calorimeter module is thus segmented in both depth and lateral directions to improve energy resolution, with a total thickness of $\sim$ 8.6 radiation lengths. Crystals are read out by photodiodes at each side, giving both longitudinal and transverse information about the energy deposition pattern. Each crystal provides three spatial coordinates: two discrete coordinates from the location of the crystal in the array and the third coordinate given by measuring the light yield asymmetry at the ends of the crystal along its long dimension. The calorimeter provides the measurement of the energy deposited by the shower initiated by the $e^+ - e^-$ pairs, and also images the shower development, enabling the estimation of the energy leakage and discrimination of hadronic showers.

The third LAT subsystem is the ACD, critically important for the identification of charged cosmic rays hitting the LAT. Details of its design can be found in Moiseev et al. (2007) and Atwood et al. (2009).

The ACD discriminates charged particles and plays an essential role in the rejection of charged background. As noted, the Earth magnetosphere will partially shield the instruments from cosmic rays due to the circular low Earth orbit and particular inclination of the telescope. Nonetheless, the average particle flux is 10^5 times the γ-ray flux and this makes the charged background rejection a fundamental issue. Moreover the design for the ACD requires the capability to reject entering charged particles with an efficiency 99.97% for detection of singly charged particles entering the FoV of the telescope. In addition, since the LAT was designed to detect photons up to hundreds of GeV, it is crucial to minimize the "self-veto" effect, i.e. hard X-ray back-scattering (often referred to as backsplash) from showers in the calorimeter (Esposito et al., 1999).

All these requirements have been addressed thanks to the experience acquired with the LAT predecessor, the Energetic Gamma Ray Experiment Telescope (EGRET). Segmenting the ACD into 89 plastic scintillator tiles provides spatial information that in turn can be correlated with the signal from tracker and calorimeter modules. Scintillation light from each tile is recorded by wavelength shifting fibers embedded in the scintillator and connected at their ends to two photomultiplier tubes (PMTs). For a better coverage, the adjacent tiles overlap in one direction, while the remaining gaps between tiles are covered by flexible scintillating fiber ribbons with $>$ 90% detection efficiency.

Data acquisition and Triggering

The DAQ elaborates the information from the other subsystems and provides a first on-board event analysis. It constructs from the subsystems triggers requests (at an average total rate of $2 - 3$ kHz) and filters the events that will be downlinked reducing them to a rate of

$\sim$ 500 Hz. The first part of the acquisition is managed by the TEM. The latter is present in each tower and it relates the information from the tower subsystems; it interfaces the signals from the tracker and from the calorimeter and generates tower-based triggers. At the entire instrument level, a global unit collects signals from all the electronics module and distributes the clock signal. In addition it provides an interface with the ACD, generates instrument-wide triggers based on the information received from the TEMs and the ACD interface and builds the events with the information received from the whole apparatus, sending them to the event processor units (EPUs).

The minimum read-out time per event is 26.5 μs, due to the transmission of the trigger signal between the different units. During the event read-out, the different subsystems send a busy signal to the global unit, which generates the overall deadtime and send it to Earth along with data. The trigger is designed in order to minimize the deadtime due to background events. Triggers are generated by any of the TEMs, depending on whether there is a signal over threshold for three planes in a row or an energy deposition threshold is exceeded in any of the calorimeter crystals (with two different thresholds for low-energy and high-energy events). Non-detector based trigger inputs are used for calibration and diagnostic purposes, either derived from a periodic clock or from an external request.

Since the data volume that can be downlinked within the allocated bandwidth is limited, a first selection of the events on board is required. The two EPUs implement the onboard filtering with the purpose of reducing the contamination by charge particles which are mainly background due to cosmic ray interactions. The onboard analysis is designed in order to maximize the efficiency for γ-ray detection keeping the background within the bandwidth allowed for downlink. Currently all events exceeding a threshold of raw energy deposited in the calorimeter (in the range $10 - 20$ GeV) are downlinked at Earth for analysis since their rate is low and do not take up much bandwidth.

The LAT orbit is such that it will spend a fraction of time in the South Atlantic Anomaly (SAA), a zone over Brazil characterized by a high density of charged particles. Due to the offset dipole geometry of the Earth magnetic field, particles are trapped in this region such that the SAA can have fluxes exceeding by several orders of magnitude those in the rest of the orbit. In such a hard radiation environment the tracker electronics would be saturated with a drastic reduction of the livetime. Besides, high currents generated in the ACD PMTs would exceed the safe operation limits causing a rapid deterioration. Therefore the instrument is not taking data while traversing the SAA and bias voltages of the PMTs are lowered from 900 V to $\sim$ 400 V (Abdo et al., 2009e). The main effect is the loss of exposure in the southern celestial hemisphere. The SAA perimeter was conservatively defined prior to launch, and re-evaluated in the commissioning phase,

so that the turn-off entails a loss in observation time of $\sim 13\%$ of the total on-orbit time (Abdo et al., 2009e).

3.1.2 *Event Reconstruction and classification*

The event analysis process performed on ground starts as soon as data are downlinked to Earth. If one considers that the LAT detects several hundred events every second, this is particularly challenging as we have to transform the individual channel signals into a particle interaction pattern. The main steps can be summarized as follows:

- Data are decompressed and individual channels information are converted to more physically motivated pattern (e.g. grouping signals in the ACD by tile).
- The reconstruction of the event is achieved applying pattern recognition and fitting algorithms commonly used in high energy particle physics experiments. Individual tracker tracks and energy clusters in the calorimeter are correlated to signals in the ACD.
- Figures of merit for the event are evaluated from the collections of tracks and clusters and then associated to the ACD information. Afterwards multivariate analysis techniques aim to determine the energy and direction of the event and to construct estimators that the event is in fact a γ-ray interaction.
- Event selection criteria are applied to populate the various γ-ray event classes.

In addition to these procedures, the processing pipeline automatically verifies the data integrity at each step and provides all the ancillary data products related to calibration and performance monitoring of the LAT. In the following paragraphs we will provide the main insights necessary for these steps. For more details we remind the reader to (Atwood et al., 2009).

The development of the analysis process initially was based and strongly relied on detailed Monte Carlo (MC) simulation of the instrument. During the first years of the mission the LAT team has gained considerable insight into the in-flight performance of the instrument. Accordingly, the experience accumulated with real data after launch has been exploited for updating the LAT data reduction. More the Instrument Response Functions (IRFs), which provide the description of the instrument performance used for data analysis, have been later corrected for discrepancies observed between flight and simulated data.

We note that part of this thesis work makes use of the event analysis elaborated prior to launch known as `Pass 6` (or `P6`) while the

most recent work presented here is based on the `Pass 7` (`P7`) dataset. The sample used will be specified in each dedicated section. In the rest of the paragraph we will discuss the main points of these event analysis. It is worth to mention that a further analysis version is being developed redefining also the event reconstruction (`Pass 8`, a.k.a. `P8`).

The LAT Monte Carlo Modeling

Fundamental in the pre-launch phase for the design of the instrument and the development of the software infrastructures, the MC modeling of the LAT has been crucial for both the event analysis and the studies of the instrument performance. It is based on GLEAM (for details about the MC framework "GLEAM" see Boinee et al., 2003). In addition a detailed simulation of particle interactions with *Fermi* was implemented in the Geant4 framework (Allison et al., 2006).

LAT MC simulations make use of different γ-ray source models (including realistic representations of the γ-ray sky) and a full model of the backgrounds (e.g. charged cosmic rays, neutrons, γ-ray emission from the Earth limb, see Ormes et al., 2007).

Validation of MC modeling of the LAT was performed through an on-ground calibration with muons and a beam-test campaign on a "calibration unit", made with detector modules with the same characteristics of those used to build the LAT, including two complete tracker/calorimeter towers. The calibration unit was exposed to photons (up to 2.5 GeV), electrons ($1 - 300$ GeV), hadrons (π and p, from a few GeV to 100 GeV) and ions (C, Xe, 1.5 GeV/n) in different irradiation facilities (see Baldini et al., 2007, for details). The beam test allowed the fine tuning of the detector modeling, as well as the determination of the Geant 4 interaction models which best reproduce the real data[5] providing also bounds to the systematic uncertainties on the absolute energy measurements, equivalent to $^{+5\%}_{-10\%}$ (Ackermann et al., 2010b).

Anyway, due to experimental constraints, among all the fact that the calibration unit was different in geometry with respect to the full-scale LAT, this evaluation of the reconstruction routines was not fully exhaustive since it did not allowed a direct check of the LAT event analysis. Therefore, parallel to the on-ground calibration, a further more detailed calibration was scheduled to be carried out in orbit. The calibration effort started after Fermi launch and the first results are provided in detail in Abdo et al. (2009e). The LAT performance was fine-tuned by optimizing internal delays and synchronizations, alignment constants and absolute timing. In addition, the determina-

5 Worth to notice that the LAT beam test led to the discover that the Landau-Pomeranchuck-Migdal effect, affecting the development of electromagnetic showers in the calorimeter, was inaccurately implemented in the standard libraries; following versions of Geant 4 were corrected according to this..

tion of detector thresholds, gains and noise was performed and in general a robust understanding of the system response was obtained.

Track and energy reconstruction

Clusters of spatially adjacent hits in the tracker are combined to determine a three dimension position in the detector thus generating track hypotheses. Two different algorithms are used to generate tracks. The first is based on the centroid and axis of the energy deposition in the calorimeter. The furthest cluster is taken randomly in the appropriate temporal window; the second one is searched for on the line connecting the putative first hit to the deposition centroid in the calorimeter. A track hypothesis can be generated when the latter is found and is populated using an adaptation of the Kalman filter (Früʼhwirth et al., 2000), propagating clusters to the following layer by means of a full covariance matrix which accounts for Coulomb scattering. After iterating the process over all the possible furthest clusters and exploring at least two layers, if a track of sufficient quality is found, it is retained. The "longest, straightest" track found by the Kalman fit is chosen as the best track, (corresponding to the higher energy charged particle hypothetically produced by the γ ray conversion). Then, the hits of the first track are flagged as used and a second track-finding algorithm starts.

The second method is used when calorimeter information is not sufficient for track finding (e.g. at low energies): like the previous one it is a blind method but the second cluster is now chosen at random in the next closest layer to the calorimeter.

After determining each track, the algorithm combines tracks into vertexes. The best tracks of each event are therefore combined together. A vertex solution is generated when the separation between two tracks is less then a predefined distance, namely 6 mm. The next unused track is selected and the process repeated.

Tracks which are not satisfactorily paired are assigned to a vertex by themselves. In addition, when the calorimeter information is available, a further solution is created, the "neutral energy" solution. This is meant to account for neutral particles (γ-rays) that during the conversion process, or immediately thereafter, carry away a significant fraction of energy (due e.g. to Bremsstrahlung). Actually in such cases the tracks can point away from the direction of the impinging γ ray, but the direction can be better reconstructed using the centroid of the energy deposition in the calorimeter.

Concerning the energy reconstruction, at first raw signals are converted into energy depositions for each crystal end. In this way they provide the total energy and the hit position for each crystal, thus resulting in a three dimension array of energies. The sum of the energies deposited provides the first raw estimate of the event energy,

while the the direction of the shower is derived from the 3D centroid and higher moments of the energy deposition.

Further corrections are applied depending on the track direction (or vertex direction). Finally, the trajectory is used to estimate the energy leakage out of the sides and back of the calorimeter along in internal gaps between the active volumes. For this purpose three different algorithms are used, based on a parametric correction using the barycenter of the shower, on a fit to the shower profile or on a maximum likelihood taking into account also the hits in the tracker[6]. For low energies ($\lesssim$ 100 MeV), a significant amount of the energy ($\sim$ 50%) can be released in the tracker: the tracker energy is determined from the silicon strip signals, i.e. the amount of energy deposition at certain depth in a tracker layer is evaluated from the number of hit silicon strips, and then added to the event energy.

Event classification and Background rejection

The purpose of the event classification is not only the estimate of the best event direction and energy among those available for each event, together with their accuracy, but also the reduction of the backgrounds in the final data sample. For these aims a series of selection criteria and classification tree[7] generated probabilities (Breiman, 1984) are used.

By means of a classification tree, the best energy estimate is chosen between the available possibilities for each event; afterwards another classification tree evaluates the probability that the measured value is within 1σ from the true value. For the determination of the direction, at first a classification tree selects between the vertex solution if available and the best one-track solution. Events are then divided into four subclasses, according to the conversion point, in the *front* or *back* section of the tracker, and to the vertexing properties, namely vertex or one-track events. For each of the subsets the probability that the measured direction is within the 68% containment angle from the true arrival direction is evaluated by a classification tree. At the end of the process a best energy and a best direction measurements are assigned to each event, along with the corresponding estimates of the accuracy of the measurements.

After energy and direction are selected, an additional background rejection stage is applied, improving the on-orbit filtering. The on-board filter is configured in order to reduce the data to fit the available band for data downlink at the Earth while keeping the largest possible efficiency for γ-ray detection (reducing the signal-to-noise ratio at $\sim 1:300$). On ground information from all LAT subsystems is examined in detail and several figures-of-merit are evaluated using

6 To be noted that the latter has been disabled in `PASS 7` analysis.

7 Automated algorithm which partitions a data set into classes generating complex event selection criteria.

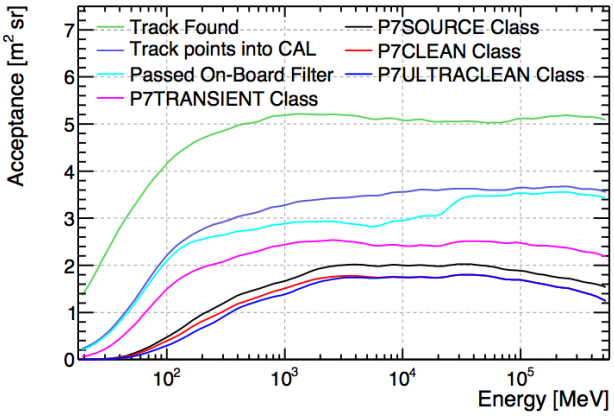

Figure 3.2 LAT acceptance integrated over the FoV as a function of energy at successive stages of the event filtering as estimated with simulated data for the `Pass 7` dataset.

automated data-mining techniques. As anticipated, the ACD has a major role for this purpose and is used in conjunction with the measured tracks. Event with tracks pointing to hits in the ACD and to gaps in the ACD shield are discarded (the latter case provides an efficiency loss only at the level of $\sim$ 2%). Further constraints rely on the event topology in the tracker and the general shower profile in tracker-calorimeter. These are then used to determine classification trees to estimate the probability of an event being a celestial γ-ray or a background particle. After the on-ground background rejection, the background is substantially (reduced by almost three orders of magnitude).

Thus, the final outcome of the on-ground event analysis is the energy and direction for the event, with corresponding confidence levels, along with several estimates of the probability the event describes, after all, a γ-ray and not a background particle. All the described ingredients are used to define standard *event classes* optimized for a range of scientific objectives and, at the same time, accounting for an obvious trade-off between efficiency, purity and resolution. A smaller, purer γ-ray dataset with enhanced spatial and energy resolution is obtained as the cuts become harder and harder. The relative selection efficiencies for the several stages of the process in the `Pass 7` dataset are illustrated in Figure 3.2.
The main event classes defined prior to launch and used in for the `Pass 6` dataset are the following:.

- The *Transient* class, suitable for studying localized, intense, transient phenomena (e.g. Gamma-ray Bursts), has the largest efficiency at the expense of a high residual background rate;

- The *Source* class, suitable for study of localized sources with a residual background rate comparable to the extragalactic diffuse rate estimated from EGRET.

- The *Diffuse* class, expected to achieve a background-rejection factor of the order of 10^6, while keeping an efficiency for γ-ray detection $\sim 80\%$. The name derived by its specific aim to study diffuse γ-ray emission.

After launch the better understanding of the backgrounds led to the definition of a purer class, called *Dataclean*, especially developed to study the extragalactic γ-ray background (Abdo et al., 2010j).

The `Pass 7` standard event classes where made in a similar a way, although indeed they included improvements and the cuts were optimized somewhat differently w.r.t. `Pass 6`.

- `P7TRANSIENT` class which corresponds to the `P6_TRANSIENT`; aims to achieve a residual background rate of a few Hz while maintaining a large efficiency for γ rays. A short time selection itself limits the amount of background counts in the ROI (generally suitable to study time intervals of $\sim$ 1000s);

- `P7SOURCE` class, the equivalent of the `P6 DIFFUSE` event class. Intended dedicated for the analysis of point sources, generally with a background rate of less than $\sim$1 Hz in the LAT FoV, it ensures a high enough signal-to-background ratio so that this has little impact on source detection and characterization;

- `P7CLEAN` class, which is roughly equivalent to the `P6 DATACLEAN` event class. For the analysis of diffuse γ-ray emission the background contamination is reduced to a level of about $\sim$0.1 Hz across the LAT FoV[8];

- `P7ULTRACLEAN` class, suitable for the analysis of extragalactic diffuse γ-ray emission[9], further cuts reduce the residual contamination for this class to $\sim$ 40% lower than that of the `P7CLEAN` class.

It is worth to notice that all the event classes have still a residual background contamination. The reducible backgrounds are given by events which, in principle, could be identified as background and eliminated. These are background events hitting the LAT and misclassified as γ rays. The irreducible backgrounds are given by background particles (cosmic rays) interacting with the dead materials

8 In this way the background contamination is below the extragalactic γ-ray background at all energies. For comparison, the total Galactic diffuse contribution is $\sim$1 Hz, depending on where the LAT is pointing, though most of that is localized along the Galactic plane.

9 The background contamination has to be reduced even further below the extragalactic γ-ray background rate to avoid introducing artificial spectral features.

surrounding the instrument (e.g. the thermal blanket) and producing a γ ray which enters the detector. Irreducible events constitutes the majority of residual backgrounds in the purest classes.

The final product of all these steps is a table where for each event is given an energy, a direction, and other fundamental quantities associated to it, LAT photon data[10] are publicly available through the *Fermi* Science Support Center (FSSC)[11], together with the orbital history of the telescope.

3.2 THE LAT INSTRUMENT RESPONSE FUNCTIONS

In High Energy Astrophysics the Instrument Response Functions (IRFs) conventionally represent a high-level model of the instrument response that enable the data analysis (IRFs; e.g. Davis, 2001). The main reason for these is twofold:

- instrument analysis is complex and can be hardly managed by the "external" astrophysics community. Therefore only few useful estimated quantities (e.g. energy, direction, inclination angle with respect to the telescope axis, ...) are provided;
- data from different instruments in different energy ranges can be compared, allowing a multiwavelength analysis.

Canonically the detector response is factored into three terms: efficiency in terms of the detector *effective area*, resolutions as *Point Spread Function* (PSF) and *energy dispersion*.

The LAT IRFs were defined and parametrized prior to launch based on the MC simulations described in § 3.1.2. The IRFs were subsequently updated to take into account effects measured in flight that were not considered in pre-launch performance estimates (`Pass6_V1`). The issues were primarily pile-up and accidental coincidence effects in the detector subsystems leaving *ghost* signals (see 3.2.3) in coincidence with good photon triggers. An updated version of the IRFs (`Pass6_V3`) was distributed with the original public release of *Fermi* data and accounted for these problems, but it was still affected by a loss of efficiency since no attempt to re-optimize the event selection was made for this dataset.

The subsequent sets of IRFs that have been released included also the effects of ghost signals in simulations and appropriate sampling of flight data is the `P7SOURCE_V6`. It has been optimized for the study of point-like sources and the production of the second LAT source catalog (2FGL, Nolan et al., 2012).

10 Only photon data are released, i.e. all the events in the publicly available meet the loose selection criteria of the Transient class.

11 http://fermi.gsfc.nasa.gov/ssc/

The LAT IRF models developed by the LAT team are released along with datasets and analysis software (see § 3.4). We address the readers to the LAT performance web page[12] for the latest developments.

In the following of the section we will review the general tasks related to the IRFs, focusing then the attention to the set that have been used in our analysis, namely `P6_V3` described in § 3.2.4 and `P7SOURCE_V6` described in § 3.2.5.

3.2.1 *IRFs Definition*

Conventionally IRFs are defined as a function R of true photon energy E' and direction $\hat{p}'$, measured photon energy E and direction $\hat{p}$ and time t. As a matter of fact the differential count rate in the instrument phase space (reconstructed energy and direction) is given by the convolution of the source differential flux per unit area at the detector with the IRFs.

$$\frac{\mathrm{d}N}{\mathrm{d}t\,\mathrm{d}E\,\mathrm{d}\hat{p}}(E,\hat{p},t) = \int \mathrm{d}E'\mathrm{d}\hat{p}'\; R(E,\hat{p}|E',\hat{p}';t)\,\frac{\mathrm{d}N}{\mathrm{d}t\,\mathrm{d}E'\mathrm{d}\hat{p}'\mathrm{d}S}(E',\hat{p}',t) \tag{53}$$

The IRFs are factorized into three functions, representing the efficiency, the angular resolution and the energy resolution plus a temporal scaling factor.

$$R(E,\hat{p}|E',\hat{p}';t) = T(t)A(E',\hat{p}')P(\hat{p}|E',\hat{p}')D(E|E',\hat{p}') \tag{54}$$

$T(t)$ is a scaling factor which accounts for temporal variations, such as instrument failures, temporary switching off, thermal expansion or the deterioration of instrument components. Noteworthy, the lack of consumables (like the gas of spark chambers in previous high-energy γ-ray telescopes) makes the LAT performance remarkably stable and therefore this term is negligible. The three functions describing the IRFs are:

- the effective area, $A(E',\hat{p}')$, which is the detection efficiency for photons of true energy E' and arrival direction $\hat{p}'$ expressed as an area (i.e. the factor converting incident fluxes per unit area into differential count rates in the instrument regardless of the reconstructed energy E and direction $\hat{p}$);

- the PSF, $P(\hat{p}|E',\hat{p}')$, the probability density that a photon with energy E' and arrival direction $\hat{p}'$ has a reconstructed direction $\hat{p}$;

- the energy dispersion, $D(E|E',\hat{p}')$, the probability density that a photon with energy E' and arrival direction $\hat{p}'$ has a reconstructed energy E.

12 http://www-glast.slac.stanford.edu/software/IS/glast_lat_performance.htm

3.2.2 *Representation of the IRFs*

The LAT IRFs are determined primarily by the hardware design, the event reconstruction algorithms and the event classification and selection. To evaluate the LAT response a dedicated MC simulation was performed prior to launch and a huge amount of γ-ray events were simulated to cover with good statistics all possible photon inclinations and energies.

The effective area is represented as a table of scalars separated in several bins in energy and inclination angle w.r.t. the detector axis and distinguishing between *front* and *back* converting events. The representation of the PSF and energy dispersion is more complex: it makes use of the parametrization of the angular and energy distribution of events. Specific details of the representation are different among the several versions of the IRFs and are always available at dedicated web pages of the FSSC[13]. Pre-launch performance estimates and related IRF set, namely `P6_V1`[14], are documented in Atwood et al. (2009).

In the next paragraphs we will overview the developments in the LAT IRF after launch and we will briefly discuss the current open issues.

3.2.3 *Open issues: ghosts events*

After the on-orbit calibration campaign of the LAT (Abdo et al., 2009e) all the insights acquired were implemented in the LAT MC simulation, and so in the generation of the IRFs. Nevertheless, some issues became evident when examining downlinked events. When comparing real data with MC simulations, unexpected interactions between γ-ray and background events were pointed out. These are referred to as *ghost event* and are observed when e.g. a photon hits the LAT while the energy released by a background particle is still being collected from sensitive volumes. A sketch example is reproduced in Figure 3.3. Prior to launch these effects were thought to be negligible and moreover, they were not observed in MC simulation as each event was generated independently, thus not considering interactions between subsequent events. The main outcome of these is a reduced efficiency. Actually a certain amount of perfectly legitimate γ-ray events may be discarded at the background rejection stage, by the event classification algorithms that were trained on MC simulations unaffected by such effects.

Indeed to correctly account for these artifacts the reconstruction analysis routines have to be redesigned. This is under development

13 http://fermi.gsfc.nasa.gov/ssc/data/analysis/documentation/Cicerone/Cicerone_LAT_IRFs/IRF_overview.html

14 The LAT IRFs are conventionally called as the event analysis version they refer to (`P#`), plus a number representing the version of the IRFs (`V#`), plus the event class.

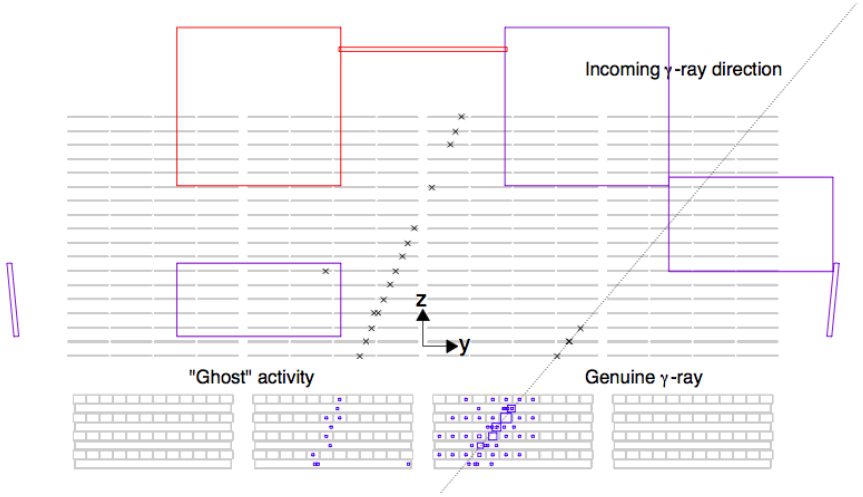

Figure 3.3 Illustration of a ghost event in the LAT. An 8.5 GeV γ-ray candidate is back-converting (on the right) while simultaneously the LAT is recording additional activity from the remnants of a charged-particle that crossed the subsystems. Small crosses represent the clusters (i.e., groups of adjacent hit strips) in the tracker, while variable-size squares indicate the reconstructed location of the energy deposition for every hit crystal in the calorimeter (the side of the square being proportional to the magnitude of the energy release). Dashed line indicates the γ ray (Abdo et al., 2009e).

by the LAT team and will be implemented in the next generation of the IRFs (`P8` analysis). Meanwhile the issue is temporary circumvented including the effect of ghost hits in the MC simulation used for generating the IRFs. Such IRFs are in turn again a good description of the LAT performance and allow unbiased studies of celestial sources.

3.2.4 *`P6_V3_DIFFUSE` IRFs*

The main improvements for the `P6_V3` IRFs (Rando et al., 2009) is the correction of the effective area for the *average* effect of pile-up and accidental coincidence effects in the LAT given its orbital characteristics. We will now briefly describe the performance of the LAT as depicted in this IRF set for the *Diffuse* events class, which were used for part of the work reported in this thesis (namely for the analysis of the blazar PKS 1830+211 presented in § 6), as well as for many published papers, notably the first-year LAT Catalog (1FGL; Abdo et al., 2010c).

Figure 3.4 shows the effective area of the LAT, separately as a function of energy for normally incident photons and as a function of incidence angle for 10 GeV photons. The peak effective area, typically lying in the $1 - 10$ GeV energy range is greater than 8000 cm^2.

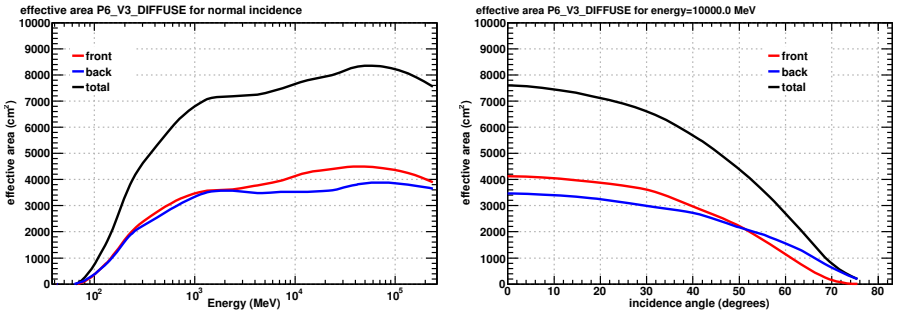

Figure 3.4 The LAT effective area as a function of energy for normally incident photons (left) and as a function of incidence angle for 10 GeV photons (right). The curves correspond to *front*-converting events (red), *back*-converting events (blue) and total (black).

The acceptance is defined here as the effective area integrated over the solid angle and is the relevant quantity in the standard survey mode. Namely, the large acceptance of the LAT led to the collection of a data sample which already exceeds by more than one order of magnitude the statistics of previous γ-ray telescopes. Figure 3.5 shows

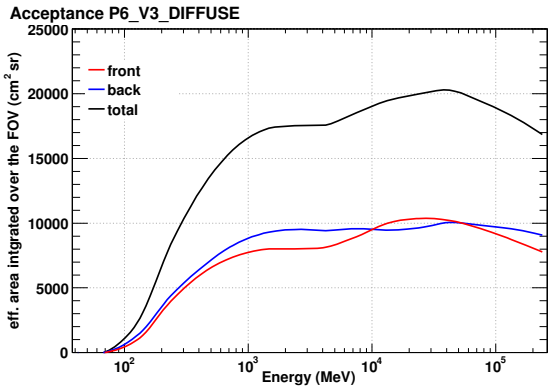

Figure 3.5 The LAT acceptance as a function of energy. The curves correspond to *front*-converting events (red), *back*-converting events (blue) and total (black).

the intrinsic acceptance, regardless of orbital characteristics; to obtain the effective acceptance the curves have to be rescaled by the live-time fraction. It is interesting to note that the acceptance has a slower turn-on with respect to the normal effective area, indicating the dependence of the FoV on energy.

In Figure 3.6 are displayed the angles for 68% and 95% event containments, as a function of energy and incidence angle as before. The strong dependence of the PSF on energy is mainly due to Coulomb scattering in the tracker. The dependence on incidence angle is in-

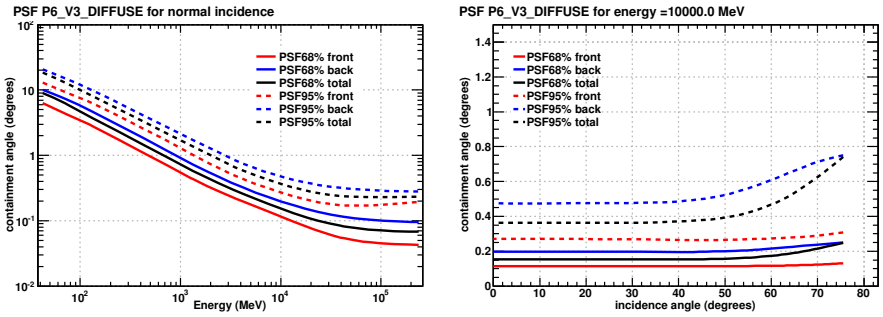

Figure 3.6 The 68% and 95% event containment angles as a function of energy for normally incident photons (left) and as a function of incidence angle for 10 GeV photons (right). The curves correspond to *front*-converting events (red), *back*-converting events (blue) and total (black).

stead mild. For comparison, the 68% containment angle at 1 GeV of EGRET was 1.7°. Worth to notice that if compared to an ideal Gaussian case, the PSF has larger tails especially at energies $\gtrsim$ 10 GeV. This can be highlighted looking at the ratio of the 95% to the 68% containment angle, shown in Figure 3.7. This ratio would be 1.62 for the

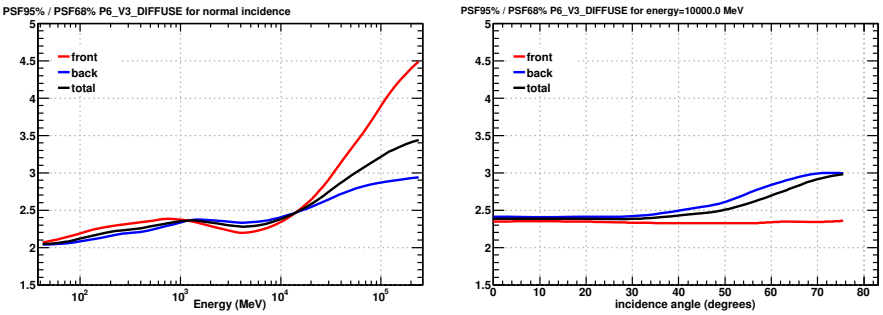

Figure 3.7 The ratio of 95% and 68% event containment angles as a function of energy for normally incident photons (left) and as a function of incidence angle for 10 GeV photons (right). The curves correspond to *front*-converting events (red), *back*-converting events (blue) and total (black).

ideal Gaussian case, while it is > 2 for the LAT PSF.

Figure 3.8 shows $\Delta E/E$ for 68% event containment, which is a measure of the instrument energy resolution. It is better than 15% over most of the LAT energy band.

The systematics affecting the LAT effective area were evaluated for this event class using bright pulsars (Rando et al., 2009), which provide a clean γ-ray sample thanks to the temporal properties of their emission. The conservative estimate of the systematics derived puts a

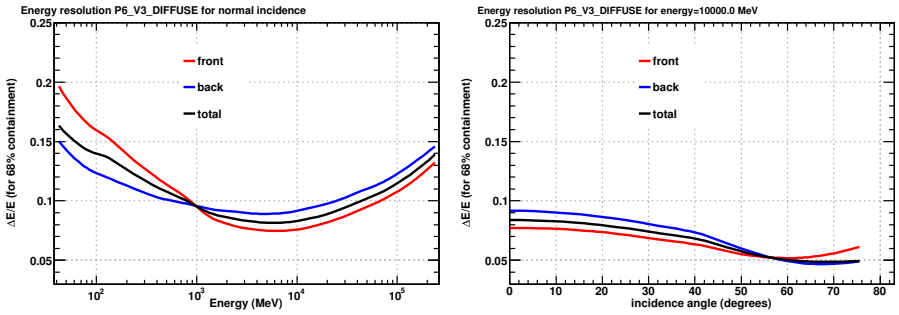

Figure 3.8 $\Delta E/E$ for 68% event containment as a function of energy for normally incident photons (left) and as a function of incidence angle for 10 GeV photons (right). The curves correspond to *front*-converting events (red), *back*-converting events (blue) and total (black).

10% upper limit on the effective area uncertainties at 100 MeV, 5% at 562 MeV and 20% at 10 GeV. The bounds to the effective area uncertainties can be assumed to linearly vary with the logarithm of energy between these values.

3.2.5 *P7SOURCE_V6 IRFs*

`Pass 7` data have been available for public analysis since 2011 August and represent a substantial improvement over `Pass 6`, primarily due to largely increased of the effective area below ∼300 MeV and improved modeling of the IRFs. Added to the better understanding of the effects of energy dispersion, this increase in effective area allowed for the first time the analysis of LAT data at energies below 100 MeV (though the reader should bear in mind specific caveats Abdo et al., 2009e).

`P6_V3` IRFs took into account the *average* effect of pile ups and accidental coincidences in the LAT. But the effect is indeed dependent on the trigger rate, or, equivalently, on the livetime fraction. In `Pass 7` the livetime-dependent correction to the effective area has been derived from MC simulations with *ghost* overlays and parametrized (also as a function of energy) with simple analytical formulas to re-weight the effective areas in the IRF convolution.
Figure 3.9 illustrates the effective area for the `P7SOURCE`. The acceptance for both datasets is shown for comparison in Figure 3.10, in addition we note that in `Pass 7` the energy dependence of the effective area is clearly smoother.

If the `P7SOURCE` dataset has smaller systematic uncertainty for the effective area, the price to pay is a slightly broader PSF. For `Pass 7` data the PSF was derived from data above 1 GeV. Below 1 GeV,

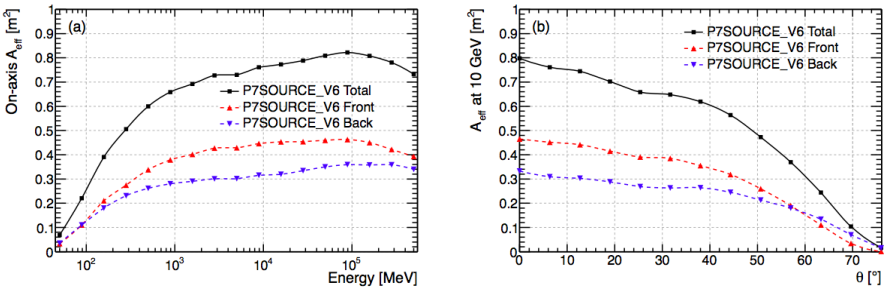

Figure 3.9 On-axis effective area as a function of the energy (left) and angular dependence (right) of the effective area at 10 GeV for the `P7SOURCE` class.

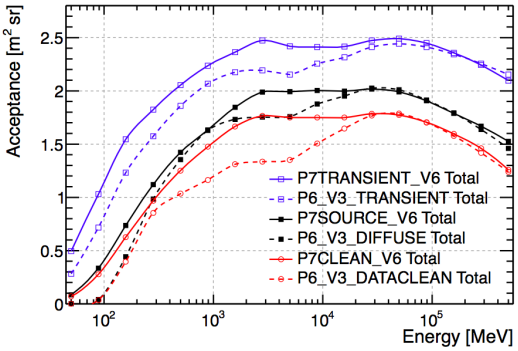

Figure 3.10 Comparison of the acceptances for the `Pass 7` and the `Pass 6` standard γ-ray classes.

where the PSF was derived from MC simulations, the PSF parameters were recalculated in order to ensure a smooth variation of the containment levels as a function of energy. The experimental PSF at energies $\gtrsim$ 5 GeV was found to be broader than expected from MC simulations. This was noticed in the distribution of events around bright sources, AGN and pulsars, and advertised as a source of systematics by the LAT collaboration (e.g. Abdo et al., 2010c). Part of the problem can be attributed to the MC simulation issues in generating the IRFs. Further possibilities have been investigated, notably the contribution from pair halos around AGN. Anyway no indication was found that this phenomenon is the explanation for the PSF being broader than predicted (Abdo et al., 2013).

Figure 3.11 compares the 68% containment angles for the `Pass 6` and `Pass 7` classes recommended for routine analyses of γ-ray point sources. To be noted that while the difference between `P6_V3_DIFFUSE` and `P7SOURCE_V6` is due mostly to the data-derived PSF, in the latter there is also a clear difference across all energies between the `P7SOURCE_V6` PSF and in-flight `P6_V11_DIFFUSE` PSF.

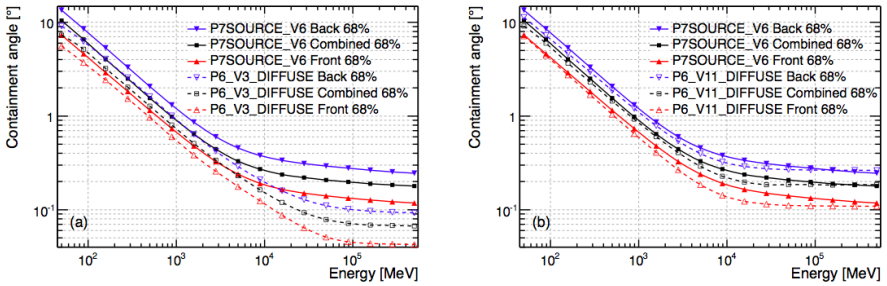

Figure 3.11 Comparison of the 68% containment radius of the PSF for `P7SOURCE_V6` with respect to `P6_V3_DIFFUSE` (left) and `P6_V11_DIFFUSE` (right). The `P6_V3_DIFFUSE` is plotted for normal incidence; `P6_V11_DIFFUSE` and `P7SOURCE_V6` do not include dependence on the incidence angle.

The energy resolution as a function of energy on-axis and incidence angle at 10 GeV for the `P7SOURCE_V6` event class is displayed in Figure 3.12. Figure 3.13 instead shows that the energy resolution for the

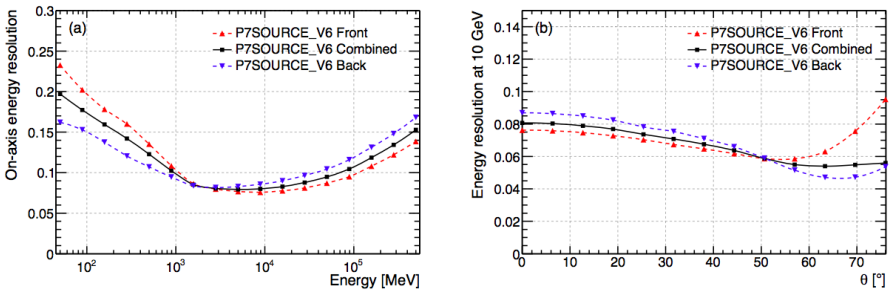

Figure 3.12 Energy resolution as a function of energy on-axis (left) and incidence angle at 10 GeV (right) for the `P7SOURCE_V6` event class.

`P7SOURCE_V6` event class is quite comparable to that of `P6_V3_DIFFUSE` over most of the LAT energy range. The most noticeable difference, namely a slight worsening below 1 GeV (and especially below 100 MeV), is a small trade-off for the much greater `Pass 7` low-energy acceptance. On the other, hand `Pass 7` has uniformly better energy resolution than `Pass 6` in the energy range above 10 GeV.

3.3 ANALYSIS METHOD: THE MAXIMUM LIKELIHOOD ANALYSIS OF LAT DATA

During its lifetime the LAT will collect hundreds of millions of photons (counts), but for most analyses typically a small subset of only a few hundred or a few thousand will be useful for scientific purpose. The data will be too sparse in many cases to allow the use of χ^2 as

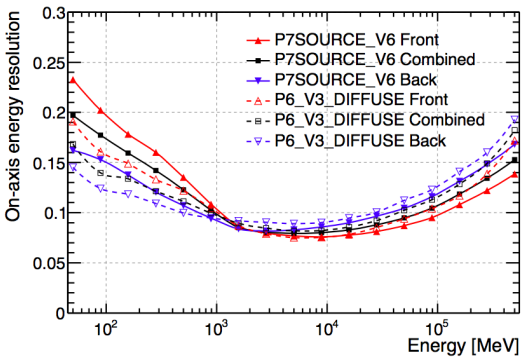

Figure 3.13 Comparison of the on-axis energy resolutions of the `P7SOURCE_V6` and `P6_V3_DIFFUSE` IRFs.

test statistic. Therefore Poisson likelihood optimization, is needed for model parameter estimation of the GeV sky.

The application of the likelihood method to photon-counting experiments was already described by Cash (1979) and successfully used for γ-ray studies over the years (e.g. it was applied in the analysis of EGRET data as parameter estimation, Mattox et al., 1996). This method is applied in the analysis of FERMI data as well. The main motivation is that it is never possible to really isolate a source in high-energy γ rays. This is mainly due to the limited statistics, the angular resolution which depends on the energy, as well as a strong and structured background given by interstellar emission, still poorly understood especially if compared to other wavelengths.

In this section we will describe the likelihood analysis based on Poisson statistics, i.e. the analysis method that was applied for the studies described in this thesis, and which is also the most broadly used method for analyzing LAT data. The technique requires to assume a model for signal detected by the telescope; in our case, the input model is the distribution of γ-ray sources on the sky, and includes their intensity and spectra. This statistic is used to estimate to what extent the observed data are consistent with a statistical hypothesis and to find the best fit model parameters. These parameters are, e.g. the description of the source's spectrum, its position, and intensity.

3.3.1 *Likelihood analysis for photon-counting experiments*

Let us assume to have a model describing the data and suppose that this model is known, except for a finite number of parameters. Let $M(E', \hat{p}', t; \{\alpha_k\})$ be the differential flux per unit area at the detector predicted by the model as a function of true photon energy E', true

photon arrival direction at the detector $\hat{p}'$, time t and of the unknown parameters $\{\alpha_k\}_{k=1,\ldots,m}$.

Eq. 53, that defines the IRFs, can be used to derive the differential count rate J in the detector phase space (reconstructed energy E and direction $\hat{p}$) predicted by the model

$$J(E,\hat{p};\{\alpha_k\}) = \int \mathrm{d}t\,\mathrm{d}E'\mathrm{d}\hat{p}'\; R(E,\hat{p}|E',\hat{p}';t)\,M(E',\hat{p}',t;\{\alpha_k\}) \tag{55}$$

as a function of reconstructed energy E, reconstructed arrival direction $\hat{p}$ and of the unknown parameters $\{\alpha_k\}_{k=1,\ldots,m}$. The counts expected in a given energy range (E_1,E_2), solid angle Ω and time interval (t_1,t_2) are then obtained as the integral of the differential count rate in the detector.

$$\Lambda(\{\alpha_k\}) = \int_{t_1}^{t_2}\mathrm{d}t\int_{\Omega}\mathrm{d}\hat{p}\int_{E_1}^{E_2}\mathrm{d}E\;J(E,\hat{p};\{\alpha_k\}) \tag{56}$$

Given the low counting rates it is worth to use for the comparison the Poisson statistics. If λ is the number of expected counts the probability density of observing n counts is

$$f(n,\lambda) = \frac{\lambda^n}{n!}\mathrm{e}^{-\lambda} \tag{57}$$

We can compare expected counts with observed counts binning them with a certain grid in arrival direction and energy. The likelihood is defined as the product for each pixel $\imath$ of the probability densities of observing $N_\imath$ counts given the expectation $\Lambda_\imath(\{\alpha_k\})$.

$$\mathscr{L}(\{\alpha_k\}) = \prod_\imath f[N_\imath,\Lambda_\imath(\{\alpha_k\})] \tag{58}$$

It is convenient to consider the logarithm of the likelihood.

$$\log\mathscr{L}(\{\alpha_k\}) = \sum_\imath N_\imath\log\Lambda_\imath(\{\alpha_k\}) - \sum_\imath\Lambda_\imath(\{\alpha_k\}) - \sum_\imath\log(N_\imath!) \tag{59}$$

The best-fit set of parameters $\{\overline{\alpha}_k\}$ is found maximizing the likelihood, or equivalently its logarithm[15], where the last term $\sum_\imath\log(N_\imath!)$ can be neglected since it is model independent. The likelihood becomes

$$\log\mathscr{L}(\{\alpha_k\}) = \sum_\imath N_\imath\log\Lambda_\imath(\{\alpha_k\}) - \Lambda_{\mathrm{tot}}(\{\alpha_k\}) \tag{60}$$

where $\Lambda_{\mathrm{tot}}(\{\alpha_k\})$ is the total number of counts predicted by the model.

An estimate of the statistical errors affecting the best-fit parameters is provided by the likelihood profile around the maximum. According to Cramer-Rao's disequation (Cramer, 1946; Rao, 1945), an upper limit to the covariance matrix terms is given by

$$\sigma^2_{ab} = \left[-\left.\frac{\partial^2\log\mathscr{L}}{\partial\alpha_a\partial\alpha_b}\right|_{\{\overline{\alpha}_k\}}\right]^{-1} \tag{61}$$

15 Numerical codes often use to minimize the opposite of the likelihood logarithm.

For limited statistics (i.e. a small number of counts) the unbinned likelihood is used since it can be calculated rapidly, but as the number of counts increases the time to calculate the likelihood becomes prohibitive, and the binned likelihood must be used. In the following we will review only the former, which is the method relevant for the analysis presented in Chapter 4 and Chapter 5.

Assume to use a grid fine enough that in each pixel the number of observed counts is either 0 or 1. Let P be the pixel set where $N_\iota = 1$, the likelihood logarithm is therefore simply

$$\log \mathscr{L}(\{\alpha_k\}) = \sum_{\iota \in P} \log \Lambda_\iota(\{\alpha_k\}) - \Lambda_{\rm tot}(\{\alpha_k\}) \tag{62}$$

In a small enough pixel $\Lambda_\iota(\{\alpha_k\}) = J(E_\iota, \hat{p}_\iota; \{\alpha_k\})\Delta t \Delta\hat{p}\Delta E$, so Eq. 62 yields

$$\begin{aligned}\log \mathscr{L}(\{\alpha_k\}) &= \sum_{\iota \in P} [\log J(E_\iota, \hat{p}_\iota; \{\alpha_k\}) + \log \Delta t + \log \Delta\hat{p} + \log \Delta E] + \\ &\quad -\Lambda_{\rm tot}(\{\alpha_k\}) = \\ &= \sum_{\iota \in P} \log J(E_\iota, \hat{p}_\iota; \{\alpha_k\}) + \log \Delta t^{N_{\rm obs}} + \log \Delta\hat{p}^{N_{\rm obs}} + \\ &\quad + \log \Delta E^{N_{\rm obs}} - \Lambda_{\rm tot}(\{\alpha_k\})\end{aligned} \tag{63}$$

where $N_{\rm obs}$ is the total number of observed photons. The mid terms are independent from the model, hence they can be neglected for the likelihood maximization. Then Eq. 63 becomes

$$\log \mathscr{L}(\{\alpha_k\}) = \sum_{\iota \in P} \log J(E_\iota, \hat{p}_\iota; \{\alpha_k\}) - \Lambda_{\rm tot}(\{\alpha_k\}) \tag{64}$$

where the first summation can be computed looping over the energies and directions of the observed photons.

This method allows also the comparison of different models, but it is not straightforward. There are some specific cases where the comparison can be performed using the likelihood ratio test (LRT), based on Wilk's theorem (Wilk, 1945). Let us consider the model $M(\{\alpha_k\}_{k=1,\dots,m})$, and let us assume $M_0(\{\alpha_k\}_{k=1,\dots,h})$ to be a simpler or more parsimonious model where $\{\alpha_k\}_{k=h+1,\dots,m}$ are fixed to given values ($m > h$). In the null hypothesis that $\{\alpha_k\}_{k=h+1,\dots,m}$ are set to the true values, the Wilk's theorem predicts the following relation for the test statistics:

$$\mathrm{TS} = 2\left(\log \overline{\mathscr{L}} - \log \overline{\mathscr{L}_0}\right) \tag{65}$$

where $\overline{\mathscr{L}}$ and $\overline{\mathscr{L}_0}$ are the maximum likelihood values found for the full model M and the simpler model M_0, respectively. Under this condition the test statistics is distributed asymptotically as a χ^2 with $m - h$ degrees of freedom[16]. When TS is large we reject the null hypothesis (the simpler model does not adequately describe data) and

16 Neglecting terms of the order of $\mathscr{N}^{-1/2}$ or higher, where $\mathscr{N}$ is the number of pixels.

we go back to the full model determining $\{\alpha_k\}_{k=h+1,\ldots,m}$ from the likelihood fit. The confidence level at which the full model M describes data better than the simpler model M_0 is

$$\text{c.l.} = \int_0^{\text{TS}} \mathrm{d}s\, \chi^2_{m-h}(s) \tag{66}$$

being $\int_{\text{TS}}^{+\infty} \mathrm{d}s\, \chi^2_{m-h}(s)$ the chance probability that the test statistics is larger than the obtained value.

As anticipated, we can resort to the LRT only in some cases. The two basic requirements are that the likelihood function met some regularity conditions and the two compared models are *nested* (as detailed in Protassov et al., 2002). The former, the regularity conditions, requires that $\log \mathscr{L}(\{\alpha_k\})$ is three times differentiable with respect to the α_k, that the derivatives are limited and the Hessian matrix is positive definite. The latter instead imply that:

1. given $M(\{\alpha_k\}_{k=1,\ldots,m})$ it must be possible obtaining $M_0(\{\alpha_k\}_{k=1,\ldots,h})$ by setting $\{\alpha_k\}_{k=h+1,\ldots,m}$ to some fixed values;

2. the null values of the parameters $\{\alpha_k\}_{k=h+1,\ldots,m}$ must be in the interior (but not on the boundary) of the set of possible values in the full model.

From the first criterion derives that, e.g., we cannot use the LRT to discriminate among two different spectral models for a source, like a power law or a black-body spectrum. The second criterion is particularly important when we add components to a model, e.g. this may be used to test if there is significant signal from a source over the expected backgrounds. Worth to notice that to met the second criterion, when adding the source to the model, its flux should not forced to be > 0, but instead allowed to be negative, so that the null hypothesis (flux null) is still in the interior of the possible values of the more complex model.

On the other hand, when one of these requirements is not satisfied the test statistics is not guaranteed to follow the reference distribution and, in turn, it is not possible to derive the false positive rate for a detection (e.g. this was pointed out when analyzing EGRET point sources Mattox et al., 1996)

3.4 THE LAT HIGH-LEVEL ANALYSIS ENVIRONMENT

Since the beginning of the second year of operations, all LAT science data is released as early as possible. To allow the broad scientific community to easily access and exploit it, the LAT team has developed a high-level analysis suite, which is referred to as *Fermi Science Tools*. It consists of all the basic tools necessary to derive astrophysical information from the lists of photons detected. Related software and

documentation are publicly available through the FSSC[17] and include several tools to rapidly explore, analyze, simulate the LAT data. In the rest of the session we will discuss only the analyses tasks relevant for our purpose.

The *Science Tools* are continuously updated and hence several version are available. Although they do not substantially differ, sometimes important bugs have been recognized and corrected. In our study different packages were used, according to the most recent *Science Tools* version available at that time.

3.4.1 *Data preparation*

Generally event selection criteria specific for an analysis are e.g. spatial region and temporal interval of interest, energy range, event class level or in case of more detailed analysis the conversion point in the detector (in the *front* or *back* section). Beside them there are few more considerations that must be taken into account. For example data used for astrophysical purposes have also to be selected on the basis of the corresponding observing time intervals: good time intervals are, e.g., those when the LAT was taking data in the configurations suitable for scientific analysis[18] and the quality of the data was judged to be "good" by the monitoring scientists.

Moreover, further selections are required to limit the contamination by γ rays produced in cosmic rays interactions with the Earth atmosphere. Actually the Earth's limb constitute a strong source of background and is largely anisotropic due to the *Fermi* pointing strategy. Atmospheric γ rays are real γ rays entering the LAT, which cannot be rejected using detector information apart from the arrival direction.

Therefore we filter them out with a zenith-angle cut, i.e. only events with an infalling direction within a maximum zenith angle for the infalling direction, are considered. The direction is chosen on the basis of the LAT orbital characteristics and the region of the sky to be studied. The current value of 100° is the one recommended by the LAT instrument team (previously it was of 105°).

Another important point that we want to stress regards the choice of the extension of the region to be selected. Due to the large LAT PSF at low energies (e.g., 68% of the counts will be within ∼3.5 degrees[19] at 100 MeV), when analyzing a single source all counts within a certain area around the source have to be included. We usually refer to this region as the "region of interest" (ROI). The ROI is selected from

17 http://fermi.gsfc.nasa.gov/ssc/data/analysis/documentation/Cicerone/

18 This excludes time periods when some event has affected the quality of the data and e.g. requires that the spacecraft be within the range of rocking angles used during nominal sky-survey observations. In addition, runs where the detector is specifically configured for calibration purposes, are excluded as well.

19 See http://www-glast.slac.stanford.edu/software/IS/glast_lat_performance.htm for a review of LAT performance.

the original event file using a dedicated tool and should be several times the characteristic PSF size in order to ensure that a large fraction of counts observed from the source of interest are included in the study. Note that since the size of the LAT PSF depends on energy and is roughly described by (PSF_{100MeV}) x $(\mathrm{E}/100)^{-0.8}$ (with E the energy in MeV), if we consider only higher energy photons (e.g., E > 1 GeV as we choose for the study of 1ES 1215+303 in § 4.3), smaller ROI radius of just a few degrees may be used.

3.4.2 *Likelihood analysis, Model Fitting*

Several likelihood computations are usually needed before the best set of parameters is found. Fitting involves varying model parameters and at times several alternative models may be tested , with parameters fixed or with different sources present or absent. However, there are a series of subsequent steps that need to be calculated only once. First is the livetime map, i.e. the time that the LAT observed a given position on the sky at a given inclination angle. It depends only on the history of the LAT orientation during the observation and not on the particular model adopted. Actually the number of counts that a source should produce depends only on the amount of time that the source spent at a given inclination angle during an observation. In this procedure good time intervals are chosen accordingly to the event selection criteria previously specified.

The cumulative livetimes are then used to precompute the exposures with procedures which differ according to the analysis strategy, binned or unbinned. Basically, this involves the integration of the effective area over the FoV weighted by the livetimes over a position-energy grid. This precomputed quantity is then used to calculate the convolution in Eq. 55, thus to obtain the number of events expected for each bin. In the convolution with the IRFs the energy dispersion is usually neglected to limit the computing time, since its impact is less important. This can be a source of systematic effects, especially if there is a strong dependence of the effective area on energy, notably at low energies (a few hundreds MeV).

Once these quantities are derived, the last step is the actual computation of the likelihood.

Fitting aims to find the set of parameters that maximizes the likelihood. Since the likelihood is a non-linear function of the parameters, numerical minimization codes for maximizing non-linear functions must be used. The maximum is found by several iteration in which the function is calculated for different sets of trial parameters; the algorithms estimate the derivatives of the function w.r.t. these parameters, and then choose new trial parameters that are progressively closer to the set that maximizes the function. this step is performed until the change in the function value between iterations is sufficiently

small (or the number of iterations reaches a maximum value). At this point the output gives the best-fit values of the model parameters and their statistical uncertainties derived from the likelihood profile (Eq. 61), as well as other important quantities (e.g. the maximum likelihood logarithm values associated to each model to perform the LRT, § 3.3.1).

Different numerical minimization codes are applied in the likelihood routines, the most used is probably `Minuit`[20], which is also the one chosen for all the studies of this thesis.

3.5 DIFFUSE γ-RAY EMISSION

Besides the IRFs and data (§ 3.1.2), the LAT team releases also templates of the diffuse components, namely the *Galactic and Extragalactic diffuse emission*. The diffuse emission in the interstellar space is due to the true diffuse emission from the galactic medium and unresolved and faint galactic sources along with an extragalactic background not yet completely understood. It is very important to provide an accurate determination of it since it dominates the γ-ray sky, constituting almost 90% of the total luminosity at GeV energies.

In the following subsections we briefly introduce these two components and also review the background models assumed for the likelihood analysis.

3.5.1 *Diffuse Galactic γ-ray Emission*

The high-energy Galactic γ-ray emission is primary produced by the interaction of energetic cosmic-ray electrons and protons with the interstellar gas and the interstellar radiation field. The main processes involved are the decay of neutral pions produced in hadron collisions, the inverse Compton scattering of the interstellar radiation field by electrons and their bremsstrahlung emission in the interstellar medium.

Therefore, the galactic component requires a model of cosmic rays propagation and must account for the distribution of the target gas and the interstellar radiation field. Such models are based on the theory of particle transport and interactions in the interstellar medium and can exploit data provided by different observations[21]. As a matter of fact the model for the Galactic diffuse emission was developed using spectral line surveys of HI and CO (as a tracer of H2) to derive the distribution of interstellar gas in Galactocentric rings. In addition,

20 http://wwwasdoc.web.cern.ch/wwwasdoc/minuit/minmain.html
http://seal.web.cern.ch/seal/MathLibs/Minuit2/html/index.html

21 An important contribution to the development of these models has been given by EGRET, even if it provided a deceptive view of the GeV energy range leading to a strong debate about the so called "GeV excess" (Hunter et al., 1997; Strong et al., 2004; Abdo et al., 2009b).

infrared tracers of dust column density were used to correct column densities in directions where the optical depth of HI was either over or under-estimated.

The model of the diffuse γ-ray emission was then constructed by fitting the γ-ray emissivities of the rings in several energy bands to the LAT observations. The fitting also required a model of the inverse Compton emission which was calculated using GALPROP and a model for the isotropic diffuse emission. The `Pass 7` Galactic diffuse model includes several improvements w.r.t the version released for `Pass 6` analysis, mainly addressed to reduce residual emission caused by imperfect modeling of large-scale diffuse structure[22]. In particular we note that it is based on two years of LAT data, a refined model grid of 0.125° (whereas `Pass 6` used a 0.5° grid), updated HI map and GALPROP-derived template for Inverse Compton, as well as it accounts for dedicated templates for large-scale regions of excess emission.

As a result of these improvements, the Galactic diffuse model provided for `Pass 7` (gal_2yearp7v6_v0.fits) is significantly larger (500MB) than the previous. This requires significant memory usage when fitting and therefore it can be difficult to use on computers with limited memory. For this reason the LAT team has prepared a reduced-sized version by decreasing the number of planes in energy ranges over which the model is well approximated as a power law. The resulting model (gal_2yearp7v6_trim_v0.fits) has the same spatial distribution but is half the size. The only caveats to be mentioned is that it should not be used in analysis below 50 MeV (the lower energy limit for either model) since the extrapolations would not be quite adequate.

3.5.2 *Isotropic Component*

The isotropic background is difficult to disentangle from the intense galactic diffuse foreground because it is relatively weak and has a continuum spectrum with no strong (distinguishing) features. Its modeling is more complex w.r.t. the galactic one, since all the components which may contribute are still not well understood and there are several systematic uncertainties that are difficult to determine precisely. First of all, the isotropic component includes any true extragalactic component as well as a residual instrumental background (e.g. charged cosmic rays misclassified by the LAT background rejection as legitimate γ rays). While both contributions are believed to be rather homogeneous, there is no guarantee that their emissivity be precisely isotropic. For instance, if the extragalactic component consists of a population of faint and unresolved point sources, small anisotropies may result from the high variability of AGNs and the latitude de-

22 Large-scale diffuse structures such as Loop 1 and the high-energy Galactic lobes have been incorporated into this model.

pendent sensitivity of the LAT instrument. The current knowledge of the foreground Galactic emission is not precise enough to assess the anisotropies of the extragalactic background. Moreover, the acceptance for residual charged particle background is not the same as for γ rays. That is, the distribution of arrival directions in instrument coordinates is not the same as for γ rays and our modeling it as isotropic with the γ-ray response functions is only an approximation.

Besides, the determination of the isotropic component depends on the adopted model for the galactic emission and on the background contamination of a specific event class, thus it should be used with the same Galactic diffuse model and event class selection that were used to derive it. In practice the isotropic spectral template provides the spectral form from a fit to the all-sky emission ($|b|>30$ deg) that is not represented in the Galactic diffuse model and therefore includes both extragalactic diffuse γ rays and remaining residual cosmic-ray emission. It is released as a two columns file with the central energy (in log MeV) for the band and the differential flux in that band (in ph/cm^s/MeV/s/sr).

4

MULTIWAVELENGTH OBSERVATION OF TEV BLAZARS

The study of the MeV-GeV range has received a strong boost since the advent of the *Fermi* satellite. Already in the first two years of operations, more than 1800 sources have been detected at these frequencies thanks to the LAT (Nolan et al., 2012). This represents a tremendous step forward in this region, especially when compared to the achievements obtained by previous γ-ray instruments (e.g. SAS-2, COS-B and EGRET).

At the same time, the window of the TeV γ-ray sky has opened wide thanks to the latest generation of Imaging Atmospheric Cherenkov Telescopes (IACTs). The number of sources detected in the VHE energy regime has significantly increased in just few years: until the beginning of 2013, 143 sources were identified as TeV γ-ray emitters[1]. It is widely demonstrated that γ-ray satellites facilities coupled with ground based Cherenkov Telescopes provide a powerful tool to substantially increase our knowledge of this extreme regime.

Among all the currently operating IACTs, MAGIC, due to its low energy threshold, is the best suitable instrument for simultaneous observation of blazars with *Fermi*. The minimum energy that a γ ray must have to be detectable from the ground with MAGIC (50 GeV, the lowest energy threshold that can be achieved by the current generation of IACTs) just matches the maximum energy reachable in space by *Fermi* (300 GeV). This wide overlapping enables nearly continuous coverage in the γ-ray regime and offers the unique opportunity

1 see e.g. http://tevcat.uchicago.edu/

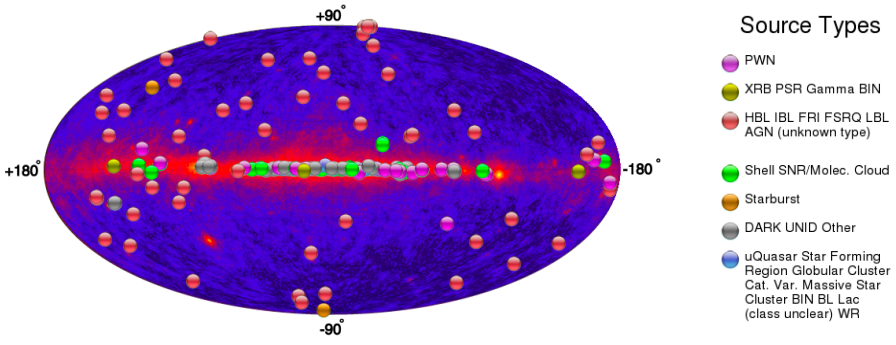

Figure 4.1 Map of the catalog of localized sources of TeV γ rays in Galactic coordinates as of January 2013, provided by the online catalog *TeVCat*. The TeV map has been overlaid to the GeV sky map as observed by the *Fermi* LAT in two years.

to test what the outcome of a close collaboration with with the next generation of γ-ray instruments (e.g. CTA and HAWC) will be.

In addition, an essential ingredient of the synergy between space and ground-base instruments is the different fields of view. In fact, since the most sensitive instruments observing the VHE band are designed for pointing strategy, the typical field of view for IACTs is of the order of a few degrees and full sky surveys are practically unfeasible. Thus, besides the common practice to use already existing catalogs in the optical, X-ray or high energy range to determine potential targets for pointed observations with VHE γ-ray telescopes, additional invaluable efforts is offered by facilities that allow a continuous monitoring of interested targets, among all the *Fermi* LAT or networks of optical telescopes.

This Chapter will address a detailed study of a sample of TeV blazars that have been observed and detected simultaneously by *Fermi* and MAGIC. Following an agreement between MAGIC and LAT Collaborations, I provided detailed studies at *low* energies complementing and integrating MAGIC observation at higher energies. The sample constitutes the almost totality of AGN observed by MAGIC.

The sample includes five BL Lacs, namely PG 1553+113, 1ES 1215+303, B3 2247+304, 1ES 0806+524, 1ES 1727+502, all belonging to the HSP (high synchrotron peaked) sub-class, like the great majority of extragalactic sources detected above 100 GeV. In addition, we will also present the first preliminary analysis on PKS 1510-089, discussing the challenging perspectives that motivated a new observation by MAGIC on this FSRQ. Results will be also complemented by multifrequencies data collected by several other facilities, an essential tool to provide a fertile context for the maximization of the scientific outcome. In the following paragraphs, we will briefly present the main multiwavelength instruments that have been involved in the study of our targets highlighting also some general information regarding their data reduction. More details about each specific source analysis, as well as the scientific results, will then be given in later paragraphs.

4.1 MULTIWAVELENGTH FACILITIES

4.1.1 *MAGIC Telescope*

The VHE γ-ray observations were carried out with the MAGIC telescopes located on the Canary Island of La Palma (28.8° N, 17.8° W at 2200 m above sea level). MAGIC consists of two 17 m IACTs sensitive to γ rays from 50 GeV up to several tens of TeV and, as mentioned before, it features the lowest trigger energy threshold among the existing operating IACTs. The two instruments can be operated independently, but since autumn 2009 they are working together in stereoscopic mode, which ensures a good sensitivity threshold at $< 0.8\%$

of the Crab Nebula flux above 300 GeV in 50 hours of observations. Detailed information of current performance and software developments can be found in Carmona et al. (2011) and Lombardi (2011). Of much interest for us, their field of view of 3.5° ∅, an angular resolution better than 0.07° and an energy resolution of 16%.

Observations presented in the following sections were performed in the false-source tracking (or *wobble*) mode, in which each telescope is alternated every 20 minutes between two sky positions at 0.4° offset from the source. This asset provides a simultaneous estimate of the background from the same data set (Fomin et al., 1994). The data analysis is carried out with the standard MAGIC analysis framework "MARS" as described in Moralejo et al. (2010) and with additional adaptations incorporating the stereoscopic observations (Aleksić et al., 2012c). The images are cleaned using timing information (see Aliu et al., 2009) and parametrized in each telescope separately following the prescription of Hillas (1985).

To reconstruct the arrival direction of the shower, the random forest regression method (RF DISP method, Aleksic et al. 2010) is used along with stereoscopic information such as the height of the shower maximum and the impact distance of the shower on the ground. After estimating the RF DISP for each telescope separately, two possible solutions are obtained along the major axis of the shower image in each telescope, respectively. Finally, the combination of the two solutions with the shortest squared angular distance between them is determined. If this angular distance is greater than 0.05^2 the event is removed from further analysis. This improves the background rejection since hadron induced showers have a larger error on the reconstruction of the arrival direction and are are more likely to suffer huge fluctuations by different reconstruction algorithms. The final arrival direction is the average of the two solutions.

Quite similar to the above approach, used to reject the hadronic background, is the signal search done with the θ^2 approach (Aleksić et al., 2012c), consisting in considering the distribution of the squared angular distance between the arrival direction of the events and a given position, which corresponds to the nominal source position, in the case of the so-called ON distribution, and to the nominal background control positions, in the case of the so-called OFF distributions.

4.1.2 *TUORLA/KVA telescope*

The Kungliga Vetenskapsakademien (KVA) optical telescopes are located at the Roque de los Muchachos observatory on La Palma, but are operated remotely from Finland. The two telescopes are attached to the same support. The larger telescope is a 60 cm ∅ Schmidt reflector and the smaller is a 35 cm ∅ Celestron. The former is used for

polarimetric observations (see e.g. Piirola et al., 2005) while the latter is used for simultaneous photometric observations with MAGIC, but also to monitor potential γ-ray candidate AGN in order to trigger VHE observations whenever the sources are in high optical states[2].

Photometric measurements are performed in the optical R band using differential photometry, i.e. by having the target and the calibrated comparison stars on the same CCD images (Fiorucci and Tosti, 1996; Fiorucci et al., 1998). The magnitudes of the source and comparison stars are measured using aperture photometry and converted to linear flux densities according to the formula $F(\mathrm{Jy}) = F_0 \times 10^{-\frac{\mathrm{mag_R}}{2.5}}$, where F_0 is a filter-dependent zero point. In particular, in the R-band $F_0 = 3080\,\mathrm{Jy}$, according to Bessell (1979). In order to obtain the AGN core flux, contributions from the host galaxy and, if any, nearby stars that contribute to the overall measured flux have to be subtracted from the obtained value. These contributions are determined according to Nilsson et al. (2003). In addition, the brightness has to be corrected for galactic absorption (Schlegel et al., 1998).

Noteworthy, since the end of 2002 the KVA telescope is operated under the Tuorla Blazar Monitoring Program[3], which is run as a support program to the MAGIC observations with the purpose of monitor candidates from the compilation of Costamante and Ghisellini (2002) as well as known TeV blazars in the optical waveband. This program has already provided crucial efforts triggering the discovery at VHE of γ-ray emission for several sources (e.g. Aleksić et al., 2012a,b).

4.1.3 *SWIFT satellite*

The prime objective of the NASA *Swift* Gamma-Ray Burst observatory, launched on November 2004 (Gehrels et al., 2004), is the detection and the follow-up of Gamma-Ray Bursts, but it has turned into a multi-purpose observatory due to its fast slewing and response capacity and its multiwavelength coverage. *Swift* is equipped with three telescopes, the Burst Alert Telescope (BAT; Barthelmy et al., 2005), which covers the 15-150 keV range, the X-ray telescope (XRT; Burrows et al., 2005) covering the 0.3-10 keV energy band, and the UV/Optical Telescope (UVOT; Roming et al., 2005) covering the 1800-6000 Å wavelength range.

The XRT data are processed with standard procedures using the `FTOOLS` task `XRTPIPELINE` distributed by HEASARC within the `HEASoft`[4] package. Events with grades 0-12 collected in photon counting mode are selected (see Burrows et al., 2005) and the latest response matri-

2 An alert is issued to MAGIC when the optical flux increases by 50% from the long term running average.

3 project web page: http://users.utu.fi/kani/

4 http://heasarc.gsfc.nasa.gov/lheasoft/

ces available in the *Swift* `CALDB` are used. For the spectral analysis, the source events are extracted in the 0.3-10 keV range within a circle centered on the target, while the background is extracted from an off-source circular region. Ancillary response files are generated with `xrtmkarf`, and account for different extraction regions, vignetting and PSF corrections. Spectral redistribution matrices are obtained by the Calibration database maintained by HEASARC. The spectra are extracted from the corresponding event files and binned using `GRPPHA` to ensure a reliable χ^2 statistics. Spectral analysis was performed using XSPEC. The neutral hydrogen-equivalent column density is fixed to the Galactic value in the direction of the source (Kalberla et al., 2005).

UVOT is equipped with several filters to observe the correspondent photometric bands (V, B, U, UVW1, UVM2, UVW2) and the standard operation mode is the "filter of the day" (required to extend the lifetime of the filter wheel). UVOT data were processed with the `uvotmaghist` task of the `HEASoft` package. The observed magnitudes have been corrected for Galactic extinction (Schlegel et al., 1998), applying the formulae by Pei (1992) and finally converted into fluxes following Poole et al. (2008).

4.1.4 *OVRO telescope*

The Owens Valley Radio Observatory (OVRO) located in California is a 40 m single-dish radio telescope. The telescope is equipped with a cooled receiver installed at prime focus with two symmetric off-axis corrugated horn feeds providing sensitivity to left circular polarization. The telescope and receiver combination produces a pair of approximately Gaussian beams which are separated in azimuth by 12.95′ referred to as "antenna" beam and "reference" beam. The center frequency of the receiver is 15.0 GHz with a 3.0 GHz bandwidth and a noise-equivalent reception bandwidth of 2.5 GHz.

4.1.5 *Metsähovi telescope*

The 13.7 m Metsähovi telescope located in Kylmälä, Finland provides radio observations at 37 GHz . The telescope has a detection limit of ~ 0.2 Jy under optimal conditions; the observation methods, and the data analysis procedure are described in e.g. Teraesranta et al. (1998).

4.2 THE SOURCE PG 1553+113 AND ITS DETECTION AS A HE-VHE γ-RAY EMITTER

First classified as a BL Lac object by (Green et al., 1986), it was discovered as VHE γ-ray emitter in 2006 by H.E.S.S. and later confirmed by MAGIC. Although previous observations operated by EGRET allowed to determine upper limits, in the HE regime it was detected for the first time only in the past few years, thanks to the *Fermi* LAT telescope. In the following sections the analysis of the data taken by the LAT from 2008 to 2009 is presented along with other multiwavelength data. Contrary to previous results reported in Abdo et al. (2010e), we find a clear indication of variability in the gamma light curve. In addition, our study reveals a hint for correlation between the optical and HE-VHE behavior. All available multifrequencies data are combined to construct and model the broadband SED of PG 1553+113 and we show that the SED can be fitted by a one-zone SSC model, as usual for BL Lac objects, which gives the main physical parameters governing the high energy emission in the blazar jet.

Part of this original work has been published in Aleksić et al. (2012d).

4.2.1 *Introduction*

PG 1553+113 is a BL Lacertae object (Falomo and Treves, 1990; Beckmann et al., 2002) located at a R.A. of $\alpha_{\mathrm{J2000}} = 15^{\mathrm{h}}55^{\mathrm{m}}43^{\mathrm{s}}.04$ and a DEC $\delta_{\mathrm{J2000}} = +11^{\circ}11'24.4''$ in the constellation of Serpens Caput. Its redshift remains still unknown despite continued efforts to determine it. Recently Abdo et al. (2010e) and Prandini et al. (2010) derived an upper limit for it; they found $z = 0.75^{+0.04}_{-0.05}$ and $z = 0.74 \pm 0.08$, respectively. The COS GTO team indicates 0.40-0.43 as an accurate estimate for its redshift (Danforth et al., 2010).

It shows a typical blazar spectral energy distribution with a double-peaked shape. The rising high energy part and the high energy peak of the PG 1553+113 SED have been studied for the first time thanks to observations made by the LAT. PG 1553+113 is placed, at times, among the most extreme of the HBLs[5], its large X-ray to radio flux ratio making this source a typical example of this class. Actually the logarithmic ratio of its 5 GHz radio flux to its 2 keV X-flux has been found to be $\log(F_{2\,\mathrm{keV}}/F_{5\,\mathrm{GHz}}) = -4.99\mathrm{to} - 3.88$ (Rector et al., 2003; Osterman et al., 2006). Other TeV blazars have exhibited high value of this ratio but only in some occasions (e.g. 1ES 0229+200, H 1426+428, 1ES 1959+650; Rector et al., 2003).

Different mean flux levels have been measured in the radio band from this source. For example, its 4.8 GHz flux is found in the range from 180 to 675 mJy (Bennett et al., 1986; Gregory and Condon, 1991; Perlman et al., 2005; Rector et al., 2003) while for fluxes between 4.8

5 A BL Lac is classified extreme when it has $\log(F_{2\,\mathrm{keV}}/F_{5\,\mathrm{GHz}}) \geq -4.5$ (Rector et al., 2003)

and 14.5 GHz Perlman et al. (2005) and Osterman et al. (2006) reported variability on month timescales. To date, no indication for superluminal motion has been evidenced in the literature although Very Long Baseline Array (VLBA) observations have resolved a jet extending at least 20 pc to the northeast of PG 1553+113 (Rector et al., 2003).

In the optical band it is a bright source with V-band magnitude of V_o ∼14 (Falomo and Treves, 1990; Osterman et al., 2006). Listed among the sources constantly observed by the Tuorla Observatory Blazar Monitoring Program (Takalo et al., 2007), the flux in the R band is monitored since 2005, and so far shows only modest variations changing from 1 to 8 mJy. Observations taken between 1986 and 1991 with the ESO telescopes found its optical spectral index, α_O, to remain almost constant ($\alpha_O \sim -1$) and its magnitude to vary by $\Delta V_o = 1.4$ (Falomo et al., 1994). Low levels of optical variability were seen by (Osterman et al., 2006) during their 2003 observing campaign.

Well detected in the X-ray band, it has been observed by most X-ray missions (Einstein, ROSAT, ASCA, BeppoSAX, RXTE, XMM-Newton, *Swift* and Suzaku). A comparative study among data collected by several of these facilities from 1998 to 2006 and carried out by Reimer et al. (2008), has pointed out a number of different flux levels in the X band, although no evidence for strong or fast (sub-hour) flux variability was found. Until now the highest energy X-ray measurement at ∼ 30 keV was obtained with the 2006 Suzaku observations, when a 10-30 keV flux of 1.35×10^{-11} erg cm^{-2} s^{-1} was observed.

The synchrotron peak of this source is located between the UV and X-ray bands (Nieppola et al., 2006b), as shown in Figure 4.2. The lack of evidence for spectral hardening in these energies seems to indicate that all of the X-ray emission detected is due to synchrotron emission.

In the γ-ray band, at MeV-GeV energies, PG 1553+113 was not detected by EGRET, all the observations leading only to upper limits. In spite of this, *Fermi* detected it already in the first three months of observations; actually it was included in the bright source list[6] (Abdo et al., 2009a) with a significance above 10σ. Listed as 0FGL J1555.8+1110 with a flux of $F_{\rm LBAS}(E > 100\,{\rm MeV}) = (8.0 \pm 1.0) \times 10^{-8}$ cm^{-2} s^{-1}and a photon index of $\Gamma_{\rm LBAS} = 1.70 \pm 0.06$, it has one of the hardest spectra of the 106 AGNs that comprise this list.

The first LAT results reported a surprisingly constant spectrum over 200 days both in normalization and slope (Abdo et al., 2010e) (in the 200 MeV - 100 GeV energy range), with a shape well described by a pure power law of index 1.68 ± 0.03, as shown in the left panel of Figure 4.4. Although this stability is supported by the H.E.S.S. and MAGIC observations, which showed rather marginal variability in the TeV range during 2005-2006, it is in contrast with the behavior commonly observed in the other TeV emitting BL Lacs. Nevertheless,

6 the high-confidence AGN associations from the first three months of Fermi data

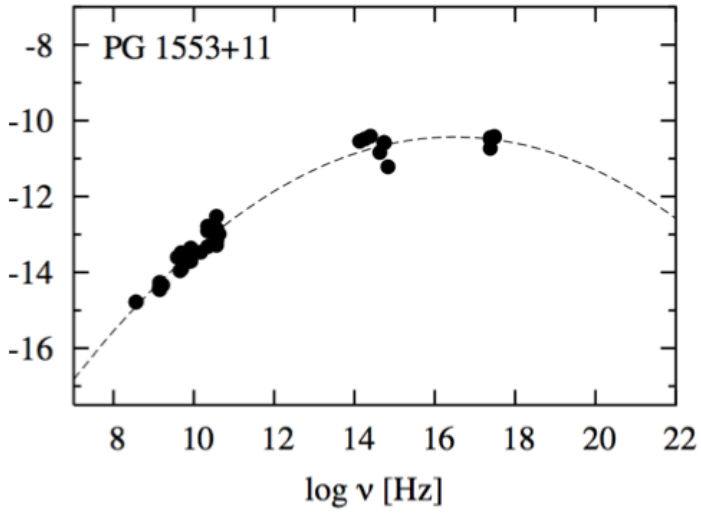

Figure 4.2 SED of PG 1553+113 , from Nieppola et al. (2006a). The synchrotron peak estimated from a parabolic fit is at 0.4 keV (corresponding to $10^{16.5}$ < Hz).

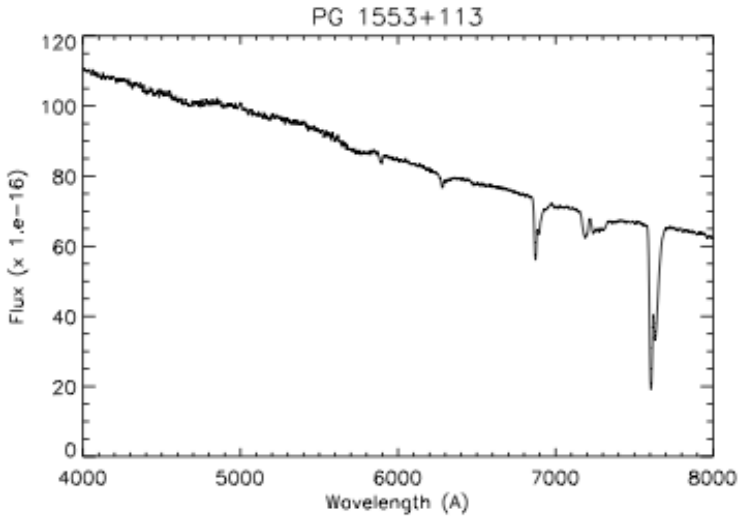

Figure 4.3 Optical spectrum of PG 1553+113 , from Treves et al. (2007). No characteristic emission or absorption lines are identified from the thermal continuum, except for the telluric absorption.

in § 4.2.4 we will present an extended study that we performed over a 17 months dataset, which provides clear indication for variability.

The Costamante and Ghisellini (2002) compilation listed PG 1553+113 among the TeV candidate BL Lac objects due to its spectral features. Few years after, in 2005, the prediction was confirmed by H.E.S.S. and MAGIC (Aharonian et al., 2006; Albert et al., 2007a), that, in 2005 and 2006 respectively, measured above 200 GeV a flux of $\sim$ 2% the Crab Nebula's one. Despite the different energy ranges and observation pe-

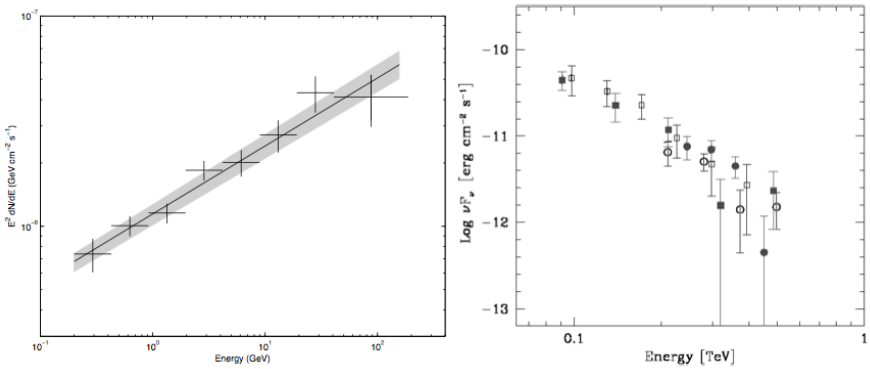

Figure 4.4 Differential energy spectra of PG 1553+113 . Left panel: spectrum measured by Fermi LAT in the HE regime. Right panel: VHE spectrum measured by H.E.S.S. in 2005 (open circles) and 2006 (filled circles) and MAGIC in 2005 (open squares) and 2006 (filled squares) from Reimer et al. (2008). Image from Abdo et al. (2010e).

riods, the spectral measurements of the two IACTs are in very good agreement, as can be noted from the right panel of Figure 4.4. The VHE spectrum appears extremely soft (photon index $\Gamma \sim 4$), as expected by the absorption of VHE photons through interaction with the EBL, if the source is located at relatively large redshift (Stecker et al., 1992).

4.2.2 *Multiwavelength Analysis Procedures*

In this paragraph we summarize the multifrequencies facilities that provided data for our study. More details on how the *Fermi* analysis has been performed are reported in § 4.2.3.

- Optical data (second panel of Figure 4.8)
  The simultaneous optical R-band data are collected on a nightly basis by the Tuorla Observatory Blazar Monitoring Program[7] (Takalo et al., 2007) using the KVA 35 cm telescope at La Palma and the Tuorla 1 meter telescope in Finland.

- X-ray data (third panel of Figure 4.8)
  14 *Swift* pointed observations of the source are available for the period April 20, 2005 - February 5, 2010. Data collected on 5 and 7 July 2009 have been summed in order to have enough statistics to obtain a good spectral fit. The XRT data are processed with standard procedures (`xrtpipeline v0.12.6`), filtering, and screening criteria by using the `HEASoft` package (v6.11). Some observations showed an average count rate of > 0.5 counts s^{-1}, thus pile-up correction was required. All spectra are rebinned

7 Additional information are available at http://users.utu.fi/kani/1m/

with a minimum of 20 counts per energy bin to allow χ^2 fitting by XSPEC (v12.7.0). The spectrum was fitted with an absorbed log parabola law (see e.g. Tramacere et al., 2007), with a neutral hydrogen column fixed to its Galactic value (3.65×10^{20} cm^{-2}; Kalberla et al., 2005).

- HE data (lower panel of Figure 4.8)
  Fermi data used for this analysis are restricted to the 1-100 GeV energy range to avoid the contamination of PG 1553+113 spectral parameters by other γ-ray emitters in the same ROI. In particular, we note that next to PG 1553+113 there is another quite bright γ-ray source, well visible in the *Fermi* counts map of Figure 4.5 (further details are discussed § 4.2.3). The LAT data were collected from MJD 54682 (August 4, 2008) to MJD 55200 (January 4, 2010) in survey mode. An unbinned analysis is performed with the standard Science Tools software package (version v09r21p00) and with the P6_V11_DIFFUSE IRFs. For this analysis, only photons belonging to the "Diffuse" class and located in a circular ROI of 10°radius, centered at the position of PG 1553+113 , are selected. In addition, photons arriving from zenith angles $> 10°$ and with rocking angle $> 52°$ are excluded to limit contamination from Earth limb γ-rays and to avoid time intervals during which Earth entered the LAT FoV, as explained in § 3.4.1. A separate analysis of the high energy emission in each time bin is performed. All point sources reported in the 1FGL catalog (Abdo et al., 2010c) within 15° of the target, including the source of interest itself, are considered in the model of the region. Those within the 10° ROI radius are fitted with a power law with spectral indexes frozen to the values obtained from the likelihood analysis of the full data set, while those beyond 10° ROI radius have their values frozen to those found in 1FGL. Upper limits at 2σ confidence level are computed when the source is not significantly detected (the test statistics threshold used in this analysis is $TS < 10$, see § 3.3.1 for more details.)
  .

- VHE data (first panel of Figure 4.8)
  The MAGIC data cover five cycles of TeV observations (2005-2009) at energies above 150 GeV. PG 1553+113 was observed for nearly 19 hours in 2005 and 2006 (Albert et al., 2007a); it was also the subject of a multiwavelength campaign carried out in July 2006 with optical, X-ray and TeV γ-ray telescopes (Albert et al., 2009a). The follow-up observations result in 28.7 hours of good quality data taken between 2007 and 2009. The signal obtained by combining the results from each year has a 8.8σ significance according to Li and Ma (1983). The significance of the signal was 5.8σ in 2007, 8.1σ in 2008 and 4.2σ in 2009. Due

to a large difference in the energy thresholds and changes in the experimental conditions, the obtained fluxes cannot be compared directly. A detailed spectral analysis is necessary in order to study the source emission. Therefore the data are analyzed separately, using dedicated sets of simulated data.

4.2.3 *Fermi-LAT data analysis*

As can be seen looking at the counts map of the region, Figure 4.5, within 2° of PG 1553+113 there is another bright *Fermi* source: 1FGL J1553.4+1255, located at $\alpha_{J2000} = 15^h53^m28^s.2$ and $\delta_{J2000} = +12°55'20.3''$ and is thus spatially coincident with the quasar QSO B1551+1305 ($z = 1.29$). It lays at an angular separations of 1.8° from the source of interest and is detected up to approximately 10 GeV with an integral flux ($E > 200\,\mathrm{MeV}$) of $(5.67 \pm 0.38) \times 10^{-8}$ cm^{-2} s^{-1}and photon index of 2.26 ± 0.05 during the first 9 months of *Fermi* observations. As pointed out in (Abdo et al., 2010e) there is evidence for variability in its photon index and flux, but neither are correlated with the signal detected from PG 1553+113 as resulted from our analysis.

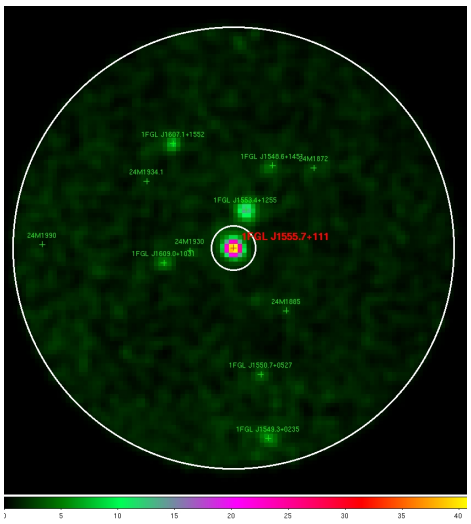

Figure 4.5 *Fermi* count map of PG 1553+113 region (10° radius) for energies 1 GeV – 100 GeV. In the center, the white circle of 1° radius indicates the source itself, next to the latter is well visible another bright source, 1FGL J1553.4+1255.

However, since this work is mainly interested in the higher energy LAT data to connect *Fermi* and MAGIC spectra in view of the determination of the inverse Compton peak, the analysis that we perform here is focused in the > 1 GeV *Fermi* range. In this way, we maximize the advantage derived by the improved LAT PSF above this energy (better than 1°) to ensure the best estimation of the source parameters.

The following paragraph will present a detailed investigation about the behavior of the source in the LAT band by means of light curves with time bin of 5 days and 10 days. The possible correlation of its behavior with other wavebands is addressed in § 4.2.5.

4.2.4 *Fermi data temporal analysis*

The flux variability in the *Fermi* band has been first investigated by means of a χ^2 fit of a constant to the fluxes from the LAT light curve (Figure 4.6). Upper limits are included in the fit following the same procedure of the 1FGL catalog. Whenever the source TS < 10 or the nominal flux uncertainty was larger than half the flux itself, the 2 σ upper limit was used in place of the best-fit flux value and the error estimate for that interval was replaced with half the difference between that upper limit and the best-fit. In this way the best-fit value and its estimated error where used even when the source was not significant. Following this procedure, a preliminary fit to the 5 day bin light curve between MJD 54682-55200 shows no evidence of variability for the analyzed period: χ^2=88.83 for 103 dof, with chance probability of 84%.

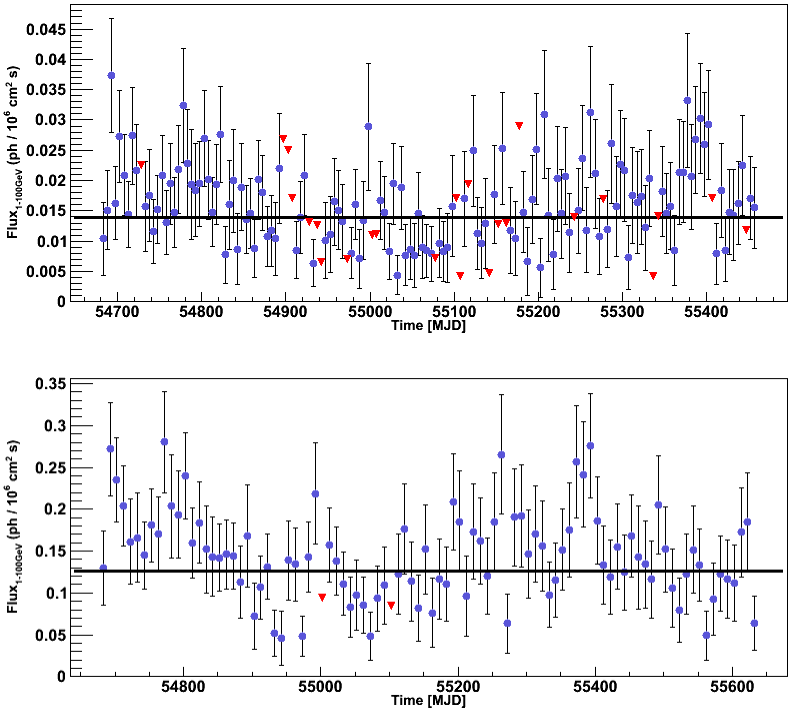

Figure 4.6 *Fermi* light curve of PG 1553+113 with binning of 5 day (upper plot) and 10 day (lower plot) in the energy range 1 GeV – 100 GeV. Red triangles indicate 2σ upper limits (TS < 10).

Anyway, it is worth noticing that this light curve contains several upper limits and the error bars relative to the flux values are quite large. Since the χ^2 test measures the scatter of data points with respect to the mean compared to that expected from the uncertainty estimates, it could be that in this case the instrument is not sensible enough to detect variations for such a time scale, with the main effect that huge error bars smear out small variations. Therefore we decided to extend the time interval with more recent data and we produced a second light curve with a larger time bin, 10 days. Repeating the precedent fit with this dataset yielded $\chi^2 = 149$ for 95 dof. The correspondent chance probability is 0.07% and provides a clear indication that the source is variable.

Additional evidence to support the latter result is obtained by means of an autocorrelation analysis. For a white noise light curve there is no correlation between nearby points. This is not directly verified by the χ^2 test, but can be checked with an autocorrelation function (ACF).

Going back to the 5 day light curve, the curve contains several ($\sim$ 20%) upper limits, mostly interpreted as lower flux points, sin such a way that ignoring them will reduce the variability. On the other hand, this will not change the conservative estimate of whether a significant variability is present or not. In addition, having upper limits produce gaps in the light curve, but, since the aim is to check if variability is present, not the time scale, ignoring the gaps, in effect compresses the light curve but will not affect the result.

This results in a smoothing and time compression by about 20% of the ACF. The advantage is that for evenly sampled data the standard ACF can be used, which is not affected by systematics and is more robust than the discrete correlation function to estimate the correlation strengths. Figure 4.7 shows the ACF for the PG 1553+113 light curve. The error bars reflect the scatter of 1 million ACFs computed from simulated light curves containing Gaussian white noise, standard deviations equal to data uncertainty values. From the simulations we deduce that the probability to get, by chance, an average ACF level (below 140 days) as high or higher than that of PG 1553+113 is $< 3 \times 10^{-4}$.

As mentioned above, in a previous dedicated study, Abdo et al. (2010e) found that during the first year monitoring period the emission of PG 1553+113 above 200 MeV was almost steady. On one hand, since in that study data are binned in two day bins, the lack of detection of significant variability could be due, also in this case, to low statistics in the determination of the spectral values. On the other hand, we note that the contrasting result could be attributed to different energy ranges studied. Abdo et al. (2010e) considered the integral flux above 200 MeV, which can be dominated by the contribution at lower energies, while the study presented here is focused in the upper edge of LAT band, close to the IC peak. Therefore, it could be that

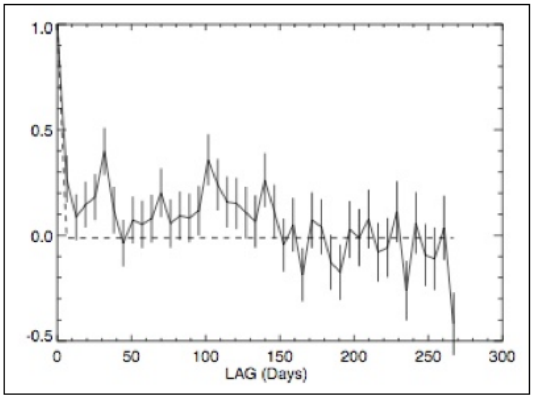

Figure 4.7 ACF for the 5 day bin light curve of PG 1553+113 . The probability to get, by chance, an average ACF level (below 140 days) as high or higher than that of PG 1553+113 as deduced from the simulations is $< 3 \times 10^{-4}$.

while at low energies the IC continuum shows marginal variability, this does not happen in proximity of the peak. In fact, small variability at GeV energies is a common feature of HBLs (see e.g. Abdo et al., 2010g). Further analysis on this task are needed to definitively clarify the origin of this inconsistency.

4.2.5 *Multiwavelength correlations*

Figure 4.8 displays the light curve of PG 1553+113 in different wavelengths. During the five years of TeV monitoring the source generally showed a marginal activity in the VHE γ-ray band. The same behavior is followed by the optical flux, whose variations are limited within a factor of four, with a maximum flux reached in 2008 and a minimum value in 2009. A low emission in 2009 is also detected at every other wavelengths, suggesting that the source entered in a low activity state during that year, with a minimum reached few days after MAGIC observations.

Figure 4.9 shows the result of a correlation study between optical and TeV simultaneous observations. The VHE γ-ray flux above 150 GeV is plotted as a function of the optical flux. For the 2007/2009 campaign, in order to increase the statistics, the plot features daily bins, however, since the optical measurements have a different time coverage, in some cases the mean VHE flux from two or more consecutive days must be evaluated. 2005 and 2006 data, from Albert et al. (2007a), are rejected from this study due to the large uncertainty on the extrapolated flux in the VHE band. The mean flux value from the 2006 multiwavelength campaign, reported in Albert et al. (2009b), is taken into account. A linear relation among the two components has a 74% probability, which suggests a correlation between these

two extreme energy bands. This result is in good agreement with the SSC model, which predicts a correlation between the synchrotron and the IC emission, since the same electron population is responsible for both effects. Due to the lack of simultaneity of other wavelengths data, the same study has not been performed for the other bands. Nevertheless, a hint of correlation between the optical R-band flux and the soft γ-ray flux is suggested by Figure 4.10, where the LAT light curve (averaged into 100 day bins) is superimposed on top of the R-band plot. The zero points for the R-band and LAT data are the same, therefore the plot is consistent with an assumption that the variability in R and gamma is directly correlated with the same relative amplitude. Extending the LAT light curve to include more recent data and the availability of more optical data will provide an additional test of this potential correlation.

The source behavior in X-rays shows a pronounced variability, in contrast to optical and VHE bands. The X-ray flux spans an interval of about one order of magnitude (with maximum in 2005 and minimum in 2009), larger than that observed in the TeV, optical and GeV bands. The different variability displayed by the synchrotron (X-ray) and inverse Compton (GeV-TeV) components seems to be somewhat in contrast with the typical behavior observed in TeV BL Lacs, showing, in general, a coordinated variability (e.g. Fossati et al., 2008). Neverthe-

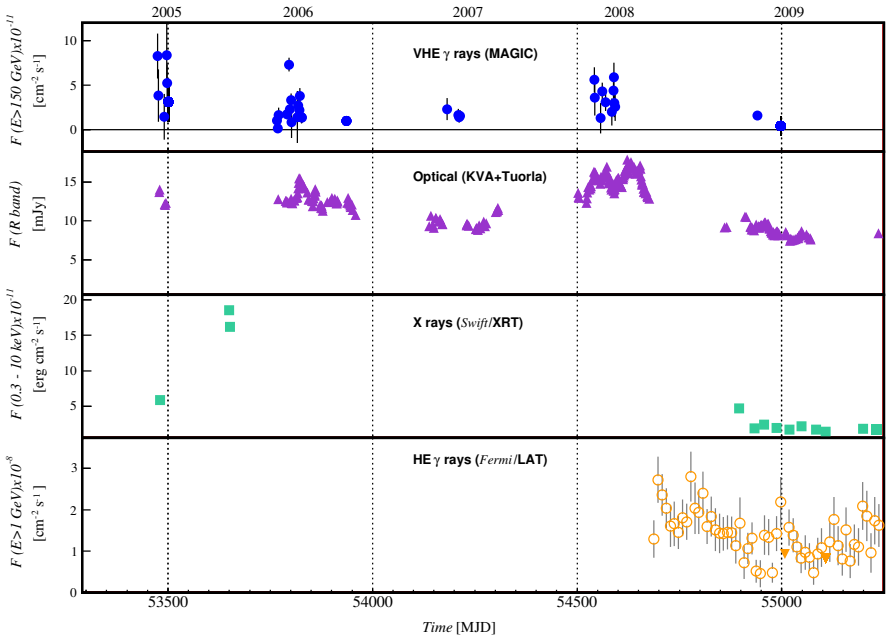

Figure 4.8 Multiwavelength light curve of PG 1553+113 from 2005 to late 2009. From upper to lower panel: VHE γ-rays above 150 GeV measured by MAGIC (filled blue circles), optical flux in the R band (violet triangles), X-rays counts rate (green squares) and HE γ-rays (1-100 GeV, open orange circles).

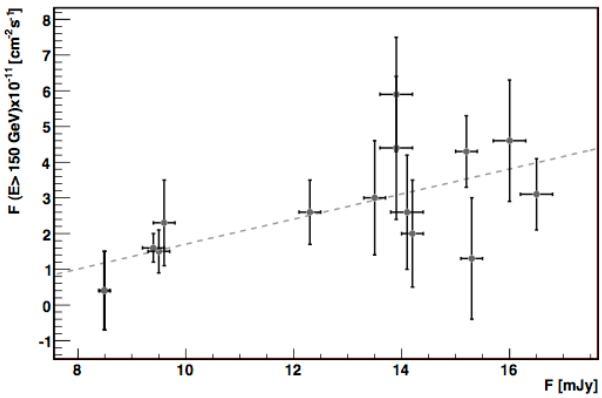

Figure 4.9 Correlation study between PG 1553+113 optical R-band flux and VHE γ-ray integral flux above 150 GeV observed from 2006 to 2009.

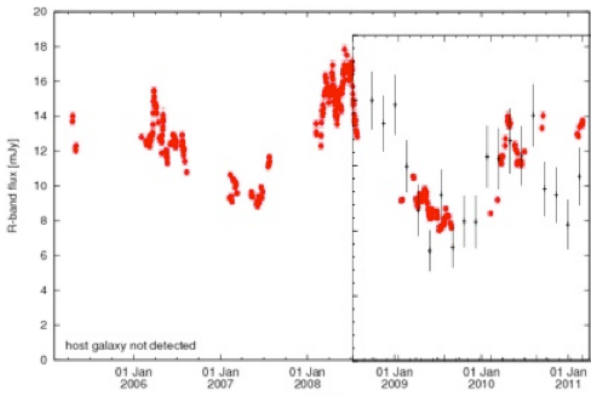

Figure 4.10 LAT light curve (averaged into 100 day bins) superimposed on top of the R-band light curve. The similar trend suggests a correlation between the two bands although a dedicated correlation study will be necessary as conclusive test.

less, we note that a similar peculiarity has been pointed out in other BL Lacs, as for example by H.E.S.S. observations of PKS 2155+304 (Aharonian et al., 2009b; Costamante, 2008), where it has been suggested a framework in which the X-ray and VHE γ-ray fluxes would be correlated during γ-ray flaring states while during the more common γ-ray quiescent states, changes in the X-ray flux would not affect the γ-ray flux, except for the high energy peak in the SED (see e.g. Abdo et al., 2010e, and references therein). The same scenario was considered to describe previous observations of PG 1553+113 by Abdo et al. (2010e).

However, the sparse sampling of the observations and the lack of a truly simultaneous monitoring, prevents any definitively conclusion for our observations. In particular, no optical nor γ-ray data are available during the period of the maximum X-ray flux in 2005. Coordi-

nated multifrequency monitoring is necessary to further investigate this important issue, especially to see whether it has to be considered an exceptional case or whether a similar behavior should be a general characteristic of BL Lacs.

4.2.6 *Modeling the Intrinsic Emission of PG 1553+113*

Figure 4.11 shows the SED of PG 1553+113 using historical data and almost simultaneous data collected in this work. Open black squares displaying radio-optical data provided by NED. In the optical band, we also show (red diamonds) the KVA minimum and maximum flux measured in the period covered by MAGIC 2005-2009 observations together with optical-UV fluxes from *Swift*/UVOT (filled black triangles) and two *Swift*/XRT spectra taken in 2005 (from Tavecchio et al., 2010, high flux state, red crosses, and intermediate state, black asterisks). A Suzaku spectrum taken in 2006 from Reimer et al. (2008, continuous red line) is also plotted. In addition, the average 15-150 keV flux measured by *Swift*/BAT during the first 54 months of survey (Cusumano et al., 2010) is shown (black star), and the average RXTE/ASM flux between March 1 and May 31, 2008 (small black square), from quick-look results provided by the RXTE/ASM team. The green triangles correspond to the LAT spectrum averaged over $\sim$ 200 days (August 2008 - February 2009) from Abdo et al. (2010e). Concerning VHE data, the 2005-2006 and 2007-2009 spectra observed by MAGIC (filled circles) are reported along with the same spectra corrected for the absorption by the EBL using the model of Domínguez et al. (2011, red open circles).

The SED is modeled with the one-zone SSC model by Maraschi and Tavecchio (2003) fully described in § 2.3.3. Here we briefly recall that the emission zone is supposed to be spherical with radius R, in motion with bulk Lorentz factor Γ at an angle θ with respect to the line of sight. Special relativistic effects are described by the relativistic Doppler factor, $\delta = [\Gamma(1 - \beta\cos\theta)]^{-1}$. The energy distribution of the relativistic emitting electrons is described by a smoothed broken power law function, with limits $\gamma_{\rm min}$ and $\gamma_{\rm max}$ and break at γ_b. The SSC emission is calculated using the full Klein-Nishina cross section. Given the large variations of the X-ray synchrotron flux, the average level of the synchrotron bump as measured by XRT is used, including also ASM and BAT fluxes to constrain the model.

The corresponding input parameters are listed in Table 4.1 along with the derived powers carried by the different components, relativistic electrons, P_e, magnetic field, P_B, and protons, P_p, (assuming a composition of one cold proton per relativistic electron) and the total radiative luminosity $L_r \simeq L_{obs}/\delta^2$. In order to investigate the role of different parameters in the model, their variation is extrapolated as a function of the intensity of the synchrotron peak. To do so, the SED

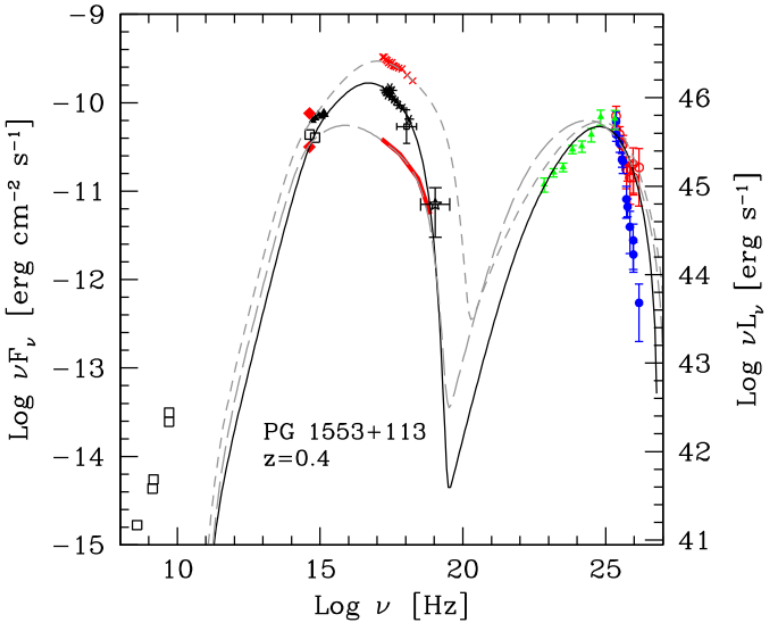

Figure 4.11 PG 1553+113 SED reconstructed in several energy bands. Open black squares are radio-optical data taken from NED, red diamonds indicate the KVA minimum and maximum flux measured, while filled black triangles are the optical−UV fluxes from *Swift*/UVOT. Other points represent: *Swift*/XRT data (high flux state, red crosses, and intermediate state, black asterisks), a Suzaku spectrum (continuous red line), *Swift*/BAT flux (black star, average 14−150 keV) and the average RXTE/ASM flux (small black square). VHE observed spectra (blue filled circles) and the same spectra corrected for the absorption by the EBL (red open circles) are shown together with the LAT spectrum averaged over $\sim$ 200 days (2008 August−2009 February, green filled triangles). The SED is modeled with a one−zone SSC model (continuous black line). A detailed description is addressed in the text.

is modeled considering the two extreme states of the synchrotron peak described above, respectively. For the SSC peak, instead, VHE data are fixed. The two curves representing the models are superimposed in light gray to Figure 4.11. The parameters obtained are listed in the last two columns of Table 4.1 and are quite similar to the ones obtained when considering the average level of the synchrotron bump, except for the two variables B and K, the magnetic field and the electron density. Indeed, these two parameters regulate the relative importance of synchrotron and SSC components. The state characterized by a low synchrotron emission has larger B and smaller K values with respect to the mean state modeled above. Conversely, the high synchrotron emission state has smaller values of B and a larger K. Finally, a comparison with the SED model obtained in the multi-

Parameter		mean value	max value	min value
$\gamma_{\rm min}$	$[10^3]$	2.5	1	5
$\gamma_{\rm b}$	$[10^4]$	3.2	3	1.3
$\gamma_{\rm max}$	$[10^5]$	2.2	5.2	4.1
n_1		2.0	2.0	2.0
n_2		4.0	3.75	3.55
B	[G]	0.5	0.8	0.2
K	$[10^3$ cm$^{-3}]$	5.35	3.8	25
R	$[10^{16}$ cm]	1	1	1
δ		35	35	35
$P_{\rm e}$	$[10^{44}$ erg/s]	2.2		
P_B	$[10^{44}$ erg/s]	1.5		
$P_{\rm p}$	$[10^{44}$ erg/s]	0.34		
$L_{\rm r}$	$[10^{44}$ erg/s]	6.3		

Table 4.1 Three different models are used to fit the PG 1553+113 SED shown in Figure 4.11. Above are listed the minimum, break and maximum Lorentz factors and the low and high energy slope of the electron energy distribution, the magnetic field intensity, the electron density, the radius of the emitting region and its Doppler factor. For the average model we report the derived power carried by electrons, magnetic field, protons (assuming one cold proton per emitting relativistic electron) and the total radiative luminosity.

wavelength campaign reported in Aleksić et al. (2010), reveals that the parameters used for building the two models are quite similar. The major differences are the value of the Doppler factor, which in this model is relatively higher ($\delta = 35$) than in the previous one ($\delta = 23$), and that of the magnetic field (0.5 G compared to 0.7 G). This difference is mainly due to the higher SSC peak frequency that we find in these data, better defined by the combined LAT and MAGIC spectra.

The derived value of the total jet power, $P_{\rm jet} = P_{\rm e} + P_B + P_{\rm p} = 4 \times 10^{44}$ erg/s, is consistent with the typical values inferred modeling similar sources (Ghisellini et al., 2011b). A relatively large minimum electron Lorentz factor $\gamma_{\rm min} \sim 10^3$ is necessary to reproduce the hard MeV - GeV continuum observed by the LAT (the HE spectral photon index derived is $\simeq 1.68 \pm 0.03$). The high value of $\gamma_{\rm min}$ implies that, as commonly derived in TeV BL Lacs, the relativistic electrons (and the magnetic field, almost in equipartition) carry more power than the cold proton component. Another characteristic that PG 1553+113 shares with the other TeV BL Lacs is that the total luminosity L_r is larger than the power supplied by electrons, magnetic field and protons. As discussed in Celotti and Ghisellini (2008), this implies that either only a small fraction of leptons is accelerated at relativistic energies (leaving a buffer of cold pairs and/or protons) or that the jet

is dissipating a large fraction of its power as radiation, eventually leading to the deceleration of the flow, as in fact observed at VLBI scales (Piner et al., 2010) and envisaged in the models of structured jets (Georganopoulos and Kazanas, 2003; Ghisellini et al., 2005).

4.2.7 *Final remarks*

In this Chapter, multiwavelength observations of PG 1553+113 in optical, X-ray and soft/hard γ-ray frequencies were presented. A clear variability is seen in the X-rays and also in HE γ-rays where LAT data, analyzed since the beginning of *Fermi* operations to June 4, 2010, indicate that the source is variable in the range 1-100 GeV. This fact, related to the energies close to the IC peak, is only apparently in contradiction with previous findings, stating a quite stable spectrum for this source in the soft ($>$ 200 MeV) γ-ray band (Abdo et al., 2010e). The different energy thresholds used in the two studies can, in fact, explain very well the discrepancy.

For MAGIC, the original observations from 2005 to 2006 are used along with the follow-up observation taken from 2007 to 2009. The overall VHE flux above 150 GeV from 2007 to 2009 shows only a modest variability on yearly time-scale, within a factor 3, corresponding to a variation between 4% to 11% of the Crab Nebula flux. No clear variability on smaller time scales is evident in the VHE data. Only the VHE and optical sample can be used for correlation studies thanks to the large simultaneous coverage. Interestingly, a hint of correlation with probability of 74% is found between MAGIC and R-band optical flux levels, which in turn shows only a modest variability within a factor 4. The data set suggests also a correlation between HE and optical band but to pin it down, further observations are needed.

Finally, for the study of the spectral energy distribution, the mean differential spectrum measured by MAGIC is combined with historical data at other wavelengths. For the SED modeling in X-rays, due to the large variations in the band that characterize the synchrotron peak, only the high energy bump and the average level of the low energy bump have been used. A more precise model requires coupling the VHE γ-ray part of the spectrum with simultaneous coverage of the synchrotron peak, in particular at optical-X-ray energies. An interesting feature of PG 1553+113 is the narrowness of the SSC peak derived from the LAT and MAGIC spectra, implying a relatively large value of the minimum Lorentz factor of the emitting electrons, 2.5×10^3. This is also required by other HBLs with hard GeV spectra (Tavecchio et al., 2010).

4.3 DISCOVERY OF VHE γ-RAYS FROM THE BLAZAR 1ES 1215+303 AND SIMULTANEOUS MULTIWAVELENGTH OBSERVATIONS

The first VHE observations of 1ES 1215+303 performed by MAGIC in 2010 yielded only a hint of a signal. At the beginning of 2011, triggered by an optical outburst, MAGIC observed again the source and this time obtained the first detection of 1ES 1215+303 at VHE. During this period, the target was monitored in the optical R-band by the KVA telescope, that also performed optical polarization measurements. Simultaneous and quasi-simultaneous data obtained with the *Swift* telescope, pointed out a high optical and X-ray state with respect to the 2010 data. The GeV γ-ray flux and the radio flux obtained with *Fermi* and Metsähovi were instead comparable in 2010 and 2011. The HE-VHE γ-ray emission from 1ES 1215+303 and its relation with the emissions at other wavelengths are presented in this Chapter. Due to the presence of several γ-ray emitter very close to the source of interest (in particular another blazar, 1ES 1218+304, has a small angular separation of $\sim 0.78^\circ$ from the target) a detailed and accurate investigation of *Fermi* data is required and will be fully addressed in § 4.3.3. Quasi-simultaneous light curves allow to establish a connection between different energy regimes and to investigate the location of the emission regions. Noteworthy, the comparison with data from previous MAGIC observations in 2010, when the source was in a lower optical state, indicates that the activity in these two bands is strictly connected, supporting the idea that, at least in some cases, optical follow-up is a good tool to increment discovery of VHE γ-ray sources. The SED obtained with the 2011 data can be modeled with a simple one zone SSC model, but it requires extreme values for the Doppler factor and the electron energy distribution.

Part of this original work has been published in Aleksić et al. (2012b).

4.3.1 *Introduction*

1ES 1215+303 (also known as ON 325) is a high synchrotron peaked BL Lac object (Abdo et al., 2010g) at redshift $z = 0.130$ (however, $z \simeq 0.237$ is also reported in the literature, e.g. Grazian et al., 2000; Akiyama et al., 2003). The source was classified as a promising candidate TeV blazar (Costamante and Ghisellini, 2002; Tavecchio et al., 2010) and has been observed several times in VHE γ-rays before its detection in 2011. The previous observations yielded only upper limits, Whipple: $(F > 430\text{GeV}) < 1.89 \times 10^{-11}\,\text{cm}^{-2}\,\text{s}^{-1}$, (Horan et al., 2004); MAGIC: $(F > 120\text{GeV}) < 3.5 \times 10^{-11}\,\text{cm}^{-2}\,\text{s}^{-1}$, (Aleksić et al., 2011a). The source was listed in the *Fermi* bright AGN catalog (Abdo et al., 2009a) with a peculiar hard spectrum ($\Gamma = 1.89 \pm 0.06$) and in this catalog 1ES 1215+303 was the only HBL source that showed significant variability.

In the first days of January 2011, 1ES 1215+303 was reported to be in a high optical state. This triggered MAGIC observations (extended

until February 2011) that resulted in the discovery of VHE γ-rays from the source (Mariotti, 2011a). In the following paragraphs, we present the results of these observations combined with simultaneous and quasi-simultaneous multiwavelength data from radio, optical, X-ray, and HE γ-rays.

4.3.2 *Multiwavelength Analysis Procedures*

The observations of 1ES 1215+303 were performed in a broad wavelength range (from radio to VHE γ-rays) by 5 different instruments. This is the first time that such large coverage is provided for this source in quasi-simultaneous observations. This section will present the data acquisition and reduction of the different instrument utilized. It must be noted that the *Fermi* data analysis of 1ES 1215+303 is particularly challenging due to the presence of several γ-ray emitting sources very close to the source of interest (in particular the blazar 1ES 1218+304; Acciari et al., 2010) and the limited LAT resolution. Therefore here we will report the standard steps of the LAT analysis while a more detailed investigation of the LAT dataset will be addressed in § 4.3.3.

- Metsähovi data (bottom panel of Figure 4.17)
  As the radio telescope detection limit is $\sim$ 0.2 Jy under optimal conditions and since 1ES 1215+303 is a rather weak source at 37 GHz, observations of this source can be possible only under good weather conditions. Typically, an acceptable measurement of the source is obtained approximately once per month. For this campaign, data were obtained simultaneously with the MAGIC observations in 2010 June, but in 2011 January-February the weather did not allow simultaneous observations with MAGIC, the closest simultaneous points are therefore taken in December 2010 and March 2011.

- Tuorla data (fourth-fifth panel of Figure 4.17)
  1ES 1215+303 has been observed regularly as part of the Tuorla blazar monitoring program since 2002. Magnitudes were converted to flux as explained in § 4.1.2. In addition, polarimetric observations of this source were obtained on six nights from January 7 to January 17, 2011. The degree of polarization and position angle were calculated from the intensity ratios of the ordinary and extraordinary beams using standard formula and semiautomatic software specially developed for polarization monitoring purposes.

- *Swift* data (third panel of Figure 4.17)
  A *Swift* ToO request was submitted on January 3, 2011. The observations started on January 4 until January 12 with four

$\sim$ 5 ks exposures in photon counting mode. The spectra were extracted from the corresponding event files and binned to ensure a minimum of 25 counts per energy bin, in order to obtain a reliable χ^2 statistics. For this source both a simple power-law and a log parabola model were applied (see § 4.3.4). The neutral hydrogen-equivalent column density was fixed to the Galactic value in the direction of the source 1.74×10^{20} cm^{-2} (Kalberla et al., 2005).
Swift/UVOT observed the source with all filters (V, B, U, UVW1, UVM2, UVW2) for four nights. UVOT source counts were extracted from a circular region of 5″ centered on the source position, while the background was extracted from a larger circular nearby source–free region. These data were processed with the `uvotmaghist` task of the HEASoft package. The observed magnitudes have been corrected for Galactic extinction $E_{B-V} = 0.024$ mag (Schlegel et al., 1998), applying the formulae by Pei (1992) and finally converted into fluxes following Poole et al. (2008).

- *Fermi* data (second panel of Figure 4.17)
  Data collected in the time interval from 2008 August 5th to 2011 March 22th have been analyzed with the standard LAT Science Tools (version v9r23p0). Only events belonging to the "Diffuse" class and located in a circular ROI of 7° radius, centered at the position of 1ES 1215+303 , were selected (using `Pass 6` event selection). In addition, we applied the cut on the zenith angle ($< 100°$) limb γ-rays and the cut on the rocking angle ($> 52°$) to limit Earth limb contamination, as described in § 3.4.1.
  The *Fermi* analysis was restricted to energies between 1-100 GeV where the LAT PSF is at its minimum and allows the best possible separation of 1ES 1215+303 from the other sources in the ROI (more details in § 4.3.3). All point sources from the 2FGL catalog (Nolan et al., 2012) located within 12° of the target were included in the model of the region. Sources located within 5° of 1ES 1215+303 position had their flux and photon index left free in the likelihood maximization, while further sources had only the flux left free. The diffuse Galactic and isotropic components were included in the fit and modeled with the publicly available files[8]. The normalizations of the components comprising the total background model were allowed to vary freely during the spectral point fitting. The unbinned likelihood method was used in combination with the `P6_V11_DIFFUSE` IRFs. The successful separation of the flux between 1ES 1215+303 and 1ES 1218+304 was verified by the absence of any significant correlation between their light curves and by means of simulations (see § 4.3.3).

8 `gll_iem_v02_P6_V11_DIFFUSE.fit` and isotropic `iem_v02_P6_V11_DIFFUSE.txt`

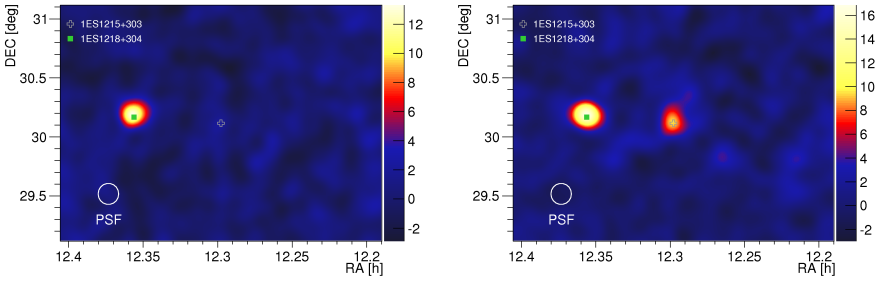

Figure 4.12 Significance maps ($>$ 300 GeV) from MAGIC observations performed during 2010 January-February and 2010 May-June (combined together, total time 22.0 hrs, left) and 2011 January-February (total time 20.3 hrs, right).

- MAGIC data (first panel of Figure 4.17)
  1ES 1215+303 was observed by MAGIC in January-February, 2010, May-June, 2010 and January-February, 2011 for a total of 48 hrs. While most of the data were taken in dark night conditions, a small fraction were taken in presence of moderate moonlight.
  Another VHE γ-ray emitter, 1ES 1218+304 is present in the same field of view of 1ES 1215+303. Figure 4.12 shows the significance map of the sky region for energies above 300 GeV for the 2010 (January-February and May-June combined) and 2011 observations. 1ES 1218+304 is clearly visible in both maps while the target was fainter in 2010 than in 2011. Since the source separation ($\sim 0.8^{\circ}$) is larger than the PSF of the MAGIC telescopes ($\sim 0.1^{\circ}$), there was no source confusion or contamination at these energies. However, these sources have nearly the same Right Ascension, so in the standard wobble setup used in the January-February 2010 observations, the background estimation region partially overlapped with the position of 1ES 1218+304. This would result in an overestimate of the background, so this region was excluded from the background estimate. In the later observations (May-June, 2010 and January-February, 2011) the wobbling offset direction was changed to have the standard background estimation regions far from the second source.
  After the data quality selection, based mainly on the rate of stereo events, the data samples of January-February 2010, May-June 2010 and January-February 2011 contain 19.4, 3.5, and 20.6 hrs of good quality data respectively. Because of the different positions of the source in the camera, background estimation procedure, and the variable nature of AGN, the data set has been separated into these 3 periods.

4.3.3 *Fermi LAT data analysis: disentangling the two sources*

As can be seen from the *Fermi* count maps of Figure 4.13 and already pointed out in § 4.3.2, 1ES 1215+303 is located in a region that contains several other high energy emitters. A 7° radius ROI includes the well known VHE emitters W Comae (green circle in Figure 4.13) and 4C +21.35, which are at a distance of $\sim 2°$ and $\sim 7°$ from our source, respectively.

Even worse, the source of interest and the blazar 1ES 1218+304 (white circle in Figure 4.13) are separated by just 0.78°. Since the best PSF for the LAT is of about 0.8° above 1 GeV, first of all we decided to restrict the *Fermi* analysis in the energy range of 1-100 GeV and then we checked possible correlations between the sources at these energies by means of simulations. Initially, we selected photons distributed in a 2° radius ROI centered on 1ES 1215+303: such radius is large enough to include most of the events belonging to 1ES 1215+303 and avoid a possible contamination due to 1ES 1218+304 or to the bright W Comae, just a couple degrees away. Despite these apparent advantages, afterwards we realized that a small ROI might not be the best choice:

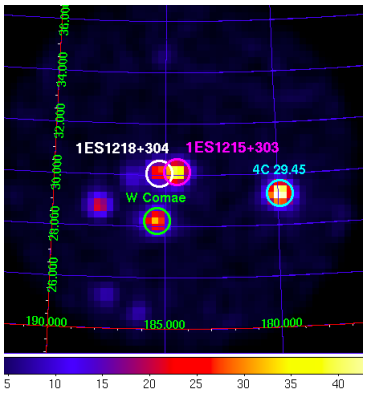

Figure 4.13 *Fermi* counts map for 1ES 1215+303 in the energy range 1 GeV-100 GeV

- we could loose a small portion of the source photons
- even with this small ROI we are still including a "tail" from 1ES 1218+304

Actually the latter point could have a strong negative impact on our analysis, since including only partially a source in the ROI could reduce the discriminating power of the likelihood technique. Therefore we decided to check the full time interval fits and light curve results repeating the analysis also with a larger ROI of 7° radius. Nonetheless, as can be seen from Table 4.2, when considering a larger ROI 1ES 1215+303 is detected with a larger significance in all the time intervals, and, in addition, the spectral parameters are compatible within the errors with the 2° radius analysis.

The multiwavelength study discussed in § 4.3.4 will make use of the 7° ROI results, while for the correlation investigation reported in the rest of the paragraph the 2° data set will be used due to computational time limitations.

Time Interval		Flux[a]	Index	TS
32 moths	$2^\circ ROI$	6.7± 0.1	2.1±0.1	1492
data set	$7^\circ ROI$	6.7 ± 0.3	2.10± 0.05	1706
2010	$2^\circ ROI$	5.1 ±0.8	2.1±0.1	165
data set	$7^\circ ROI$	4.9± 0.7	2.1± 0.1	181
2011	$2^\circ ROI$	6.7 ± 1.0	2.0± 0.1	86
data set	$7^\circ ROI$	7.3± 1.6	2.0± 0.2	105

Table 4.2 Fit results for 1ES 1215+303 . Different ROI sizes have been investigated; for all the time intervals considered in the analysis the fit results between the $2^\circ ROI$ and $7^\circ ROI$ agree well within the errors. [a]: Flux is in units of [10^{-09} cm^{-2} s^{-1}]

Correlation investigation between 1ES 1215+303 1ES 1218+304

The 32 month LAT data set has been fitted to derive fluxes and indices (mean) values of all ROI sources and these values have been used as reference parameters for the simulations. All the sources located in the 2° radius ROI (centered on 1ES 1215+303 position) have been simulated assuming a power law spectral shape. Afterwards, we fitted these data sets together and recorded the parameters values for both sources (i.e. 1ES 1215+303 and 1ES 1218+304).
The latter represent the *measured* parameters and if the target source is influenced by the presence of the other, these measurements should be affected. Under this condition we expect that the *measured* values should significantly differ from the *true* values (input parameters of the simulation). To compare statistically these values we produced 100 simulations datasets. Moreover, the same analysis has been repeated simulating a lower flux for 1ES 1215+303 (a flux 20% lower with respect to the mean value): the aim is to point out possible differences when the flux ratio of 1ES 1215+303 and 1ES 1218+304 changes. To see how much the target source is influenced by the presence of the other in Figure 4.14 we plot the relative error for these measurements (i.e. the difference between the *measured* and *true* flux, divided by the mean *measured* value) multiplied by 100. The top red (black) histogram plots the 1ES 1215+303 (1ES 1218+304) results. The bottom histograms of Figure 4.14 refer to simulations with the 1ES 1215+303 flux decreased of 20% with respect to the *true* value. The 1ES 1215+303 distribution is centered at zero in both cases, indicating that no particular deviations could be due to the possible influence of 1ES 1218+304. The latter instead has a clear bi-modal distribution that could be due to a contamination of the measurement or also to an artifact of simulations due to the low flux of the source, next to the instrument sensitivity limits. A more specific investigation

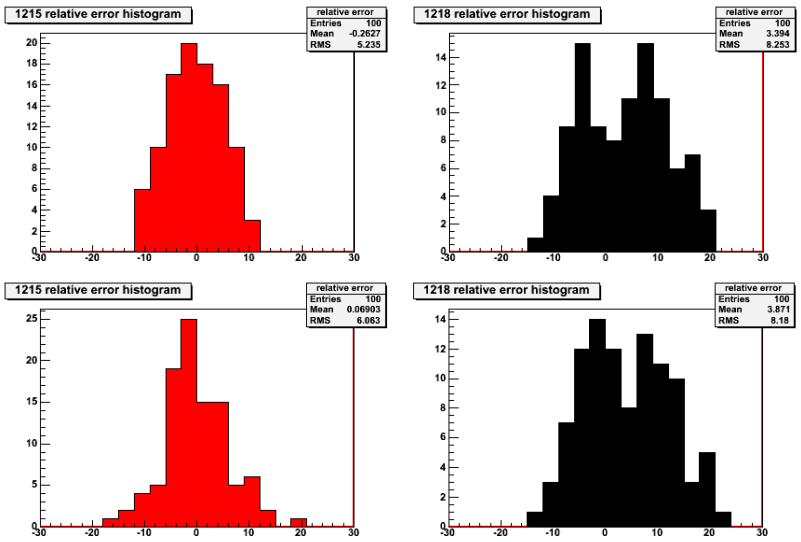

Figure 4.14 The histograms show the difference between the *measured* and *true* flux, divided by the mean *measured* value and multiplied for 100. The top red (black) histogram plots the 1ES 1215+303 (1ES 1218+304) results. The bottom histograms refer to simulations with the 1ES 1215+303 flux decreased of 20% with respect to the *true* value.

has been subsequently addressed studying the light curves behaviors and using a cross correlation analysis. A first indication for potential correlations can be evidenced looking at the light curves of the two

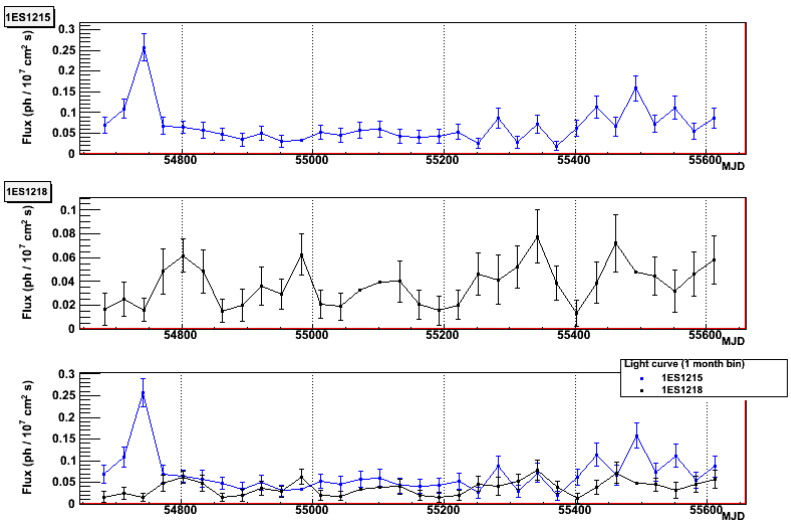

Figure 4.15 *Fermi* light curves of 1ES 1215+303 (blue) and 1ES 1218+304 (black) with binning of 1 month in the energy range 1-100 GeV. Points without error bars indicate 2σ upper limits and were computed for time intervals where $TS < 4$).

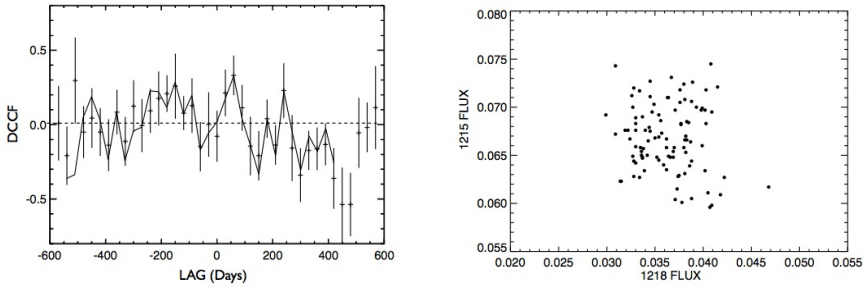

(a) (b)

Figure 4.16 Panel a displays the Cross Correlation Function (solid line) and Discrete Cross Correlation Function (DCCF), the latter plotted as points with error bars. The two correlation functions are consistent with zero correlation at lag = 0; Panel b shows a scatter plot of the fluxes simulated for 1ES 1215+303 and 1ES 1218+304.

closest sources in Figure 4.15. Their fluxes follow distinct trends with 1ES 1215+303 showing a high state at the beginning and at the end of the studied period while 1ES 1218+304 seems to be slightly less bright and characterized by a flickering activity. Correlation between the light curves can be produced by:

1. "leakage" of flux: if the flux of one source is changing part of that is "picked up" by the second source (probably a positive correlation).
2. the fitting of two overlapping source profiles tend to give an anti-correlation between the source flux estimates.

Using the light curve fluxes we can test the first hypothesis by a cross correlation of the two source light curves. Figure 4.16 (panel a) shows both a standard Cross Correlation Function (CCF, solid line) and a Discrete Cross Correlation Function (DCCF, points with error bars). The two correlation functions agree, as they should, and are consistent with zero correlation at lag = 0. The conclusion is that there is no indication of correlation between the source light curves, with an approximate upper limit of 0.2. The second correlation effect can be investigated by correlating the set of 100 simulations. The scatter plot between the two light curve fluxes (Figure 4.16, panel b) shows no strong correlation and the Pearson coefficient $(r = -0.11)$ is marginally significant. Moreover, if there is a mixing between the two sources we can use the 100 simulations to see if the 1ES 1218+304 flux is affected by the 20% change in 1ES 1215+303 flux. The result is that the decrease in 1ES 1215+303 flux gives a change in 1ES 1218+304 by $-0.2 \pm 0.4\%$, which is negligible. Since 1ES 1215+303 is brighter than 1ES 1218+304 the effect in the other direction should not be larger. Therefore, we can conclude that the two sources are correctly sep-

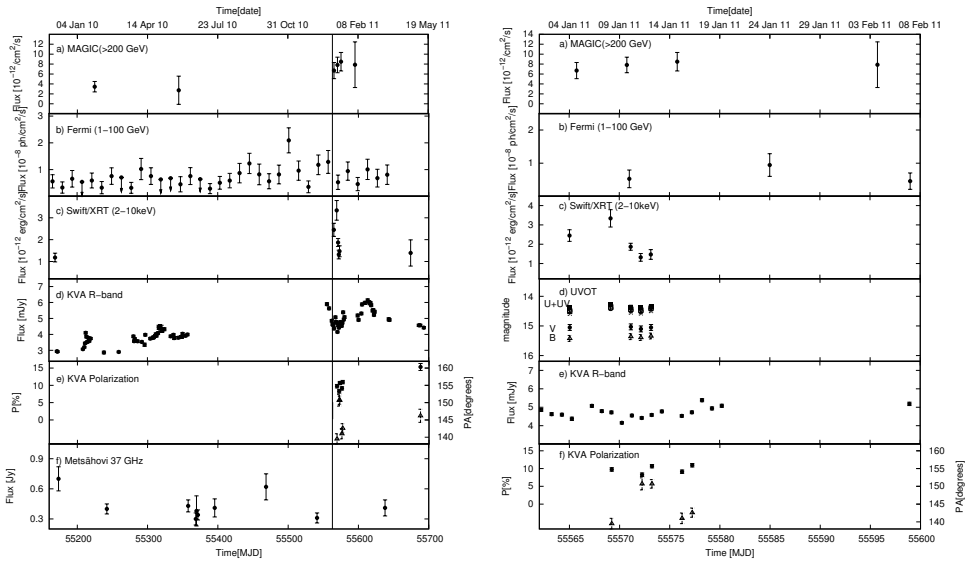

Figure 4.17 Left: *Long term light curves of 1ES 1215+303*: 2011 MAGIC data (panel a) are binned in 5-day intervals, 2010 data are divided in January-February and May-June bins. The LAT light curve (panel b, 14 day bin, arrows are 2σ upper limits); XRT data (panel c, simultaneous and archival data); R-band light curve (panel d, hourly average flux, the error bars are smaller than the symbols in most cases). Panel e reports the optical polarization (filled circles, left axis) and polarization position angle (triangles, right axis) with hourly averages. 37 GHz radio light curve is shown in panel f. The vertical line indicates the beginning of the MAGIC 2011 observation campaign; Right: Zoom into the time interval of the MAGIC observations in January-February 2011.

arated in our analysis and we can combine the LAT 1ES 1215+303 results with the other multiwavelength information (see § 4.3.4).

4.3.4 *Results*

Figure 4.17 displays the multiwavelength light curve of 1ES 1215+303 for the studied period. The VHE trend (panel a, 5-days bins) above 200 GeV of the 2011 data is well described by a constant flux of $(7.7 \pm 0.9) \times 10^{-12}\,\mathrm{cm}^{-2}\mathrm{s}^{-1}$ ($\chi^2/n_{\mathrm{dof}} = 0.56/3$), which corresponds to about 3.5% of the Crab Nebula flux. Assuming that the hint of a signal seen in the 2010 data is a γ-ray excess the corresponding flux was $F(> 200\,\mathrm{GeV}) = (3.4 \pm 1.0) \times 10^{-12}\,\mathrm{cm}^{-2}\mathrm{s}^{-1}$, which is less than half of the flux measured in 2011. In this case, the hypothesis of constant flux between 2010 and 2011 can be excluded at the level of 3.1σ.

The derived VHE γ-ray spectrum for the 2011 observations is described by a single power law ($\chi^2/n_{\mathrm{dof}} = 5.2/3$, see Figure 4.18) with the following values: $F = (2.27 \pm 0.25) \times 10^{-11}\,\mathrm{TeV}^{-1}\,\mathrm{cm}^{-2}\,\mathrm{s}^{-1}$ and the index is -2.96 ± 0.14 in the fitting range 70 GeV-1.8 TeV. The

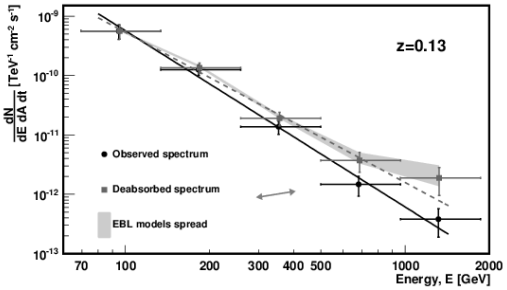

Figure 4.18 Observed and deabsorbed VHE γ-ray spectra of 1ES 1215+303 considering a redshift of 0.130. The EBL model of Domínguez et al. (2011) was used, the gray area shows the spread of the EBL models. The arrow shows the systematic error of the measurement.

MAGIC spectrum was deabsorbed using different EBL models (Domínguez et al., 2011; Kneiske and Dole, 2010; Franceschini et al., 2008; Primack et al., 2005) and the maximum high UV EBL model described in MAGIC Collaboration et al. (2008) for $z = 0.130$. The results are shown in Figure 4.18. As denoted in the Figure by the shaded area, at this redshift the EBL models agree well. The EBL model of Domínguez et al. (2011) was used to calculate the final intrinsic spectrum since this model is based on an observational approach.

The *Fermi* light curve (left Figure 4.17, panel b) was obtained in the energy range from 1 to 100 GeV, with binning of 14 day for the time interval from 2008 August to 2011 March. The major flare reported also in Abdo et al. (2009a) at the beginning of the *Fermi* mission is clearly apparent in the first bins. Afterwards, there is a hint of enhanced activity during November 2010 (MJD 55500, duration only one bin, i.e. 14 days) but very little variability otherwise, especially at the two MAGIC observation epochs (January-June 2010 and January-February 2011). To maximize the source detection significance in the HE energy bins the SED used for the modeling was derived combing *Fermi* data covering the whole MAGIC observation epochs. The LAT SEDs for these intervals are shown in Figure 4.19. In the 2010 data set the integral flux is $F_{1-100\,\mathrm{GeV}} = (4.9 \pm 0.7) \times 10^{-9}$ cm^{-2} s^{-1}and the photon index 2.1 ± 0.1, while in the 2011 data set the calculated values are $F_{1-100\,\mathrm{GeV}} = (7.3 \pm 1.6) \times 10^{-9}$ cm^{-2} s^{-1}and $\Gamma = 2.0 \pm 0.2$ (see also Table 4.2). The mean detected flux was $\sim$ 50% higher in January-February 2011 than in January-June 2010, but due to large error bars the increase is not statistically significant. The spectral index is constant within the error bars.

In the X-ray range (*Swift*/XRT, left Figure 4.17, panel c) the source showed the highest flux on January 8, 2011 (MJD 55569.1) and previous/subsequent observations from December 2009 (MJD 55168.7) to

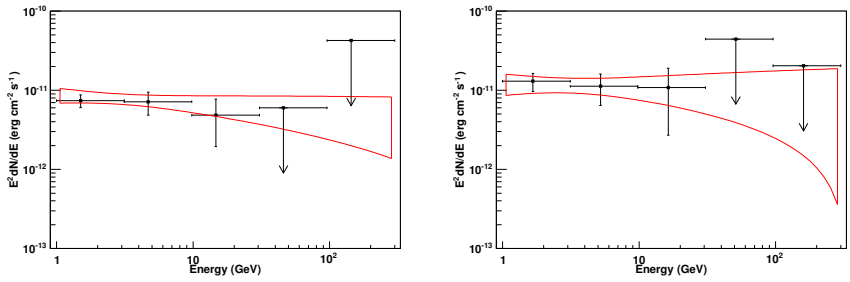

Figure 4.19 *Fermi* SED derived for January-June 2010 (left) and January-February 2011 (right). Upper limits at 2σ have been computed when the TS in the energy band were lower than 4. The bow-ties (red contours) are derived from the unbinned likelihood analysis.

April 2011 (MJD 55674.2) indicated significantly lower flux. For the X-ray spectra both log parabola (in the form $\sim E^{-a-b*log(E)}$, with E being the energy in keV) and a simple power-law fit were tested. The best fit was achieved with a log parabola law model in the range 0.3-10 keV for four observations while a simple power law, in the range 0.5-10 keV, provided a better fit for three of the observations. Generally, a log parabolic fit suggests that there is curvature in the X-ray spectra but for 1ES 1215+303, the difference between log parabolic and power law fits is so small that no strong conclusions can be drawn. Because of the different fits a comparison between the spectral slopes is difficult, but for the highest flux night the spectral index was marginally harder than for the low state observations. The *Swift*/UVOT results (right Figure 4.17, panel d) from January 2011 ToO observations showed constant brightness with V-band magnitude $= 15.06 \pm 0.10$, B $= 15.38 \pm 0.10$, U $= 14.53 \pm 0.08$, UVW1 $= 14.43 \pm 0.08$, UVM2 $= 14.35 \pm 0.06$, and UVW2 $= 14.46 \pm 0.06$. However, in all bands the source was clearly brighter than in the previous observation (December 2009: V $= 15.60 \pm 0.10$, B $= 15.95 \pm 0.10$, U $= 15.12 \pm 0.08$, UVW1 $= 15.07 \pm 0.08$, UVM2 $= 15.00 \pm 0.06$, and UVW2 $= 15.15 \pm 0.06$).

Indeed the largest variations have been registered in the optical R-band (left Figure 4.17, panel d) where the source was clearly variable on daily and yearly time-scales. The host galaxy contributes for a flux of 0.99 ± 0.09 mJy (Nilsson et al., 2007) and when this contribution was subtracted from the measured flux, the AGN core was found to be $\sim$ 40% brighter in 2011 (average total flux 3.64 mJy) than in January-June 2010 (average total flux 2.55 mJy). Similarly, it was found that during the 2011 observations the flux varied by $\sim$25% (core flux between 3.2 mJy and 4.1 mJy).

In the radio band (left Figure 4.17, panel f) the source was rather weak and does not show strong variability. The 37 GHz flux had a

similar level (0.3-0.4 Jy) in 2010 and 2011, although there were no radio observations during January-February 2011.

Multiwavelength light curve behavior
In the VHE regime the source showed a lower flux in 2010 (January-February and May-June) than in 2011 (by a factor of 2). The large uncertainties in the LAT measurement do not allow to conclusively say whether a similar flux enhancement also occurred in the 1-100 GeV energy range. In X-rays the source was in a high state (enhanced by a factor of 2) in January 2011 with respect to previous observations. In the optical band the average flux during MAGIC observations in 2010 was 3.5 mJy, while in 2011 it was 4.6 mJy. Thus, the source was clearly in outburst during early 2011, at least in VHE γ-rays, X-rays, and the optical band. There were no simultaneous radio observations, but both the previous and subsequent observations showed low flux, suggesting that the outburst might have originated rather close to the central engine where the emission region is opaque at radio wavelengths. However, as the simultaneous observations are missing, the existence of a simultaneous radio flare cannot be excluded.
During the January-February 2011 observations (right Figure 4.17), the MAGIC light curve is consistent with a constant flux. The source was in a rather low state in the *Fermi* energy range and no short term variability was detected. In X-rays and optical the source was variable during the MAGIC observations: the first two X-ray exposures gave a higher flux than for the latter three. The X-ray spectra show hints of hardening with higher flux, but they are statistically the same. The MAGIC observations started when the optical flux was decreasing, but during January 2011 the optical light curve showed several small flares. On the nightly time scale the X-ray and optical light curve seem to follow the same pattern indicating a common emission region for the two energy ranges.

Polarization measurements
In addition to multi-wavelength variability studies, the optical polarization measurements have proven to be a powerful tool to analyze the emission scenarios in the blazar jets (e.g. Marscher et al., 2008). Polarization traces the magnetic field of the jet. A net polarization oriented either parallel or perpendicular to the projected jet axis can be confused by shocks and the signatures are visible in optical polarization. The optical polarization measurements of 1ES 1215+303 in January 2011 show little variability in polarization degree (average $\sim$ 9%) or PA (varying between $\sim$ 140°-150°) during the MAGIC observations, but the follow-up observations from April 2011 (left Figure 4.17, panel e) show a higher polarization, $\sim$ 15%. Unfortunately, the polarization observations missed the peak of the first optical outburst and our data sample is very small. Ikejiri et al. (2011) monitored the photo-polarimetric behavior of the source in 2008-2009 and their

observations seem to show similar polarization trends (i.e. a decreasing polarization during outbursts). They also found that the PA was almost constant at $\sim 150^{\circ}$, which agrees with our observations and with the historical data from 1981-1989 (Wills et al., 2011) showing PA values from $\sim 130 - 170^{\circ}$. Such preferred position angles have been observed for several BL Lac objects (e.g. Jannuzi et al., 1994) and implies long-term stability of the structure of the region producing the polarized emission, e.g. the existence of a optical polarization core. To first order, if the optical outburst was produced by a shock traveling along the jet, one would expect the polarization degree to increase during the outburst. However, if there is a standing shock (optical polarization core) present, another shock with a different magnetic field orientation colliding with the standing component could produce an outburst in the total flux, but decrease the observed level of polarization (Villforth et al., 2010). A detailed photo-polarimetric study based on more data would be needed to further test this hypothesis.

Modeling the Intrinsic Emission of 1ES 1215+303

The multiwavelength SED of 1ES 1215+303 in both MAGIC observation epochs is shown in Figure 4.20. The 2011 high energy bump is constructed using the MAGIC deabsorbed spectrum (using the EBL model of Domínguez et al., 2011) and the simultaneous *Fermi* spectrum (collecting all photons from January-February 2011). As stated at the beginning of the paragraph, the low energy bump was variable during the considered period and is constructed for the night MJD 55569 that showed the highest *Swift* flux and for which there are simultaneous KVA and UVOT observations. In the R-band the host galaxy contribution was subtracted, the contamination can be present also in the V, B, and U bands of the UVOT data, but this contribution should be negligible in the UV. As we have no direct measurements of the host galaxy contribution in V, B and U bands we extrapolated the magnitudes from the R-band value using the galaxy colors of elliptical galaxies at $z = 0.2$ (Fukugita et al., 1995).

For the 2010 MAGIC data set, the spectrum could not be derived due to the low significance of the signal but we report the flux between 300 GeV and 1 TeV (assuming the same spectral index as in 2011). The simultaneous LAT spectrum was calculated for the whole interval from January to June, 2010. Simultaneous X-ray observation are missing, while for the optical we use the average (host galaxy subtracted) flux from nights when MAGIC was also observing. This "low state SED" is presented for illustrative purposes only and was not modeled, since both the synchrotron and IC peaks are poorly constrained.

The SED of 2011 shows two peaks, with the synchrotron peak frequency slightly above the optical band, as found for many other VHE γ-ray emitting BL Lac objects. The X-ray spectral index is also typical for a BL Lac source. The second peak seems to be located between the *Fermi* and MAGIC points ($\sim$10 GeV) as for many of the VHE γ-ray

model	$\gamma_{\rm min}$ [10^3]	$\gamma_{\rm b}$ [10^4]	$\gamma_{\rm max}$ [10^6]	n_1	n_2	B [G]	K [cm^{-3}]	R [10^{16} cm]	δ	χ^2/d.o.f
high δ (dashed)	1	3	1.0	2.0	4.2	0.02	8×10^3	0.8	60	3.36
high γ_{min} (solid)	8	9.2	2.5	3.0	4.85	0.055	1.3×10^8	1.0	30	6.94
min χ^2 (long dashed)	1	1.6	16.1	1.8	3.7	0.01	3.22×10^2	3.75	36	1.04

Table 4.3 Input parameters for the three models shown in Figure 4.20. The following quantities are reported: the minimum, break, and maximum Lorentz factors and the low and high energy slope of the electron energy distribution, the magnetic field intensity, the electron density, the radius of the emitting region and its Doppler factor. In addition in the last column we report the χ^2/d.o.f assuming 2%, 10% and 40% systematical errors for optical-X-ray, GeV γ-rays and VHE γ-rays respectively.

emitting BL Lacs. The locations of the synchrotron and IC peaks agree with values derived in Abdo et al. (2009a) for this source, but the synchrotron peak luminosity was slightly higher than in the previous observation by Giommi et al. (2012b). The emission characteristics of BL Lac objects is generally well reproduced by the one-zone leptonic model, and for the 2011 SED of 1ES 1215+303 we used the one-zone SSC model by Maraschi and Tavecchio (2003) described in § 2.3.3. Briefly, the emission region is assumed to be spherical, with radius R, filled with a tangled magnetic field of intensity B and relativistic electrons, emitting synchrotron and synchrotron self-Compton radiation. The electrons follow a smoothed broken power law energy distribution with normalization K between $\gamma_{\rm min}$ and $\gamma_{\rm max}$, with slopes n_1 and n_2 below and above the break at $\gamma_{\rm b}$. The relativistic boosting is fully accounted for by the Doppler factor δ. As noted in § 2.3.3, this model cannot account for the spectrum at the lowest frequencies, that is generally assumed due to outer regions of the jet, and not relevant for the modeling of the high energy emission.

The optical-UV and X-ray data define a narrow synchrotron component peaking around 10^{15} Hz. At high energies, the SSC bump is well constrained by the *Fermi* and MAGIC data to peak at about 10 GeV. This particular structure of the SED is not easy to reproduce. In particular, the relatively wide separation between the two peaks inevitably implies a large value of the Doppler factor if standard parameters are used for the electron energy distribution (e.g. Georganopoulos and Kazanas, 2003; Tavecchio and Ghisellini, 2008). Our best attempt to reproduce the data in the standard framework provides the parameters given in Table 4.3 and is displayed as the dashed line of Figure 4.20. As expected from the discussion above, we find a large Doppler factor, $\delta = 60$, well above the typical range of Doppler factors obtained from the modeling of the emission of similar sources (e.g. Tavecchio et al., 2010) and disagreeing with the lower values required by the FR I-BL Lac unification scheme (Urry and Padovani,

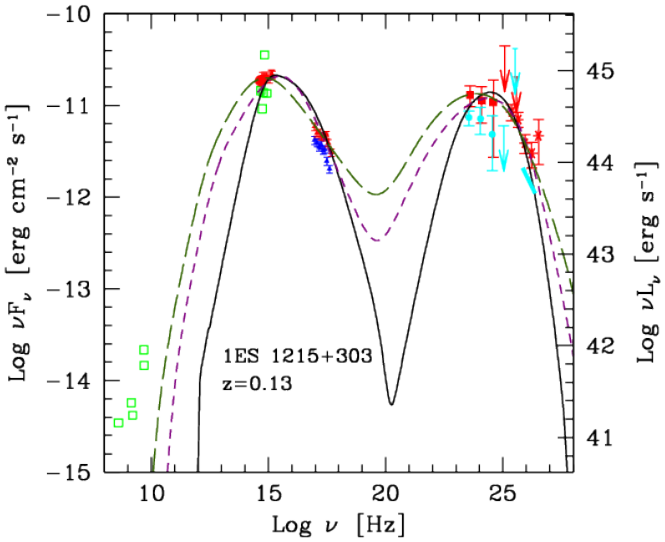

Figure 4.20 SED of 1ES 1215+303 for January-February 2011 data (red symbols) modeled with a one-zone SSC model. From high to low energies: the deabsorbed MAGIC spectra (asterisk), the LAT data (filled squares), Swift/XRT and Swift/UVOT data (triangles: red for MJD 55569, blue for MJD 55565) and simultaneous KVA data (filled circle). The cyan symbols report the January-June 2010 data of LAT (filled circles and arrows) and MAGIC (thick oblique line). Green open squares are archival data. The dashed line is the model fit using the extreme Doppler factor δ=60, while the solid line is the model fit with high γ_{min} and the long dashed (dark green) line reports the set of parameters that produced smallest χ^2 (see Table 4.3).

1995). However, a viable possibility to reproduce the observed SED using smaller Doppler factors exists if a relative large Lorentz factor of the emitting electrons, $\gamma_{\rm min} = 8 \times 10^3$, is assumed. This, coupled with a steep high energy electron energy distribution ($n_2 = 4.85$), allows us to properly reproduce the narrow synchrotron bump and to locate the SSC peak at high enough energies using a moderately large boosting, $\delta = 30$. This solution resembles the one discussed for the case of BL Lacs showing hard spectra in the soft X-ray and TeV band (Katarzyński et al., 2005; Tavecchio et al., 2009; Kaufmann et al., 2011). Interestingly, such parameters (large $\gamma_{\rm min}$, steep slope) are consistent with the prediction of some simulations of particle acceleration by relativistic shocks (e.g. Virtanen and Vainio, 2003; Sironi and Spitkovsky, 2011). For example, for a proton-electron composition, it is expected that the electrons are heated when crossing the shock to a typical

Lorentz factor of Γ=$\Gamma_{\rm rel}\, m_p/m_e$, where $m_p/m_e = 1836$ is the proton to electron mass ratio and $\Gamma_{\rm rel}$ = 2-3 is the relative Lorentz factor between the upstream and the downstream flows. From this Γ (that is equivalent to our parameter $\gamma_{\rm min}$), electrons are subsequently accelerated, forming a non-thermal tail that is well approximated by a steep ($n = 3.5$) power law.

The goodness of the fit can be judged by eye or by χ^2-minimization procedure. For the fits presented above the "eye estimate" was used, as for the latter the systematic errors of the data from different instruments are in the key role. However, we also tested the automatic χ^2-minimization procedure of Mankuzhiyil et al. (2011) with estimated systematical errors of 2%, 10% and 40% for optical-X-ray, GeV γ-rays and VHE γ-rays respectively. The γ_{min} is fixed to same value as in our high δ model (10^3) to allow easier comparison. The resulting parameters are shown in Table 4.3 and the fit with long-dashed (dark green) line in Figure 4.20. The minimal χ^2 fit results in lower δ, but in a high γ_{max} and rather large emission region radius R compared to other fits, but still compatible with the day scale variability observed in X rays and optical.

4.3.5 *Final remarks*

The optical outburst observed in 1ES 1215+303 on January 2011 triggered MAGIC observations which resulted with the first detection of the source at TeV energies. The simultaneous and quasi-simultaneous multiwavelength data collected during that period have been presented in this Chapter as well as a careful analysis of LAT data. The study of 1ES 1215+303 at MeV-GeV energies with the LAT was complicated by the presence of other strong HE-VHE emitters next to the target. Despite this, the detailed analysis here described excluded (in the energy range 1-100 GeV) possible contaminations of the target parameter measurements from the neighboring sources.

The collected multiwavelength data set is the most extensive energy coverage for 1ES 1215+303 to date. The optical-VHE γ-ray outburst seems to have been accompanied by an X-ray outburst, while in the LAT band the flux increased only marginally. The optical photo-polarimetric data suggests that the high state could be caused by a shock traveling down the jet that collides with a standing shock with a differently oriented magnetic field. The X-ray and VHE γ-ray high states could then also originate from this collision.

The 1ES 1215+303 SED of 2011 data set was modeled using a one-zone SSC model since it provides a good description of the SED of many VHE γ-ray emitting BL Lac objects. However, for this source the synchrotron and IC peaks are narrow, the separation between the two peaks is wide, and a simple one-zone SSC model with typical parameters did not adequately reproduce the observed SED. To fit the

SED, a high Doppler factor or a narrow electron energy distribution are required. While high Doppler factors are disfavored by the unified models, the high γ_{min} value could be a viable solution in the light of simulations modeling the acceleration of electrons in a relativistic shock in a proton-electron jet. This should be further investigated, e.g. using the fully self-consistent SSC model with particle acceleration due to shock and stochastic acceleration by Weidinger et al. (2010), as will be seen for the case of B3 2247+304 (see § 4.4.3 for more details).

Given the rather extreme conditions needed for the one-zone model, the presence of a velocity structure in the jet (Ghisellini et al., 2005) is also possible and should be tested for modeling the SED. The narrow synchrotron and IC peaks should well constrain the model. Additionally, the more complex emission scenario suggested by the photo-polarimetric behavior of 1ES 1215+303 should be tested in future using e.g. the approach of Marscher (2011), who investigated the emission from a turbulent ambient jet plasma that passes through either the standing or moving shocks in the jet.

4.4 DISCOVERY OF VHE γ-RAY EMISSION FROM THE BL LAC B3 2247+304

Listed in the first *Fermi* LAT catalog of AGNs (Ackermann et al., 2011) as 1FGL J2250.1+3825 with a very hard spectrum (spectral index of -1.6 ± 0.1), B3 2247+304 confirmed this characteristic also in the subsequent second *Fermi* catalog, where it appears by the name 2FGL J2250+3825 and has a spectral index of -1.84 ± 0.11 (Nolan et al., 2012). On October 2009, it has been included in the list of potentially interesting TeV objects released to the IACT experiments by the *Fermi* LAT collaboration (*Fermi* LAT Collaboration 2009, priv. comm.). As confirmation of this, Neronov et al. (2011) found a hint of signal at $2.73\,\sigma$ in the LAT data above 100 GeV over the period August 2008-April 2010. This Chapter discusses the first detection of VHE γ-ray emission triggered by the optical high state of the source and presents the light curve and SED of B3 2247+304 assembled using TUORLA optical data along with simultaneous X-ray, HE and VHE data obtained by *Swift*, *Fermi* and MAGIC, respectively. While in optical and X-ray the source appear to be in a clear high state, in the VHE-HE regime this cannot neither be confirmed or ruled out. Actually, the measured VHE flux is compatible with previous observations while *Fermi* is not sensitive enough to point out variations on small time scales for this source. In addition, the SED has been fitted with a one-zone SSC model and the obtained values are close to typical parameters of BL Lacs.

This original work has been published in Aleksić et al. (2012a)

4.4.1 *Introduction*

B3 2247+304 (RGB J2250+384) is a fairly poor studied blazar at redshift $z = 0.118$ (Falco et al., 1998) and position R.A. of $\alpha_{\rm J2000} = 22^{\rm h}50^{\rm m}06^{\rm s}.6$ and DEC $\delta_{\rm J2000} = +38^{\circ}25'58''$ (Ficarra et al., 1985). Its host galaxy parameters are typical for BL Lac objects, with host magnitude R=15.92 and a fainter variable core R=17.17 (Nilsson et al., 2003). The source was included in the sample presented in Nieppola et al. (2006b) with a reported X-ray flux $F_{>1\,\rm keV} > 2$ mJy. Donato et al. (2001) classifies it as an HBL object with a measured X-ray flux of $F_{>1\,\rm keV} = 6$ mJy. Nevertheless, Véron-Cetty and Véron (2006) listed the source only as a BL Lac candidate and the classification has not yet been confirmed. The HE hard spectrum highlighted in the first year of *Fermi* operations supported the hypothesis that B3 2247+304 could be a VHE emitter, although previously MAGIC observation lead only to upper limits.
These observations were carried out in August and September 2006, as part of the systematic search of VHE γ-rays from X-ray bright BL Lac objects (Aleksić et al., 2011a)[9]. and yielded an upper limit of

9 The stacked dataset of all X-ray selected blazars resulted in a significant γ-ray excess, which hints towards the fact that the sources were emitting at a very low level.

$F_{>140\,\mathrm{GeV}} > 1.6 \times 10^{-11}\,\mathrm{cm}^{-2}\,\mathrm{s}^{-1}$. The source has been monitored in the R-band by the Tuorla blazar monitoring program ever since and during the month of September 2010 an unusual high optical state observed by the KVA telescope triggered the MAGIC observation. The evidence for source activity was supported by the detection of an enhanced emission in X-rays found in *Swift* data. The VHE observations ended up with the detection of the source above 200 GeV at a 5σ significance.

4.4.2 *Multiwavelength Analysis Procedures*

Multiwavelength monitoring has been provided at optical wavelengths by the KVA telescope operated by Tuorla observatory, while in the X-ray and gamma-ray bands by the *Swift* and Fermi satellites, respectively. VHE data are provided by the MAGIC Telescope.

- MAGIC observations
  B3 2247+304 was observed with the MAGIC telescopes during 13 nights between September 30 and October 30 2010 collecting a total of 21.2 hours of data, of which 5.3 hours were discarded based on the event rate (probably related to a bad *seeing*). The effective time of this observation, correcting for the dead time of the trigger and readout systems is 14.2 hours. The measured excess in the distribution of θ^2 between the reconstructed direction of the events after cuts and the position of B3 2247+304 corresponds to a significance of 5.6σ (calculated using Eq. 17 from Li and Ma, 1983). The source position and extension, determined by a 2D Gaussian fit of the sky map produced with the cuts above, are consistent with a point-like source placed at the position of B3 2247+304 within 0.015°, well within the statistical uncertainty and the systematic pointing uncertainties of MAGIC.
- Optical observations
  The observation performed by Tuorla group indicated that during the years 2006-2009, B3 2247+304 was a quite faint and steady source at R $\sim$ 1.8 mJy, while during late summer 2010 it went to a high optical state, reaching an average flux level of 2.4 mJy. The source also stayed at this level throughout the observing season (see Figure 4.22). In late September, an alert was sent to MAGIC and VHE observations started on September 30th.
- *Swift* observations
  Target of Opportunity observations were requested, and from October, 5 to 16, 2010 *Swift*/XRT observed the source for $\sim$ 5 ks every night, in Photon counting (PC) mode. *Swift* archival data from August 10th, 2009, February 18, 2010 and April 18, 2010 are considered to allow a comparison of the X-ray emission

level with respect to previous observations. Spectral analyses performed by means of `XSPEC`, used two models: a simple power law model and a log-parabolic model as in Massaro et al. (2004) with an absorption hydrogen-equivalent column density fixed to the Galactic value in the direction of the source, namely 1.2×10^{21} cm^{-2}. Both models provide similar results in terms of goodness of fit above ~ 0.7 keV. However, below this energy the differences were in general negligible due to low statistics.
Swift/UVOT observed the source in the "filter of the day" mode, that is a different filter has been used for different observations. This does not allow to compare the UV fluxes among different days. UVOT source counts extracted from a circular region of 5" centered on the source position, while the background is extracted from a larger circular nearby source-free region. These data were processed with the `uvotmaghist` task of the HEASoft package. The observed magnitudes have been corrected for Galactic extinction $E_{B-V} = 0.149$ mag (Schlegel et al., 1998).

- *Fermi* data analysis
  LAT data were collected during the time interval from August 5, 2008 to April 7, 2011 (MJD 54683 - 55658), and were analyzed with the *Fermi* Science Tools package (version v9r23p0). Only events belonging to the "Diffuse" class and located within 12° of B3 2247+304 were used in this analysis. The usual cut on the maximum zenith angle ($< 100°$) was applied to reduce the contamination from the Earth-limb gamma-rays (as described in § 3.4.1). The background model used to extract the γ-ray signal includes a Galactic diffuse emission component and an isotropic component[10], the normalizations of these components comprising the total background model were allowed to vary freely during the spectral point fitting. The spectral fluxes were derived with the post-launch `P6_V11_DIFFUSE` IRFs, and applying an unbinned maximum likelihood technique (fully discussed in § 3.3.1) to events in the energy range spanning from 300 MeV to 300 GeV. All the sources from the 2FGL catalog (Nolan et al., 2012) located within 7° radius of B3 2247+304 were included in the model of the region. The initial parameters in the model of the region were set to those of the 2FGL catalog, leaving the normalization parameters free in the fitting procedure. For the period of the MAGIC observations (30 days between September 30 and October 30, 2010), the source was not significantly resolved, and hence only 95% confidence level upper limits were obtained. In the light curve presented in Fig.4.22, for each time

10 The templates used were: gll_iem_v02_P6_V11_DIFFUSE.fit and isotropic_iem_v02_P6_V11_DIFFUSE.txt.

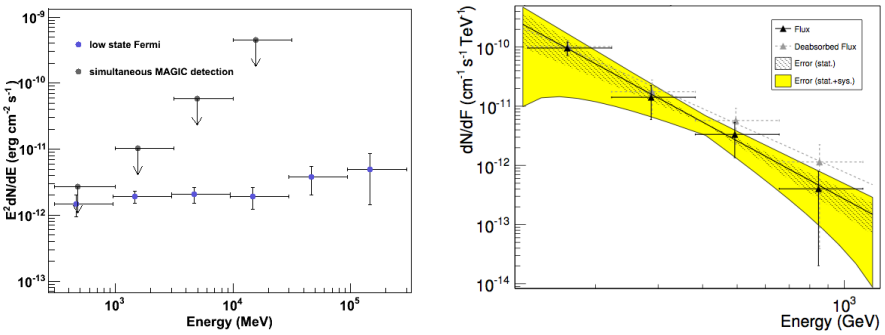

Figure 4.21 Left: Fermi spectrum obtained using almost 3 years (blue points) and 3 months of LAT data simultaneous to MAGIC (back points, 2σ upper limits). Right: MAGIC unfolded differential energy spectrum. The black data points refer to the measured spectrum, while the gray dashed points account for the attenuation of the EBL. The solid black and dashed gray lines are power-law fits to the respective data points (fit results are given in § 4.4.3). The dashed band corresponds to the statistical error of the fit to the measured spectrum, while the white band surrounding it is the sum of the statistical and systematic errors of the fit.

bin, if the TS value of the source was $TS < 4$ the values of the fluxes were replaced by 2σ upper limits[11].

4.4.3 *Results*

The spectrum obtained using the whole LAT data set (covering 975 days from August 5, 2008 until April 7, 2011) is consistent with that reported in the 2FGL catalog (Nolan et al., 2012): the spectral index is -1.81 ± 0.08 (it was -1.84 ± 0.11 in the 2FGL catalog) while the integrated flux above 300 MeV is $3.4 \pm 0.6 \times 10^{-9}$ cm^{-2} s^{-1} (consistent as well with the catalog value: $F_{300MeV-1GeV} = 3.2 \times 10^{-9}$ cm^{-2} s^{-1}).

In the VHE regime the integral flux of the source above 200 GeV is estimated to be $(5.0 \pm 0.6_{\rm stat} \pm 1.1_{\rm sys}) \cdot 10^{-12}$ ph cm^{-2}s^{-1}. The differential energy spectrum is well described by a simple power-law with photon index $\gamma = -3.2 \pm 0.5_{\rm stat} \pm 0.5_{\rm sys}$, and flux normalization (at 300 GeV) of $f_0 = (1.4 \pm 0.3_{\rm stat} \pm 0.2_{\rm sys}) \cdot 10^{-11}$ ph cm^{-2}s^{-1}TeV^{-1}. Taking into account the attenuation due to pair production with the EBL, the spectrum is compatible with a power law with photon index $\gamma = -2.7 \pm 0.5_{\rm stat} \pm 0.5_{\rm sys}$ and flux at 300 GeV $f_0 = (2.0 \pm 0.3_{\rm stat} \pm 0.3_{\rm sys}) \cdot 10^{-11}$ ph cm^{-2}s^{-1}TeV^{-1} (Figure 4.21). The two different EBL models that were considered, Domínguez et al. (2011) and Kneiske

11 The upper limits were computed using the Bayesian method where the likelihood is integrated from 0 up to the flux that encompasses 95% of the posterior probability.

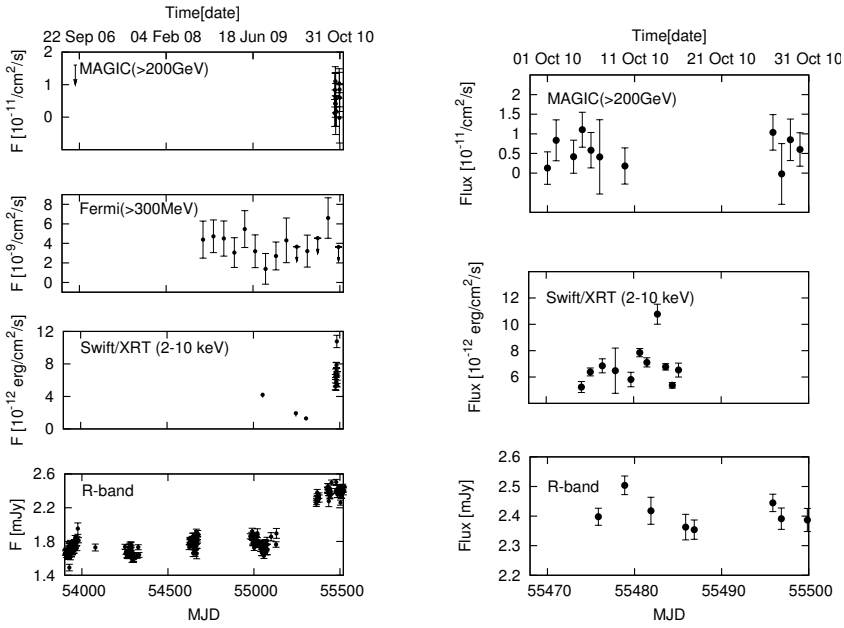

Figure 4.22 Panel a. Long term light curves of B3 2247+304 in VHE γ-rays, HE γ-rays (two months time intervals), X-rays and optical KVA R-band. Panel b. Zoom into the time interval of the MAGIC observations in September-October 2010.

and Dole (2010), were found to be in good agreement with each other, well within the statistical uncertainties.

Multiwavelength correlations

Long term light curves of B3 2247+304 in VHE γ-rays (MAGIC), HE γ-rays (*Fermi*), X-rays (*Swift*) and optical (Tuorla Observatory) are shown in Figure 4.22. The detection in VHE γ-rays is compatible with the previous upper limit from 2006 and thus no variability can be established in this energy band. However, in X-rays and in the optical band a clear increase of the flux in fall 2010 is evident, while the LAT light curve is consistent with a constant flux. A fit with a constant to the eleven *Fermi* flux points where the source is significantly detected, give a flux value of $(3.7 \pm 0.5) \cdot 10^{-9}$ ph cm^{-2}s^{-1}, with a reduced χ^2 of 0.7 with ten degrees of freedom. This result is also in agreement with what pointed out in the 2FGL. The variability index[12] reported in the latter catalog is $TS_{\rm var} < 27$ and indicates that the source is not variable, although it might be that the LAT is not sensitive enough for detecting short term variations at this flux level. The temporal evolution

12 In the 2FGL to test for variability in each source the $TS_{\rm var}$ index is used. It is derived from the value of the likelihood in the null hypothesis that the source flux is constant across the full 2-year period, and the value under the alternate hypothesis where the flux in each bin is optimized. A value of $TS_{\rm var} > 41.6$ is used to identified variable sources at a 99% confidence level.

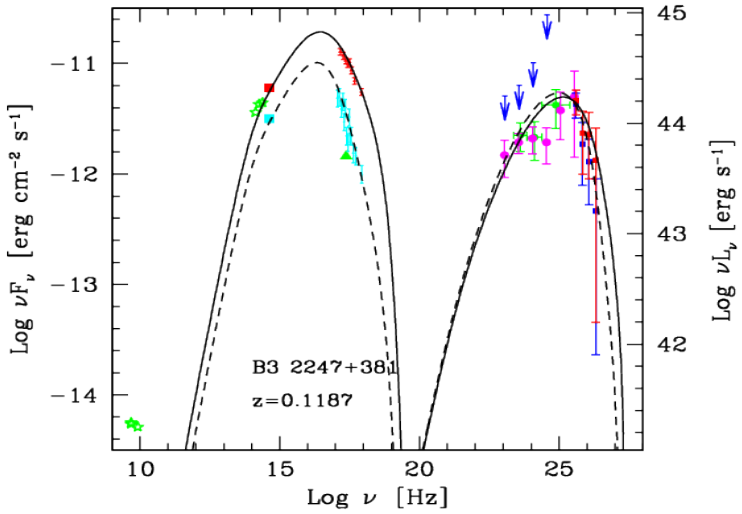

Figure 4.23 Spectral energy distribution of B3 2247+304 (red: EBL corrected MAGIC spectral points). *Fermi* data points from 1FGL and from this work are indicated by green crosses and pink points, respectively. *Fermi* data for the time interval of the MAGIC observation are the blue arrows (95% confidence upper limits). Low (high) state *Swift* data are light blue (red) points and low (high) state KVA R-band data are light blue (red) squares. Green and light blue points represent non-simultaneous low state data. The solid line is a SSC-model fit to the high state observations while the dotted line is a fit to the low state observations. The SED modeling is discussed in § 4.4.3.

of the VHE γ-ray, X-ray and optical emission from B3 2247+304 during September-October 2010 observation shows no strong variability on time scales of a night (see Figure 4.22). In particular, the MAGIC light curve above 200 GeV is consistent with a non-variable source, having a reduced χ^2 of 0.6 with ten degrees of freedom. During one night the X-ray flux is significantly higher (almost factor 2) than the other X-ray points, but unfortunately we do not have simultaneous optical or MAGIC data for that night.

SED modeling

The SED of B3 2247+304 is presented in Figure 4.23: green crosses are 1FGL *Fermi* data points (Abdo et al., 2010c), while the pink points represent the *Fermi* results from this analysis (more than 2.5 years of data). Blue arrows show the 95% confidence upper limits computed from LAT data for the time interval of the MAGIC observation. Low (high) state *Swift* data were taken on April 18 2010 (October 5-16, 2010). The host galaxy contribution has been subtracted from the KVA R-band data (red and light blue squares), following Nilsson et al.

Table 4.4 Input parameters for the high and low states of the SSC model shown as solid (high state) and dashed (low state) lines in Figure 4.23. For more explanations see text.

Flux State	$\gamma_{\rm min}$	$\gamma_{\rm b}$	$\gamma_{\rm max}$	n_1	n_2	B	K	δ	R
						G	cm^{-3}		cm
High	$3 \cdot 10^3$	$7.1 \cdot 10^4$	$6 \cdot 10^5$	2.0	4.35	0.06	$2.5 \cdot 10^3$	35	$8 \cdot 10^{15}$
Low	$3 \cdot 10^3$	$6.8 \cdot 10^4$	$5 \cdot 10^5$	2.0	5.35	0.08	$1.15 \cdot 10^4$	30	$4 \cdot 10^{15}$

(2007). Green and light blue points represent non-simultaneous low state data.

The SED is reproduced with a one-zone SSC model (see § 2.3.3 for a more detailed description of the model by Tavecchio et al., 1998). The solid line is a SSC-model fit to the high state observations while the dotted line is a fit to the low state observations. Briefly, in the model used the emission region is assumed to be spherical, with a radius R, filled with a tangled magnetic field of intensity B. The relativistic electrons follow a smoothed broken power-law energy distribution specified by the limits $\gamma_{\rm min}$, $\gamma_{\rm max}$ and the break at $\gamma_{\rm b}$ as well as the slopes n_1 and n_2 before and after the break, respectively. Relativistic effects are taken into account by the Doppler factor δ. The used input model parameters are shown in Table 4.4.

The change of the Compton and synchrotron luminosity ratio between the low and the high state are reproduced by acting mainly on the electron normalization, the source radius and the Doppler factor (with slight changes also to the other parameters). The steeper X-ray slope in the low state implies a larger value of n_2.

The comparison with parameters derived for BL Lac objects (see e.g. Tavecchio et al., 2010) reveals that the parameters used for B3 2247+304 are close to the typical values. As for other sources, the somewhat larger (lower) value of the Doppler factor δ (the magnetic field intensity B) with respect to “standard" values is mainly due to the relatively large separation between the synchrotron and IC peaks.

Additionally, for the high state, the SED is modeled with the one-zone SSC code from Weidinger et al. (2010) which is shown in Figure 4.24. In contrast to the model from Tavecchio et al. (1998) all parameters are basic physical parameters and the electron and photon spectrum and their breaks are derived self-consistently with a continuous injection of monochromatic electrons at the energy $\gamma_0 = 10^4$ and injection rate $K = 8.4 \cdot 10^4$ cm^{-3} s^{-1}. The spectrum is the resulting steady-state solution. The environment is defined by the magnetic field $B = 0.07$ G, the acceleration efficiency $t_{acc}/t_{esc} = 1.09$ (i.e. the particle spectral index is $s = 2.09$ and the resulting $\gamma_{\rm max} = 4.8 \cdot 10^5$), and the blob radius $R = 1.3 \cdot 10^{16}$ cm. The break in the e$^-$ spectrum of 1 at $\gamma_b = 2.9 \cdot 10^4$ arises self-consistently from IC and synchrotron cooling. The common parameters of both models agree very well.

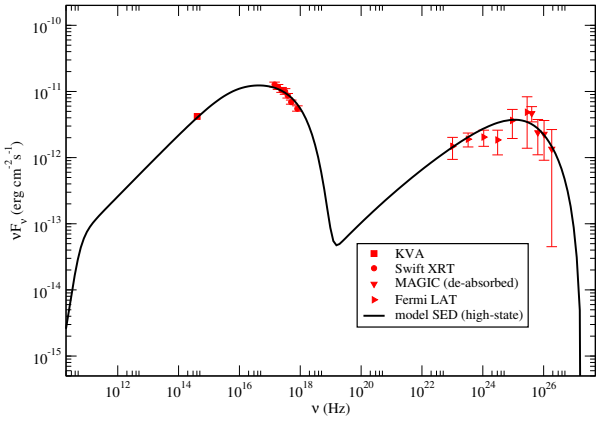

Figure 4.24 The solid line shows the SED model using Weidinger et al. (2010). The data points are described in the inlay of the figure. The fit parameters are reported in the text.

4.4.4 *Final remarks*

In this Chapter we have presented broadband observation that led to the discovery of VHE γ-rays from B3 2247+304 . Simultaneous *Fermi*, *Swift* and optical data, and other non-simultaneous datasets complemented the MAGIC observations. Although the source is found in an optical high state, the observed VHE γ-ray flux is consistent with the upper limit from previous observations and therefore it cannot be concluded if the source was in a higher VHE γ-ray state during the observations.

The analysis of *Swift* data indicates that during the MAGIC observations the source was in high state in X-rays while in GeV γ-rays no indication of enhanced activity can be seen. Worth to recall anyway that in the *Fermi* energy range the source is very weak, which limits the capability of detecting statistically significant flux-variability on time scales of a few months. From the spectral energy distribution shown in Figure 4.23, results that the synchrotron component of the SED is showing a significantly larger emission in the high state, while the inverse Compton component is consistent with only minor changes. To be noted, however, that the weak detection in the HE and VHE γ-ray band limits the determination of the inverse Compton component.

The optical monitoring of candidate VHE γ-ray blazars has proven to be a successful tool for their discovery. However, in the case of B3 2247+304 (like for Mrk 180 and 1ES 1011+496) a connection between the optical high state and the VHE γ-ray emission cannot be established since the upper limit from previous observations (during a low optical state) is higher than the detected VHE γ-ray flux dur-

ing the discovery. Therefore, further observations are still needed to study the connection between these two wavebands.

4.5 SPECTRAL VARIABILITY AND MULTIWAVELENGTH STUDIES OF THE HBL OBJECT 1ES 0806+524

Target of a monitoring campaign 1ES 0806+524 , has been followed from radio to γ-ray energies from November 2010 to June 2011. During this period the source showed variability in all wavebands except for the radio band. In particular a remarkable optical increase triggered TeV observations that resulted in the detection of a VHE γ-ray flare on February 24, 2011. Considerations on the source behavior in a multiwavelength context point out correlations between the different bands and infer an upper limit on the short-term variability timescale of one-day. In addition, the collected data allow to study the SED of 1ES 0806+524 and derive the physical parameters characteristics for the flaring and quiescent state in which the source has been observed.

Part of this work has been presented in Schultz et al. (2012), final results will be included in the upcoming publication Aleksić et al. (2013a).

4.5.1 *Introduction*

1ES 0806+524 is located at a R.A. of $\alpha_{\mathrm{J2000}} = 08^{\mathrm{h}}09^{\mathrm{m}}49^{\mathrm{s}}$ and a DEC $\delta_{\mathrm{J2000}} = +52^{\circ}18'58''$ is classified as BL Lacertae object (Schachter et al., 1993). It was suggested as a VHE candidate (Costamante and Ghisellini, 2002) with a predicted intrinsic flux of $F_{E>0.3\,\mathrm{TeV}} = 1.36 \times 10^{-11}\,\mathrm{cm}^{-2}\,\mathrm{s}^{-1}$. Previous VHE observations lead by the Whipple Collaboration and the HEGRA Collaboration yielded only flux upper limits: the former above 300 GeV (Horan et al., 2004; de la Calle Pérez et al., 2003) and the latter above 1.09 TeV (Aharonian et al., 2004).
The VERITAS Collaboration reported the first detection of the source in the VHE γ-ray band in 2008 (Acciari et al., 2009). The collected data set spanned from November 2006 to April 2008 and consisted in a significance detection of $6.3\,\sigma$. The integral flux above 300 GeV reported is 1.8% of the Crab Nebula flux, which is compatible with an earlier upper limit obtained by MAGIC observations in 2005 (5.6 % C.U. above 230 GeV (Albert et al., 2008a); 7.2 % C.U. above 140 GeV (Aleksić et al., 2011a). However, no significant variability could be established for this object and the spectrum was obtained only for a subset of data taken during winter 2007/2008. Accordingly, the spectral characteristics were poorly defined: actually the spectral index $(3.6 \pm 1.0_{\mathrm{stat}} \pm 0.3_{\mathrm{sys}})$ was determined only in a narrow range between 300 GeV and 700 GeV and a standard SSC jet emission model was sufficiently accurate to describe the data.
In this Chapter we present the study of the multiwavelength behavior of 1ES 0806+524 over the period from November 2010 to June 2011 with particular attention to the interval January-March 2011 during which the source was highly significant detected by MAGIC in a flaring state. We analyze in detail the variability and the spectral evolu-

tion of the source and finally model the spectral energy distribution using data of observations in VHE by MAGIC, HE γ-rays carried out by *Fermi*, in X-rays performed by the *Swift* satellite and in the optical R-band by the KVA. Radio data coverage is also provided thanks to the OVRO telescope at 15 GHz.

4.5.2 *Multiwavelength Analysis Procedures*

We summarize the multifrequencies facilities that have been involved in this campaign that covered the period from November 2010 to June 2011. A brief description of the specific procedure needed for data collection and reduction is also provided. Considerations on the general multiwavelength behavior of the source will be addressed in the following session (§ 4.5.3).

- OVRO data (lower panel of Figure 4.28)
  1ES 0806+524 observations have been carried out at 15GHz in the framework of a blazar monitoring program (Richards et al., 2011) measuring the source flux density twice a week. Occasional gaps in the data sample are due to poor weather conditions or instrumental problems. Observations were performed using a Dicke-switched dual-beam system, with a second level of switching in azimuth to alternate between source and sky in each of the two horns which removes much atmospheric and ground interference (Readhead et al., 1989). The calibration was referred to 3C 286 with an assumed flux density of 3.44 Jy at 15 GHz.
- TUORLA/KVA data (forth panel of Figure 4.28)
  1ES 0806+524 was one of the objects on the original target list and has therefore been monitored regularly since the beginning of the program. The object had been relatively dormant over the years, showing little variability but no particular flaring activity until the spectacular flare beginning at the end of 2010. This flare prompted an alert to MAGIC and a request for ToO observations of the source, which were granted on February 2011.
- *Swift* data (third panel of Figure 4.28)
  Following the VHE γ-ray flare detection by MAGIC (Mariotti, 2011c), *Swift* ToO observations were requested and performed from February 26 to March 2 2011 for five nights. A high activity state of the source was confirmed indicating a clear variability in X-rays (Stamerra et al., 2011). A total of $\sim$ 2 ksec snapshots were obtained withthe *Swift*/XRT in the photon counting (PC) mode, for a overall exposure time of 10 ksec each night. The spectral analysis was performed with XSPEC adopting both a simple power law and a log–parabolic model (Massaro et al., 2004) that include a hydrogen–equivalent column density fixed

to the Galactic value $nH = 4.1 \times 10^{20}\,\mathrm{cm}^{-2}$ (Kalberla et al., 2005). Both models yield similar results regarding the fit goodness above ~ 0.35 (0.5) keV.
Swift/UVOT data were taken with the "filter of the day" (either U, UVW1, UVM2, or UVW2 filter) chosen daily by the Swift science planners. A direct comparison of the ultraviolet bands between different days was therefore not possible. The background has been estimated in a neighboring source-free circular region with a 10″ radius. UVOT source counts were extracted from a circular region of 10″ centered on the source position. The background was estimated from a 10″ circle (of a nearby source free region). The uvotmaghist task provided in the HEASoft package was used for data processing. A correction of the observed magnitudes for the Galactic extinction was performed according to Fitzpatrick (1999) and for the host galaxy contribution according to Nilsson et al. (2007).

- *Fermi* data (second panel of Figure 4.28)
  The *Fermi* data sample covers observations from November 22, 2010 to June 13, 2011 and was analyzed with the ScienceTools software package (version 09-27-01). A 10° radius ROI was selected centered on the 2FGL catalog position of 1ES 0806+524. To reduce the contamination from the Earth-limb γ-rays produced by the cosmic-rays interaction with the upper atmosphere, data were restricted to a maximum zenith angle of 100° and time periods when the spacecraft rocking angle exceeded 52° were excluded (as described in § 3.4.1). For the γ-ray signal extraction, the background model included two components: a galactic diffuse emission and a diffuse one which are provided by the publicly available files[13]. During the spectral point fitting, the normalizations of these components comprising the entire background model were defined to vary freely. In combination with an unbinned maximum likelihood technique applied to events in the energy range from 300 MeV to 300 GeV the post-launch IRFs `P7SOURCE_V6` were used to derive the spectral fluxes. Sources from the 2FGL catalog (Nolan et al., 2012) located within 15° of 1ES 0806+524 were incorporated in the model of the region by setting the spectral models and the initial parameters for the modeling to those reported in the 2FGL catalog. In the fitting procedure, the parameters of sources located within 10° radius centered on the source of interest were left free while parameters of sources located within the 10°-15° annulus were fixed.
  During the studied period, the source is not significantly detected. Consequently, flux upper limits at 95% confidence level

13 In this analysis we used the templates: gal_2yearp7v6_trim_v0.fits and iso_p7v6source.txt

were calculated for each time bin where the TS value for the source was lower than 4 (which corresponds to $\sim 2\sigma$).

- MAGIC data (first panel of Figure 4.28)
  The TeV observations were carried out between January and March 2011 during 13 nights for a total of $\sim$ 24 h. February to March observations were triggered by an increasing flux in the optical R-band as part of a ToO program. After applying quality selection cuts based on the event rate, $\sim$ 3 h of data were discarded. Corrections for the dead time of the readout system yield an effective observation time of 16.1 h. Due to some issues found in the MAGIC data reduction (at the time of the writing) the results shown are to be considered preliminary. We remind to (Aleksić et al., 2013a) for details on the analysis and final results.

4.5.3 *Results*

In the VHE range ($E > 250$ GeV), using all the data collected by MAGIC during this campaign, the source was detected with a significance of 9.9σ (according to Li and Ma, 1983). From a 2D Gaussian fit to the sky map, the excess was consistent with a point-like source located at the catalog position of 1ES 0806+524 within 0.033°, well within the statistical uncertainty and the systematic pointing uncertainty of MAGIC.
During the MAGIC observations, the source underwent a high state on February 24 (Mariotti, 2011c). In this night the flux showed a significant (4.3σ) increase of about four times with respect to the averaged flux of the previous and successive nights. After excluding the flare of February 24 from the data set, the remaining MAGIC observations (13.1 h) still showed a significant detection of 7.3σ.

The integral flux (above 250 GeV) of the overall period excluding the flare was estimated to be $(3.1 \pm 0.1_{\text{stat}} \pm 0.4_{\text{sys}}) \times 10^{-12}\,\text{cm}^{-2}\,\text{s}^{-1}$. This is in good agreement with the flux level above 300 GeV reported by VERITAS for the source detection (Acciari et al., 2009). In the night of the flare instead the integrated flux was estimated to be $(1.4 \pm 0.3_{\text{stat}} \pm 0.1_{\text{sys}}) \times 10^{-11}\,\text{cm}^{-2}\,\text{s}^{-1}$, about an order of magnitude higher than the low state value (see Figure 4.25).

For the overall interval of the campaign (i.e. November 2010 to June 2011) 1ES 0806+524 was highly significantly detected also by *Fermi* ($TS = 643$, which corresponds to more than 25σ). The overall spectrum has been modeled with a power law characterized by a flux of $(2.3 \pm 0.1) \times 10^{-8}\text{cm}^{-2}\,\text{s}^{-1}$ and a hard spectral index of 1.91 ± 0.04. During these 8 months, as evidenced by the 3 years light curve (from August 2008 to September 2011) displayed in Figure 4.26, the source has been constantly detected at GeV energies on a monthly time scale

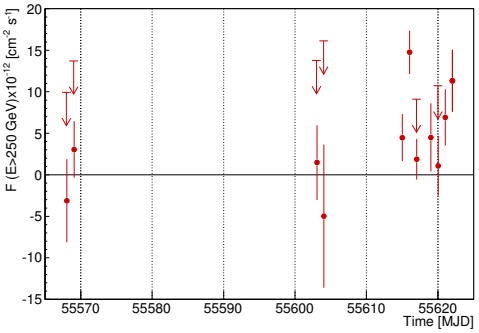

Figure 4.25 VHE γ-ray flux (E $>$ 250 GeV) of 1ES 0806+524 during 2011 MAGIC observations indicating a short term variability of the source. The red arrows correspond to the 95% confidence upper limits. The flare on February 24 is clearly visible, while a (statistically insignificant) increase of the flux towards the end of the observation period is also observed.

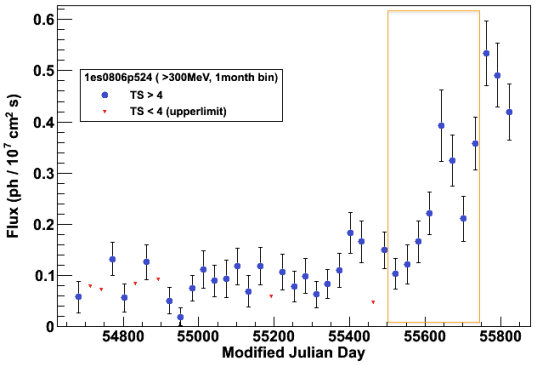

Figure 4.26 *Fermi* light curve of 1ES 0806+524 from August 2008 to September 2011 with binning of one month. A flux increase is evidenced (yellow box) during the 8 months of the period studied in this work. 95% upper limits (red symbols) are calculated when the source TS is lower than 2σ.

(yellow interval in Figure 4.26) and a clear flux increase is seen in the last bins, from the beginning of the VHE observations.

Multiwavelength behavior

Figure 4.28 shows the multiwavelength light curves of 1ES 0806+524 for the 8 months of the campaign, from November 2010 to June 2011. The individual light curves are daily binned except for the light curve in the HE band provided by *Fermi*, where a binning of 7 days has been applied. The dashed lines indicate the individual mean flux level of the respective observation periods.

Besides the first flare observed by MAGIC on the 24 of February 2011, the TeV data showed a hint of increasing flux towards March 2 but

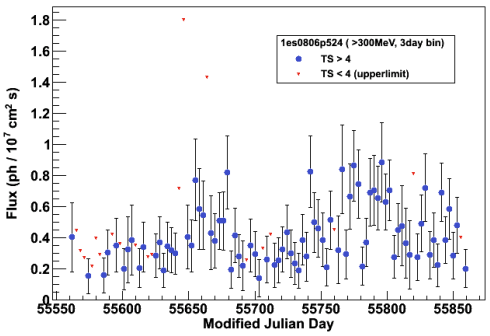

Figure 4.27 1ES 0806+524 3 day bin light curve with (January-September 2011). No particular trends can be evidenced for such short time scale with the LAT.

the overall VHE light curve (Figure 4.25) yields a probability of 0.4% for a non–variable source. No intra–night variability was found at VHE during the high state within the statistical and systematic uncertainties. Since the nights before and after the flaring event on 24 of February 2011 showed a significantly lower flux, we can assume as an upper limit a short term variability of the time scale of one day.

As can be seen from the 3 day bin LAT light curve produced for the time interval of 2011 MAGIC observations (Figure 4.27) unfortunately the source was too weak for *Fermi* to resolve it in single days. This light curve does not evidence an increase in the data points, nonetheless it can be noted from the 1 month bin light curve (Figure 4.26) that the number of significant detections increased in February-March 2011 (number of upper limits decreases). Moreover, the GeV flux for this period was higher, at least a factor of two with respect to the monthly mean. To compare the HE trend with the behavior at other energies a good compromise is is found using a 7 day bin light curve (second panel of Figure 4.28). With this binning, a smooth flux increase was observed from the beginning of March until the beginning of May 2011 reaching a maximum of $(5.2 \pm 1.3) \times 10^{-8}\,\mathrm{cm}^{-2}\,\mathrm{s}^{-1}$ with a delay compared to the other wavelengths. However, given the long integration time of 7 days, no clear conclusion regarding simultaneous source variability can be drawn. Nonetheless, the variability in the HE γ-ray data is evident in the low probability of 7% for a constant source emission.

In X-rays (2-10 keV) the averaged flux is $(8.7 \pm 1.0) \times 10^{-12}\,\mathrm{erg\,cm}^{-2}\,\mathrm{s}^{-1}$ showing an enhancement on March 2 to $(13.0 \pm 0.5) \times 10^{-12}\,\mathrm{erg\,cm}^{2}\,\mathrm{s}^{-1}$, with indications of spectral hardening (Stamerra et al., 2011). Compared to previous observations performed on February 1, 2011, the measured flux is 2-3 times higher and is comparable to the flux level measured in March 2008 during the first detection of the source in VHE γ-rays. Hence, the *Swift*/XRT observations confirm the high activity state of the source exhibiting a clear variability in X-rays with a probability of a constant flux of 6.9×10^{-21}.
As aforementioned *Swift*/UVOT observations have been carried out with different filters in the ultraviolet bands. The brightness of (14.4 ± 0.03) mag measured on March 2 in the UV-W2 and UV-M2 bands

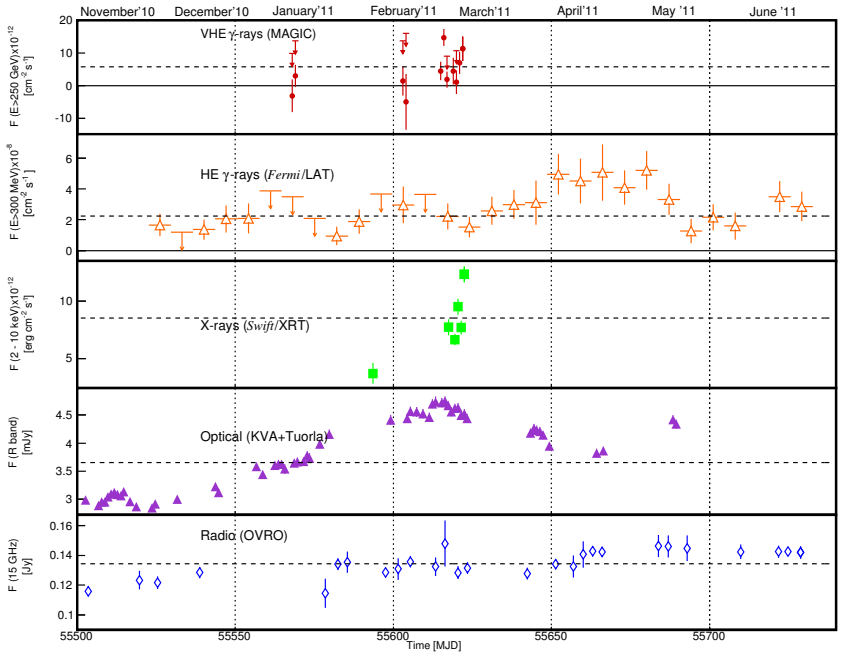

Figure 4.28 From top to bottom: multiwavelength light curve of 1ES 0806+524 covered in VHE γ-rays by MAGIC (red, filled circles), in HE γ-rays (orange, blank triangles) by *Fermi* LAT, in X-rays (green, filled squares) by *Swift*/XRT, in the R-band (violet, filled triangles) and in radio (blue, blank diamonds) by the KVA and OVRO telescope respectively. Upper limits of 95% confidence are indicated by downward arrows. Dashed lines indicate the individual mean flux level of the respective observation periods.

is almost unchanged with respect to February 1 where a brightness of (14.5 ± 0.03) mag was measured. However, 1ES 0806+524 appears about 1 mag brighter compared to the UV flux observed in March 2008. During the observations, the UV band photometry is compatible with a constant flux within the errors.
In the R-band, the core flux showed a strong enhancement over the long-term base level (2.8 mJy) starting from November 2010 (Figure 4.29). After the outburst in VHE γ-rays the optical flux began to decrease steadily. The hypothesis of a constant flux during observations from November 2010 to May 2011 can be rejected with high confidence.
The long-term radio light curve provides a probability of $\sim 6.2 \times 10^{-5}$ for a non-variable source with an average flux level of 0.14 Jy. Compared to observations from November 2010, the radio data show a marginal flux increase from mid-January to May 2011, exceeding the mean flux level of the overall observation period.

SED modeling

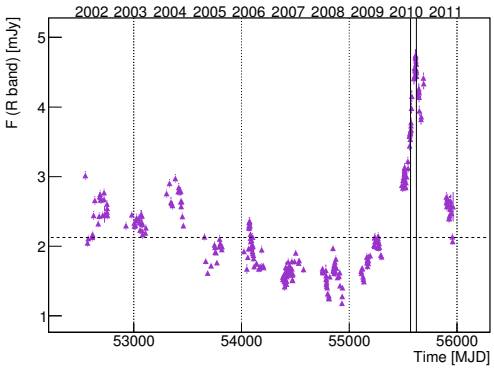

Figure 4.29 1ES 0806+524 long term light curve in the optical R-band observed by the KVA telescope. The black vertical lines correspond to the period of the 2011 VHE observations.

The spectral energy distributions of the source describing the high and low source state during the MAGIC observations, together with simultaneous data from *Fermi*, *Swift*, the KVA and OVRO telescopes are presented in Figure 4.32 and Figure 4.33. Simultaneous and quasi simultaneous data have been combined according to the high and low state as observed in VHE γ-rays. Unfortunately, the high state data does not include simultaneous HE γ-ray data, as *Fermi* did not significantly resolve 1ES 0806+524 during the flares in VHE γ-rays and X-rays. Therefore, a 2σ upper limit has been derived for this time interval and an averaged SED covering the 8 months of observations has been included for comparison purposes. The latter data are not included in the fitting of the high state SED. In addition, archival data in the radio band taken from the NED, and in the R band from the VHE γ-ray discovery (Acciari et al., 2009) have been included. Concerning *Swift* data, the high state comprises observations carried out

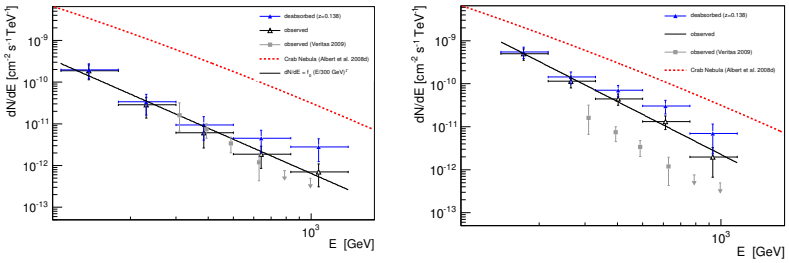

Figure 4.30 Unfolded low (left) and high (right) state differential energy spectra of 1ES 0806+524 observed by MAGIC. The black triangles correspond to the measured spectra fitted by a simple power law (solid black line); the blue filled triangles are corrected for EBL. In the high state a flux increase of about a factor of four is apparent. The spectrum observed by VERITAS and the upper limits derived from those observations (gray, filled squares and arrows respectively) are shown for comparison (Acciari et al., 2009) along with the Crab Nebula spectrum (red dashed line Albert et al., 2008b). The low state spectrum agrees well within statistical errors with the previous observation.

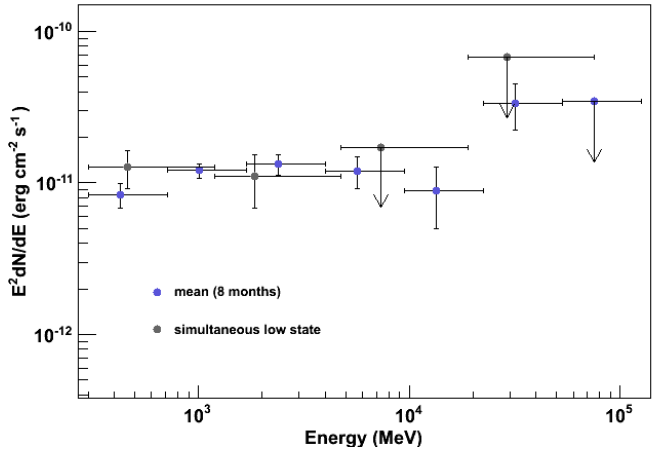

Figure 4.31 SEDs of 1ES 0806+524 in the *Fermi* LAT band (300 MeV – 300 GeV). simultaneous to MAGIC observations (black points) and averaged over 8 months (blue points). Arrows indicate 2σ upper limits.

from February 27 and March 2 whereas the low state encompasses observations from February 1 to March 1. Because of the absence of variability in the radio band during MAGIC observations from January to March, all available data have been included for both source state data samples.

A one-zone SSC model is applied to reproduce the SEDs of both source states (for a detailed description see Maraschi and Tavecchio, 2003). As explained in paragraph § 2.3.3, this model assumes a spherical emission region of radius R, filled with a tangled magnetic field of intensity B. A population of relativistic electrons is approximated by a smoothed broken power law that is parametrized by the minimum, break and maximum Lorentz factors $\gamma_{\rm min}$, $\gamma_{\rm b}$ and $\gamma_{\rm max}$ as well as by the slopes n_1 and n_2 before and after the break respectively. Using the Doppler factor δ, relativistic effects are taken into account.
The physical parameters derived to reproduce the SEDs of both source states are reported in table 4.5. The values are similar to those typically inferred for other HBL objects (see e.g. Tavecchio et al., 2010). For both the high and low state SED the physical parameters referring to the electron spectrum are compatible, while the electron density K shows an increase by a factor of almost 5 during the high state. Furthermore, the emission region R during the high state is approximately half the radius of the emission region of the low state.
In table 4.5 are also reported the power carried by the jet through electrons ($P_{\rm e}$), magnetic field (P_B) and protons ($P_{\rm p}$, derived assuming the presence of one cold proton per emitting electrons). Magnetic field and protons appear subdominant, the electrons carrying most of the

$\gamma_{\rm min}$ [10^3]	$\gamma_{\rm b}$ [10^4]	$\gamma_{\rm max}$ [10^5]	n_1	n_2	B [G]	K [10^3 cm^{-3}]	R [10^{16} cm]	δ	$P_{\rm e}$ [10^{43} erg/s]	P_B [10^{43} erg/s]	$P_{\rm p}$ [10^{43} erg/s]
1	2	7	2	3.85	0.05	19	1.17	28	44.8	0.10	7.7
1	2	7	2	3.90	0.05	4	1.90	28	22.0	0.26	3.3

Table 4.5 Input model parameters for the high (first line) and low (second line) states SED reported in Figure 4.32 and 4.33. We report the minimum, break and maximum Lorentz factors and the low and high energy slope of the electron energy distribution, the magnetic field intensity, the electron density, the radius of the emitting region and its Doppler factor. We also report the derived power carried by electrons, magnetic field, protons (assuming one cold proton per emitting relativistic electron).

jet power, whose total value, $P_{\rm jet} = P_{\rm e} + P_B + P_{\rm p} \sim 10^{44}$ erg s^{-1} is also typical (e.g. Ghisellini et al., 2011b). While the jet power carried by the electrons and protons doubles during the source flare, the magnetic field power is reduced. Based on a causality argument, the physical parameters derive a minimal variability timescale of ~ 0.2 days, perfectly compatible with the variability time scale of one day inferred from the VHE light curve:

$$t_{\rm var,min} = R/(c \cdot \delta) \tag{67}$$

With respect to the 2008 VHE data from Acciari et al. (2009), the inverse Compton peak is more constrained by the MAGIC data of the high source state. The comparison between the physical parameters obtained from the low state SED of this work to multiwavelength observations of 1ES 0806+524 in 2008, is not straightforward, as Acciari et al. (2009) applied an SSC model whose electron spectrum is approximated by an unbroken power law. However, the magnetic field strength and the radius of the emission region are in acceptable agreement. The synchrotron and inverse Compton peak positions derived for the 2008 SED and our observations are located at the same order of frequency. The optical data in the R band shown by Acciari et al. (2009) show clear variations with respect to measurements performed during MAGIC observations, possibly tracing a quite hard spectrum.

4.5.4 *Final remarks*

During the 2010-2011 observation campaign discussed in this work a relatively short γ-ray flare that lasted no longer than one night has been detected at VHE. From this relatively short, high activity state, whose occurrence in weak sources like 1ES 0806+524 is rather rare, a short-term variability of one-day time scale has been inferred at VHE. While the optical-VHE γ-ray outburst has been accompanied by an outburst in X-rays, the increase in flux in HE γ-rays has been

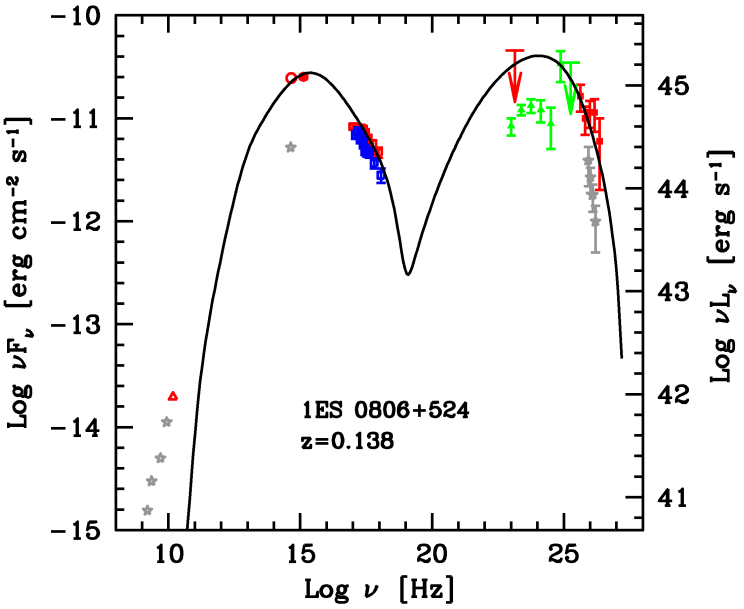

Figure 4.32 SED of 1ES 0806+524 for the high state. VHE data have been corrected for EBL absorption (red, blank squares). The averaged spectrum of LAT data (green, filled triangles) is shown beside the upper limit derived for February 24 (red, arrow). Other data are provided in X-rays (blue and red, filled squares) and U band (red, filled circles), optical R-band (red, blank circle) and radio (red, blank triangle). Archival radio and optical data are also shown (gray, blank stars) as well as VHE data (gray, filled stars) from VERITAS. The solid line represents the one–zone SSC modeling of the high state observations, for which data marked in red have been taken into account except radio data and the upper limit in HE γ-rays.

observed later and on longer time scales. No clear variability in the radio band was found.

Given the simultaneous multiwavelength coverage in several energy bands, correlation studies have been performed to probe the probability of simultaneous incidence of the high states which occurred in some of the observed wavebands. These results will be presented in the upcoming publication (Aleksić et al., 2013a). Here we only anticipate that although VHE observations were triggered optically, apparently no evidence for a correlation in short-term is found between these wavebands.

As resulted from this work, in the HE regime *Fermi* cannot follow the fast activity shown by BL Lacs at TeV energies. Therefore for the

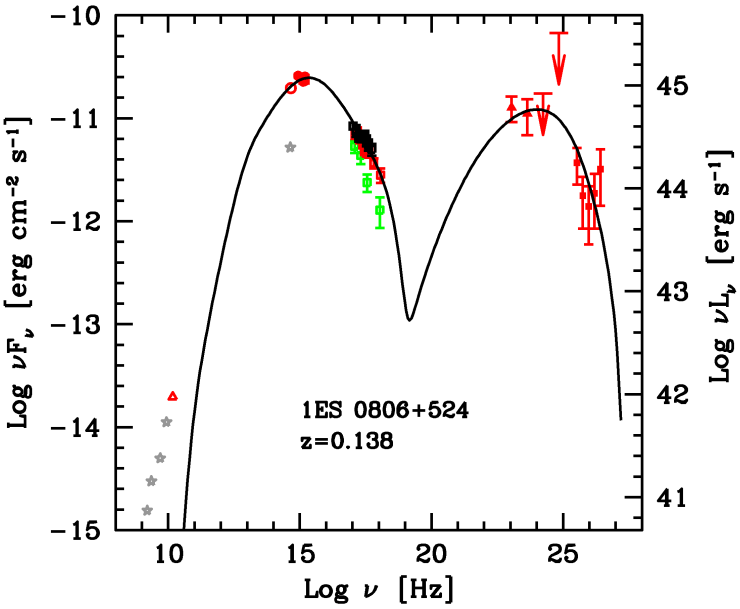

Figure 4.33 SED of 1ES 0806+524 for the low state. The VHE data are corrected for EBL absorption (red, blank squares). Simultaneous and quasi–simultaneous data are provided in HE γ-rays (filled, red triangles), X-rays (filled squares[14]) and in the U band from February 1 to March 1 (red, filled circles), R-band (red, blank circle) and radio at 15 GHz (red, blank triangle). Archival radio and optical data are also shown (gray, filled stars). The solid line represents the one-zone SSC-modeling of the low state observations, considering data marked in red except radio data.

high state we could not derive a reasonable HE spectrum but only an upper limit. Nevertheless, the several multifrequency data collected for both the flaring and quiescent activity of 1ES 0806+524 allowed to perform a one-zone SSC modeling of the SEDs for the respective data sets. Considering the source high state in a multifrequencies context the SED indicated a mild inverse Compton dominance and physical parameters similar to those typically inferred for other HBL objects.

14 Green colored data correspond to observations from February 1, while observations from February 28 and March 1 are indicated in red and black. Due to exact superimposition of the spectra, data from February 25 and 27 are not visible.

4.6 DISCOVERY OF VHE γ-RAYS FROM THE BLAZAR 1ES 1727+502 AND SIMULTANEOUS MULTIWAVELENGTH OBSERVATIONS

VHE observations of 1ES 1727+502 were primarily motivated by the predictions of Costamante and Ghisellini (2002). Observations with the MAGIC telescope were performed during 14 nights between May 6 and June 10, 2011 and resulted with the detection of VHE γ-ray emission from 1ES 1727+502 at a statistical significance of 5.5σ. Remarkably, this was the first report of VHE γ-rays detection from this source. No significant short-term variability was found in any of the wavebands investigated here. The source showed a hard spectrum in the HE band and was significantly detected by *Fermi* in intervals of three months. Unfortunately, this prevented to derive a spectrum simultaneous to the VHE detection. Nevertheless, several simultaneous and quasi-simultaneous data in the optical, X-ray, γ-ray bands allowed a good description of both synchrotron and IC emission peaks. The assembled multiwavelength SED is modeled using a one-zone synchrotron self-Compton model obtaining typical fit parameters of this class of sources.

Part of this work has already been presented in De Caneva et al. (2012), final results will be included in the upcoming publication (Aleksić et al., 2013b).

4.6.1 *Introduction*

1ES 1727+502 is a HBL object located at a redshift of 0.055 (de Vaucouleurs et al., 1991). First tentative VHE observations were already carried out in 1995-1996 with the Whipple 10 m γ-ray telescope but resulted only in upper limits (Horan et al., 2004). Further observations were performed with MAGIC between 2006-2007, before the stereoscopic configuration was operative, and yielded an upper limit on the integral flux of $3.6 \times 10^{-11}\,\mathrm{cm}^{-2}\,\mathrm{s}^{-1}$ above 140 GeV (11.8% of the Crab Nebula flux, Albert et al., 2008b). This last dataset was combined with data from 20 other pre-selected blazars observed by MAGIC between 2004 and 2009. By applying a stacking method analysis it was found that at least some of the included sources were emitting VHE γ rays (Aleksić et al., 2011a).

In June 2010, the detection of a high optical state of 1ES 1727+502 triggered target of opportunity observations with the MAGIC telescopes. Unfortunately, VHE data were unusable due to adverse atmospheric conditions.

The hard spectrum in the HE band (spectral index 1.96 in the 1FGL catalogue, Abdo et al., 2010c), combined with the improved sensitivity achieved by the MAGIC telescopes with the stereoscopic configuration, motivated renewed MAGIC observations in 2011, which resulted with the detection of the source (Mariotti, 2011b).

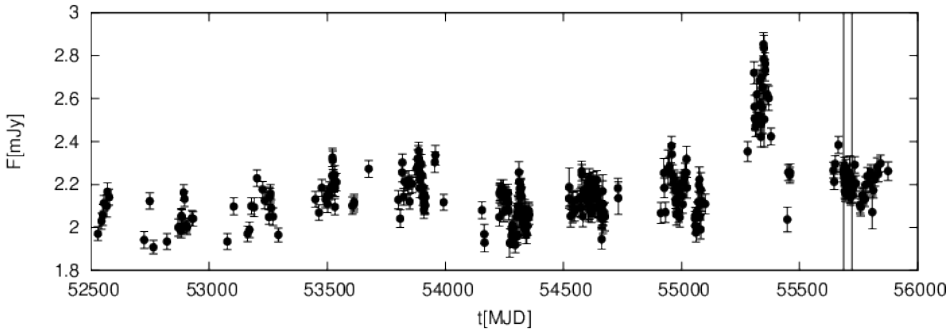

Figure 4.34 10 years light curve of 1ES 1727+502 in the optical *R*-band from the Tuorla blazar monitoring program. The contribution of the host galaxy has not been subtracted. Vertical lines indicate beginning and end of the MAGIC observing window in 2011.

4.6.2 *Multiwavelength Analysis Procedures*

The multifrequencies instruments that have been used in this study are briefly presented here. For a description of the specific procedure needed for data collection and reduction we refer to § 4.1. Considerations on the general multiwavelength behavior of the source will be addressed in § 4.6.3.

- Optical data (Figure 4.34)
  1ES 1727+502 has been observed continuously in the optical R-band as part of the Tuorla blazar monitoring program (details in § 4.1.2) for almost ten years, starting from 2002. Worth to mention that 1ES 1727+502 has a bright host galaxy, contributing with $> 50\%$ to the flux in the optical R-band (Nilsson et al., 2007); this contribution was subtracted from the measured flux used in the SED. Overall, the source showed mainly quiescent behaviour (as shown in Figure 4.34). Only an increased R-band flux is recorded starting in March-April 2010, with a peak value of 2.85 ± 0.05 mJy on May 31, 2010 which exceeded the trigger criteria (see 4.1.2) for MAGIC observations. However, adverse atmospheric conditions compromised the quality of MAGIC data that in turn were discarded. The source had almost returned to its quiescent flux, $\sim 2.0 - 2.2$ mJy, in September 2010 and remained in this state also during MAGIC observations performed in 2011.
- *Swift* data
  Unfortunately, there are no *Swift* observations contemporaneous to the VHE detection. To build the SED we used archival *Swift*/XRT observation taken on 2010 April 5 and *Swift*/UVOT observations performed during the same date in all filters (V, B, U, W1, M2, W2). We note that during this interval the optical flux was already increasing even if it reached the highest

Table 4.6 Results of *Swift*/UVOT observations from 2010 April 5. Flux is reported in units [10^{-12} erg cm^{-2} s^{-1}].

Band	Flux
V	5.4± 0.7
B	6.0±0.7
U	6.7±0.4
W1	6.0±0.3
M2	6.3±0.3
W2	7.2±0.3

value, on 2010 May 31. Although there were no simultaneous observation with the KVA telescope, the R-band SED point has a value of the flux, $4.93 \pm 0.2 \times 10^{-12}$ erg cm^{-2} s^{-1}, comparable to the spectral points obtained from UVOT data (see Table 4.6.2). Consequently, the archival UVOT data can be regarded as representative of the baseline optical-UV flux and can be included in the compilation of the multiwavelength SED.

- *Fermi* data (Figure 4.7)
  1ES 1727+502 has been continuously observed with the LAT and the data sample used for this analysis covers observations from August 5, 2008 to August 5, 2011. The analysis was performed with the standard analysis tools, namely *Fermi* Science Tools (software package version 09-27-01). Only good quality events within 10° of the source were selected. Moreover, recommended cuts were applied restricting the dataset to a maximal zenith angle of 100° and excluding time periods when the spacecraft rocking angle exceeded 52° (more details in § 3.4.1). To extract the spectral information, we used the standard background models[15] for the Galactic diffuse emission and the isotropic diffuse emission that were described in § 3.5. During the spectral point fitting the normalizations of these components, comprising the entire background model, were left free to vary. In combination with an unbinned maximum likelihood technique applied to events in the energy range from 300 MeV to 300 GeV (Mattox et al., 1996) the post-launch IRFs (`P7SOURCE_V6`) were used to derive the spectral fluxes. Sources from the 2FGL catalogue (Nolan et al., 2012) located within 15° of 1ES 1727+502 were incorporated in the model of the region by setting their spectral models and the initial parameters for the modeling to those reported in the 2FGL catalogue. In the fitting procedure the parameters of sources located within 10° radius centered on the source of interest were allowed to vary freely, while parameters of sources located within the 10°-15° annulus were fixed. When performing the fit for the light curve and SED bins, the spectral indexes of the sources were frozen to the best-fit values obtained from the time-independent analysis. Since the source

15 In particular, this analysis used the following templates: gal_2yearp7v6_trim_v0.fits and iso_p7v6source.txt

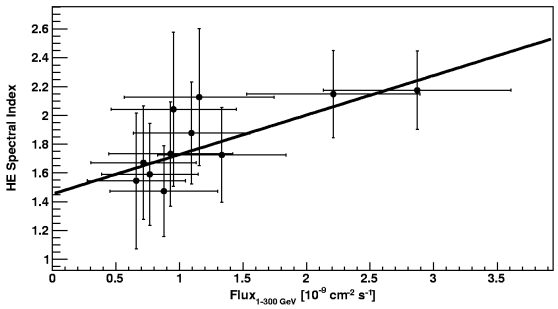

Figure 4.35 Scatter plot of flux–spectral index derived in the HE band from the 3 months light curve. Due to the large uncertainties in the measurements, no conclusions can be deduced on the parameter correlation ($\chi^2 = 1.8, n_{dof} = 9$).

is not always significantly detected, flux upper limits at 95% confidence level were calculated for each time bin where the test statistic value for the source was TS<4.

- VHE data (Figure 4.37)
  The final MAGIC data sample amounts to 14.0 hours and were reduced as described in § 4.1.1. The excess found in the θ^2 plot in the energy range above 150 GeV corresponds to a significance of 5.5σ (Li and Ma, 1983), marking this observation as the first detection of 1ES 1727+502 in the VHE γ-ray regime. The integral flux above 150 GeV is $(2.12 \pm 0.43)\%$ of the Crab Nebula flux. The VHE light curve for the range 200 GeV - 2 TeV is shown in Figure 4.37.

4.6.3 *Results*

During the time when MAGIC detected the source, *Fermi* did not have a significant detection. Therefore, we decided to adopt a slightly larger interval to be used for the SED modeling, namely a 3 month period (centered on the VHE observations). In Table 4.7 we report the fit results for the latter and the average values obtained fitting 3 years of LAT data. Compared to the average behavior measured in three years of observations, the HE flux is higher ($3.5 \pm 0.5 \times 10^{-9}$ ph cm^{-2}s^{-1}), while the spectral index has a compatible value (1.90 ± 0.08). The large uncertainties in the measurements prevented us to derive any conclusion also concerning the possible correlation between flux and spectral index for the studied period, as seen from the flux-spectral index scatter plot ($\chi^2 = 1.8, n_{dof} = 9$) of Figure 4.35 obtained in the HE band. The VHE differential flux obtained (EBL absorption corrected using the model from Domínguez et al., 2011) can be described by a power law function $dF/dE = f_0(\mathrm{E}/300\,\mathrm{GeV})^{-\Gamma}$

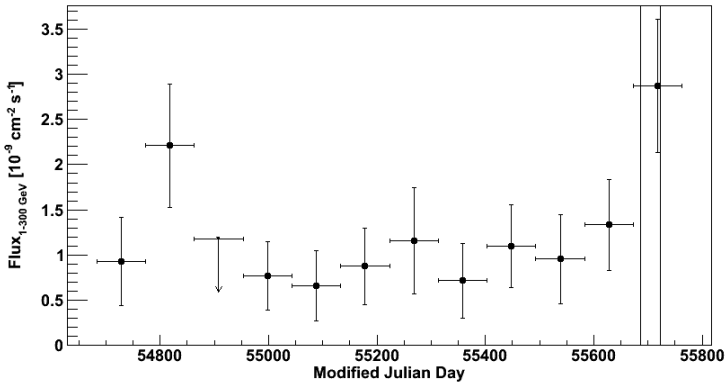

Figure 4.36 Light curve with a binning of three months of the *Fermi*–LAT data between 1 GeV and 300 GeV. The downward pointing triangle correspond to a 95% upper limit. The emission is consistent with a constant flux, albeit a trend towards a higher flux in the last bin, partially coincident with the MAGIC observations, is evident.

Table 4.7 *Fermi* results of the likelihood fit for 1ES 1727+502 in the time intervals considered in the analysis. [a]: Flux (300 MeV - 300 GeV) is in units of [10^{-09} cm^{-2} s^{-1}]

Time Interval	**PowerLaw**			
	Flux[a]	Index	TS	$-\log\mathscr{L}$
Three years interval	3.5 ± 0.5	1.90± 0.08	280	829523
Three month MAGIC observation	7.2±1.9	2.0± 0.2	64	68400

with the following values of the parameters: flux normalization $f_0 = (9.6 \pm 2.5) \times 10^{-12}\,\mathrm{cm^{-2}\,s^{-1}\,TeV^{-1}}$ and spectra index $\Gamma = (2.7 \pm 0.5)$.

Multiwavelength light curve behaviour

The 3 year *Fermi* light curve, is presented in Figure 4.36. Possible variations in the source emission have been tested following the same likelihood method described in the 2FGL catalogue. The result here obtained is consistent with a constant flux ($TS_{var} = 6$ for 11 n_{dof}), albeit a trend towards a higher flux in the last bin, partially coincident with the MAGIC observations, is evident. A similar behavior is observed in the optical band. Overall, the source was found mainly in a quiescent state (as shown in Figure 4.34) with the exception of an increased R-band flux starting in March-April 2010, with a peak value of 2.85 ± 0.05 mJy on May 31, 2010. Afterwards, the source had almost returned to its quiescent flux, $\sim 2.0 - 2.2$ mJy, and remained in this state also during observations performed in 2011.

Figure 4.37 shows the VHE γ-ray light curve between 200 GeV and 2 TeV. In order to have a uniform distribution of days with observa-

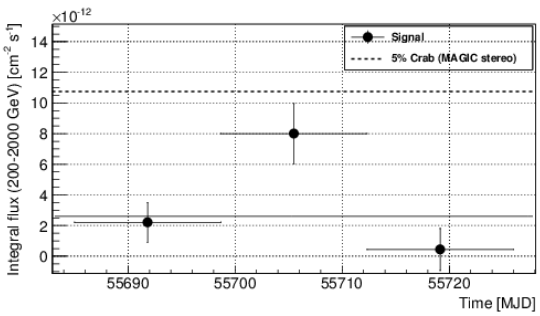

Figure 4.37 MAGIC light curve for 1ES 1727+502 in the energy range from 200 GeV to 2 TeV. The Crab Nebula flux scaled to 5% is shown for comparison (dashed line, Albert et al., 2008b). Flux points are binned in 14 day intervals, the line represents the average flux during the entire observing period.

tions in the bins and due to the weakness of the signal, a 14 day binning is applied starting from May 4, 2011. The resulting light curve has five observation nights in the first and last bin and four in the second bin. The emission is compatible with a constant flux of $(2.6 \pm 0.8) \times 10^{-12}\,\mathrm{cm}^{-2}\,\mathrm{s}^{-1}$. While the relatively low probability of a constant flux (0.6%) might indicate variability, the statistical significance is 2.5 sigma, insufficient evidence for variability. The sparse binning and additional systematic errors due to moonlight and larger zenith angles can indeed fully explain this effect.

SED modeling

All multiwavelength data available have been combined for the compilation of the SED, which has been fitted with a one-zone SSC model (Maraschi and Tavecchio, 2003). This scenario has been already fully described in § 2.3.3. Here we only recall that it involves a blob of radius R, populated by relativistic electrons and filled with a tangled magnetic field of intensity B, moving down the jet with a Doppler factor δ. The electrons emit synchrotron radiation, producing the low-energy peak in the SED. The γ rays are produced by the same electron population up-scattering the synchrotron photons, resulting in the second peak in the SED. The electron spectrum can be described by Eq. 52. The values of the parameters obtained from the fit are: the Lorentz factors $\gamma_{min} = 100, \gamma_b = 3 \times 10^4, \gamma_{max} = 6 \times 10^5$; the slopes $n_1 = 2, n_2 = 3.5$; the electron density $K = 8 \times 10^3\,\mathrm{cm}^{-3}$. The parameters that describe the astrophysical environment are the magnetic field $B = 0.1\,\mathrm{G}$, the radius $R = 7 \times 10^{15}\,\mathrm{cm}$ and the Doppler factor $\delta = 15$ of the emitting region. A comparison with other HBL objects shows that these values are typical for this class of sources (Costamante and Ghisellini, 2002).

4.6.4 *Final remarks*

The discovery of 1ES 1727+502 as VHE γ-ray emitter indeed proves the importance of combining data at different wavelengths, namely radio, optical, X-ray, and γ-ray, to help identify new potential VHE γ-ray emitters. Besides, it confirms the prediction made by Costamante and Ghisellini (2002) and Donato et al. (2001) using X-ray, optical and radio data. They predicted a flux of $0.7 \times 10^{-12}\,\mathrm{cm}^{-2}\,\mathrm{s}^{-1}$ above 300 GeV while the observed VHE flux is a factor of two higher ($1.6 \times 10^{-12}\,\mathrm{cm}^{-2}\,\mathrm{s}^{-1}$).

The source displays little variability in the optical R-band and is bright in the X-ray band. During the period reported in this study, the source is found in a quiescent state in the optical band and low variability is seen also in *Fermi* data. In the HE range it has a hard spectrum and even if the emission is consistent with a constant flux, at the end of these observations we note an enhancement (though not significant) in the flux w.r.t. the average flux over three years.

The SED of 1ES 1727+502 has been modeled with a single-zone SSC model and the resulting parameters are compatible with those obtained for other sources of the HBL class. Furthermore, this is also confirmed when comparing the source properties with the characteristics of VHE blazar sample. Actually, when comparing the VHE parameters of 1ES 1727+502 with the results from the stacked AGN sample observed by MAGIC (Aleksić et al., 2011a), the spectral index is found compatible with the average spectral index of the stacked sample: 2.7 ± 0.5 compared to 3.16 ± 0.51. In addition, when compared to the sample of all blazars detected in VHE γ-rays, its spectral index has the value of a typical BL Lac, while the flux is one of the lower fluxes detected so far (González et al., 2012).

16 http://tools.asdc.asi.it/

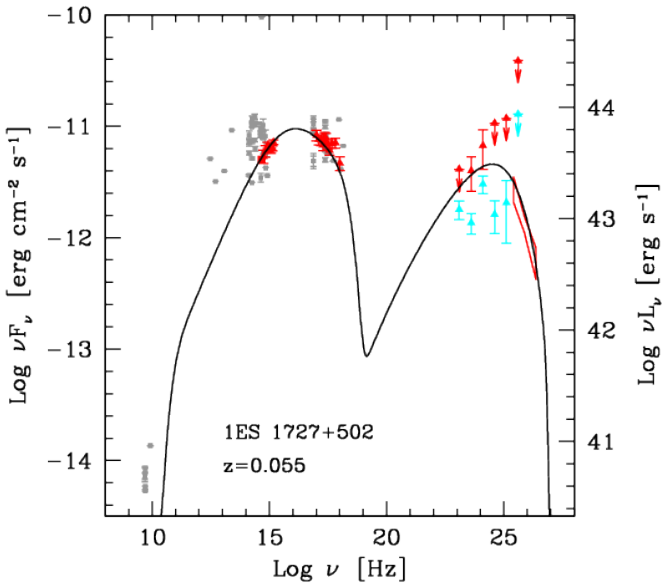

Figure 4.38 Multiwavelength SED of 1ES 1727+502 fitted with a one zone synchrotron Self Compton model, MAGIC observations, (red butterfly) have been corrected for the EBL absorption (see text for details). The data used for the fit (red triangles) are: optical from KVA, archival UV and optical from *Swift*/UVOT, archival X-ray from *Swift*/XRT, HE γ rays from *Fermi* (triangles, three months centred around the MAGIC observing period) and VHE γ rays from MAGIC. The 3 year LAT data (light blue triangles) and archival data (grey) from the ASI/ASDC archive[16]are also shown.

4.7 DETECTION OF VHE γ-RAYS FROM THE FSRQ PKS 1510−08 AND SIMULTANEOUS MULTIWAVELENGTH OBSERVATIONS

PKS 1510−08 is one of the most active objects among the *Fermi* blazars, where quiescent periods are interspersed with high activity states characterized by strong flux density increase at all wavebands. Following the report of its γ-ray flaring state at the beginning of 2012 from *Fermi* (D'Ammando and Gasparrini, 2011) and AGILE (Lucarelli et al., 2012), PKS 1510−08 was observed by MAGIC. These observations resulted in a detection of VHE γ rays from the source with $> 5\sigma$ significance (Cortina, 2012). A detailed study is ongoing and it involves a large number of multiwavelength facilities and all final outcomes will be presented in the upcoming publication Aleksić et al. (2013c). In this Chapter, we report the preliminary results of the *Fermi* analysis. In addition, we show the multiwavelength behavior during this flaring epoch in the optical HE and VHE bands and we discuss our results in multiwavelength context.

Part of this work will be included in the upcoming publication Aleksić et al. (2013c).

4.7.1 *Introduction*

Among more than fifty blazars detected at VHE by ground based Cherenkov telescopes, only three belong to the subclass of FSRQs: PKS 1510–089, PKS 1222+216 and 3C 279. The detection of this particular type of sources in the TeV band is challenging, mainly because of their steep soft spectra. Historically, FSRQs have not been considered good candidates to emit VHE γ-rays also for their characteristics. The synchrotron peak located at low frequencies implies efficient cooling, which makes unexpected the production of energetic γ rays, since the BLR clouds may absorb the γ-ray emission via pair production. Besides, the large redshift at which they are located, also implies strong absorption of VHE γ-rays by the EBL.

Nevertheless, in 2006 MAGIC detected VHE γ rays from the FSRQ 3C 279 (Errando et al., 2008, z=0.536) and this discovery was followed by a second detection in 2007 (Aleksić et al., 2011c) and detections of PKS 1510−08 (z=0.36) (Wagner, 2010) in 2009 and PKS 1222+216 (z=0.45) in 2010 (Aleksić et al., 2011b). The three FSRQs exhibit very different behavior. For example PKS 1222+21, with the fast variability observed in 2010, challenged simple one-zone emission models so that more complicated scenario have been proposed.

PKS 1510−08 is a γ-ray bright quasar, located at a R.A. of $\alpha_{\rm J2000} = 15^{\rm h}12^{\rm m}49^{\rm s}.6$ and a DEC $\delta_{\rm J2000} = -09^\circ06'11.9''$. It exhibits a highly bent radio jet structure with fast superluminal speeds, as derived from multi-epoch VLBA observations. For this objects Jorstad et al. (2005) measured one of the fastest apparent motions (up to $46c$) among all blazars and derived a half-opening angle of 0.2° with the correspond-

ing radius of the jet cross section at about 10 pc being $\sim 10^{17}$ cm (Marscher et al., 2010). Its broad-band spectrum is representative of other FSRQs and, in particular, the radiative output is dominated by the γ-ray inverse Compton component, while its synchrotron emission peaks around IR frequencies.

PKS 1510−08 was discovered as a γ-ray source by EGRET, and during the EGRET observations it was found to be only slightly variable in this band (Hartman et al., 1999). Despite this, since 2008, the source has entered a very active period and many rapid and intense flaring episodes have been detected by *Fermi* and AGILE. Moreover, the high variability level detected in γ rays has been observed across the entire electromagnetic spectrum. In the beginning of 2009 it showed bright flares in radio, optical, X-ray and γ-ray energy regimes (Marscher et al., 2010; Abdo et al., 2010b; D'Ammando et al., 2011). In the γ-ray range the flaring event consisted of eight flares. In X-rays, flaring was moderate and not correlated with the γ-ray activity whereas optical and radio outbursts seemed to follow the high activity states in γ rays with time delays of a few days in the optical, up to a few months as we account for the longer wavelengths of the radio band (Abdo et al., 2010b).

During the γ-ray flares the optical polarization angle was rotating by $> 720^{\circ}$ and during the major optical flare, the optical polarization increased to $> 30\%$. Furthermore, the strong γ-ray flares observed in September 2008 and April 2009 were likely related to the ejection of a new superluminal jet component (Marscher et al., 2010). In 43 GHz VLBA maps, a superluminal knot emerged from the VLBA core with a zero-separation epoch, or essentially simultaneous with this sharp optical flare. Marscher et al. (2010) concluded that the γ-ray flaring activity was taking place in a knot seen in the VLBA images at later times, placing the emission region far out from the central engine.

The observed diversity displayed by the behavior of the source in the various energy bands during the γ-ray flares is a further challenge for the interpretation of the mechanism responsible for the high-energy emission, in particular because the observed variability of the ratio between synchrotron to γ-ray requires that there are local sources of seed photons for inverse Compton scattering within a jet and just outside the jet. However, based on the ratio between optical and γ-ray variability, Abdo et al. (2010b) concluded that the γ-ray emission favors EC model with the seed photons provided by the BLR clouds. We will discuss this hypothesis in details in § 4.7.6, also in the light of recent findings.

4.7.2 *Multiwavelength data*

Between the end of 2011 and the beginning of 2012, the detection of intense rapid γ-ray flares triggered multiwavelength follow up of

PKS 1510–089. The monitoring of PKS 1510−08 was guaranteed in all energy bands, including the VHE observation performed by MAGIC in spring 2012 (Cortina, 2012). A large number of multiwavelength facilities are therefore involved in this study, namely: Metsähovi, OVRO (15 GHz data), UMRAO (operating at frequencies centered at 4.8, 8.0, and 14.5 GHz), MEDICINA (5 and 8.4 GHz), KVA, RINGO-2 (Liverpool, optical data), *Swift* (X and optical data) F-GAMMA program[17], Perkins and Steward observatory, GASP[18], REM, SMA[19], *Fermi*, AGILE (γ-ray data) and MAGIC (VHE γ-ray data).

The analysis of the multiwavelength data is still ongoing and will be included in the upcoming publication. Concerning the VHE dataset, the source was observed by MAGIC starting on February 3, 2012 and observations continued until April 3. Unlike other MAGIC detections of FSRQs, PKS 1510−08 signal was collected from several nights. Worth to mention that the source had been previously detected to emit VHE γ rays by the H.E.S.S. telescope array in 2009 during a previous major optical outburst. PKS 1510−08 was found in high optical state also in February-March 2012, although it was almost an order of magnitude smaller, but still the second brightest flare since the beginning of *Fermi* continuous monitoring. In the following paragraph we report the *Fermi* analysis and some preliminary results.

4.7.3 *Fermi LAT data reduction*

PKS 1510−08 has been continuously observed by *Fermi*. The data used for this analysis were collected from January 1, 2012 to April 7, 2012. They were analyzed with the standard *Fermi* Science Tools software package (version 09-27-01 see § 3.4.1). Only good quality events within 10° of PKS 1510−08 were selected and the standard quality cuts were applied (namely, zenith angle $< 100°$ and spacecraft rocking angle $< 52°$, see § 3.4.1). As described in § 3.5, we included a background model[20] to account for a Galactic diffuse emission and an isotropic one, whose normalizations were left free to vary during the spectral point fitting, performed, as usual, by maximizing the likelihood function. To derive the source spectral information an unbinned maximum likelihood technique was applied to events in the energy range from 100 MeV to 300 GeV (Mattox et al., 1996) in combination with the post-launch IRFs `P7SOURCE_V6`. Sources from the 2FGL catalog (Nolan et al., 2012) located within 15° of PKS 1510−08 were incorporated in the model of the region by setting the spectral models and the initial parameters for the modeling to those reported in the 2FGL catalog. In the fitting procedure the parameters of sources

17 The framework of a *Fermi*-GST related monitoring program of γ-ray blazars.

18 http://www.oato.inaf.it/blazars/webt

19 The Submillimeter Array (SMA) on Mauna Kea (Hawaii) monitored the source in the 230 GHz (1.3 mm) band.

20 In particular, we used gal_2yearp7v6_v0_trim.fits and iso_p7v6source.txt

located within 10° radius centered on the source of interest were left free, while parameters of sources located within the 10°-15° annulus were fixed. When performing the fit for the light curve and SED bins, the spectral indices of the sources were freezed to the best-fit values obtained from time-independent analysis. In particular, two different models, a simple power law and LogParabola shape, have been tested for the spectrum of the source of interest. The latter was found to represent better the spectrum by means of to the likelihood ratio test (see § 4.7.4).
Since the source is not always significantly resolved, flux upper limits at 95% confidence level were calculated for each time bin where the test statistic value for the source was $TS < 25$ (roughly 5σ). The *Fermi* SED presented in Figure 4.41 is simultaneous with MAGIC observations, i.e. it was obtained combining all events of time intervals coincident with the last two TeV detections (from February 19 to March 5 and from March 15 to April 3, 2012).

4.7.4 *HE Results*

At the beginning of 2012 PKS 1510−08 showed renewed abrupt activity in the HE energy range which was coincident with the detection of VHE γ rays from the source. To characterize the source emitted spectrum in the *Fermi* band we investigated two different models: power law and LogParabola.

The spectrum of PKS 1510−08 in the 2FGL has been modeled with a LogParabola spectral shape with parameters flux $= (1 \pm 0.01) \times 10^{-6}\,\mathrm{cm}^{-2}\,\mathrm{s}^{-1}$ and indices $\alpha = 2.29 \pm 0.01$ and $\beta = 0.058 \pm 0.007$. We checked if also for the time intervals interested in our study this spectral shape has to be preferred or if a more simple power law model can still describe accurately well the spectrum of the source. To be noted that the two models can be considered nested (see details in § 3.3.1) therefore we can apply the likelihood ratio test to decide which is the best model for our dataset. To check which model provided the most accurate description for the source spectrum we produced light curves with 7 day and 1 day binning with both models, where the spectral indexes were left free to vary. The light curves are shown in Figure 4.40 and Figure 4.39, where red points are flux values evaluated with the LogParabola model, while black points are the one obtained with the power law model. As can be seen when looking at the light curves, the estimation of the flux seems to be not strongly affected by the spectral change: actually red and black points are almost coincident, and the same is true for their uncertainties; although the difference being obviously evidenced when looking at the higher flux values. Therefore, for small time intervals (1 day interval),

21 The 2 upper limits compatible with zero correspond to time intervals during which the LAT was not being operated in the standard Science operation mode.

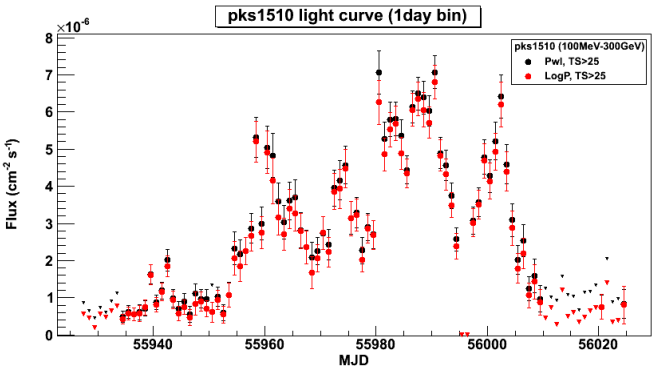

Figure 4.39 PKS 1510−08 *Fermi* light curve[21] (1 day bin) covering the period during which VHE γ rays were observed from the source. The source spectrum was modeled with the power law (black points) and with a LogParabola (red points). The overall trend indicates that the estimation of the source parameters with the two different models agrees very well in most cases.

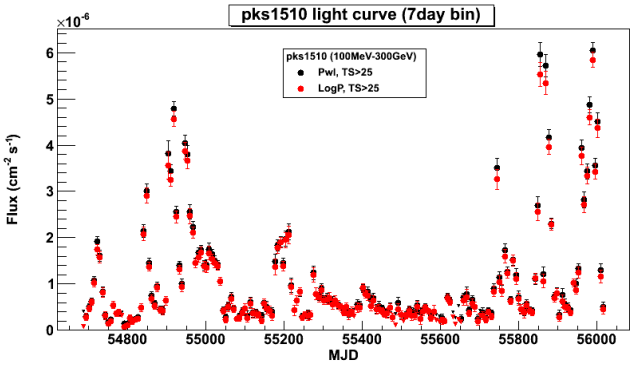

Figure 4.40 PKS 1510−08 light curve (7 day bin) covering 3 years of LAT data. The source spectrum was modeled with the power law (black points) and with a LogParabola (red points).

we did not find substantial variation in the derived parameter values between the two models, although we noted that the difference in likelihood is found significant in at least some cases, especially when the source is brighter.

This is also confirmed from the fit results presented in Table 4.8. The latter reports the parameters values obtained from the fit of the time intervals used for the SED evaluation (see Figure 4.41) with both models. Since the source is strongly variable at HE, to produce the SED that will be used together with other multiwavelength dataset, we divided the interested time window (shown in Figure 4.42) in three time intervals. In particular, we selected a time interval coincident with the MAGIC detection of the source, i.e. from February 19

Time Interval	PowerLaw				LogParabola					σ^b
	Flux[a]	Index	TS	$-\log\mathscr{L}$	Flux[a]	Alpha	Beta	TS	$-\log\mathscr{L}$	
Magic observation	3.97 ± 0.08	2.39 ± 0.02	12241	107077	3.82 ± 0.08	2.24 ± 0.03	0.09 ± 0.02	12243	107056	6
mean state	2.67 ± 0.04	2.40 ±0.01	19943	269334	2.56± 0.04	2.26± 0.02	0.09 ± 0.01	19942	269299	16
low state	0.79 ± 0.04	2.52 ± 0.04	1417	99964	0.75 ±0.04	2.35 ±0.07	0.12 ±0.04	1422	99959	3

Table 4.8 *Best Fit Model for PKS 1510−08* . Comparison of different spectral model for PKS 1510−08 . The LogParabola model is significantly preferred with respect to the power law in all the time intervals considered for this analysis.
[a]: Flux (100 MeV - 300 GeV) is in units of $[10^{-6}\,\mathrm{cm}^{-2}\ \mathrm{s}^{-1}]$; [b]: significance with which the LogParabola model has to be preferred w.r.t. the simple power law model (σ calculated as $[2\,(\log\mathscr{L}_{Pwl} - \log\mathscr{L}_{LogP})]^{1/2}$).

to March 5 and from March 15 to April 3, 2012 (avoiding the first VHE point for the very large error); a time window in which the source displayed low activity in the *Fermi* band (basically this was done looking at the *Fermi* light curve with time bins of 1 day, Figure 4.40, and choosing all the upper limit intervals); finally the rest of data where combined together as representative of a "mean" HE state. The three SEDs are presented in Figure 4.41 and the comparison of the models highlights the differences already pointed out by the light curve investigations. According to the likelihood ratio test, the LogParabola is to be preferred with high significance, in particular, when considering the high and mean state ($\sigma = 6$ and $\sigma = 16$, respectively, in Table 4.8). The LAT (LogParabola) spectral index α seems slightly harder for higher source states, although compatible with the mean value of this dataset and not too far from the 2FGL value. The power law index found for the high and mean states are perfectly compatible, while when comparing them to the low state the higher when brighter trend is evident.

If for the variability study both models can describe well the source emission, when we have to combine the LAT spectrum with the MAGIC spectrum indeed the better accuracy is provided by the LogParabola model. We conclude that when the source is in a rather low state (thus the statistic is low) a power law model can adequately describe its HE emission, whereas for high states a LogParabola has to be preferred.

4.7.5 *Multiwavelength lightcurves*

Figure 4.42 shows the multiwavelength light curve of PKS 1510−08 in VHE, HE, X-ray and optical bands. The R-band light curve evidences

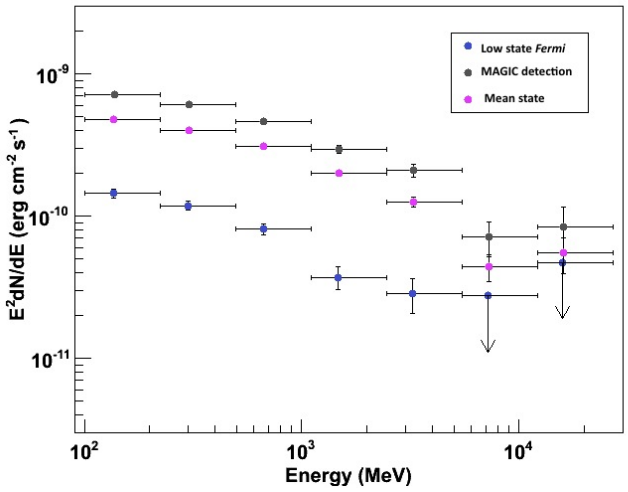

Figure 4.41 SED for the three intervals studied in this work: the high state (black points) was obtained combining all events of time intervals coincident with detection of VHE emission from the source (i.e. from February 19 to March 5 and from March 15 to April 3, 2012); the mean and low state (magenta and blue points, respectively) were selected according with the variability shown by the source in the LAT band (see text for details).

an increasing flux peaking on MJD 55982 reaching a maximum flux of 2.23 ± 0.39 mJy. Afterwards it shows three minor outbursts (peaking on MJD 55987.6, 55990.6 and 55999.6). As noticed in the previous flaring epochs, also in this one the optical band seems to correlate quite well with the general γ-ray trend and time delays of few days are still observed. During these observations, XRT detected the source with a 0.3-10 keV flux in the range $(0.7 - 1.2) \times 10^{-12}$ erg cm^{-2} s^{-1} (forth panel of Figure 4.42). This values are comparable with the flux observed in March 2009, during a period of high γ-ray activity (D'Ammando et al., 2011). The overall trend seen at HE is indeed very dynamic, the source entered in high state around MJD 55957 and then maintained a particular intense activity showing at least three other major outbursts. In particular, the highest flux detected for this period ($7.7 \pm 0.6 \times 10^{-6}$cm^{-2} s^{-1}) is also exceeding the remarkable value reached in the previous period of outbursts.

The second panel shows the spectral changes by the source in the *Fermi* band (obtained from the 1 day light curve, where the modeling of the source was done leaving the power law index free). Although there seems to be a hardening of the spectrum, at least during the first VHE detections, we note that the measurements are within the evaluated statistic uncertainties. Finally, we note that the first VHE γ rays (significant) detection is in coincidence with a first high state at

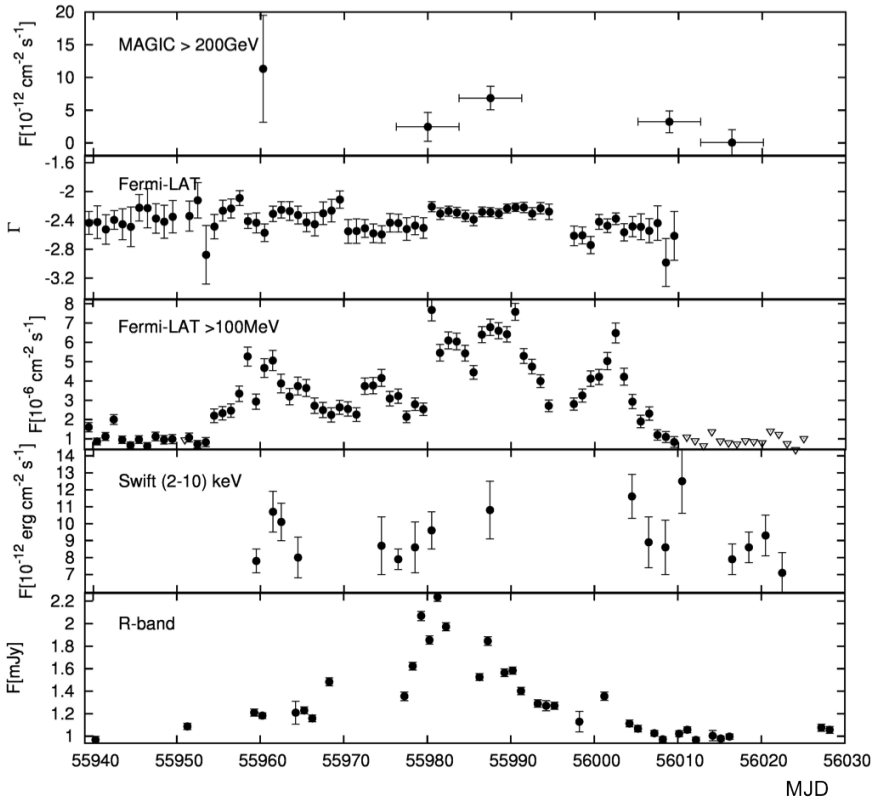

Figure 4.42 Multiwavelength light curve of PKS 1510−08 from spring 2012 in VHE, HE, X-ray and optical bands. The second panel shows the power law spectral index variations in the LAT band; for the evaluation of the LAT light curve (third panel) the spectral index was fixed.

HE and optical energy ranges, whereas the second one corresponds to decreasing-low state at the same energies. Indeed, the further multiwavelength data collected will be crucial to better characterize the overall source behavior.

4.7.6 *Final Remarks*

Besides the outcome obtained from this first partial study, the upcoming results, supported by the results of a large number of multifrequency datasets, will have to provide an explanation for a complicated and challenging scenario. This new detection of PKS 1510−08 by MAGIC, but more generally the detection of FSRQ objects at TeV energies, has been one of the biggest surprises of the VHE γ-ray astronomy. These findings, along with other new evidences, like the abrupt high amplitude flux variations on the sub-daily timescales in the GeV range observed on several sources (Nalewajko, 2012), strongly challenges the validity of one-zone inverse Compton scenarios, so far

largely adopted for the modeling of the high energy γ-ray emission in these sources.

Actually, if on the one hand it has been widely accepted that the dominant γ-ray emission region was located near the central core, probably within the BLR, on the other hand the radiation emitted must be accelerated to TeV energies, as it is observed. Therefore a natural contrast arises: If VHE γ-ray emission is produced that close to the central engine it would be absorbed via photon-photon annihilation involving the infrared-UV soft photons provided by the BLR and also by the circumnuclear dust. In addition, we recall that the VHE γ-ray detections are, at least in some cases, coincident with zero-separation epochs of new knots emerging from the 43 GHz VLBA core (Marscher et al., 2010), suggesting that VHE γ-rays could be emitted in these knots, tens of parsecs from the central engine.

These issues have been already tackled by several authors (Tanaka et al., 2011; Tavecchio and Ghisellini, 2012) and the most accepted model is that the VHE emission must be produced instead at further distances from the core and beyond the BLR, although we have to stress that the observed fast variability requires a rather compact emission region. The large quantity and quality of simultaneous data collected in this study will indeed help to provide decisive answers in this framework.

5

THE BRIGHTEST FLARING AGNS DETECTED BY *FERMI* IN THE FIRST 3.5 YEARS OF OPERATION

A continuous monitoring of the γ-ray sky, allowed by the perfect synergy between the LAT capabilities with the jointly effort of the Flare Advocate framework, led to the detection of 134 bright flaring episodes during the first 3.5 years of *Fermi* operations.

In this Chapter, we present the analysis of all these flaring activities with the same procedure and method. In this way, we obtain a homogeneous data sample to be compared with the whole catalog of sources detected by the LAT (2FGL and 2LAC clean sample[1], noting that the latter is a subset of the former, containing all 2FGL sources associated statistically with AGNs). The correspondent findings are presented along with a comparison between the AGN detected by EGRET and the objects observed in high flaring state by *Fermi*. In addition, in Appendix A, we provide details for the more peculiar sources of the sample.

This work have been presented in Buson et al. (2012) and will be included in the upcoming publication (Abdo and et al., 2013).

5.1 INTRODUCTION

One of the most challenging astrophysics topic has been the study of the variable Universe in the high energy γ-ray domain. In this direction, a major step forward in the MeV-GeV has been achieved thanks to the *Fermi* satellite. *Fermi* is the first facility that has an all-sky variability monitor in the energy range 100 MeV-300 GeV. Notably, the usual LAT operation mode, the scanning sky-survey mode (see § 3.1), provides coverage of the full sky every two orbits (about 3 hours), therefore offering a great opportunity for rapid flare detection and follow-up observations. The LAT huge improvements w.r.t. its predecessor instruments (e.g. EGRET) turned out to be a powerful tool for detecting and characterizing a large numbers of γ-ray sources.

Invaluable effort, complementing the instrument all-sky monitoring of variability and transients, is the Flare Advocate duty activity (also known as Gamma-ray Sky Watcher, FA-GSW), a scientific service belonging to the LAT Instrument Science Operations and devoted to a first quick look inspection and daily review of the γ-ray sky observed by the LAT, performed with continuity all the year round through weekly shifts.

1 Hereafter we will refer only to the 2LAC clean sample

The FA-GSW service highlights basic facts and information about the γ-ray sky of potential interest for the LAT science groups, through a day-by-day inspection and review of the all-sky photon count maps collected and the results of the quick look science analysis pipeline. Summaries about LAT detections of variable sources, transients, brightness trends, flaring sources, new sources on six-hour and 1-day intervals are communicated along with any relevant news to the external multiwavelength and TeV Cherenkov communities using the LAT-multiwavelength mailing-list[2], posting ATels, automatic burst GCNs and special GCNs for blazar flares and other (non-GRB type) transients[3], and publishing weekly reports in the "*Fermi* Sky Blog"[4]. The successful combination has already led to a large number of interesting, but also unexpected, results (see Fig. 5.1 and Fig. 5.2). For ex-

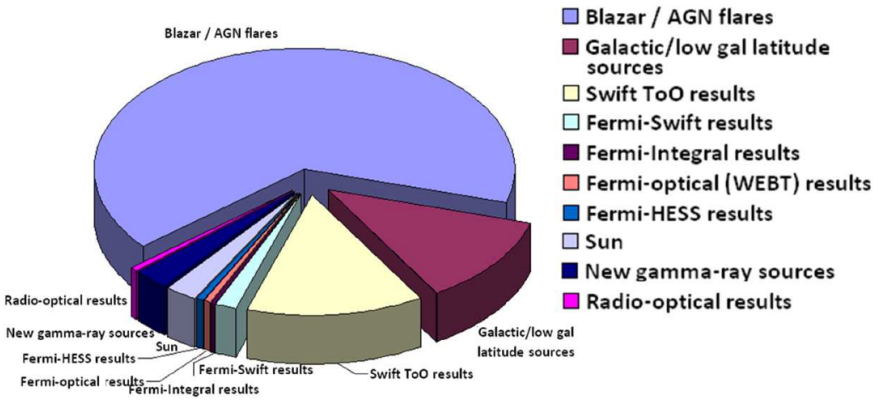

Figure 5.1 ATels published on behalf of the *Fermi* Lat Collaboration from July 24, 2008 to August 28, 2012 (in total 203) grouped by topic (Ciprini and Fermi-LAT Collaboration, 2012).

ample, among the main outcomes triggered by the FA-GSW service are unidentified transients near the Galactic plane (e.g. J0910-5041, J0109+6134, Galactic center region) or associated to Galactic sources (like the Crab Nebula flaring activity, the *nova* explosion in V407 Cygni Figure 5.3 and Abdo et al. (2010f), the microquasar Cyg X-3, the binary star system 1FGL J1018.6-5856) and intense MeV emission from the quiet and active Sun. All complemented by the recurrent detection of many flares from γ-ray blazars as well as short/long activity duty cycles of bright γ-ray blazars, like the extraordinary outbursts of 3C 454.3, large flares of 4C +21.35, the high state of PKS 1510–089 between 2011-2012 that led to the detection of VHE γ-ray emission (see Section 4.7), and the apparently inexplicable flaring ac-

2 Sign up for "gammamw" mailing list at address: http://fermi.gsfc.nasa.gov/ssc/library/newsletter/
3 Web address: http://gcn.gsfc.nasa.gov/gcn/gcn3_archive.html
4 Web address: Fermi Science Support Center, http://fermisky.blogspot.com

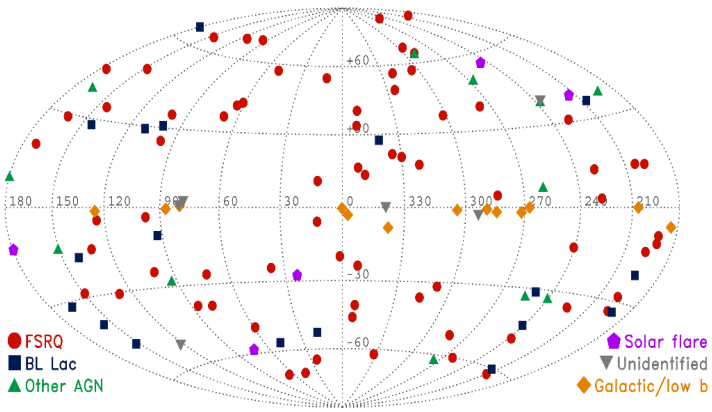

Figure 5.2 Outline of the all-sky map distribution, in Galactic coordinates, of the new γ-ray sources, flares and transients found by *Fermi* and announced through ATels. Different symbols are used for different typology of sources. Most of the sources reported here were pointed out by the FA-GSW service (Ciprini and Fermi-LAT Collaboration, 2012).

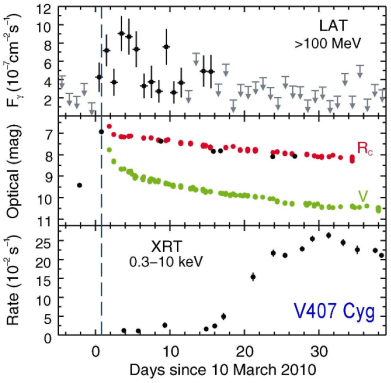

Figure 5.3 The first γ-ray *nova*: V407 Cygni. A new unidentified source was noticed by the FA analysis on March 13-14, 2010 in the Cygnus region. It ended up that the LAT was detecting γ-ray emission at the onset of the *nova* optical outburst (at 5.7σ); the signal detection persisted for two weeks (Abdo et al., 2010f).

tivity of PKS 1830–211, a peculiar gravitationallly lensed system that will be discussed in detail in Chapter 6.

In this Chapter, we will focus on the general characteristic of the sample by itself, paying particular attention to the general properties of the AGNs pointed out by the FA-GSW activity. We note that among them, the overwhelming of flaring sources is composed by blazars, as one would expect. Actually, although they constitute a relatively rare sub-class of AGN (10% of the entire AGN population), these objects constitute the largest known population of γ-ray sources as well as the great majority of sources detected by the *Fermi* LAT.

5.2 FLARE ADVOCATE FRAMEWORK

The FA-GSW duty service is based on the automated quicklook data analysis of Level 2 (L2) at the *Fermi* Instrument Science Operation

Center (ISOC) of SLAC. L2 processing (instrument monitoring pipeline, background monitoring, quick look science analysis) is triggered by the first availability of Level 1 (L1) processed data and performed on longer time intervals (6 hours, 1 day, 1 week) referred therefore as Automated Science Processing (ASP). The ASP analysis pipeline running on the final astrophysical science data (photon event files FT1, and spacecraft data files FT2 fits files) is composed of several scientific tasks (Chiang, 2007; Cameron, 2007):

1. automatic analysis of γ-ray bursts (impulsive transients) through refinement of parameters for LAT-detected GRBs, detection and characterization of GRBs not detected onboard, search and analysis of delayed high-energy afterglow emission;
2. flux history monitoring based on the maximum likelihood method of predefined list of sources (Data Release Plan, DRP, sources) with subsequent addictions of publicly announced sources (flaring blazars, transient sources announced in ATels);
3. blind guess-detection on all-sky photon counts maps accumulated in 6-hours, 1-day, 1-week intervals, through a fast method based on two-dimensional Mexican Hat wavelet transform, thresholding and sliding cell algorithms (Ciprini et al., 2007);
4. transient and flare identification based on variability test;
5. interactive LAT source catalogs;
6. multi-mission/multifrequency tools and archives (e.g. the error circle explorer and spectral energy distribution builder) linked to ASP and provided by the ASI Science Data Center (ASDC[5], Roma).

The role and activity of the FA-GSW shifter is therefore twofold.

- *Gamma-ray Flare Advocate task*: flaring sources approaching daily flux of 10^{-6} cm^{-2} s^{-1}deserves special attention (detection, localization, flux, photon index to be checked, photon counts maps and exposure maps to be outlooked). Internal/public notes, ATels, Target of Opportunity (ToO) are submitted, multiwavelength observation campaigns are organized when needed.
- *Gamma-ray Sky Watcher task*: results from the ASP pipeline in 1-day and 6-hour time intervals are checked, searching for transients, increasing/decreasing brightness trends, and new γ-ray source candidates and looking at positional associations.

The FA-GSWs on duty carries out also several ToOs following up of *Fermi* LAT flares or new sources to the *Swift* satellite, showing an ideal synergy between these two missions. They also involved radioastronomy community in joint observing programs and organized

5 Web address: http://fermi.asdc.asi.it

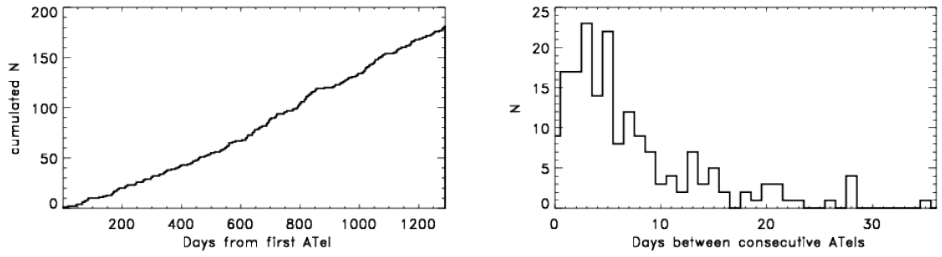

Figure 5.4 Distributions of the 181 ATels published on behalf of the *Fermi* LAT Collaboration from July 24, 2008 (ATel#1628) to February 1, 2012 (ATel#3904), i.e. in about 3.53 years.

multiwavelength observing campaigns targeted on single blazar and Galactic sources. ATels are one of the main products of the FA-GSW service[6] and the average rate of published ATels is about one per week. In Fig. 5.4 the time separation distribution and the cumulative number distribution of the 181 ATels published on behalf of the *Fermi* LAT Collaboration in about 3.5 years, from July 24, 2008 (ATel#1628) to February 1, 2012 (ATel#3904), are reported.

5.3 SAMPLE COMPOSITION

Since the beginning of its operations, the LAT detected enhanced activity from several sources. In the period from August 4, 2008 to February 4, 2012, 91 of them fulfilled the ATel criterion as they underwent at least one flaring state overcoming the predefined flux threshold (i.e. flux $> 10^{-6}$ ph cm^{-2} s^{-1}, which is a typical value used for defining a source in flare). In the following study, we will describe all these sources as a whole, in particular considering these extreme flaring episodes, to see if we can individuate similarities or differences among them and also w.r.t. the more general great majority of objects observed by the LAT.

Among these source, some showed extraordinary activity more times so that the total number of high states that will be considered in this work is 132. The complete list of them is reported in Appendix A. To be noted that the first alert provided by the LAT, ATel#1628, was posted on July 24, 2008 but since during this period the LAT instrument was still under the commissioning phase these data will not be included in the present work. Among the 91 sources, 83 have a measured redshift and 7 were not listed in the 2FGL catalog (Nolan et al., 2012). Four of the latter are not listed in the 2FGL since they did not pass the $TS = 25$ threshold for being included, i.e. SBS 0846+513, PMN J1123–6417, PMN J1913–3630, PKS 1915–458. Interest-

6 At the following web address it is possible to find a catalog of the γ-ray sources subjects on one *Fermi* ATel: http://www.asdc.asi.it/feratel/

ing to note that the other three are the source PKS 2123–463, that was subsequently associated with 2FGL J2125.0–4632 ($z = 1.67$) thanks to multiwavelength observation/correlation, whereas the γ-ray transients that have been associated with PKS 0646–306 ($z = 1.153$) and TXS 1530–131 do not have any counterpart in *Fermi* catalogs. This further demonstrates the FA-GSW activity as an useful tool to identify γ-ray sources and more, to broaden the set of known (distant) γ-ray sources, on average too faint to be picked up during years, but sometimes bright enough for being significantly detected in small periods. Worth to mention also that nine sources of this sample were detected at TeV energies (Ap Lib, S5 0716+74, BL Lacertae, 3C 66A, PKS 2155−304, 3C 279, 4C 21.35, PKS 1510−089 and the radio galaxy NGC 1275). As mentioned earlier, in some occasions the LAT ATel suggested TeV observations which then resulted with the successful detection of the source.

The obtained sample is composed by different classes of sources[7]: 68 FSRQ, 14 BL Lac, 2 AGN, 4 AGU, 2 NLSyI and one Radio Galaxy. The first thing to note is that in our sample FSRQs dominate over BL Lacs, whereas in the 2LAC catalog it was found that BL Lacs outnumbered FSRQs (Nolan et al., 2012). A contradiction could arise since our sources (at least the large majority) are basically a sub-sample of 2LAC. Anyway, this can be explained considering that our sample is build *a priori* selecting sources that exhibited extreme fluxes coupled with the fact that in the 2LAC sample the fluxes of the FSRQs were found to extend to higher values than the one of BL Lacs. (as discussed in Abdo et al., 2010g).

Furthermore, when looking at the composition of the BL Lacs of our sample in terms of LSP, ISP, and HSP[8], one would expect hard spectrum BL Lacs be relatively more numerous w.r.t. LSP and ISP. Actually, according with 2LAC findings, among BL Lacs HSP sources dominate over ISP and LSP, the percentages being 53%, 20% and 27%, respectively. In spite of that, the 14 BL Lac objects of this sample detected with integral photon flux $> 10^{-6}$ cm^{-2} s^{-1}can be divided into 6 LSPs, 6 ISPs and only 2 HSPs. But also this can be reconciled with further considerations regarding the 2LAC sources. Nolan et al. (2012) evidenced that the mean fractional variability (sampled on time scales of 1 month), as given by the normalized excess variance, is higher for FSRQs than for BL Lacs. Accordingly, the normalized excess variance for BL Lacs was found to decrease from LSP to ISP and HSP BL Lac objects. From their study, it become apparent that only a small fraction of the HSP BL Lacs detected by the LAT shows significant variability (27 out of 160), substantially less than LSP BL Lacs (25 out of

7 This classification agrees with that used in 2LAC: AGU refers to sources without a good optical spectrum or without an optical spectrum at all, AGN refers to sources that are not confirmed blazars nor blazar candidates. For more details we address the reader to Ackermann et al. (2011).

8 The classification based on the position of the SED peak as described in Section 1.6.

61) and ISP BL Lacs (30 out of 81). Therefore, we can conclude that although BL Lacs with harder spectra are generally detected more easily with *Fermi* than FSRQs, at the same time they are less variable and less prone to huge flux enhancements with respect to LSP and ISP. In addition, noting that almost all *Fermi* FSRQs are LSP, also the previous contrast is naturally overcome.

Finally it is worth to notice that this sample constitutes only 10% of all the sources detected in 2 years of *Fermi* operations referring now to the 2FGL catalog. Therefore, up to now, only a small percentage of the 2FGL sources displayed variability reaching extreme flux values, and those are basically all blazars.

5.4 LAT OBSERVATIONS AND DATA ANALYSIS

The *Fermi* LAT analysis tools are always under development and new, different IRFs are released along with new reprocessed data sets (as described in § 3.4). Analogously, the ASP pipeline follows this updates and as a matter of fact the product of the analysis, during the time, are provided with different software versions and IRFs. For this reason, the first thing that we had to do is to ensure that all sources of our sample are studied by means of the same tools, thus safeguarding the homogeneity of the derived sample parameters. Therefore we re-analyzed all flaring episodes according with the most recent tools available. We selected all events belonging to the "source" class distributed within 10° of each source of interest for the time interval reported in the correspondent ATel (one day interval). When a time interval larger than a day was indicated in the ATel we looked at the daily ASP light curve and analyzed the data related to the first daily peak showed by the ASP light curve. According with the procedure explained in § 3.4.1, data were restricted to a maximal zenith angle of 100° and time periods when the spacecraft rocking angle exceeded 52° were excluded. For each flaring episode we first used the `pointlike` tool to derive the best estimation on the position of the flaring source. Subsequently, the analysis was performed with the standard analysis Science Tools software package (version 09-27-01) available from the FSSC. An unbinned maximum likelihood technique (Mattox et al., 1996) described in § 3.3.1 was applied to events in the energy range from 100 MeV to 300 GeV in combination with the post-launch IRFs `P7SOURCE_V6` to derive the spectral parameters.

The model for each ROI contained templates[9] for the diffuse Galactic foreground emission and a spectrum for the isotropic emission. Sources reported in the 2FGL catalog (Nolan et al., 2012) located within 15° of the targets were incorporated in the model of the ROI as well. For these individual LAT sources and the sources of interest

9 In particular for this analysis the templates gal_2yearp7v6_v0_trim.fits and iso_p7v6source.txt were used.

themselves we assumed a power-law model. In the fitting procedure, the parameters describing the sources located within a 10° radius centered on the source of interest were left free to vary, while the parameters of sources located inside the 10°-15° annulus were fixed, as well as the isotropic normalization parameter. We performed a first fit to estimate reliable starting values for the parameters in the ROI and removed from the model sources with a low significance. For this purpose, we used the TS to evaluate the significance of the detection for each γ-ray source in the ROI: sources with TS lower than 5 were removed from the ROI model. A minimization procedure was then applied to the data to derive the final parameters for each source, namely fluxes, spectral indices and detection significance as well. When the source of interest was not significantly resolved, i.e. the TS[10] value was lower than 25, flux upper limits at 95% confidence level were calculated. The 2σ upper limits were computed according to the `IntegralUpperLimit` method (Nolan et al., 2012).

As aforementioned, we focus on flare episodes that have been reported in at least one ATel. Worth to note that often several sources are detected in (daily) γ-ray high state with respect to their mean/quiescent state, but not always they deserve fast public alert, and therefore they are not promptly advertised to the scientific community. A future more complete study will have to include also these episodes.

All the results from our analysis are reported in Appendix A where in Table we indicate for each flaring episode the 2FGL counterpart (when available), best position, associated source, peak time, peak flux, peak index, luminosity. In addition consideration on the sample general properties will be addressed in § 5.6.

5.5 COMPARISON WITH EGRET

Radio-loud AGNs, mostly blazars, are known to display strong variability over the whole electromagnetic spectrum, from radio to γ-ray energies. In particular, intense γ-ray emission above 100 MeV has been discovered by EGRET, designating the blazar class (Hartman et al., 1999). A dramatic example of large variability amplitude on long timescale is offered by the γ-ray emission of 3C 279 in the EGRET era. The flux was observed to change by more than two orders of magnitude between two observations performed in 1993 and 1996 (Hartman et al., 2001). The γ-ray activity timescale of blazars detected by EGRET went from a few days (e.g. PKS 1622−297) to several weeks (e.g. PKS 0208−512). Anyway, the large spread in time variability and the sparse EGRET coverage made it difficult to characterize γ-ray variability time scales and the fraction of time spent in flaring activity (e.g. γ-ray duty cycle).

10 As noted in § 3.3.1, the square root of TS in the case of two degrees of freedom is distributed as a χ^2, therefore $TS = 25$ roughly corresponds to 5σ.

Among the 271 pointlike sources detected in γ-rays by EGRET (see e.g. Mukherjee, 2001) 66 were blazars plus a radio galaxy (Centaurus A), and a number of them showed variability, being observed several times at different amplitude (Hartman et al., 1999). Comparing the AGNs detected by EGRET with the objects observed in flaring activity by *Fermi*-LAT during the first 3.5 years of operation, we find that 29 of the 67 EGRET sources have been detected during a γ-ray flaring activity by *Fermi* LAT. Taking into consideration the γ-ray sources detected by EGRET with a flux $> 10^{-6}$ cm^{-2} s^{-1} 10 of the 16 flaring sources observed by EGRET (see e.g. Mukherjee, 2001) have shown intense γ-ray activity also during the *Fermi* operation. This is an indication that the high activity of these sources continued over two decades, even if in some case the source underwent a quiescent phase before increasing again its activity. A typical example is PKS 0528+134, that was observed by EGRET during different flaring episodes between 1991 and 1997 (Mukherjee et al., 1999), while it remained quiescent during the *Fermi* observation up to a new flare in 2011 June (D'Ammando, 2011). On the contrary, e.g. 3C 279 was active for most of the time during both the EGRET and *Fermi* observations. However, most of the flaring AGNs detected by the LAT did not show significant γ-ray activity during the EGRET observations. In this context, it is indicative the behavior observed on 3C 454.3 and PKS 1510−089, the two brightest extragalactic blazars in the *Fermi* sky. While they showed only a moderate activity during the EGRET observations, they displayed an intense and dynamic behavior during the *Fermi* monitoring, reaching a remarkable γ-ray flux higher than 10^{-5} cm^{-2} s^{-1}(Sanchez and Escande, 2010; Hungwe et al., 2011).

In addition, we should take into consideration also the different operating mode of EGRET and LAT: inertial pointing versus all-sky scanning survey mode. In light of this, we cannot exclude that some strong γ-ray flares from these sources have been missed for lack of observation coverage in the EGRET era. Nevertheless, the presence of blazars detected by EGRET and not by *Fermi* suggests a possible significant change of activity for some objects at least between the epochs of EGRET and *Fermi* operation.

5.6 GENERAL PROPERTIES OF THE SAMPLE

The sources of this sample appear to be equally distributed in the northern and southern hemisphere. Figure 5.5 shows the histogram of the Galactic latitude distribution for the source of this study (dashed line) and the one for the 2LAC sources (solid line, gray area), the only evident difference is found at low latitudes ($|b| < 10°$), but this is only due to the way in which the 2LAC clean sample is defined[11]. Also

11 The 2LAC clean sample uses the *a priori* criterion to select only sources at high Galactic latitude, i.e. $|b| > 10°$.

the redshift distribution of this sample, Figure 5.6, does not indicate strong differences with respect to the 2LAC one.

Figure 5.7 shows the flux distribution of our sample as the ratio between the flux calculated for the time interval reported in the ATel and the average value reported in the 2LAC. We find that, on average, the sources of this sample have fluxes a factor 11 higher than their 2LAC averages. Although there are some exceptional cases for which we measure a flaring flux $>$ 40 times its average value (as in the case of 2FGL J0532.0-4826, 2FGL J1153.2+4935, 2FGL J1848.6+3241). The flux distributions of the two main classes of our sample are plotted in the inset of Fig. 5.7: FSRQs are represented by the solid line while BL Lacs by the dashed line. These distributions do not indicate strong differences between the classes, although we note that the higher flux increments are displayed only by the former. The distribution of the photon index derived for the flaring state is presented in Figure 5.8, evidencing the two classes of blazars: BL Lacs are plotted with a dashed line, and FSRQs with a solid line. The histogram represents the difference between the average 2LAC index and the index measured during the flare. While BL Lac indices remain almost constant, FSRQs seem to flatten their spectra during the flaring state.

The γ-ray luminosity distribution, i.e. the K-corrected γ-ray flux multiplied by $(4\pi d_L^2)$, where d_L is the luminosity distance, is presented in Figure 5.9. The highest luminosities are observed for 2FGL J1833.6−2104 (also known as PKS 1830−211 and discussed in Chapter 6) and 2FGL J1504.3+1029 ($L_\gamma = 1.9 \times 10^{50}$ erg s^{-1} and $L_\gamma = 1.2 \times 10^{50}$ erg s^{-1}, respectively). These values are very close to the record value of 2.12×10^{50} observed for the exceptional 3C 454 outburst of November 2010 (Abdo et al., 2011).

5.7 FINAL REMARKS

As discussed in this Chapter, it appears clear that the FA-GSW duty complements the all-sky surveying of *Fermi* LAT as the liaison between the LAT team and the multiwavelength astrophysical and astroparticle community, triggering, quite often, multiwavelength follow-up observations.

In this Chapter, we focused on the flaring episodes (exceeding the predefined threshold flux of 10^{-6} ph cm^{-2} s^{-1}) detected in *Fermi* data during the FA-GSW activity of the first 3.5 years of operations. After analyzing them with a common procedure, we compared the main properties of this homogeneous, flux-limited sample with that of the whole catalog of sources detected by *Fermi* in the first 2 years, i.e. the 2FGL and 2LAC catalogs. No strong differences are found between the two samples. A future perspective would be to extended this investigation to study in details not only the high flux peak, but also

the general high state of these sources, for example comparing the flaring characteristics (e.g. rising and falling times, symmetry of the flares). A similar work was done by Nalewajko (2012), but using only the brightest flares (and in turn reducing the study to only 4 sources). Nevertheless, we have to note that such study would be challenging as some sources of this sample displayed a low intensity over large periods (e.g. years, but also weeks), the most extreme cases being significantly detected only in the day of the outburst.

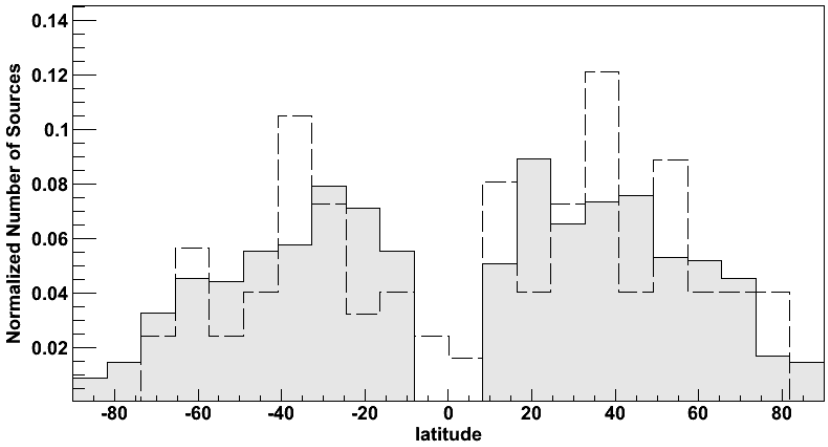

Figure 5.5 Distribution of Galactic latitude: solid line (gray area) represents the overall distribution corresponding to the 2LAC sample, dashed line this sample (normalized counts on vertical axis).

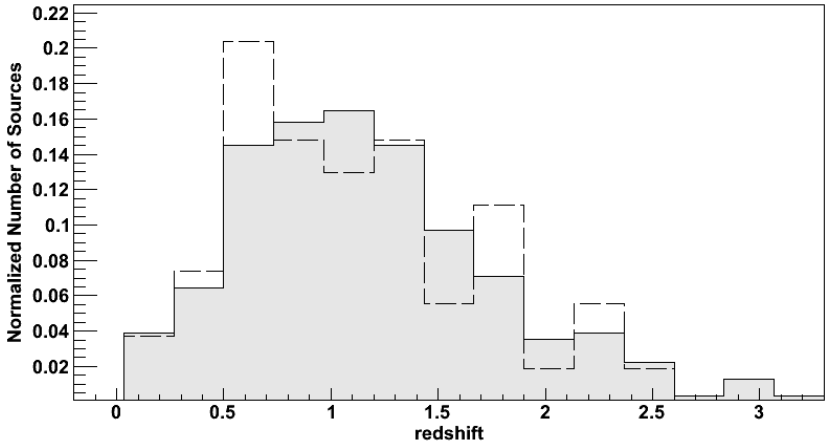

Figure 5.6 Redshift distribution: solid line (gray area) represents the overall distribution corresponding to the FSRQ 2LAC clean sample, dashed line the FSRQ of this sample (normalized counts on vertical axis).

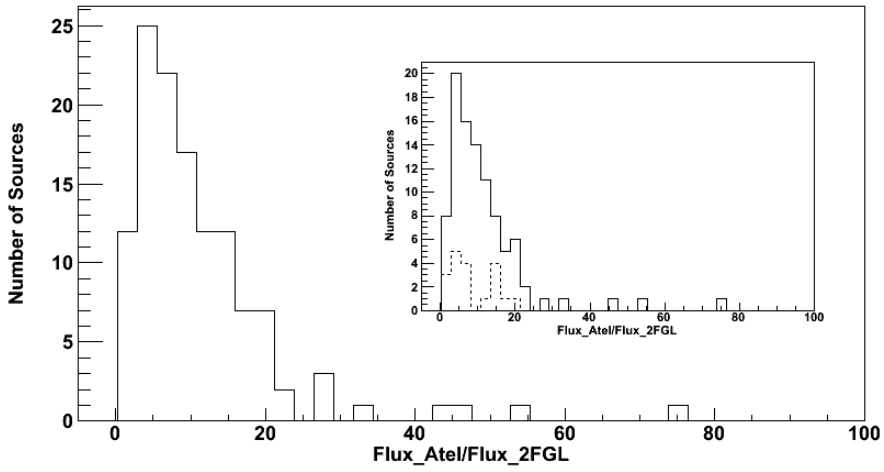

Figure 5.7 Histogram of the ratio between the flux measured in the time interval reported in the Atel and the mean 2FGL flux; in the inset are shown the two main different classes: FSRQ solid line, BL Lacs dashed line.

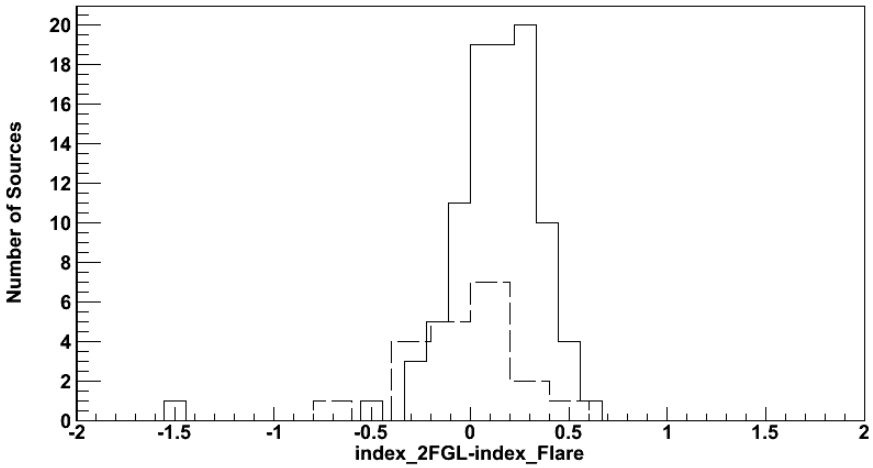

Figure 5.8 Histogram of the difference between the mean 2LAC index and the index measured in the time interval reported in the ATel. FSRQ are plotted with solid line, BL Lacs with dashed line; here only sources belonging to the 2LAC clean sample are considered.

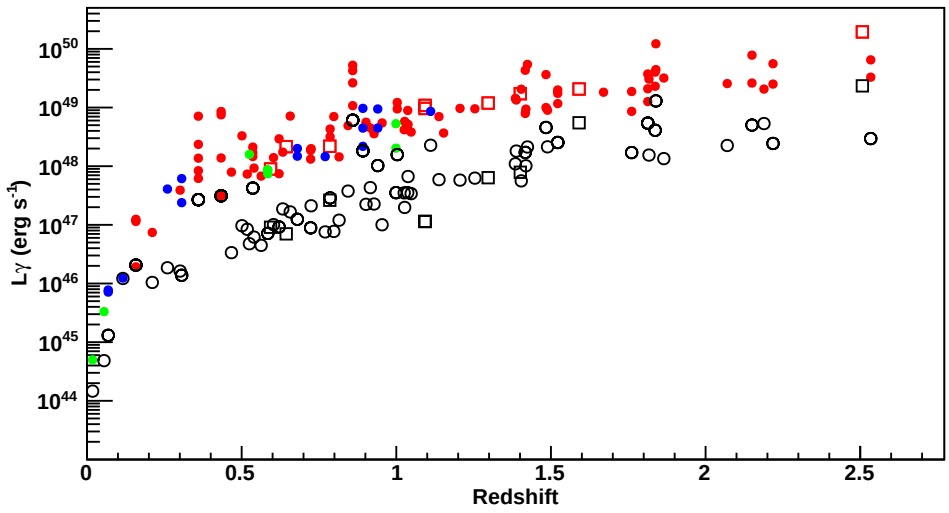

Figure 5.9 Gamma-ray luminosity versus redshift. The luminosity values measured in the time interval reported in the ATel are indicated with filled circles: FSRQs in red, BL Lacs in blue, other type of AGNs in green. Sources that do not belong to the 2LAC clean sample have been indicated with squares. The empty circles and squares indicates the 2LAC correspondent luminosities, when available.

6

DETECTION OF γ-RAY FLARING ACTIVITY FROM THE GRAVITATIONALLY LENSED BLAZAR PKS 1830+211

PKS 1830+211 is a bright γ-ray gravitationally lensed FSRQ. Based on radio observations, one expects a time delayed variability from the lens image of the source to follow 25 days after a primary flare, with flux a factor of 1.5 below. Three main flaring events have been detected in the first three years of *Fermi* survey. Contrary to previous published claims, we find no substantial evidence for such a delayed high-level γ-ray activity. Moreover we derive a lower limit of about 6 on the flux ratio observed between the source and the lens image.
LAT observations also triggered follow up with Target of Opportunity *Swift* observations. The high dust extinction prevents *Swift*-UVOT from detecting the source, while *Swift*-XRT finds a hard spectrum with photon index about 1.2, with no evidence for X-ray variability in the 2 weeks following the γ-ray outburst. The lack of correlation between the X-ray and γ-ray variability is somewhat typical for FSRQs like this source. The simultaneous SED built for the outburst epoch can be modeled with inverse Compton scattering of thermal photons from the dusty torus external to the relativistic jet. This Chapter will discuss implications of the LAT data both in terms of blazar emission models and the source as a gravitational lens.

This work will be included in the upcoming publication Abdo and et al. (2013a).

6.1 INTRODUCTION

PKS 1830+211 has met with considerable attention, due to the fact that it is clearly a gravitationally lensed source. It was discovered as a single source in the Parkes catalog (Shimmins et al., 1969), but later radio observations by the Very Large Array (VLA) and Australian Telescope Compact Array (ATCA) clearly revealed two sources, one in the northeast (NE) and one in the southwest (SW), separated by $0.98''$ and connected by an Einstein ring (Pramesh Rao and Subrahmanyan, 1988; Jauncey et al., 1991). When the source, lens, and observer lie along a straight line, the theory of gravitational lensing shows that a circle, known as the Einstein ring, is formed (Schneider et al., 1992), while inside this main ring there are smaller relativistic rings (Virbhadra and Ellis, 2000). The NE image seems to have a flux density about 1.5 times as bright as the SW one. Molecular absorption lines revealed lensing galaxies located at $z = 0.886$ (Lovell et al., 1996;

Frye et al., 1999; Lehár et al., 2000) and $z = 0.19$ (Lovell et al., 1996; Wiklind and Combes, 1996, 1998). Optical imaging shows the same lens separation from the core ($0.98''$) and an unusually strong radio Einstein ring (Jauncey et al., 1991; Nair et al., 1993; Jones and SHEVE Team, 1993). These lensing galaxies were confirmed by Gemini and *Hubble* Space Telescope (HST) (Courbin et al., 2002), while further galaxies are identified in the field of the source (Lehár et al., 2000, 2002). A detailed exploration of this system at optical wavelengths is hampered by its proximity on the sky to the Galactic plane and Bulge (the Galactic coordinates of PKS 1830+211 being $l = 12.17°$, $b = -5.71°$), leading to considerable dust extinction (Djorgovski et al., 1992; Courbin et al., 1998; Gregg et al., 2002) and absorption by rich molecular species (Menten et al., 2008). Despite this, progress has been made in studying the source in the optical and near infrared (IR). Courbin et al. (1998, 2002) and Frye et al. (1999) used a deconvolution algorithm to create optical/near-IR images of the region, and found the counterparts to the radio sources, including highly reddened images of the lensing galaxies. IR spectroscopy allowed for the redshift of the quasar itself ($z = 2.507$) to be directly measured (Lidman et al., 1999).

However, even before the redshifts of PKS 1830+211 or its lensing galaxies were known, attempts were made to model the source as a lens (Subrahmanyan et al., 1990; Kochanek and Narayan, 1992; Nair et al., 1993). Since photons for the source and the image take different paths to reach Earth, it is expected that there will be a time delay between the photons which arrive from the different images. That is, the image will have time delayed "echo" flare which respect to the original NE source, with a constant time delay[1]. Furthermore, this time delay should be the same for all wavelengths, since gravitational macrolensing is an achromatic process. Because PKS 1830+211 as a blazar known to be highly variable at all wavelengths, this opens up the possibility that this time delay can be measured. Accurate modeling, combined with a measured time delay between the source and the image, and redshift measurements of PKS 1830+211 and the lensing galaxies, could be used to measure Hubble's constant[2], H_0. This has accounted for much of the interest in PKS 1830+211.

A time delay of $\Delta t = 26^{+4}_{-5}$ days was previously measured from the light curves of the two lensed images by Lovell et al. (1998) with ATCA. The authors used the values of the delay obtained, along with the model of Nair et al. (1993), to measure Hubble's constant to be $H_0 = 69^{+16}_{-9}$ km s^{-1} Mpc^{-1}, which is consistent with the most re-

1 The term "echo" is used somewhat inaccurately by Barnacka et al. (2011), because the source flare in the SW counter-image of PKS 1830+211 arrives us by refraction, not reflection.

2 We adopt a flat ΛCDM (concordance) cosmology with values given within 1σ of the WMAP results (Komatsu et al., 2009), namely $h = 0.71$, $\Omega_m = 0.27$ and $\Omega_\Lambda = 0.73$, where Hubble's constant $H_0 = 100h$ km s^{-1} Mpc^{-1}.

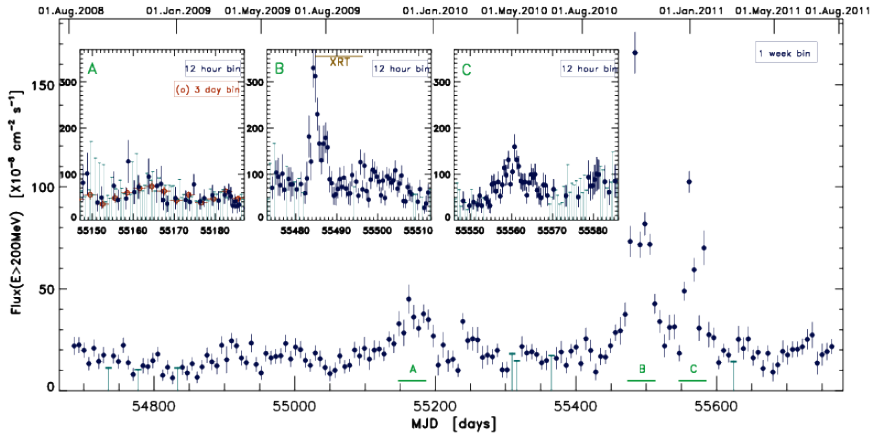

Figure 6.1 *Main panel*: 3-year (1085 days) LAT γ-ray light curve of PKS 1830−211 in weekly bins, from August 4 2008 to July 25 2011 (MJD 54682.65 to 55767.65,). *Left inset panel (A)*: light curve detailing the period around the slightly active phase of 2009 October in 12-hour (filled symbols) and 3-day (open symbols) bins. *Center and right inset panel (B and C)*: light curves detailing the period around the main outburst of October 2010 and the second double flare of 2010 December and 2011 January, in 12-hour bins. Vertical lines refer to 2-σ upper limits on the source flux. Upper limits have been computed for bins where $TS < 4$, $N_{pred} < 3$, or $\Delta F > F/2$.

cent high precision measurements (e.g., Komatsu et al., 2009). Using molecular absorption features, Wiklind and Combes (2001) find a time delay of 24^{+5}_{-4} days, consistent with the value 26^{+4}_{-5} days found by Lovell et al. (1998). More detailed modeling of the lensing system, using the time delay of $\Delta t \approx 25$ days find similar values of H_0 (e.g., Lehár et al., 2000; Witt et al., 2000). A different time delay of $\Delta t = 44 \pm 9$ days was measured from the radio light curves of the two lensed images by van Ommen et al. (1995) using the VLA. Lovell et al. (1998) attribute the difference between their measured time delay and the one found by van Ommen et al. (1995) as being caused by "not correctly accounting for the contribution of the Einstein ring flux density when calculating the magnification ratio". PKS 1830+211 is emerging as a compound and rather complicated macrolensing system making it not as useful for Hubble constant measurements as other simpler extragalactic gravitational lens.

In addition to being the brightest gravitationally lensed source and one of the brightest sources in the sky at centimeter wavelengths, PKS 1830+211 is also bright at hard X-rays and MeV energies. The X-ray spectra, as measured by *Chandra*, XMM-*Newton*, and INTEGRAL, are very hard ($\Gamma_X \sim 1$), and high absorbing column densities are found, accounting for a spectral break below ~ 4 keV (de Rosa et al., 2005; Bassani et al., 2006; Foschini et al., 2006; Zhang et al., 2008a,b).

No significant variability on both short or long timescale was observed in over 7 years of hard X-ray observations by INTEGRAL-IBIS (Zhang et al., 2008b). The source can also be found in the 58-month BAT catalog[3].

Recently, PKS 1830+211 was detected by *AGILE* (Striani et al., 2009; Donnarumma et al., 2010, 2011) and can be found in the first and second *Fermi* Large Area Telescope (LAT) source catalogs (1FGL J1833.6−2103 and 2FGL J1833.6−2104, respectively; Abdo et al., 2010c; Nolan et al., 2012). The 2FGL point source localization, found using the `pointlike` method (Burnett, 2007) was R.A.= 278.413°, Dec.= −21.075°, with the 68% error containment ellipse of semi-major and semi-minor axes $r_{65}^{max} = 1.09'$and $r_{65}^{min} = 1.05'$. The radio source PKS 1830+211 and the intervening galaxies are within the γ-ray error ellipse, as are a few nearby field galaxies; however, there is no source other than PKS 1830+211 with radio flux density $\gtrsim$ 10 mJy, making it highly likely to be the source of the γ-rays. Although the NE and SW images of PKS 1830+211 cannot be resolved in γ rays, the LAT continuously monitors this blazar, as it does the entire sky.

PKS 1830+211 showed a marked γ-ray Compton luminosity dominance in the EGRET era and was one of the few blazars to be detected by COMPTEL making it an MeV blazar. The broadband spectral energy distribution (SED) of PKS 1830+211 was modeled by de Rosa et al. (2005), assuming the broadband data were magnified by a factor of 10 by the lens. They found that the SED could be reproduced by a combination of synchrotron, synchrotron self-Compton (SSC), and external Compton (EC) scattering of primarily dust torus photons. Foschini et al. (2006) modeled this source without correcting the SED data for extinction or magnification, which are not well-known. The main difference with their modeling and that of de Rosa et al. (2005) is that Foschini et al. (2006), as well as Celotti and Ghisellini (2008) use the broad-line region (BLR) as their main seed photon source rather than a dust torus, and they obtain a higher magnetic field. Both fits result in reasonable parameters.

A large outburst from the γ-ray point source positionally consistent with PKS 1830+211 was observed by *Fermi* LAT on October 2010, peaking on October 14 and 15 (Ciprini, 2010). This triggered a rapid-response target of opportunity (ToO) observations by the *Swift* satellite thanks to an accepted Guest Investigator program[4]. *AGILE* reported a high state flux measure obtained from October 15 through 17 2010 (Donnarumma et al., 2010), that was investigated in Donnarumma et al. (2011). For the first time point source neutrino flux upper limits are obtained for PKS 1830+211 with the IceCube neutrino telescope (Abbasi et al., 2009).

3 http://heasarc.gsfc.nasa.gov/docs/swift/results/bat

4 *Swift* Cycle AO-6, program dedicated to very bright flares from *Fermi* LAT blazars (PI: L. Reyes)

In this Chapter, we explore the γ-ray spectral and temporal properties of PKS 1830+211 as observed by the *Fermi* LAT, with particular attention paid to this main outburst of October 2010 and the second brightest flaring period occurred in December 2010 through January 2011 (Section 6.2). In Section 6.3 the *Swift* observations and results from the ToO observing campaign are presented. In Section 6.4 we discuss the γ-ray variability properties and provide a critical assessment of the 4σ evidence of a 27.1-day time delay caused by macrolensing, as claimed in Barnacka et al. (2011). Their finding was based on a double power spectrum analysis applied to a 2-day bin light curve of the LAT flux truncated before the peak of the 2010 outburst, with lower energy threshold cut of 100 MeV, where the contribution and contamination of neighbor sources and the Galactic diffuse emission are important, and extracted with an aperture photometry method. Multifrequency *Fermi* and *Swift* SEDs of the object and spectral modeling are reported in Section 6.5, and conclusions are summarized in Section 6.6.

6.2 *fermi* LAT OBSERVATIONS

The *Fermi* analysis was performed with the standard LAT Science Tools software package (version v9r23p1) and was based on data collected in the period from August 4 2008 to July 25 2011 (from MJD 54682.65 to 55767.65, almost 36 months or 3 years). We first produced a LAT spectrum for PKS 1830+211 over this entire time interval, using the `P6_V3_DIFFUSE` IRFs, and selecting events of the "Diffuse" class in a circular ROI with 7° radius centered on the target position from the 1FGL catalog. The energy range 200 MeV - 100 GeV is used w.r.t. usual low-energy cut of 100 MeV to reduce the contamination of the Galactic plane diffuse emission.

The standard quality cuts were applied, namely events within zenith angle $> 105°$ and time intervals during which the spacecraft rocking angle was $> 52°$ were excluded (more details in § 3.4.1). The model of the region accounted for all neighboring sources and the diffuse emission together with the target source. The source PKS 1830+211 was fit with a power law model[5] with the γ-ray photon index (Γ_γ) left free in the fit.

The Galactic and the isotropic background models[6] were used with their normalizations left as free parameters. In addition, all γ-ray sources up to 10° around the target were included in the model. Among these the pulsar PSR J1809−2332 was modeled with an exponentially cutoff power law (Abdo et al., 2010l) in which the photon index at low energy, the cutoff energy and the normalization factor

5 The power-law spectrum between minimum and maximum energies (E_{min} and E_{max}) is described by: $dN/dE \propto E^{-\Gamma_\gamma}$ with γ-ray photon index Γ_γ.

6 gll_iem_v02.fit and isotropic_iem_v02.fit

were left free. All other sources were modeled using a power law spectrum. The normalization and the gamma photon index were left free for each point source within a 5° radius of PKS 1830−211.

Sources within 5° and 7° had just their normalizations free (using for each source the fixed photon index reported in the 1FGL catalog), while sources within 7° and 10° had all parameters fixed. The power-law fit to PKS 1830+211 over the entire period in the $0.2 - 100$ GeV energy range gave an integrated flux of $(20.43 \pm 0.44) \times 10^{-8}$ cm^{-2} s^{-1} and a steep γ-ray photon index of $\Gamma_\gamma = 2.55 \pm 0.02$.

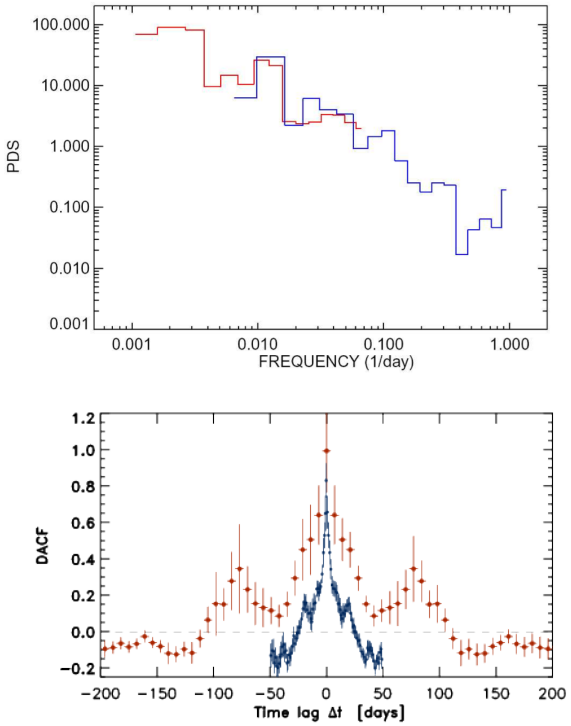

Figure 6.2 *Top panel*: Power density spectra, PDS, normalized to fractional variance per frequency unit f extracted for both the 3-year, weekly bin (red line, starting from the left, low frequency side), and the 150-day (MJD interval: 55471-55621), 12-hour bin (dark blue line, ending of the right, high frequency side) LAT flux light curves of PKS 1830−211. *Bottom panel*: Discrete autocorrelation function, DACF, for both the 3-year, weekly bin (bigger red points extended till to 200-day time lag) and the 150-day, 12-hour bin (blue tiny points extended to 50-day time lag) LAT flux light curves of PKS 1830−211.

Afterwards we produced a LAT light curve for PKS 1830+211 in the 200 MeV - 100 GeV energy range. We did this by setting the photon index for this source in the individual time bins equal to the value obtained for the spectral fit over the entire range, $\Gamma_\gamma = 2.55$. Figure 6.1 shows the weekly (7-day bins) γ-ray light curve from August 4, 2008 to July 25, 2011. In the inset panels 12-hour bin light curve

plots (each of 40 days length) are produced around three outburst epochs ("A", "B", "C" intervals highlighted in the plot). The 12-hour bin light curve of the larger panel was produced for the entire time interval going from the main October 2010 outburst (represented in the inset panel "B") to the second highest flare of December 2010 - January 2011 (represented in the inset panel "C"), namely a 150-day long time series from October 2, 2010 (MJD 55471) to March 1, 2011 (MJD 55621). This higher resolution light curve is used for the variability temporal analysis (see Section 6.4 and Figures 6.2 and 6.6). For both the 3 year long, weekly binned and 150-day long, 12-hour binned, light curve upper limits have been computed for bins where $TS < 4$, $N_{pred} < 3$, or $\Delta F_\gamma > F_\gamma/2$. We explore the γ-ray variability properties of PKS 1830+211 further in Section 6.4.

6.3 *swift* OBSERVATIONS: DATA ANALYSIS AND RESULTS

The *Swift* satellite performed 10 ToO observations on PKS 1830+211 between October 15 and 27, 2010 for a GI program[2] triggered by the high γ-ray activity of the source and the main γ-ray outburst peaking on October 14, 2010 and 15. The *Swift* observations were performed from MJD 55484.685 to 55496.380 with all three on-board instruments: XRT, UVOT, BAT (see § 4.1.3).

6.3.1 Swift-*BAT observations*

The hard X-ray flux of this source is below the sensitivity of the BAT instrument for the short exposures of the *Swift* ToO observations performed on October 2010. The source was not detected between October 14 and 18, 2010 (net exposure of about 200 ks) by INTEGRAL (Donnarumma et al., 2011). By contrast, PKS 1830+211 is detected in the BAT 58-month catalog, generated from the all-sky survey from November 2004 to August 2009. Therefore, we used the 8-channel spectrum available at the HEASARC[7]. The 14–195 keV spectrum is well described by a power law with photon index of 1.50±0.13 (χ^2_{red}/d.o.f. = 0.89/6). The resulting unabsorbed 14-195 keV flux is (9.0±0.8)×10^{-11} erg cm^{-2} s^{-1}.

6.3.2 Swift-*XRT observations*

The XRT data were processed with standard procedures (more details in § 4.1.3). The source count rate was low during all the observations (count rate < 0.5 counts s^{-1}) and pile-up correction was not required.

Previous soft X-ray observations of PKS 1830+211 revealed a hard spectrum ($\Gamma_X \sim 1$) and absorption in excess to the Galactic column

7 http://heasarc.gsfc.nasa.gov/docs/swift/results/bat

due to the lensing galaxy at $z = 0.886$ (Mathur and Nair, 1997; Oshima et al., 2001; de Rosa et al., 2005). In particular, de Rosa et al. (2005) derived a value of column density for this extra absorption of $1.94^{+0.28}_{-0.25} \times 10^{22}$ cm^{-2} from a broad band spectra with *Chandra* and INTEGRAL data. *XMM-Newton* observations of PKS 1830+211 were modeled by Foschini et al. (2006) with a broken power law model, with the photon index changing from ∼1.0 to ∼1.3 at about 3.5 keV. The joint fit of *XMM*/INTEGRAL data performed by Zhang et al. (2008b) confirmed that the broken power law is the best model fit, with column density, photon indexes and energy break parameters very similar to those found in the previously-cited works. A fit with a thermal plasma model at the redshift of PKS 1830+211 (with solar abundances and temperature $kT = 0.39 \pm 0.06$ keV) produced by a possible warm absorber, as suggested by Fabian et al. (2001b), was also used by Foschini et al. (2006) to fit *XMM-Newton* data. We fit the individual XRT spectra of October 2010 with an absorbed power law, with a neutral hydrogen column fixed to its Galactic value (2.05×10^{21} cm^{-2}; Kalberla et al., 2005) and an extra absorption fixed to the value found de Rosa et al. (2005). The resulting unabsorbed 0.3–10 keV fluxes and the photon indexes for each observation are reported in Figure 6.3. The unabsorbed flux derived from XRT observations lies between 1.3 and 1.7 $\times$ 10^{-11} erg cm^{-2} s^{-1}. To investigate in more detail the X-ray spectral properties of the source we accumulated all the events collected during this campaign for extracting an average spectrum with higher statistics. As a first step we fit the average spectrum with the same model used for the single observations obtaining, as with the single observations, an acceptable fit. Leaving the value of the column density of the extragalactic absorber free to vary, a comparable fit is recovered, with larger uncertainties on the parameters. We found instead an improvement in the fit substituting the simple power law with a broken power law model, significant at the 99.9% confidence level according to the F-test. The parameters are in good agreement with the values obtained in the previous works on the source, except for the higher value of the photon index above the break, but it could be due to the lack of hard X-ray data to constrain the model at higher energies. The 0.3–10 keV flux detected by XRT in October 2010 is only slightly higher than those observed in the past XMM-*Newton* and *Chandra* observations of the source, indicating no significant activity in soft X-ray during the γ-ray flare detected by LAT. Results of the fit of the average XRT spectrum are reported in Table 6.1.

A joint fit to the XRT+BAT spectrum with an absorbed broken power law and a cross-correlation factor between XRT and BAT of $1.30^{+0.36}_{-0.28}$ led to a further slight improvement (χ^2_{red}/d.o.f. = 1.09/133), with photon indexes Γ_{X1} = 1.05±0.10 and Γ_{X2} = 1.53±0.11 below and

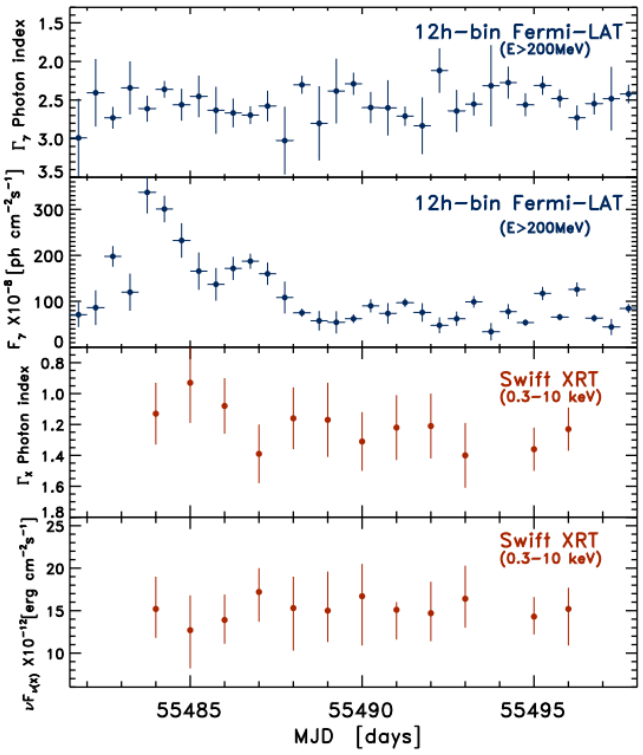

Figure 6.3 Multi-panel plot with simultaneous *Fermi* LAT and *Swift* XRT flux and photon index light curves.

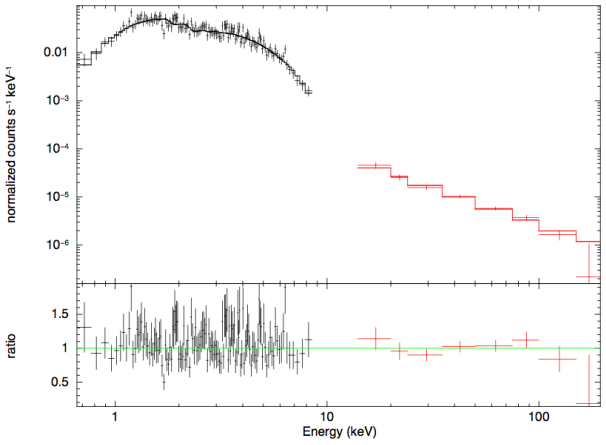

Figure 6.4 Joined *Swift* XRT spectrum from the accumulated data obtained during the multiwavelength campaign from October 15 to 24 2010, and *Swift* BAT spectrum from all the accumulated archival data (58-month observations, 2004 November – 2009 August).

above a break energy of $3.59^{+0.83}_{-0.51}$ keV. The result of this joint fit can be found in Figure 6.4.

Table 6.1 Summary of the *Swift*/XRT analysis of PKS 1830−211.

Power law Model						
Exp[a]	N_H^b	Γ_{X1}	E_{break}	Γ_{X2}	Flux (0.3–10)[c]	χ^2_{red}/d.o.f.
20.3	1.94 (fix)	1.20±0.06	–	–	1.64 ± 0.11	1.19/129
20.3	$2.09^{+0.54}_{-0.36}$	$1.23^{+0.11}_{-0.08}$	–	–	$1.65^{+0.27}_{-0.18}$	1.19/128
Broken Power law Model						
Exp[a]	N_H^b	Γ_{X1}	E_{break}	Γ_{X2}	Flux (0.3–10)c	χ^2_{red}/d.o.f.
20.3	1.94 (fix)	1.05±0.10	$3.65^{+1.35}_{-0.60}$	$1.56^{+0.39}_{-0.20}$	$1.53^{+0.14}_{-0.11}$	1.13/127

a Net exposure in kiloseconds adding the single XRT observations performed between October 15 and 24, 2010.

b Column density of the extragalactic absorber at redshift z=0.886 in units of 10^{22} cm^{-2}. A Galactic absorption of 2.05×10^{21} cm^{-2} (Kalberla et al., 2005) is added.

c Unabsorbed flux in the $0.3 - 10$ keV energy band.

6.3.3 Swift-*UVOT Observations*

During the *Swift* pointings, the UVOT (Poole et al., 2008) instrument observed PKS 1830+211 in the v, b, u, and $uvw1$, $uvm2$ and $uvw2$ photometric bands. We co-added all of the individual images collected in the ten observations to obtain a single image for each filter. Nevertheless, due to the high extinction in the direction of PKS 1830+211, the source was not detected above 3-σ in any of the UVOT bands, so we computed a 3-σ flux upper limit (lower limit in magnitude) for each filter: $v > 18.0$, $b > 19.5$, $u > 19.3$, $uvw1 > 16.9$, $uvm2 > 20.0$, and $uvw2 > 21.0$.

6.4 GAMMA-RAY TIME VARIABILITY PROPERTIES

The bright, continuous γ-ray emission from PKS 1830+211 during the first 3 years of *Fermi* operation, both during quiescent and flaring episodes, allowed for firm LAT detections on weekly (and often shorter) timescales, as seen in Figure 6.1 reporting the likelihood flux ($E > 200$ MeV) light curve. In part this is in contrast to the behavior of other FSRQs, which are not detected for relatively long periods of time and exhibit longer epoch of high state and flaring emission, such as PKS 1510−08 (Abdo et al., 2010b), 4C +21.35 (PKS 1222+216, Tanaka et al., 2011) and recently 3C 454.3.

A light curve with temporal resolution of 12-hour bins was extracted during the brightest and most active epochs ("A", "B" and "C" inset panels of Fig. 6.1, and top panel of Fig. 6.6). The "A" interval is centered about the epoch of the first active event seen by the LAT, near the end of 2009. This slow brighter phase took $\sim$ 3 weeks to reach its peak, followed by a $\sim$ 6 week decay, as seen in the weekly light curve (Figure 6.1). In the 12-hour binned light curve,

most points are upper limits. We also computed a light curve around this flare in 3-day bins. The flaring behavior is not obvious in this light curve, even if the higher activity state is evident in the weekly bin light curve. The announcement of a detection by AGILE on October 12 and 13, 2009 (MJD 55116-55117, Striani et al., 2009) at $E > 100$ MeV energy band, occurred some weeks before the "A" phase.

To explore the behavior of PKS 1830+211 during the main outburst (contained in the "B" epoch) and the second brightest flaring period (contained in "C" epoch) in greater detail, we performed power-law fits to the source in 12-hour bins, with both the flux and photon indexes (Γ_γ) left as free parameters (while to produce the light curves in Figure 6.1 Γ_γ was fixed). Note that 12 hours corresponds to ~ 8 *Fermi* orbits, so that exposures from bin to bin are roughly the same. The results can be found in Figure 6.5, where we searched possible evolutionary trends of the γ-ray spectral photon index as a function of the flux level.

The top of Figure 6.5 shows the two largest peaks of the main and structured outburst of October 2010. This is characterized by a rapid increase of a factor of ~ 2.6 in flux in 12 hours between October 14 and 15, 2010 (MJD 55483 and 55484) peak of $F(> 200 \text{ MeV}) = (330 \pm 42) \times 10^{-8}$ cm^{-2} s^{-1}in ~ 12 hours, yet taking ~ 48 hours to fall, resulting in an asymmetric temporal shape. The total peak lasts ~ 2.5 days, and seems to be followed by another weaker peak also lasting ~ 2.5 days. Both peaks do not show significant rotation in the Γ_γ-flux hysteresis diagram, because of the statistically constant photon index and relatively large uncertainties on flux and Γ_γ with respect to the variations.

The hysteresis diagram for flare "C" in Figure 6.1, which occurred between about December 25, 2010 and January 6, 2011 (MJD 55555 - 55567) is seen in the bottom of Figure 6.5. This flare displays a temporal structure characterized by two peaks of about 2.5 days duration each. The first peak shows hints of a plateau while the second peak of approximately 2.5-day duration, reaches a flux value of $(159 \pm 27) \times 10^{-8}$ cm^{-2} s^{-1}, roughly half of the peak flux of the "B" flare. During the second 2.5 days peak, the flare softens significantly (bins 6, 7, and 8 in the bottom of Figure 6.1) to $\Gamma_\gamma \sim 2.8$, before turning to its typical spectrum of $\Gamma_\gamma \sim 2.4$ during the decay.

Two PDS normalized to fractional variance per unit frequency ($f = 1/t$) (rms^2 I^{-2} Day^{-1}), are shown in Figure 6.2. One is calculated from the weekly light curve over 3 years, and one from the shorter 12-hour binned time series extracted for 150 days between October 2, 2010 (MJD 55471) and March 1, 2011 (MJD 55621) (light curve in Figure 6.6, top panel, and zoomed portions in inset panels of Fig. 6.1). In agreement with Abdo et al. (2009a), we conservatively choose to consider upper limits as values close to zero obtaining the two goals of still evenly sampling the light curve and avoiding the bias caused

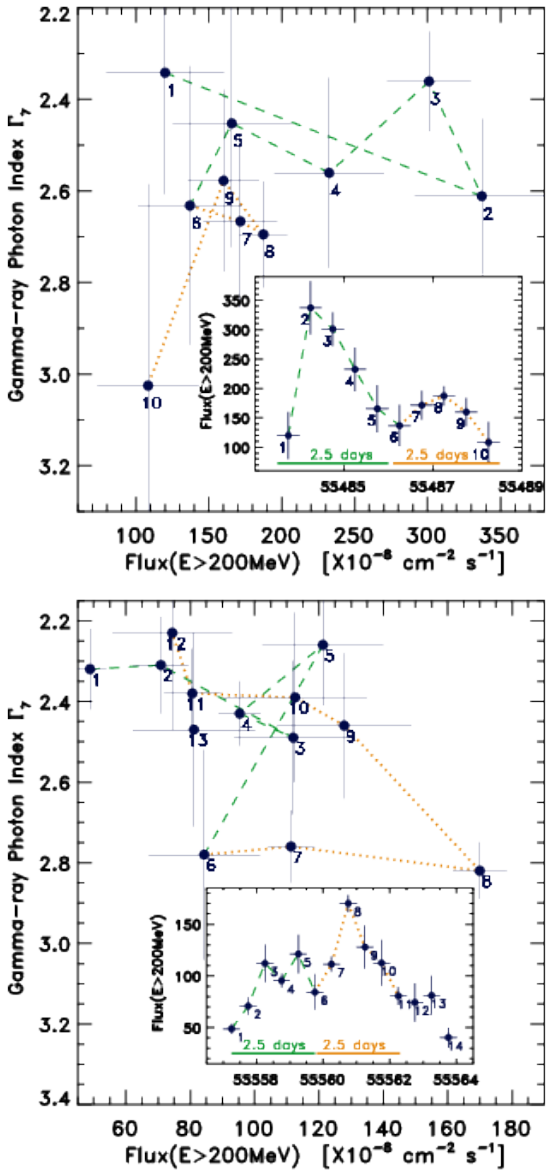

Figure 6.5 Evolution of the γ-ray photon index of PKS 1830−211 as a function of the γ-ray flux resolved by *Fermi* LAT in 12-hour time bins during the peak of the main outburst phase of October 2010 (top panel) and during the peak of the third flare event of December 2010 - January 2011 (bottom panel). These peaks are contained in the "B" and "C" panels of Figure 6.1 respectively but, in this case, the photon index was left free in the `gtlike` fit analysis. Bars represent 1σ errors.

by introducing gaps. The white noise level was estimated from the rms of the flux errors and was subtracted for each PDS.

Both PDS in Figure 6.2 are in good agreement with each other, meaning that the fractional variability and its time scale distribution during the more active phases ("B" and "C" epochs) are the same as during the longer, fainter, and less variable intervals between the flaring events. The merged PDS is fit with a simple $1/f^{\alpha}$ power law,

with a slope $\alpha = 1.2 \pm 0.1$, while the low-frequency PDS is fit with $\alpha = 1.0 \pm 0.16$, and the high frequency one with $\alpha = 1.25 \pm 0.15$. This implies that the variability is closer to a "flickering" (red noise) than to "Brownian" (brown or shot noise) behavior.

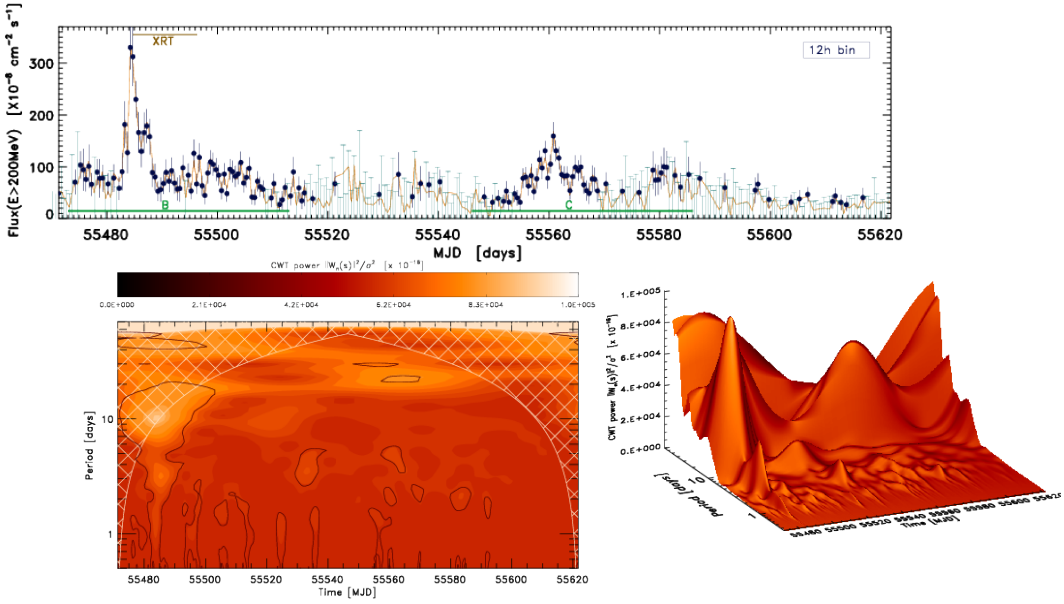

Figure 6.6 *Top panel*: the entire 150-day (MJD interval: 55471-55621) flux signal light curve in 12-hour bins of PKS 1830−211 from 2010, October 2 to 2011, March 1 containing the "B" and "C" epochs respectively (detailed in Fig.6.1), and containing the main outburst and the second largest flare. *Bottom panels*: plane contour plot of the continuous wavelet transform power density spectrum (2D PDS from CWT) for this time series obtained using a Morlet, complex valued, mother function. Filled color contour plot is the 2D energy density function of the CWT scalogram, Thick black line contours represents the 90% confidence levels of true signal features against white and red noise backgrounds, while cross-hatched regions represent the "cone of influence", where spurious edge effects caused by finite time-series edges become important. The figure on the right is a 3D pictorial version of the same plot.

The 150-day and 12-hour bin light curve (the top of Fig. 6.6) was also analyzed using a Continuous Wavelet Transform (CWT) analysis, aiming to highlight localized signal power features of variability. By decomposing the light curve into time-frequency Fourier spaces, we are able to determine both the dominant modes of variability, as with the PDS, as well as how those modes vary in time, producing a diffuse and continuous two-dimensional (2D) time-frequency (or time-period) image plot representing the wavelet 2D power spectrum ("the scalogram", Fig. 6.6, bottom panel). In such a filled color contour plot we report the 2D energy density function of the scalogram, specifi-

cally the normalized modulus of the CWT ($\|W_n(s)\|^2/\sigma^2$, where the normalization $1/\sigma^2$ gives a measure of the power relative to white noise), computed using a Morlet mother waveform. This complex valued function composed of a plane wave modulated by a Gaussian function, provides the best tradeoff between localization over the time series and the period/frequency resolution. Thick black line contours represents the 90% confidence levels of true signal features against white and red noise backgrounds, while cross-hatched regions represent the "cone of influence", where spurious edge effects caused by finite time-series edges become important.

In Figure 6.6 most of the CWT power not influenced by edge effects is concentrated within the period scales (y-axis) ranging from 8 to 30 days, even if there is appreciable power at longer periods (e.g. at 40-50 days) but these falling in the cone of influence. For period timescales below 2 days (y-axis) there are not localize peak characterized by strong power (high intensity level colors of contour plot).

The main outburst of October 2010 is well-decomposed and resolved in time and frequency spaces with the bulk of the power released between about MJD 55475 and 55495 (October 6 - 26, 2010) peaking at MJD 55484 (October 15, 2010), in agreement with the light curve described at the beginning of this section. The corresponding frequency-space period is 10 days, which can indicate the extension and characteristic timescale of the main outburst event. This can be approximatively associated with the total duration of the main outburst "B". It is also characterized by a resolved frequency space component of 3 days at MJD 55486 (October 17) in agreement with the 2.5 peaks previously mentioned (Fig. 6.5, top panel).

This timescale still appears significant but drifted to longer values of about 3.5 days and 4.5 days respectively during the events at around MJD 55535 (December 5, 2010) and MJD 55563 (January 2, 2011 i.e. the flare epoch "C"). This second brightest flare is identified by a significant power peak with characteristic timescale of about 21 days, between about MJD 55560 and 55565 (December 30, 2010 and January 4, 2011) in agreement with the previous description and Figures 6.1 and 6.5 (bottom panel). Summarizing between the main outburst "B" and the second brightest flare "C", we observed with the LAT a slight shift from a characteristic timescale near 10 days to a timescale near 20 days, and this suggests the later flare has twice the duration of the first flare, yet is approximately half as bright in emitted γ-ray power. Both these timescales are considered characteristic of the coherent and separated, even if structured, outburst events of October 2010 and December 2010 - January 2011, and do not represent any evidence for a detection of signal of delayed flaring event following one of these two outburst. Such supposed delayed γ-ray flares would appear as independent and relatively strong power peaks in the CWT scalogram separated by about 25 days, in x-axis, from the

two outbursts, but there is no significant (black line contours) separate intense peak (color contour peaks) in the plot at about 25 days right from the two major flare events.

6.4.1 *Lensing time delay*

In general, minor variability on timescales of a few weeks and months can be seen in the 3-year LAT weekly light curve obtained with likelihood fit analysis in each temporal bin, without any significant signature of a time delayed flare induced by the image of the PKS 1830+211 lens. Based on the time delay of $\Delta t = 26^{+4}_{-5}$ days measured by Lovell et al. (1998) and 24^{+5}_{-4} days measured by Wiklind and Combes (2001), the main outburst beginning between October 14 and 15, 2010 (MJD 55483-55484), should have a delayed lensed event occurring within the time interval MJD 55503 - 55514 (November 3 - 14, 2010). If the delay measurement of 44 ± 9 days (van Ommen et al., 1995) is correct, this would put the γ-ray flare from the lens image starting around November 27, 2010 (MJD 55527 ± 9).

The magnification factor μ is the ratio of the flux of the lens image to the flux of the unlensed source, and is equal to the ratio of the solid angles of the image, and the unlensed source $\mu = \Delta\Omega/\Delta\omega_0$. In the radio band the magnification ratio between the flux level of the original and the connected delayed event from the image is about 1.5, as evaluated from the full radio dataset of Lovell et al. (1998), but the ratio may not be constant, varying from values between about 1.0 to 1.8 (Wiklind and Combes, 1998). *Fermi* LAT monitoring detected no hints of a delayed flare in following the "B" and "C" γ-ray flare epochs, indicating that the delayed flare does not exist or that the magnification ratio in γ rays does not match that observed in the radio bands.

Barnacka et al. (2011) claimed a detection of a 27.1 ± 0.6 days time delay signal in the LAT light curve of PKS 1830+211, using a 2-day bin flux light curve with $E > 100$MeV obtained with simple "aperture photometry" over count maps from August 4, 2008 to October 13, 2010 (i.e., one day before the record peak flux detected on October 14 and 15, see Figure 6.1). We stress that LAT flux light curves created through aperture photometry are not rigorous flux measurements, for several reasons. In order to extract accurate light curves of PKS 1830+211 we used the same `P6_V3_DIFFUSE` IRFs used in Barnacka et al. (2011), cutting the events at $E > 200$ MeV for a better PSF, and using the likelihood method, that allows to obtain a greater sensitivity, more accurate flux measurements, less spurious fluctuations and less timeseries noise, and to correctly take into account backgrounds. The position of PKS 1830+211 is remarkably close to the southern Galactic Bulge where the γ-ray diffuse emission and its modeling are particularly important, and is not far from a bright pul-

sar that needs of a dedicated modeling in the likelihood. The best fit model parameters are therefore calculated in every time bin interval.

An oscillatory pattern was found in the power spectrum of their photometry light curve, as well as autocorrelation function peaks. No significant evidence for a clear following-up γ-ray flare from the lens image was found in our data, in particular from the "B" and "C" outbursts. DACF (Figure 6.2, lower panel), applied to the 150-day long 12-h bin light curve gives a relative peak placed at about 20 days. When applied to the 3-year weekly bin light curve the DACF shows a relative peak placed at about 11-12 weeks. The PDS shows a possible break at about 53 days (0.019 days^{-1}; Figure 6.2, upper panel), although it could easily be noise. In addition the 27-day characteristic timescales claimed in Barnacka et al. (2011) is also the first harmonic of the 54-day timescale corresponding to the precession period of the *Fermi* spacecraft orbit. This precession is consistent with the addition of the systematic errors in `Pass 6` IRFs data caused by the variation in effective area due to charged particles during orbital precession, a known effect that is caused by a change in exposure over the orbital precession period. The evidence for a lensing-induced following-up flare in this blazar has not been confirmed in our work, since an image-flare "B" would clearly be detectable. We discuss some possible explanations in Section 6.6.1.

6.5 BROADBAND SPECTRAL ENERGY DISTRIBUTION

The SED of PKS 1830+211 around the October 2010 outburst (epoch "B") is shown in Figure 6.7. The data have been de-magnified by a factor of 10, following Nair et al. (1993) and Mathur and Nair (1997).

As an FSRQ, it is unlikely that a pure synchrotron/SSC can explain the entire SED of PKS 1830+211; as discussed in Section 2.3 and as we have seen also in the case of PKS 1510−089, almost always an EC component is needed for this class of objects. This was confirmed by our failed attempts to find a reasonable fit with a SSC model (a similar result was found by de Rosa et al., 2005). The high activity observed in γ-rays has no significant counterpart in soft X rays, but that data can be described by a single EC component, suggesting that the X-ray photons are originated in the low-energy tail of the same electron distribution. To fit the simultaneous October 2010 SED with an EC model, we assume that the emitting region is at a considerable distance from the black hole, outside the BLR, and that the primary seed photon source is from a dust torus emitting blackbody radiation in the infrared. There is some debate about the location of the γ-ray emitting region, although a large distance from the black hole seems justified for FSRQs by detailed campaigns by the *Fermi* and radio observatories (e.g., Marscher and Jorstad, 2010). The dust torus was assumed to be a one-dimensional annulus with radius r_{dust} centered

on the black hole and aligned perpendicular to the jet, and emitting blackbody radiation with temperature T_{dust} and luminosity L_{dust}. Our best fit is shown as the blue curve in Figure 6.7, and the parameters of the fit are described in Table 6.2. The model and parameters are described in detail by Dermer et al. (2009). The emitting region size scale chosen is consistent with a variability time scale of 12 hours, observed for the main outburst ("B").

We found that an electron distribution with two spectral breaks (three power laws) was necessary to reproduce the SED. A very hard p_1 was necessary to fit the hard XRT spectrum. The other electron indexes, p_2 and p_3, were chosen to be the same as the fit by de Rosa et al. (2005). Due to the simultaneous non-detection at UV/optical wavelengths, our model is not strongly constrained. Notice that the Compton-scattered peak is $\sim 10^3$ times larger than the synchrotron peak, and that this is really a lower limit on the Compton-dominance, due to the lack of an optical detection. For the outburst "B" SED fit, the total jet power, $P_{j,B} + P_{j,e} \approx 3.3 \times 10^{45}$ erg s^{-1} is below the Eddington luminosity for a 10^9 $M_\odot$ black hole ($L_{Edd} \approx 1.3 \times 10^{47}$ erg s^{-1}), as one would expect, and the magnetic field and nonthermal electrons are within approximately a factor of 4 from equipartition. Again, as with the fit by de Rosa et al. (2005), this fit is also able to explain the X-ray and γ-ray emission with a single EC component. The fit is also similar to the one by Foschini et al. (2006).

We also built a "quiescent state" SED of PKS 1830+211 from non-simultaneous data. This is made up of the 58-month BAT spectrum, the *Planck* Early Release Compact Source Catalogue (ERCSC) spectrum, combined with the LAT spectrum from the first 26 months of *Fermi* operation. This LAT spectrum excludes the prominent flaring activity in October 2010 and December 2010 / January 2011, and so should be a fairly good representation of the source in the low state. We also included archival data from radio/mm, Gemini-N, *HST*, *Chandra* (2001 January), *INTEGRAL*-IBIS (2003), COMPTEL, and EGRET (de Rosa et al., 2005; Foschini et al., 2006; Zhang et al., 2008b). We found that we could reproduce the quiescent state SED by varying only two parameters from the high state SED, namely the highest electron index (p_3) and the cutoff of the electron distribution (γ_{max}). This fit provides a decent fit to the archival data, except for the COMPTEL bowtie. However, since these are non-simultaneous, this should not be considered a major deficiency in the modeling.

Finally, the model fit from de Rosa et al. (2005) is shown for comparison. The model is quite similar to ours, although it provides a bit better fit to the archival optical and COMPTEL data.

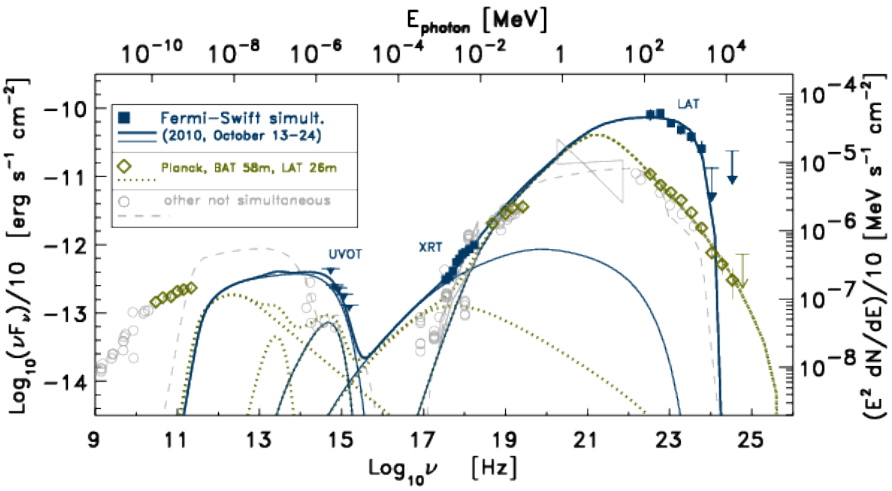

Figure 6.7 The SED of PKS 1830−211. This includes simultaneous *Fermi* LAT and *Swift* XRT and UVOT (upper limits only) data, averaged over the October 13-24 2010 campaign and corresponding to the γ-ray outburst (all plotted as blue/dark square symbols). Also plotted are a non-simultaneous 26-month (August 4 2008 - October 4 2010) LAT spectrum, the BAT 58-month spectrum, and the *Planck* ERCSC spectrum (all plotted as gree/dark open diamond symbols). Archival data from radio/mm, Gemini-N, HST, *Chandra* (2001 January), INTEGRAL-IBIS (2003), COMPTEL (bowtie), and EGRET are taken from literature (de Rosa et al., 2005; Foschini et al., 2006; Zhang et al., 2008b) and are plotted as light grey open circles with a light gray dashed-line model. All data are corrected for a factor of 10 magnification (although note that the magnification may not be the same for all frequencies; see section 6.6.1). Also plotted are fits with a synchrotron/SSC/EC model to the flaring state (blue/dark solid curves) and quiet state (green/dark dotted curves). The dust and disk emission are the same for both models. *Planck* ERCSC, *Swift* BAT and *Fermi* LAT archival data are taken into account as representative of the source in a low activity state with little variability. These data can be fitted with model parameters similar to the flaring model, only changing two parameters: $p_3 = 4$, and $\gamma_{max} = 10^5$. In this fit, the archival optical emission comes mainly from the accretion disk, so that this fit is also poorly constrained.

6.6 DISCUSSION AND CONCLUSIONS

In this Chapter we have presented detailed *Fermi* and *Swift* observations of the gravitationally-lensed and MeV-peaked FSRQ PKS 1830+211. The first hints for an increased γ-ray activity of this source was detected in November 2009, followed by larger and evident flaring episodes in mid-October 2010 and at the period between December 2010 and

Table 6.2 Model fit parameters

Parameter	Symbol	Oct 13–24 2010 fit	Quiescent fit
Bulk Lorentz Factor	Γ	20	20
Doppler Factor	δ_D	20	20
Magnetic Field	B	1 G	1 G
Variability Timescale	t_v	12 hours	12 hours
Comoving Blob radius	R'_b	1×10^{18} cm	1×10^{18} cm
Jet Height	r	10^{19} cm	10^{19} cm
Low-Energy Electron Spectral Index	p_1	1.0	1.0
Medium-Energy Electron Spectral Index	p_2	1.8	1.8
High-Energy Electron Spectral Index	p_3	2.8	4.0
Minimum Electron Lorentz Factor	γ'_{min}	10	10
First Break Electron Lorentz Factor	γ'_{brk1}	30	30
Second Break Electron Lorentz Factor	γ'_{brk2}	300	300
Maximum Electron Lorentz Factor	γ'_{max}	6×10^3	1×10^5
Dust torus temperature	T_{dust}	1.1×10^3 K	1.1×10^3 K
Dust torus radius	r_{dust}	2×10^{18} cm	2×10^{18} cm
Dust torus luminosity	L_{dust}	3.1×10^{45} erg s^{-1}	3.1×10^{45} erg s^{-1}
Jet Power in Magnetic Field	$L_{j,B}$	1.6×10^{44} erg s^{-1}	1.6×10^{44} erg s^{-1}
Jet Power in Electrons	$L_{j,e}$	3.7×10^{45} erg s^{-1}	3.0×10^{45} erg s^{-1}
Total Jet Power	$L_{j,tot}$	3.8×10^{45} erg s^{-1}	3.1×10^{45} erg s^{-1}

January 2011. PKS 1830+211 stands out for a number of reasons, besides the fact that it is a macrolensed system characterized by so called strong-type gravitational lensing (Bisnovatyi-Kogan and Tsupko, 2012), which we discuss further in Section 6.6.1).

PKS 1830+211 is the third most distant object detected in flaring activity so far by *Fermi* LAT behind TXS 0536+145 (Orienti and D'Ammando, 2012) and B3 1343+451 (Buehler, 2009; Ojha et al., 2011). The apparent isotropic γ-ray luminosity ($E > 100$ MeV) of PKS 1830+211 over the first 31 months of *Fermi* operation is $\sim 1.1 \times 10^{49}$ erg s^{-1}, comparable to the brightest high redshift ($z \gtrsim 2$) blazars in the First LAT AGN Catalog (Abdo et al., 2010k, 1LAC) that were studied in detail in Ghisellini et al. (2011a).

The γ-ray flux from this source was at its peak on October 14-15, 2010, reaching a flux of $F(E > 200 \text{ MeV}) \approx 300 \times 10^{-8}$ ph cm^{-2} s^{-1}, as seen in the 12-hour binned light curve. This is a factor of 17 greater than the average 3-year flux. The corresponding apparent isotropic γ-ray luminosity of 1.9×10^{50} erg s^{-1} is greater than that observed from PKS 1622−297 during the 1995 flare (Mattox et al., 1997), and from 3C 454.3 in December 2009 (Ackermann et al., 2010a), and roughly comparable to the November 2010 outburst from this source (Abdo et al., 2011). For this bright flare, if one uses the variability timescale in the proper frame of the source $\Delta t \approx 12 \text{ hours}/(1+z) \approx 1.3 \times 10^4$

s, and a de-magnified luminosity of $L_\gamma \approx 2 \times 10^{49}$ erg s^{-1}, one calculates $L_\gamma/\Delta t \approx 1.6 \times 10^{45}$ erg s^{-2}. This value is a bit below the record-holder for AGN, from the November 2010 burst from 3C 454.3 (Abdo et al., 2011), but it still exceeds the Elliot and Shapiro (1974) limit of $L_{Edd}/(R_S/c) \approx 1.3 \times 10^{43}$ erg s^{-2} (where R_S is the Schwarzschild radius), and the limit which includes Klein-Nishina effects, 1.6×10^{44} erg s^{-2} (Liang and Liu, 2003).

No correlated variability for this γ-ray flare was detected in X-rays by *Swift*-XRT, which is somewhat typical for FSRQs (e.g., Marscher and Jorstad, 2010; Abdo et al., 2010a; Hayashida et al., 2012), although not universal (e.g., Raiteri et al., 2011). Orphan γ-ray flaring activity in PKS 1830+211 was already found in AGILE data (Donnarumma et al., 2011). This fact, in addition to the lack of detection in optical/UV by *Swift*/UVOT and hard X-ray by INTEGRAL/IBIS during the October 2010 γ-ray flare discovered by *Fermi*, indicates the mechanism producing the γ-ray flare only marginally influences the X-ray part of the spectrum. There may be correlated variability between γ-ray and optical emission, also typical for FSRQs (e.g., Marscher and Jorstad, 2010; Raiteri et al., 2011), but without any optical detections, it is impossible to tell. The lack of X-ray and γ-ray correlation can support the lack of evident signals of macrolensing at high energies.

The hard and soft X-rays are thought to be a combination of the contributions from SSC and EC, and the soft X-ray roll-off is explained in terms of a natural interplay between SSC and EC components (Foschini et al., 2006). The extremely hard X-ray photon indexes have been found for a number of other blazars (Sikora et al., 2009), and seem to indicate very hard electron distributions at low energies.

The main outburst of October 2010 was found asymmetric with a fast rise of a factor about 2.6 in flux in 12 hours, as observed in a few γ-ray blazar flares in the past (for example in PKS 1502+106, Abdo et al., 2010h), while the majority of them were observed to be symmetric (Abdo et al., 2009a). The asymmetry of the main outburst might imply particle acceleration and cooling times that are greater than the light crossing time, i.e., $t_{\rm inj}, t_{\rm cool} > R/c$ (in the jet comoving frame). In addition this asymmetric (fast rise, slower decay) peak shape could also be evidence for a contribution by Comptonization of photons produced outside the jet. Gamma-ray flares produced by short-lasting energetic electron injections and at larger jet opening angles are predicted to be more asymmetric showing much faster increase than decay, the latter determined by the light travel time effects (Sikora et al., 2001). In jet-cylindrical geometry models, characterized by SSC processes, are also expected to provide only symmetric flares (Sokolov and Marscher, 2005).

A 2.5-day flux peak timescale appears to characterize the main outburst of October 2010 and the second brightest flare of January 2011, as also suggested by CWT analysis. The fractional variability and its

timescale distribution during the more active phases are found to be similar to the the ones shown in the longer, fainter and less variable intervals between the flare events, and the PDS can be described by a $1/f^{1.2}$ power law. This means a γ-ray flickering, red-noise, variability. The occurrence of a specific variation is inversely proportional to its strength, with more weight towards higher frequencies (short timescales) rather than low frequencies, as often founds for γ-ray BL Lac objects (Abdo et al., 2009a). The *Fermi* routine detections on weekly and even shorter timescales of PKS 1830+211 supports this similarity. On the other hand the curved or broken γ-ray spectrum is in agreement with other LAT spectra observed for typical FSRQs (Abdo et al., 2010i,m).

From the "B" main outburst of October 2010 to the "C" second brightest flare of December 2010 - January 2011 there was a shift from a characteristic timescale qualifying the outburst from 10 days to about 20 days for the second flare event, therefore doubling the emission region sizes, while halving the emitted γ-ray flux intensity. The steep γ-ray ray spectrum of MeV-peaked sources like PKS 1830+211 can contribute to the cosmic X-ray background and the extragalactic γ-ray background, depending by luminosity functions as well as SED models. Simultaneous observations by the hard X-ray observatory NuSTAR and the LAT could help to infer the position of the high-energy peak. Our 3-year LAT data analysis points to temporal behavior and flaring activity attributed to intrinsic variability within the source, rather than to events caused by gravitational macrolensing.

6.6.1 *Why has no time delay been observed in gamma rays?*

The intense flaring from PKS 1830+211, the brightest γ-ray detected lensed quasar, has opened up the possibility of measuring γ-ray time delays from the different images of the gravitational lens. However, as we have convincingly shown in Section 6.4, the expected delay of $\approx$ 25 days with a flux ratio $\approx$ 1.5 (e.g., Lovell et al., 1998) was not detected, despite claims to the contrary (Barnacka et al., 2011). From the γ-ray light curve (inset "B" of Figure 6.1) we can estimate that the flux ratio between the source and the image for γ rays must be significantly greater than a factor of 6. Related to such main October 2010 outburst event this represents a magnification ratio lower limit for GeV γ rays.

PKS 1830+211 is both a case of strong lensing (characterized by a double image) and a case of compound lensing. For an ideal lens in vacuum the flux images ratios in different energy bands should be the same as the deflection is achromatic (Schneider et al., 1992). On the other hand it has been suggested that plasma dispersive properties and inhomogeneities can cause gravitational deflection angle to be

dependent by the photon energy, change the observed flux and complicate the phenomena of lensing magnification (Bisnovatyi-Kogan and Tsupko, 2010).

It could be that the delay, as measured from radio observations, is not correct. However, this seems unlikely, since two independent measurement are in agreement (Lovell et al., 1998; Wiklind and Combes, 2001). Although macrolensing is an achromatic process, different flux ratios have been measured from other lensed quasars (e.g., Blackburne et al., 2006; Chen et al., 2011). Those authors attributed this to microlensing substructure in the lensing system and a different spatial origin of the emission at different wavelengths (X-ray and optical emission in those cases). This has been shown to be possible though lens modeling (Dobler and Keeton, 2006). Modeling of microlensing events has also shown that microlensing durations can be different for different wavelengths when the emission originates from different size scales (Jovanović et al., 2008). It is certainly possible that the radio and γ-ray emission in blazars comes from different regions of the jet with different size scales. This is due to the well-known fact that variability at these different wavelengths is on considerably different timescales, and that compact synchrotron emission from jets is strongly self-absorbed at radio frequencies. The magnification ratio could be also different for radio and γ-ray emission.

Microlensing structures or light path time delays sampling intrinsic quasar spectral variability are though to explain optical spectral differences between quasar image components (e.g., Wisotzki et al., 1993; Sluse et al., 2007). Another aspect is the presence of a strong (cluster-scale) gravitational potential, even with macrolensing only. Source emission anisotropy may create spectroscopic differences along the slightly different lines of sight, yielding to differences in relativistic beaming of the images and a certain probability that one of the lensed image and delayed flare event may be not observable (Perna and Keeton, 2009). However the Einstein angle is small for isolated quasar potential therefore source anisotropy is not significant in the case of PKS 1830+211.

Following Oshima et al. (2001), we can use the lower limit of ~ 6 in the γ-rays magnification flux ratio to put an upper limit on the size of the γ-ray emitting region (Grieger et al., 1991; Yonehara et al., 1998). We find that this must be $R'_b \gtrsim 5.6 \times 10^{14} m^{1/2}$ cm, where m is the mass of a microlens in solar masses. This is consistent with the γ-ray variability timescale, although it is larger than the size used in SED modeling (section 6.5). The continuous variability monitoring by *Fermi* on a multi-year scale will provide chances to detect further relevant flare events in PKS 1830+211 and allow further investigations.

7

CONCLUSIONS AND OUTLOOK

The study of the extragalactic sky at γ-ray energies has been revolutionized after the launch of the *Fermi* satellite. In particular, filling the gap in the MeV-GeV band, the LAT promoted a remarkable impulse in the framework of the high-energy astrophysics phenomena, especially in blazars. In addition to a mere increase the number of detected objects of the extragalactic sky, at the same time /f era is characterized also by several paradigm shifts which affected also AGN modeling.

The detailed analysis of LAT data carried out in this Thesis has revealed to be a central resource to achieve more insights on their mechanisms. However, notwithstanding the importance of the information provided by the γ-ray observations, correlated multiwavelength studies have proven to be the key for a major step forward in understanding the many open questions left in this field. As a matter of fact, the research here presented has been developed creating a strong cooperation between several facilities in a wide multifrequency framework and exploiting as much multifrequency information as available.

Through a detailed study of several source prototypes of the blazar class, it has been shown that optical (X-ray) triggers and *Fermi* continuous monitoring of (but not only) VHE γ-ray candidates are a successful way to enhance the detection probability of new VHE γ-ray sources. In addition, the many broadband data collected allowed to build time-resolved SEDs, from radio to the VHE γ-ray regime, which were used to investigate the physical mechanisms of blazars, and discriminate among different emission models.

By modeling different SEDs observed simultaneously or quasi simultaneously by *Fermi* and MAGIC, emerges that the general frameworks so far adopted (namely SSC and EC scenarios) are good approximations for describing, on average, the radiation emitted by blazars, but if going into much details on a single observations is required, more complex scenarios sometimes are required. Actually, if on one hand the SEDs of the BL Lacs studied are generally adequately described by one-zone SSC models (as was for 1ES 1727+502 and B3 2247+304), on the other hand we have seen that different assumptions have to be made for other sources, as in the case of 1ES 1215+303 for example, where the narrowness of the synchrotron and IC peaks and the wide separation between the two peaks, required rather extreme conditions for the one-zone SSC model. This behavior, supported by the complex emission scenario indicated by the photo-polarimetric data, pushes to investigate different approaches,

like, just as an example, the one proposed by Marscher (2011) in which γ-ray emission could arise from the collision of turbulent ambient jet plasma with either standing or moving shocks in the jet.

Even more intriguing the observations of 1ES 0806+524. Despite the fact that VHE observations were triggered optically, apparently no evidence for a short-term correlation is found between these two wavebands. The relatively short VHE γ-ray flare, which lasted no longer than one night (rather rare in weak sources like 1ES 0806+524), was accompanied by an X-ray outburst, while no particular variation was seen in the radio range. An increase in flux in HE γ-rays has been observed later and on longer time scales w.r.t. the TeV high state, although we note that *Fermi* detected the source significantly only on timescale of $\sim$ 14 days. Unfortunately, the fast activity shown by weak sources at TeV energies can hardly be followed with the LAT.

Another peculiar behavior has been shown by PG 1553+113, which, unlike the usual pattern of BL Lacs, was quiet in the VHE and optical bands, while exhibiting a pronounced variability in X-rays and in the HE. Previous observations of the source suggested that the hard X-ray flux of the source could change significantly without influencing the activity in the γ-ray regime, except for influencing the emission at the peak of the SED at these energies (Abdo et al., 2010e). In this way, X-ray variability could be accompanied by VHE γ-ray quiescence.

The physical explanation could be provided by a SSC scenario in which the electrons responsible for the variable X-ray emission are at higher energies than those upscattering the bulk of the synchrotron photons to the VHE γ-ray regime. In addition, the scatterings of the variable, hardest X-rays would be suppressed mostly due to the Klein-Nishina effect, but also because of the decreasing target photon density at these energies. However, no definitive conclusion has been drawn since the measurements were of the order of the statistical uncertainties in the VHE regime.

Nevertheless, as a similar behavior was observed in another BL Lac (PKS 2155−304) it is still to be addressed whether such behavior is expected, in general, from the BL Lacs. To test the proposed scenario, the obvious choice would be to observe BL Lacs simultaneously with γ-ray, X-ray and VHE instruments. Studies on correlations between the increase of the hard X-ray flux and the absence of VHE variability, complemented by the determination of the arrival of $>$ 100 GeV photons in the LAT data, could provide a major probe in favor of such model (Abdo et al., 2010e). However, we note that such investigations would be quite demanding, due the low detection rate of high energy (>100 GeV) photons with *Fermi*.

Challenging outcomes are expected from the study of the only FSRQ among the TeV blazar analyzed in this Thesis, i.e. PKS 1510−089. The source is a key target, being the second FSRQ, among only other three objects (at the time of the writing), detected so far at TeV ener-

gies. The observation of VHE γ rays from FSRQs strongly call into questions the validity of one-zone inverse Compton scenarios, so far largely adopted for the modeling of the high energy γ-ray emission in these sources. To reconcile the VHE γ-ray emission, that to be observed must be produced away from the core, with the observed fast variability, that requires a rather compact emission region, the emerging agreement is that γ-rays must be produced at farther distances from the core. A possible scenario that have been proposed for their origin is a large-scale jet perturbation that is intrinsically unstable, or propagates through an inhomogeneous medium. Worth to note, the fact that many major blazar flares have been explained by disturbances propagating along the jet that later on were associated with superluminal radio knots (Marscher and Jorstad, 2010). These structural changes in the inner radio jet, and the apparent correlations between some major γ-ray flares with the coherent rotation of the optical polarization vector, have been used to support the "far-dissipation zone" scenario for PKS 1510−08 by several authors (e.g. Marscher and Jorstad, 2010; Orienti et al., 2013). Multiwavelength campaigns have pointed out a general rather complex behavior for this source and investigations are still not mature enough to draw definitive conclusions. The large number of instruments involved in our study will offer a good opportunity to study the source in all bands and in several (simultaneous) time periods, strengthened by new VHE γ-ray data.

Beyond the wealth of information contained in the LAT data itself, the *Fermi* capability of all-sky monitoring of variable sources, in addition to the fact that HE observations can be almost always reliably extrapolated to the VHE region, provides a good tool to schedule observations with the rather narrow field-of-view ground-based TeV instruments, preparing a fertile field for IACTs discoveries. In the near future, with the development of CTA, and an improvement of a factor 5-10 in sensitivity in the 100 GeV-10 TeV range and an extended energy range both above and below these values, the simultaneous operation of ground-based and space facilities will allow us to continue broadband γ-ray observation with unprecedented sensitivity, thus providing a guaranteed benefit to the AGN science, by shedding light on open questions, like the structure of the inner jet, the origin of the seed photons for the inverse Compton process, the size of the emission region and, more in general, the underlying emission mechanisms at work in blazars.

The improved capabilities of CTA will allow for a more detailed investigation of VHE emission by extragalactic sources, not only AGNs, and will not only increase our knowledge about the sources themselves, but will also be a valuable mean to deepen our knowledge of the Universe. In fact, AGN observations, and blazars in particular, have also been suggested as probes of other physical phenomena,

such as the acceleration and propagation of ultra-high energy cosmic rays and more speculatively, the production of axion-like particles. All of this in addition to other field already explored nowadays, like providing constraints on the EBL and on the strength of the Intergalactic Magnetic Field (e.g. Ackermann et al., 2012).

Not only astrophysics, but also cosmology: As we discussed earlier, careful monitoring of γ-ray blazar flares allowed by the LAT is an asset itself, but it can be the mean to highlight particularly interesting, unexpected objects, like the complex gravitational lens system of PKS 1830−211. System like this have been widely used to derive measurements of the Hubble constant. In our analysis of the major outbursts, we did not find any evidence for events caused by gravitational lensing and this prevented any further speculation.

Anyway we have to stress that this was just the first gravitational lensed system that has been studied in γ-rays, and although in this case it was not possible to measure the γ-ray delay, there are other gravitational lens systems similar to this one that, at least in principle, can be detected by the LAT. To confirm it, between August and September 2012 the FA-GSW analysis evidenced repeated, increased γ-ray activity from another gravitationally lensed blazar, the FSRQ S3 0218+35 (Giroletti et al., 2012b,a; Ciprini, 2012), thus offering a unique opportunity to identify and measure the expected gravitationally-lensed delayed emission in γ rays. For this source, the γ-ray delay was observed and was found consistent with all existing measurements (Abdo and et al. , 2013b).

The detection of these γ-ray flaring events related to gravitational lens paves the way for a new research stream looking for similar systems in other blazars, drawing the attention to surveys of FSRQs aiming at detecting gravitational lenses (Myers et al., 2003; Browne et al., 2003). For instance in the CLASS sample, which hosts several γ-ray candidate blazars (e.g. Healey et al., 2007) there are about 22 gravitational lenses out of 16503 radio sources (studied at $>$ 30 mJy at 8 GHz), almost the same ratio so far obtained in γ-ray with the 2LAC (2 detections out of about 1000 blazars). Although these systems have not yet been detected in γ rays, the FA-GSW service could be in principle useful to detect any flaring γ-ray activity from these objects, as was done for PKS 1830+211 and S3 0218+35, and attempt to measure the delay between the direct and the "echo" flare.

Furthermore, a still unexplored strategy would be the discovery of new gravitationally lensed system by means of delay measurements in γ rays. In principle, this could be possible for lenses with smaller separations than widely surveyed, e.g. unresolved in the initial VLA 8 GHz 0.2" resolution scans in the CLASS survey. In addition, it has to be taken into account that lens surveys in the Southern hemisphere are not yet completely covered (Lovell et al., 1996; Sadler et al., 2006). A similar approach was proposed by Pindor (2005) for future wide-

field optically based surveys. In particular, a key point for such study would be the different magnification ratio in radio and γ rays as the one observed in the case of S3 0218+35. This would actually open the possibility for some sources to be bright in γ rays and fainter in radio, so that potential gravitationally lensed systems could be hosted among the currently unidentified *Fermi* objects. The all-sky monitoring capability of the LAT in γ rays enables such studies, leading to the potential discovery of gravitationally lensed γ-ray blazars in general and radio-faint ones in particular, among the unidentified Fermi-LAT sources (Torres et al., 2003).

Many exciting results are expected for the research presented and the picture that comes out from this work is that the field of γ-ray Astrophysics still has lots of open question that we would like to answer in the future. The likelihood of continued achievements is certain, both for the known sources and for new discoveries, also thanks to a science return guaranteed by *Fermi*, CTA and the several planned instrumental developments (e.g. the High Altitude Water Cherenkov Observatory, HAWC).

ACKNOWLEDGMENTS

I have to acknowledge my advisor, Denis Bastieri, for allowing me the freedom to choose and pursue my own projects while supporting me and providing insight on the research at hand, and Greg Madejski for offering precious advice and hospitality at SLAC.

Many thanks to all the other present and former members of the *Fermi* LAT group in Padova, especially to Riccardo Rando and Luigi Tibaldo that always kindly share expertise and time.

The research that I pursue during the last years has been enable by the LAT, which is driven by the *Fermi* Collaboration members, and with them I am deeply indebted. In particular I owe thanks to Gino Tosti, Stefan Larsson, Paola Grandi and Francesco Massaro for useful discussions and time. On the other hand I have also to thank the MAGIC collaboration, in particular all the people with which I carried out my research.

I owe thanks to Paolo Padovani for accepting of serving on my reading committee and to the other members of the jury, Giovanni Busetto, Alessandro De Angelis, James Olsen and Marco Resigno for accepting to take part on my exam committee. Many thanks to my friends and my "little secretary" that with their pleasant company have made less arduous this work.

Most of all, I thank my parents, Giorgio and Luisa, who have always stood beside me, and my family, for making me who I am today and supporting me all these years.

Consistency is the last refuge of the unimaginative
Oscar Wilde

A

NOTES ON INDIVIDUAL SOURCES

This appendix collects some major information regarding the more interesting sources that have been included in the study of Chapter 5. These objects are among the brightest ($F_{100MeV-300GeV} > 10^{-6}$ cm^{-2} s^{-1}) sources detected by *Fermi* in the first 3.5 years of monitoring.

PMN J0948+0022 and SBS 0846+513: These two objects are optically classified as Narrow-Line Seyfert 1 galaxies, FWHM (Hβ $<$ 2000 km s^{-1}, [OIII]/Hβ $<$ 3, and a bump due to Fe II (see e.g. Pogge, 2000). The first detection by *Fermi* LAT of γ-ray emission from PMN J0948+0022 confirmed the presence of a relativistic jet in this type of AGN (Abdo et al., 2009c), followed by the detection of other 4 radio-loud Narrow-Line Seyfert 1s in γ rays (Abdo et al., 2009d; D'Ammando et al., 2012b).

PKS 0208−512: PKS 0208−512 is a flat spectrum radio quasar already detected in γ rays by EGRET as 3EG J0210-5055 (Hartman et al., 1999). PKS 0208-512 has shown the hardest γ-ray spectrum of all EGRET sources (Γ = 1.69 $\pm$ 0.05) with clear evidence of variability (Bertsch et al., 1993). Detected also at lower energies by COMPTEL, PKS 0208−512 has been claimed to be a MeV blazar. PKS 0208−512 was classified as a highly polarized quasar or blazar by (Impey and Tapia, 1988, 1990). A 5 GHz VLBI image from 1992 November revealed a core-jet structure, with a one-side jet extending to approximately 20 mas by Impey and Tapia (1988, 1990). X-ray emission is also seen in the arcsec-scale jet but fades drastically after a 90° bend in the radio jet (Marshall et al., 2005). Strong and variable X-ray emission was first detected by ROSAT (Voges et al., 1999). A lower limit to the Doppler factor of 10.2 was estimated using the ROSAT X-ray observation (Dondi and Ghisellini, 1995). This implies superluminal motion in the compact core. Comparison of the 1992 and 1993 images taken 6.5 months apart suggests a proper motion of 0.6$\pm$0.7 mas yr^{-1}, corresponding to an apparent speed of (17$\pm$20)c (Shen et al., 1998). This source is classified as an AGN of uncertain type in the 2FGL catalog.

NGC 1275: NGC 1275 is a bright giant elliptical galaxy located at the center of the Perseus cluster. The increased high γ-ray activity of NGC 1275 reported by *Fermi* LAT (Donato et al., 2010a) triggered the discovery of the source at VHE by MAGIC (Mariotti and MAGIC Collaboration, 2010). This is the only radiogalaxy for which evidence for time variability was found in γ rays by *Fermi* LAT up to now (Abdo

et al., 2010d).

PKS 0521−36: This source first classified as an N galaxy (Bolton et al., 1965), and then as a BL Lac object (Burbidge and Hewitt, 1987, 1990), showed in optical and UV strong narrow and broad emission lines typical of Seyfert 1 galaxies (Ulrich, 1981; Scarpa et al., 1995). This object contains an optical/radio jet extending to the northwest (Scarpa et al., 1999, and references therein), which was detected also in the X-rays (Birkinshaw et al., 2002). PKS 0521−36 was marginally detected by EGRET (Lin et al., 1995). No beaming effect is needed for the core brightness temperature, consistent with the non-detection of superluminal motion (Tingay and Edwards, 2002). Pian et al. (1996) derived a viewing angle of 30° with bulk Lorentz factor of 1.2. VLBA image showed that the same position angle found on the parsec-scale jet is maintained, without any significant bending, over 3 orders of magnitude (Giroletti et al., 2004). This is consistent with a relatively large angle of view, in agreement with the absence of superluminal motion showed by Tingay and Edwards (2002) and the findings of Pian et al. (1996).

CRATES J0531−4827: The source was detected during the Parkes-MIT-NRAO (PMN) surveys. This object is included in the CRATES catalog of flat spectrum objects (Healey et al., 2007), believed to be a blazar. No redshift measurement is available and not even further multiwavelength information.

B2 0619+33: B2 0619+33 is a flat spectrum radio source with unknown redshift. The source is not listed in the catalogs of the 2MASS and ROSAT all-sky surveys, and no object is visible at the given position in the Digitized Sky Survey (DSS2) plates. However, ground and space-based observations triggered by the γ-ray flare have detected a counterpart of the γ-ray/radio source for the first time in X-ray (Donato et al., 2010b), optical (Smith, 2010) and near-infrared bands (Carrasco et al., 2010).

PKS 1118-056: PKS 1118−056 is classified as a FSRQ although it is indicated as a giga-hertz peaked (GPS) radio source by Torniainen et al. (2008). Radio sources of this type would be unusual among the γ-ray AGN reported in the 1FGL and 2FGL catalogs.

PMN J1123−6417: This object is a likely AGN of uncertain type at a low Galactic latitude (b=-3 deg). The association of PMN J1123-6417 with the γ-ray source was confirmed by Mahony et al. (2010) using the Australia Telescope 20-GHz (AT20G) survey catalog. This source is present in the Fermi LAT Bright Source List as 0FGL J1123.0−6416 and in the First Fermi catalog as 1FGL J1123.6−4555 but it was not

included in the 2FGL catalog. This could be due to a significant decrease of the flux in the second year of the *Fermi*-LAT operation.

PKS 2123−463: PKS 2123−463 has been associated in the First Fermi-LAT source catalog with the γ-ray source 1FGL J2126.1−4603, but no association was reported in the Second Fermi-LAT source catalog, although a γ-ray source, 2FGL J2125.0−4632 at 0.52° from the radio position of PKS 2123−463 was reported. The identification of the γ-ray source with PKS 2123−463 has been confirmed in D'Ammando et al. (2012a).

PKS 0502+049: ATel#3573 reported that on August 19, 2011 the source MG1 J050533+0415 was in high state. The flare was wrongly attribute to this source. Actually a dedicated analysis resulted with the significant detection of the source PKS 0502+049 (ts=91, a.k.a. 2FGL J0505.5+0501) which is about a degree away from MG1 J050533+0415. The latter instead was not detected (ts=0).

4C +21.35 and PKS 1510−089: The discovery of the FSRQs 4C +21.35 and PKS 1510−089 at VHE by MAGIC and H.E.S.S., respectively (Mose Mariotti, 2010; Wagner, 2010), was triggered in both cases by high γ-ray activity detected by *Fermi* LAT and AGILE (Donato, 2010; D'Ammando et al., 2009; Abdo et al., 2010b).

TXS 1530−131: The preliminary best-fit location of the γ-ray source (R.A.=233.16 deg, Dec.=-13.35 deg, J2000) has a 95% containment radius of 0.32 deg (statistical errors only) for observations from 2011 May 23 to August 23. The flat spectrum radio source TXS 1530-131, present in the CGRaBS catalog of candidate γ-ray source, lies on the edge of this error circle.

3C 345: This source is a prominent variable quasar from radio to X-rays, particularly bright at radio wavelengths. It has an extended radio structure that is observable from sub-pc to kpc scales which is archetypal for a relativistic blazar jet (Lobanov and Zensus, 1999). The identification of 3C 345 as a γ-ray emitter was unclear during the EGRET-era. A γ-ray source near the position of 3C 345 was reported in the three-month bright *Fermi* source list as 0FGL J1641.4+3939 (Abdo et al., 2009a) and First *Fermi* LAT catalog as 1FGL J1642.5+3947 (Abdo et al., 2010c), but an association with 3C 345 was possible with high confidence only based on 20 months of *Fermi* LAT and multifrequency data (Schinzel et al., 2011).

CGRaBS J1848+3219: Large variability was not seen in radio observations of CGRaBS J1848+3219 from 400 MHz to 4.8 GHz in the 1980s and 1990s, with an increase of the flux during 2004–2005 (Kida et al.,

2010). The radio spectrum was flat from 360 MHz to 4.8 GHz. X-ray variability was reported also by Fuhrmeister et al. (2007). This source has not been detected at optical and infrared wavelengths. Sowards-Emmerd et al. (2005) and Healey et al. (2008) identified it as a γ-ray blazar candidate. In γ rays this source was detected starting from the *Fermi* LAT bright source list as 0FGL J1847.8+3223 (Abdo et al., 2009a).

PMN J2250−2806: PMN J2250−2806 is a flat spectrum radio source in the CGRaBS catalog listing candidate γ-ray blazar before the launch of the *Fermi* satellite (Healey et al., 2008).

Table 1. *Fermi* LAT flaring AGNs reported in Astronomer's Telegrams.

2FGL Name	R.A.	Dec.	z	Name	ATel #	Peak time	Peak Flux[e]	2FGL Flux[e]	Type[a]	ATel Swift #	Ref	EGRET[b]
2FGL J0102.7+5827	01 02 45.7623	+58 24 11.136	0.644	TXS 0059+581	3864	01-11-2012	100	5.28	FSRQ	···	···	···
2FGL J0109.9+6132	01 09 46.3443	+61 33 30.455	0.785	TXS 0106+612	2414	02-01-2010	80	14.3	FSRQ	2420	1	···
2FGL J0112.8+3208	01 12 50.3330	+32 08 17.433	0.603	4C +31.03	2054	05-20-2009	133	9.35	FSRQ	···	···	···
2FGL J0210.7-5102	02 10 06.2004	−51 01 01.891	0.999	PKS 0208-512	3338	05-09-2011	110	9.45	AGU	···	···	F
2FGL J0211.2+1050	02 11 13.177	+10 51 34.798	...	CGRaBS J0211+1051	3120	01-23-2011	100	3.83	BLL	3129	···	···
2FGL J0222.6+4302	02 22 39.6114	+43 02 07.799	...	3C 66A	1759	10-02-2008	70	18.3	BLL	···	2	Y
2FGL J0237.1-6136	02 36 53.2457	−61 36 15.183	0.467	PKS 0235-618	2669	06-10-2010	111	6.13	FSRQ	2673	···	Y
2FGL J0237.8+2846	02 37 52.406	+28 48 08.990	1.206	4C +28.07	3670	10-03-2011	140	9.56	FSRQ	3676	···	···
2FGL J0238.7+1637	02 38 38.9301	+16 36 59.275	0.940	AO 0235+164	1744	09-07-2008	200[c]	22.9	BLL	···	3	Y
2FGL J0245.9-4652	02 46 00.11	−46 51 17.4	1.385	PKS 0244-470	2440	02-12-2010	100	12.4	FSRQ	···	···	···
2FGL J0252.7-2218	02 52 47.9536	−22 19 25.465	1.419	PKS 0250-225	1933	02-17-2009	50	10.0	FSRQ	2039	···	···
2FGL J0303.4-2407	03 03 26.50	−24 07 11.3	0.26	PKS 0301-243	2591	04-28-2010	140	5.92	BLL	···	···	···
2FGL J0319.8+4130	03 19 48.1601	+41 30 42.106	0.01759	NGC 1275	2737	07-14-2010	70	17.5	RDG	···	4	···
2FGL J0403.9-3604	04 02 02.5994	−36 13 11.947	1.417	PKS 0402-362	3655	09-22-2011	380	18.7	FSRQ	3659	···	···
2FGL J0423.2-0120	04 23 15.80073	−01 20 33.0655	0.916	PKS 0420-01	2402	01-21-2010	80	13.3	FSRQ	···	···	Y
2FGL J0428.6-3756	04 28 40.4242	−37 56 19.579	1.111	PKS 0426-380	2366	01-02-2010	140	28.4	BLL	···	···	···
2FGL J0442.7-0017	04 42 38.661	−00 17 43.42	0.844	NRAO 190	2049	05-16-2009	177	16.4	FSRQ	···	···	Y
2FGL J0457.0-2325	04 57 03.1792	−23 24 52.018	1.003	PKS 0454-234	1898	01-11-2009	196	33.9	FSRQ	···	···	Y
2FGL J0505.5+0501	05 05 23.1847	+04 59 42.725	0.954	PKS 0502+049	3573	08-19-2011	120	2.93	FSRQ	···	···	···
2FGL J0523.0-3628	05 22 57.98465	−36 27 30.8509	0.055	PKS 0521-36	2683	06-17-2010	100	12.9	AGN	2689	···	···
2FGL J0530.8+1333	05 30 56.4167	+13 31 55.150	2.07	PKS 0528+134	3412	06-05-2011	110	8.47	FSRQ	···	···	F
2FGL J0532.0-4826	05 31 58.61	−48 27 35.9	...	CRATES J0531-4827	2907	09-25-2010	150	4.11	AGU	···	···	···
2FGL J0532.7+0733	05 32 38.9984	+07 32 43.345	1.254	OG 050	3750	11-07-2011	110	8.48	FSRQ	3773	···	···
2FGL J0538.8-4405	05 38 50.3614	−44 05 08.934	0.892	PKS 0537-441	2591	04-27-2010	130	44.1	BLL	···	···	Y
2FGL J0622.9+3326	06 22 52.22194	+33 26 10.410	...	B2 0619+33	2829	09-03-2010	100	5.34	AGU	2848	···	···
PKS 0646-306[d]	06 48 14.0964	−30 44 19.659	1.153	PKS 0646-306	3878	22-01-2012[1]	50	...	FSRQ	3894	···	···
2FGL J0654.2+4514	06 54 23.7136	+45 14 23.545	0.928	B3 0650+453	3580	08-22-2011	100	6.58	FSRQ	3609	···	···
2FGL J0714.0+1933	07 13 55.6791	+19 35 00.408	0.54	MG2 J071354+1934	2110	07-03-2009	100	6.67	FSRQ	···	···	···
2FGL J0721.9+7120	07 21 53.4484	+71 20 36.363	...	S5 0716+71	3487	07-12-2011	140	20.7	BLL	···	···	Y
2FGL J0725.3+1426	07 25 16.8077	+14 25 13.747	1.038	4C +14.23	2243	10-13-2009	150	12.6	FSRQ	2253	···	···
2FGL J0730.2-1141	07 30 19.1124	−11 41 12.599	1.591	PKS 0727-115	2860	09-21-2010	140	38.2	FSRQ	2901	···	···
2FGL J0742.6+5442	07 42 39.7906	+54 44 24.666	0.723	GB6 J0742+5444	3196	02-26-2011	120	5.14	FSRQ	···	···	···
2FGL J0808.2-0750	08 08 15.536	−07 51 09.88	1.837	PKS 0805-07	2136	07-22-2009	160	14.4	FSRQ	···	···	···
2FGL J0841.6+7052	08 41 24.3652	+70 53 42.173	2.218	S5 0836+71	3831	12-25-2011	170	6.42	FSRQ	3835	···	Y
SBS 0846+513[d]	08 49 57.9768	+51 08 29.023	0.5837	SBS 0846+513	3452	06-21-2011	80	...	NLSyI	···	5	···
2FGL J0854.8+2005	08 54 48.874	+20 06 30.64	0.306	OJ 287	2256	10-22-2009	100	6.08	BLL	···	···	Y
2FGL J0909.1+0121	09 09 10.0916	+01 21 35.6179	1.025	PKS 0906+015	2543	04-08-2010	120	9.30	FSRQ	2582	···	···
2FGL J0920.9+4441	09 20 58.4584	+44 41 53.985	2.18879	S4 0917+44	1902	01-15-2009	90	15.9	FSRQ	···	···	···
2FGL J0948.8+0020	09 48 57.3201	+00 22 25.558	0.5846	PMN J0948+0022	3429	06-10-2011	150	9.19	NLSyI	···	6	···
2FGL J1033.9+6050	10 33 51.4289	+60 51 07.334	1.40095	S4 1030+61	2622	05-14-2010	150	7.42	FSRQ	2628	···	···
2FGL J1121.5-0554	11 21 25.1080	−05 53 56.440	1.297	PKS 1118-05	1932	02-17-2009	40	7.79	FSRQ	1943	···	···

Table 1—Continued

2FGL Name	R.A.	Dec.	z	Name	ATel #	Peak time	Peak Flux[e]	2FGL Flux[e]	Type[a]	ATel Swift #	Ref	EGRET[b]
PMN J1123-6417[d]	11 23 19.48	−64 17 35.7	...	PMN J1123-6417	3394	05-30-2011	140	...	AGU	···	···	···
2FGL J1126.6-1856	11 27 04.3924	−18 57 17.440	1.048	PKS 1124-186	3207	03-02-2011	90	7.76	FSRQ	···	···	···
2FGL J1153.2+4935	11 53 24.4666	+49 31 08.830	0.334	SBS 1150+497	3353	05-15-2011	340	2.57	FSRQ	3353	···	···
2FGL J1159.5+2914	11 59 31.8339	+29 14 43.827	0.724565	Ton 599	2795	08-15-2010	120	12.0	FSRQ	···	···	F
2FGL J1224.9+2122	12 24 54.4583	+21 22 46.388	0.43	PKS 1222+216	2687	06-18-2010	1246	59.2	FSRQ	2698	7	Y
2FGL J1229.1+0202	12 29 06.6997	+02 03 08.598	0.158	3C 273	2168	08-19-2009	318	67.6	FSRQ	···	8	F
2FG J1239.5+0443	12 39 32.7556	+04 43 05.233	1.76095	MG1 J123931+0443	1888	12-29-2008	150	9.35	FSRQ	1888	9	···
2FGL J1246.7-2546	12 46 46.8020	−25 47 49.287	0.633	PKS 1244-255	1894	01-05-2009	80	14.3	FSRQ	···	···	···
2FGL J1256.1-0547	12 56 11.1665	−05 47 21.523	0.536	3C 279	2886	09-27-2010	390	55.0	FSRQ	···	10	F
2FGL J1312.8+4828	13 12 43.354	+48 28 30.94	0.501	GB6 B1310+4844	2306	11-26-2009	120	10.1	FSRQ	2316	···	···
2FGL J1332.0-0508	13 32 04.4646	−05 09 43.305	2.15	PKS 1329-049	2837	09-06-2010	300	17.0	FSRQ	···	···	···
2FGL J1345.4+4453	13 45 33.1724	+44 52 59.73	2.534	B3 1343+451	3793	11-29-2011	120	6.30	FSRQ	···	···	···
2FGL J1428.0-4206	14 27 56.2975	−42 06 19.437	1.522	PKS 1424-418	3329	05-05-2011	110	16.7	FSRQ	···	···	Y
2FGL J1457.4-3540	14 57 26.7117	−35 39 09.971	1.424	PKS 1454-354	1701	09-04-2008	200[c]	19.8	FSRQ	···	11	···
2FGL J1504.3+1029	15 04 24.9797	+10 29 39.198	1.83928	PKS 1502+106	1650	08-06-2008	200[c]	57.6	FSRQ	···	12	···
2FGL J1512.8-0906	15 12 50.5329	−09 05 59.828	0.361	PKS 1510-089	3694	10-19-2011	1590	100	FSRQ	···	13	Y
2FGL J1517.7-2421	15 17 41.8131	−24 22 19.475	0.048	AP Lib	3187	02-21-2011	140	5.90	BLL	···	···	···
2FGL J1522.1+3144	15 22 09.9917	+31 44 14.382	1.484	B2 1520+31	3050	11-18-2010	180	41.1	FSRQ	···	···	···
TXS 1530-131[d]	15 32 45.3747	−13 19 10.086	...	TXS 1530-131	3579	08-22-2011	120	...	FSRQ	3629	···	···
2FGL J1625.7-2526	16 25 46.8916	−25 27 38.326	0.786	PKS 1622-253	3424	06-07-2011	200	13.8	FSRQ	···	···	Y
2FGL J1626.1-2948	16 26 06.0208	−29 51 26.970	0.815	PKS 1622-297	2531	03-29-2010	57	5.25	FSRQ	···	···	F
2FGL J1635.2+3810	16 35 15.493	+38 08 04.50	1.81313	4C +38.41	3333	05-08-2011	210	28.8	FSRQ	···	···	F
2FGL J1642.9+3949	16 42 58.8099	+39 48 36.993	0.593467	3C 345	2226	09-29-2009	60	10.5	FSRQ	···	14	···
2FGL J1700.2+6831	17 00 09.2928	+68 30 06.962	0.301	GB6 J1700+6830	1986	03-22-2009	99	9.49	FSRQ	1991	···	···
2FGL J1709.7+4319	17 09 41.0876	+43 18 44.547	1.027	B3 1708+433	3026	11-09-2010	120	4.56	FSRQ	···	···	···
2FGL J1733.1-1307	17 33 02.7057	−13 04 49.547	0.902	PKS 1730-13	3002	11-02-2010	170	8.40	FSRQ	···	···	F
2FGL J1748.8+7006	17 48 32.8401	+70 05 50.768	0.77	S4 1749+70	3171	02-15-2011	70	2.36	BLL	···	···	···
2FGL J1800.5+7829	18 00 45.6839	+78 28 04.018	0.68	S5 1803+78	3322	05-02-2011	110	7.60	BLL	···	···	···
2FGL J1833.6-2104	18 33 39.8882	−21 03 39.772	2.507	PKS 1830-211	2943	10-14-2010	520	50.2	FSRQ	···	···	Y
2FGL J1848.5+3216	18 48 22.0885	+32 19 02.603	0.798	CGRaBS J1848+3219	2954	10-18-2010	220	3.73	FSRQ	2963	···	···
2FGL J1849.4+6706	18 49 16.0723	+67 05 41.679	0.657	CGRaBS J1849+6705	3478	07-06-2011	250	11.0	FSRQ	···	···	···
PMN J1913-3630[d]	19 13 20.870	−36 30 19.90	...	PMN J1913-3630	2966	10-21-2010	130	...	FSRQ	···	···	···
PKS 1915-458[d]	19 19 16.66	−45 43 38.4	2.47	PKS 1915-458	2666	06-04-2010	36	...	FSRQ	2679	···	···
2FGL J2025.6-0736	20 25 40.6604	−07 35 52.688	1.388	PKS 2023-07	2175	08-23-2009	142	18.8	FSRQ	···	···	Y
2FGL J2056.2-4715	20 56 16.3598	−47 14 47.627	1.489	PKS 2052-474	2160	08-09-2009	87	18.8	FSRQ	···	···	Y
PKS 2123-463[d]	21 26 30.7042	−46 05 47.892	1.67	PKS 2123-463	3808	12-14-2011	110	...	FSRQ	3815	···	···
2FGL J2143.5+1743	21 43 35.54457	+17 43 48.7875	0.211	OX 169	2393	01-18-2010	140	17.0	FSRQ	···	···	···
2FGL J2147.4-7534	21 47 12.7303	−75 36 13.225	1.138	PKS 2142-75	2539	04-04-2010	110	11.8	FSRQ	···	···	···
2FGL J2158.8-3013	21 58 52.0651	−30 13 32.118	0.116	PKS 2155-304	2944	10-13-2010	100	16.5	BLL	···	···	Y
2FGL J2202.8+4216	22 02 43.29137	+42 16 39.9799	0.0686	BL Lacertae	3368	05-20-2011	140	17.0	BLL	3377	15	F
2FGL J2201.9-8335	22 02 19.73	−83 38 11.5	1.865	PKS 2155-83	2373	01-05-2010	140	6.73	FSRQ	···	···	···

Table 1—Continued

2FGL Name	R.A.	Dec.	z	Name	ATel #	Peak time	Peak Flux[e]	2FGL Flux[e]	Type[a]	ATel Swift #	Ref	EGRET[b]
2FGL J2225.6-0454	22 25 47.2593	−04 57 01.391	1.404	3C 446	3675	10-08-2011	150	6.10	FSRQ	···	···	···
2FGL J2232.4+1143	22 32 36.4089	+11 43 50.904	1.037	CTA 102	3320	04-29-2011	140	9.29	FSRQ	···	···	Y
2FGL J2236.5-1431	22 36 34.08716	−14 33 22.1897	...	PKS 2233-148	2589	04-23-2010	70	6.73	BLL	2589	···	···
2FGL J2250.8-2808	22 50 44.4923	−28 06 39.330	0.525	PMN J2250-2806	1989	03-25-2009	136	5.92	AGN	···	···	···
2FGL J2253.9+1609	22 53 57.7479	+16 08 53.560	0.859	3C 454.3	3041	11-16-2010	5600	240	FSRQ	···	16	F
2FGL J2311.0+3425	23 11 05.3288	+34 25 10.905	1.817	B2 2308+34	2783	08-07-2010	90	7.79	FSRQ	···	···	···
2FGL J2329.2-4956	23 29 20.880	−49 55 40.68	0.518	PKS 2326-502	2783	08-07-2010	110	12.3	FSRQ	···	···	···
2FGL J2330.9-2144	23 31 04.03	−21 48 15.3	0.563	PMN J2331-2148	2101	06-26-2009	82	5.42	FSRQ	···	···	···
2FGL J2345.0-1553	23 45 12.4623	−15 55 07.834	0.621	PMN J2345-1555	2408	01-27-2010	100	6.67	FSRQ	···	···	···

Note. — 1. Vanderbrouke et al. 2010, ApJL, 718, 166; 2. Abdo et al. 2011, ApJ, 726, 43; 3. Abdo et al. 2012, submitted to ApJ; 4. Abdo et al. 2009, 699, 31; 5. D'Ammando, Orienti, et al. 2012, submitted to MNRAS; 6. Abdo et al. 2009, 699, 976; 7. Tanaka et al. 2011, ApJ, 733, 19; 8. Abdo et al. 2010, ApJL, 714, L73; 9. Pacciani et al. 2012, submitted to MNRAS; 10. Abdo et al. 2010, Nature, 463, 886; 11. Abdo et al. 2009, ApJ, 697, 934; 12. Abdo et al. 2010, ApJ, 710, 810; 13. Abdo et al. 2010, ApJ, 721, 1425; 14. Schinzel et al. 2011, A&A, 532, 150; 15. Abdo et al. 2011, ApJ, 730, 101; 16. Abdo et al. 2009, ApJ, 699, 817.
[a]: FSRQ = flat spectrum radio quasar type of blazar; BLL = BL Lac type of blazar; AGN = other non-blazar AGN; AGU = active galaxy of uncertain type.
[b]: Y = source detected by EGRET; F = source detected by EGRET with flux $> 10^{-6}$ ph cm^{-2} s^{-1}.
[c] the flux (E > 100 MeV) was above 200×10^{-8} photons cm^{-2} s^{-1}.
[d] source not detected in the 2FGL catalog. [e] flux is in units of 10^{-8}ph cm^{-2} s^{-1}.

Table 2. *Fermi* LAT flaring AGNs reported in multiple Astronomer's Telegrams.

2FGL Name	R.A.	Dec.	z	Name	ATel #	Peak time	Peak Flux[b]	2FGL Flux[b]	Type[a]	ATel Swift #
2FGL J0210.7-5102	02 10 06.2004	−51 01 01.891	0.999	PKS 0208-512	1759	09-25-2008	85	9.45	AGU	···
2FGL J0238.7+1637	02 38 38.9301	+16 36 59.275	0.940	AO 0235+164	1784	10-14-2008	500[c]	22.9	BLL	···
2FGL J0403.9-3604	04 02 02.5994	−36 13 11.947	1.417	PKS 0402-362	2413	02-01-2010	100	18.7	FSRQ	···
2FGL J0457.0-2325	04 57 03.1792	−23 24 52.018	1.003	PKS 0454-234	3703	10-22-2011	170	33.9	FSRQ	···
2FGL J0538.8-4405	05 38 50.3614	−44 05 08.934	0.894	PKS 0537-441	1759	09-15-2008	91	44.1	BLL	···
2FGL J0538.8-4405	05 38 50.3614	−44 05 08.934	0.894	PKS 0537-441	2124	07-08-2009	100	44.1	BLL	···
2FGL J0730.2-1141	07 30 19.1124	−11 41 12.599	1.59	PKS 0727-115	1919	01-01/28-2009	50	38.2	FSRQ	···
2FGL J0742.6+5442	07 42 39.7906	+54 44 24.666	0.72	GB6 J0742+5444	3445	06-19-2011	110	5.14	FSRQ	···
2FGL J0808.2-0750	08 08 15.536	−07 51 09.88	1.837	PKS 0805-07	2048	05-14-2009	83	14.4	FSRQ	···
2FGL J0841.6+7052	08 41 24.3652	+70 53 42.173	0.914	S5 0836+71	3260	04-03-2011	120	6.42	FSRQ	···
2FGL J0854.8+2005	08 54 48.874	+20 06 30.64	0.306	OJ 287	3680	10-10-2011	100	6.08	BLL	···
2FGL J0948.8+0020	09 48 57.3201	+00 22 25.558	0.5846	PMN J0948+0022	2733	07-09-2010	130	9.19	AGN	···
2FGL J1153.2+4935	11 53 24.4666	+49 31 08.830	0.334	SBS 1150+497	3313	04-25-2011	150	2.57	FSRQ	
2FGL J1224.9+2122	12 24 54.4583	+21 22 46.388	0.43	PKS 1222+216	2021	04-16-2009	46	59.2	FSRQ	···
2FGL J1224.9+2122	12 24 54.4583	+21 22 46.388	0.43	PKS 1222+216	2349	12-15-2009	340	59.2	FSRQ	···
2FGL J1224.9+2122	12 24 54.4583	+21 22 46.388	0.43	PKS 1222+216	2584	04-24-2010	810	59.2	FSRQ	···
2FGL J1229.1+0202	12 29 06.699	+02 03 08.598	0.158	3C 273	1707	09-05-2008	200[d]	67.6	FSRQ	···
2FGL J1229.1+0202	12 29 06.699	+02 03 08.598	0.158	3C 273	2200	09-15-2009	310	67.6	FSRQ	···
2FGL J1239.5+0443	12 39 32.7556	+04 43 05.233	1.76	MG1 J123931+0443	3445	06-19-2011	110	9.35	FSRQ	···
2FGL J1256.1-0547	12 56 11.1665	−05 47 21.523	0.536	3C 279	1864	12-05-2008	150	55.0	FSRQ	···
2FGL J1256.1-0547	12 56 11.1665	−05 47 21.523	0.536	3C 279	2154	07-29/08-04-2009	138	55.0	FSRQ	···
2FGL J1332.0-0508	13 32 04.4646	−05 09 43.305	2.15	PKS 1329-049	2728	07-07-2010	100	17.0	FSRQ	2739
2FGL J1345.4+4453	13 45 33.1724	+44 52 59.73	2.534	B3 1343+451	2217	09-25-2009	102	6.30	FSRQ	···
2FGL J1428.0-4206	14 27 56.2975	−42 06 19.437	1.524	PKS 1424-418	2104	06-28-2009	60	16.7	FSRQ	···
2FGL J1428.0-4206	14 27 56.2975	−42 06 19.437	1.524	PKS 1424-418	2583	04-21-2010	100	16.7	FSRQ	···
2FGL J1504.3+1029	15 04 24.9797	+10 29 39.198	1.83	PKS 1502+106	1905	01-21-2009	180	57.6	FSRQ	···
2FGL J1512.8-0906	15 12 50.5329	−09 05 59.828	0.361	PKS 1510-089	1743	09-13-2008	200[d]	100	FSRQ	···
2FGL J1512.8-0906	15 12 50.5329	−09 05 59.828	0.361	PKS 1510-089	1897	01-08-2009	200[d]	100	FSRQ	···
2FGL J1512.8-0906	15 12 50.5329	−09 05 59.828	0.361	PKS 1510-089	2033	04-25-2009	650	100	FSRQ	···
2FGL J1512.8-0906	15 12 50.5329	−09 05 59.828	0.361	PKS 1510-089	3473	07-04-2011	830	100	FSRQ	···
2FGL J1522.1+3144	15 22 09.9917	+31 44 14.382	1.487	B2 1520+31	2026	04-20-2009	100	41.1	FSRQ	···
2FGL J1625.7-2526	16 25 46.8916	−25 27 38.326	0.786	PKS 1622-253	2231	10-04-2009	190	13.8	FSRQ	···
2FGL J1635.2+3810	16 35 15.493	+38 08 04.50	1.814	4C 38.41	2136	07-22-2009	138	28.8	FSRQ	···
2FGL J1635.2+3810	16 35 15.493	+38 08 04.50	1.814	4C 38.41	2456	02-23-2010	150	28.8	FSRQ	···
2FGL J1800.5+7829	18 00 45.6839	+78 28 04.018	0.68	S5 1803+78	2386	01-11-2010	90	7.60	BLL	···
2FGL J2202.8+4216	22 02 43.29137	+42 16 39.9799	0.0686	BL Lacertae	2402	01-21-2010	80	17.0	BLL	···
2FGL J2253.9+1609	22 53 57.7479	+16 08 53.560	0.859	3C 454.3	1628	07-10/21-2008	200	240	FSRQ	···
2FGL J2253.9+1609	22 53 57.7479	+16 08 53.560	0.859	3C 454.3	2200	09-15-2008	600	240	FSRQ	···
2FGL J2253.9+1609	22 53 57.7479	+16 08 53.560	0.859	3C 454.3	2328	12-02-2009	2200	240	FSRQ	2329
2FGL J2253.9+1609	22 53 57.7479	+16 08 53.560	0.859	3C 454.3	2534	04-03-2010	1200	240	FSRQ	···
2FGL J2345.0-1553	23 45 12.4623	−15 55 07.834	0.621	PMN J2345-1555	2972	10-24-2010	60	6.67	FSRQ	···

Note. — [a]: FSRQ = flat spectrum radio quasar type of blazar; BLL = BL Lac type of blazar; AGN = other non-blazar AGN; AGU = active galaxy of uncertain type. [b]: Flux is in units of [10^{-08} ph cm^{-2} s^{-1}]. [c]: The flux (E > 100 MeV) was estimated over 6 hours. [d]The flux (E > 100 MeV) was above 200×10^{-8} photons cm^{-2} s^{-1}.

Table 3. *Fermi* LAT flaring AGNs - recalcolated values.

2FGL name	R.A.[c]	Dec.[c]	Name	Peak time	Peak Flux[a]	Index	Luminosity[d]
2FGL J0102.7+5827	01 03 34.061	+58 19 31.410	TXS 0059+581	01-11-2012	73.93 ± 19.97	1.91 ± 0.16	2.2e+48
2FGL J0109.9+6132	01 11 26.913	+61 21 51.767	TXS 0106+612	02-01-2010	85.49 ± 22.79	2.18 ± 0.19	2.2e+48
2FGL J0112.8+3208	01 12 36.769	+32 06 35.986	4C +31.03	05-20-2009	132.41 ± 23.15	2.33 ± 0.16	1.4e+48
2FGL J0210.7-5102	02 11 00.271	−51 03 47.995	PKS 0208-512	09-25-2008	79.75 ± 18.62	2.01 ± 0.17	5.3e+48
2FGL J0210.7-5102	02 09 17.040	−50 47 41.280	PKS 0208-512	05-09-2011	52.74 ± 15.71	2.36 ± 0.27	2.0e+48
2FGL J0211.2+1050	02 11 34.114	+10 51 57.706	CGRaBS J0211+1051	01-23-2011	52.84 ± 17.53	2.11 ± 0.24	...
2FGL J0222.6+4302	02 22 14.168	+42 57 56.923	3C 66A	10-02-2008	77.36 ± 19.16	2.12 ± 0.18	...
2FGL J0237.1-6136	02 37 16.923	−61 31 57.418	PKS 0235-618	06-10-2010	121.18 ± 24.54	2.21 ± 0.17	7.9e+47
2FGL J0237.8+2846	02 38 03.618	+28 56 21.741	4C +28.07	10-03-2011	154.53 ± 29.25	2.39 ± 0.19	9.7e+48
2FGL J0238.7+1637	02 38 44.600	+16 42 34.439	AO 0235+164	09-07-2008	133.51 ± 23.83	1.92 ± 0.12	9.5e+48
2FGL J0238.7+1637	02 39 00.457	+16 17 07.905	AO 0235+164	10-14-2008	71.70 ± 19.24	1.97 ± 0.17	4.5e+48
2FGL J0245.9-4652	02 45 56.955	−46 47 20.177	PKS 0244-470	02-12-2010	92.02 ± 23.85	1.99 ± 0.18	1.4e+49
2FGL J0252.7-2218	02 52 44.933	−22 25 14.758	PKS 0250-225	02-17-2009	28.96 ± 10.60	1.74 ± 0.20	9.4e+48
2FGL J0303.4-2407	03 03 11.595	−24 12 14.022	PKS 0301-243	04-28-2010	121.80 ± 19.73	1.92 ± 0.11	4.1e+47
2FGL J0319.8+4130	03 19 28.985	+41 27 44.320	NGC 1275	07-14-2010	46.96 ± 17.57	1.95 ± 0.23	5.0e+44
2FGL J0403.9-3604	04 05 12.184	−36 05 05.640	PKS 0402-362	09-22-2011	75.19 ± 20.60	2.28 ± 0.23	7.9e+48
2FGL J0403.9-3604	04 04 10.257	−36 15 44.399	PKS 0402-362	09-22-2011	379.70 ± 48.00	2.21 ± 0.11	4.3e+49
2FGL J0423.2-0120	04 23 22.057	−01 22 32.670	PKS 0420-01	01-21-2010	67.08 ± 16.28	1.92 ± 0.16	4.5e+48
2FGL J0428.6-3756	04 28 34.135	−37 51 00.554	PKS 0426-380	01-02-2010	111.56 ± 22.69	2.06 ± 0.15	8.6e+48
2FGL J0442.7-0017	04 42 54.321	−00 28 51.079	NRAO 190	05-16-2009	204.47 ± 34.19	2.38 ± 0.16	4.9e+48
2FGL J0457.0-2325	04 56 22.954	−23 27 48.035	PKS 0454-234	01-11-2009	216.78 ± 25.96	2.25 ± 0.11	9.5e+48
2FGL J0457.0-2325	04 57 16.222	−23 30 59.425	PKS 0454-234	10-22-2011	174.59 ± 20.97	1.99 ± 0.09	1.2e+49
2FGL J0505.5+0501	05 05 14.224	+04 59 38.269	PKS 0502+049	08-19-2011	99.34 ± 26.86	2.04 ± 0.16	5.5e+48
2FGL J0523.0-3628	05 23 50.598	−36 18 14.231	PKS 0521-36	06-17-2010	81.30 ± 19.35	2.36 ± 0.23	3.3e+45
2FGL J0530.8+1333	05 31 11.851	+13 32 45.781	PKS 0528+134	06-05-2011	95.69 ± 31.23	2.46 ± 0.29	2.6e+49
2FGL J0532.0-4826	05 31 33.784	−48 20 26.718	CRATES J0531-4827	09-25-2010	175.02 ± 47.70	2.27 ± 0.20	...
2FGL J0532.7+0733	05 32 32.440	+07 24 57.889	OG 050	11-07-2011	87.60 ± 24.84	2.04 ± 0.19	9.5e+48
2FGL J0538.8-4405	05 39 16.780	−44 05 47.645	PKS 0537-441	09-15-2008	74.27 ± 17.88	1.93 ± 0.17	4.5e+48
2FGL J0538.8-4405	05 40 05.402	−43 58 45.300	PKS 0537-441	07-08-2009	71.06 ± 22.15	2.29 ± 0.26	2.2e+48
2FGL J0538.8-4405	05 38 43.535	−44 10 07.446	PKS 0537-441	04-27-2010	115.26 ± 18.40	1.82 ± 0.10	9.7e+48
2FGL J0622.9+3326	06 22 54.834	+33 14 55.920	B2 0619+33	09-03-2010	85.45 ± 21.65	2.06 ± 0.18	...
PKS 0646-306[e]	06 47 53.852	−30 42 13.993	PKS 0646-306	01-22-2012	57.66 ± 17.46	2.24 ± 0.25	3.7e+48
2FGL J0654.2+4514	06 55 22.481	+45 14 09.627	B3 0650+453	08-22-2011	106.88 ± 21.91	2.31 ± 0.17	3.6e+48
2FGL J0714.0+1933	07 13 32.146	+19 27 46.398	MG2 J071354+1934	07-03-2009	77.80 ± 21.78	2.09 ± 0.20	9.3e+47
2FGL J0721.9+7120	07 21 17.288	+71 07 12.852	S5 0716+71	07-12-2011	130.12 ± 21.14	2.27 ± 0.15	...
2FGL J0725.3+1426	07 25 26.027	+14 28 23.410	4C +14.23	10-13-2009	115.68 ± 28.36	2.31 ± 0.21	5.1e+48
2FGL J0730.2-1141	07 33 27.840	−11 49 21.360	PKS 0727-115	01-29-2009	78.87 ± 0.00[b]	2.10 ± 0.34	...
2FGL J0730.2-1141	07 29 44.440	−11 37 39.727	PKS 0727-115	09-21-2010	126.11 ± 33.97	2.16 ± 0.19	2.1e+49
2FGL J0742.6+5442	07 43 39.357	+54 39 22.446	GB6 J0742+5444	02-26-2011	90.78 ± 18.21	2.19 ± 0.17	1.9e+48
2FGL J0742.6+5442	07 43 48.384	+54 40 47.031	GB6 J0742+5444	06-19-2011	69.43 ± 18.02	2.24 ± 0.21	1.3e+48
2FGL J0808.2-0750	08 08 56.674	−07 47 07.192	PKS 0805-07	05-14-2009	47.23 ± 17.89	1.80 ± 0.21	2.3e+49

Table 3—Continued

2FGL name	R.A.[c]	Dec.[c]	Name	Peak time	Peak Flux[a]	Index	Luminosity[d]
2FGL J0808.2-0750	08 08 05.299	−07 48 32.865	PKS 0805-07	07-22-2009	150.70 ± 24.69	2.08 ± 0.12	4.0e+49
2FGL J0841.6+7052	08 40 39.755	+71 20 45.934	S5 0836+71	04-03-2011	67.48 ± 19.55	2.91 ± 0.39	2.5e+49
2FGL J0841.6+7052	08 40 01.164	+70 48 06.602	S5 0836+71	12-25-2011	171.21 ± 26.06	2.59 ± 0.18	5.6e+49
SBS 0846+513[e]	08 50 35.378	+51 10 52.731	SBS 0846+513	06-21-2011	66.52 ± 18.09	2.14 ± 0.20	8.7e+47
2FGL J0854.8+2005	08 53 28.778	+20 11 52.938	OJ 287	10-22-2009	100.93 ± 21.81	2.21 ± 0.18	2.4e+47
2FGL J0854.8+2005	08 54 45.998	+20 05 33.893	OJ 287	10-10-2011	90.05 ± 17.97	1.81 ± 0.12	6.1e+47
2FGL J0909.1+0121	09 09 40.599	+01 07 55.140	PKS 0906+015	04-08-2010	82.52 ± 24.60	2.19 ± 0.23	4.2e+48
2FGL J0920.9+4441	09 20 44.183	+44 32 21.743	S4 0917+44	01-15-2009	61.28 ± 15.90	2.27 ± 0.22	2.1e+49
2FGL J0948.8+0020	09 48 49.976	+00 24 31.700	PMN J0948+0022	07-09-2010	94.25 ± 24.40	2.40 ± 0.24	8.5e+47
2FGL J0948.8+0020	09 45 59.775	+00 20 15.300	PMN J0948+0022	06-10-2011	89.06 ± 27.57	2.49 ± 0.27	7.4e+47
2FGL J1033.9+6050	10 34 16.077	+60 51 04.398	S4 1030+61	05-14-2010	166.23 ± 29.03	2.27 ± 0.16	1.7e+49
2FGL J1121.5-0554	11 21 44.743	−06 03 15.307	PKS 1118-056	02-17-2009	63.31 ± 13.71	1.85 ± 0.14	1.2e+49
PMN J1123-6417[e]	11 23 12.212	−64 18 45.893	PMN J1123-6417	05-30-2011	95.34 ± 0.00[b]	2.20 ± 0.34	...
2FGL J1126.6-1856	11 27 06.964	−19 10 21.148	PKS 1124-186	03-02-2011	67.28 ± 15.71	2.15 ± 0.19	3.8e+48
2FGL J1153.2+4935	11 53 25.646	+49 31 41.318	SBS 1150+497	04-25-2011	140.26 ± 24.35	2.10 ± 0.14	9.6e+48
2FGL J1153.2+4935	11 53 27.956	+49 37 37.465	SBS 1150+497	05-15-2011	193.55 ± 25.15	2.23 ± 0.12	1.1e+49
2FGL J1159.5+2914	12 01 13.344	+29 18 35.990	Ton 599	08-15-2010	105.26 ± 23.30	2.24 ± 0.19	2.0e+48
2FGL J1224.9+2122	12 24 50.830	+21 01 32.625	PKS 1222+216	04-16-2009	80.98 ± 19.61	2.48 ± 0.24	3.1e+47
2FGL J1224.9+2122	12 25 17.030	+21 26 33.854	PKS 1222+216	12-15-2009	336.43 ± 39.80	2.42 ± 0.12	1.4e+48
2FGL J1224.9+2122	12 24 50.859	+21 23 42.048	PKS 1222+216	04-24-2010	705.31 ± 48.97	1.93 ± 0.05	7.5e+48
2FGL J1224.9+2122	12 24 39.732	+21 25 58.490	PKS 1222+216	06-18-2010	1165.60 ± 61.35	2.07 ± 0.04	8.6e+48
2FGL J1229.1+0202	12 29 58.746	+02 07 02.409	3C 273	09-05-2008	74.46 ± 19.65	2.89 ± 0.33	1.9e+46
2FGL J1229.1+0202	12 28 38.305	+02 06 34.397	3C 273	08-19-2009	457.80 ± 48.97	2.79 ± 0.14	1.2e+47
2FGL J1229.1+0202	12 28 38.019	+02 06 09.850	3C 273	09-15-2009	263.69 ± 31.51	2.31 ± 0.11	1.1e+47
2FGL J1239.5+0443	12 39 24.945	+04 44 10.248	MG1 J123931+0443	12-29-2008	33.95 ± 12.44	2.05 ± 0.24	8.6e+48
2FGL J1239.5+0443	12 39 06.393	+04 46 59.239	MG1 J123931+0443	06-19-2011	89.47 ± 21.97	2.17 ± 0.19	1.9e+49
2FGL J1246.7-2546	12 46 21.195	−25 43 10.967	PKS 1244-255	01-05-2009	114.95 ± 23.58	2.17 ± 0.16	1.7e+48
2FGL J1256.1-0547	12 56 07.091	−05 47 16.349	3C 279	12-05-2008	166.83 ± 24.72	2.15 ± 0.12	1.7e+48
2FGL J1256.1-0547	12 56 32.332	−05 41 18.260	3C 279	08-01-2009	172.05 ± 25.35	2.27 ± 0.13	1.5e+48
2FGL J1256.1-0547	12 54 43.187	−05 30 03.811	3C 279	09-27-2010	348.31 ± 78.43	2.64 ± 0.27	2.1e+48
2FGL J1312.8+4828	13 12 48.974	+48 24 42.608	GB6 B1310+4844	11-26-2009	102.39 ± 17.65	1.70 ± 0.10	3.3e+48
2FGL J1332.0-0508	13 31 28.875	−04 59 49.901	PKS 1329-049	07-07-2010	81.76 ± 25.05	2.28 ± 0.25	2.6e+49
2FGL J1332.0-0508	13 33 32.824	−05 05 04.628	PKS 1329-049	09-06-2010	251.20 ± 62.99	2.32 ± 0.16	7.8e+49
2FGL J1345.4+4453	13 46 29.317	+44 46 23.863	B3 1343+451	09-25-2009	69.91 ± 18.22	2.42 ± 0.25	3.3e+49
2FGL J1345.4+4453	13 45 22.084	+44 50 25.835	B3 1343+451	11-29-2011	122.98 ± 20.46	2.19 ± 0.14	6.5e+49
2FGL J1428.0-4206	14 27 27.379	−42 04 35.987	PKS 1424-418	06-28-2009	90.82 ± 22.32	1.94 ± 0.15	2.0e+49
2FGL J1428.0-4206	14 27 53.133	−42 07 04.933	PKS 1424-418	04-21-2010	66.47 ± 18.11	1.87 ± 0.16	1.7e+49
2FGL J1428.0-4206	14 27 52.124	−42 16 02.705	PKS 1424-418	05-05-2011	82.85 ± 25.01	2.19 ± 0.23	1.2e+49
2FGL J1457.4-3540	14 57 35.551	−35 39 35.338	PKS 1454-354	09-04-2008	286.40 ± 31.27	1.93 ± 0.08	5.4e+49
2FGL J1504.3+1029	15 04 39.921	+10 28 16.422	PKS 1502+106	08-06-2008	432.70 ± 44.61	2.05 ± 0.08	1.2e+50
2FGL J1504.3+1029	15 04 30.035	+10 28 46.672	PKS 1502+106	01-21-2009	207.34 ± 28.34	2.27 ± 0.12	4.4e+49

Table 3—Continued

2FGL name	R.A.[c]	Dec.[c]	Name	Peak time	Peak Flux[a]	Index	Luminosity[d]
2FGL J1512.8-0906	15 12 18.673	−09 15 39.351	PKS 1510-089	09-13-2008	248.27 ± 33.80	2.46 ± 0.13	6.2e+47
2FGL J1512.8-0906	15 12 52.722	−09 05 32.862	PKS 1510-089	01-08-2009	254.87 ± 35.07	2.24 ± 0.12	8.4e+47
2FGL J1512.8-0906	15 13 03.065	−09 10 32.723	PKS 1510-089	04-25-2009	578.63 ± 54.45	2.51 ± 0.10	1.4e+48
2FGL J1512.8-0906	15 12 41.692	−08 59 30.422	PKS 1510-089	07-04-2011	808.13 ± 72.11	2.32 ± 0.08	2.4e+48
2FGL J1512.8-0906	15 12 53.346	−09 06 26.590	PKS 1510-089	10-19-2011	1429.30 ± 85.39	2.04 ± 0.05	7.1e+48
2FGL J1517.7-2421	15 17 41.813	−24 22 19.474	AP Lib	02-21-2011	74.26 ± 0.00[b]	2.36 ± 0.30	...
2FGL J1522.1+3144	15 22 07.075	+31 38 35.285	B2 1520+31	04-20-2009	76.81 ± 17.56	2.20 ± 0.19	1.0e+49
2FGL J1522.1+3144	15 21 50.314	+31 43 32.172	B2 1520+31	11-18-2010	162.21 ± 25.40	1.91 ± 0.10	3.6e+49
TXS 1530-131[e]	15 33 22.863	−13 33 12.258	TXS 1530-131	08-22-2011	71.58 ± 25.11	1.83 ± 0.20	...
2FGL J1625.7-2526	16 24 19.213	−25 34 28.524	PKS 1622-253	10-04-2009	151.16 ± 45.47	2.33 ± 0.23	3.2e+48
2FGL J1625.7-2526	16 26 11.324	−25 25 42.946	PKS 1622-253	06-07-2011	174.24 ± 25.96	2.21 ± 0.12	4.3e+48
2FGL J1626.1-2948	16 26 18.685	−29 42 28.976	PKS 1622-297	03-29-2010	59.82 ± 21.74	2.29 ± 0.28	1.4e+48
2FGL J1635.2+3810	16 35 18.607	+38 05 02.509	4C +38.41	07-22-2009	107.24 ± 20.99	2.34 ± 0.17	2.1e+49
2FGL J1635.2+3810	16 35 21.579	+38 05 13.533	4C +38.41	02-23-2010	59.98 ± 20.22	2.24 ± 0.26	1.3e+49
2FGL J1635.2+3810	16 35 39.290	+38 01 22.789	4C +38.41	05-08-2011	201.41 ± 29.01	2.46 ± 0.15	3.7e+49
2FGL J1642.9+3949	16 43 32.304	+40 01 15.452	3C 345	09-29-2009	68.01 ± 18.80	2.16 ± 0.22	9.0e+47
2FGL J1700.2+6831	17 00 02.601	+68 31 05.047	GB6 J1700+6830	03-22-2009	111.54 ± 19.59	2.02 ± 0.13	3.9e+47
2FGL J1709.7+4319	17 09 50.361	+43 14 34.785	B3 1708+433	11-09-2010	93.28 ± 20.92	2.07 ± 0.16	5.8e+48
2FGL J1733.1-1307	17 33 05.209	−12 59 20.260	PKS 1730-13	11-02-2010	145.35 ± 26.28	2.15 ± 0.13	5.6e+48
2FGL J1748.8+7006	17 48 23.829	+70 07 08.938	S4 1749+70	02-15-2011	67.70 ± 16.74	2.26 ± 0.21	1.5e+48
2FGL J1800.5+7829	18 02 15.553	+78 29 26.371	S5 1803+78	01-11-2010	84.67 ± 16.56	2.04 ± 0.15	2.0e+48
2FGL J1800.5+7829	18 01 55.513	+78 32 25.675	S5 1803+78	05-02-2011	116.88 ± 21.81	2.46 ± 0.19	1.5e+48
2FGL J1833.6-2104	18 33 43.169	−21 01 05.686	PKS 1830-211	10-14-2010	426.62 ± 73.84	2.49 ± 0.15	1.9e+50
2FGL J1848.5+3216	18 48 11.460	+32 19 10.738	CGRaBS J1848+3219	10-18-2010	171.85 ± 48.64	1.98 ± 0.12	7.0+48
2FGL J1849.4+6706	18 48 48.551	+67 08 00.144	CGRaBS J1849+6705	07-06-2011	236.91 ± 27.64	1.91 ± 0.08	7.1e+48
PMN J1913-3630[e]	19 12 57.307	−36 29 07.098	PMN J1913-3630	10-21-2010	101.39 ± 20.38	1.83 ± 0.12	...
PKS 1915-458[e]	19 18 46.005	−45 46 31.199	PKS 1915-458	06-04-2010	49.27 ± 0.00[b]	2.12 ± 0.40	...
2FGL J2025.6-0736	20 25 55.841	−07 42 48.668	PKS 2023-07	08-23-2009	125.89 ± 21.51	2.22 ± 0.14	1.3e+49
2FGL J2056.2-4715	20 55 15.798	−47 13 19.884	PKS 2052-474	08-09-2009	61.64 ± 19.78	2.12 ± 0.24	9.0e+48
PKS 2123-463[e]	21 26 06.992	−46 02 03.070	PKS 2123-463	12-14-2011	102.76 ± 22.61	2.20 ± 0.19	1.8e+49
2FGL J2143.5+1743	21 42 50.232	+17 49 41.505	OX 169	01-18-2010	129.38 ± 30.43	2.67 ± 0.26	7.4e+46
2FGL J2147.4-7534	21 42 43.003	−75 33 05.011	PKS 2142-75	04-04-2010	132.98 ± 29.32	2.41 ± 0.21	7.0e+48
2FGL J2158.8-3013	21 58 46.202	−30 18 00.385	PKS 2155-304	10-13-2010	71.20 ± 21.11	2.48 ± 0.29	1.2e+46
2FGL J2201.9-8335	22 01 21.108	−83 45 38.365	PKS 2155-83	01-05-2010	123.26 ± 25.16	2.13 ± 0.16	3.2e+49
2FGL J2202.8+4216	22 04 12.544	+42 09 11.457	BL Lacertae	01-21-2010	59.91 ± 17.44	2.06 ± 0.20	7.1e+45
2FGL J2202.8+4216	22 03 02.857	+42 24 09.886	BL Lacertae	05-20-2011	107.63 ± 22.34	2.30 ± 0.17	7.7e+45
2FGL J2225.6-0454	22 24 46.895	−04 35 36.529	3C 446	10-08-2011	128.14 ± 37.75	3.90 ± 0.61	2.1e+49
2FGL J2232.4+1143	22 32 41.821	+11 45 54.098	CTA 102	04-29-2011	133.93 ± 25.75	2.05 ± 0.14	8.9e+48
2FGL J2236.5-1431	22 35 38.619	−14 22 35.987	PKS 2233-148	04-23-2010	92.22 ± 29.55	2.25 ± 0.25	...
2FGL J2250.8-2808	22 51 15.957	−28 06 27.054	PMN J2250-2806	03-25-2009	142.17 ± 22.31	2.09 ± 0.13	1.6e+48
2FGL J2253.9+1609	22 54 14.870	+16 15 35.834	3C 454.3	09-15-2008	482.71 ± 46.45	2.58 ± 0.11	1.1e+49

Table 3—Continued

2FGL name	R.A.[c]	Dec.[c]	Name	Peak time	Peak Flux[a]	Index	Luminosity[d]
2FGL J2253.9+1609	22 54 14.477	+16 10 29.185	3C 454.3	12-02-2009	2008.40 ± 85.43	2.34 ± 0.04	5.3e+49
2FGL J2253.9+1609	22 54 14.342	+16 07 49.543	3C 454.3	04-03-2010	1086.90 ± 75.03	2.43 ± 0.07	2.6e+49
2FGL J2253.9+1609	22 53 52.993	+16 08 58.100	3C 454.3	11-16-2010	1562.80 ± 70.95	2.31 ± 0.04	4.3e+49
2FGL J2311.0+3425	23 11 15.542	+34 20 20.498	B2 2308+34	08-07-2010	75.91 ± 19.17	1.87 ± 0.16	3.1e+49
2FGL J2329.2-4956	23 28 33.929	−49 49 32.560	PKS 2326-502	08-07-2010	140.70 ± 34.24	2.81 ± 0.28	7.3e+47
2FGL J2330.9-2144	23 31 32.278	−21 59 55.907	PMN J2331-2148	06-26-2009	50.28 ± 13.90	2.08 ± 0.21	6.8e+47
2FGL J2345.0-1553	23 45 38.461	−15 57 02.387	PMN J2345-1555	01-27-2010	96.74 ± 15.48	1.86 ± 0.11	2.9e+48
2FGL J2345.0-1553	23 46 10.477	−15 55 39.004	PMN J2345-1555	10-24-2010	43.03 ± 13.13	2.08 ± 0.23	7.4e+47

Note. — [a]: Flux is in units of [10^{-08} ph cm^{-2} s^{-1}]. [b]: The value reproted is the 95% upper limit estimated above 100 MeV since the source was not significantly detected in this interval (ts<25). [c]: recalculated position as desribed in paragraph **??**. [d]: lumonosity is in units of [erg cm^{-2} s^{-1}]. [e]: source not listed in the 2FGL catalog.

BIBLIOGRAPHY

Abbasi, R., et al. (2009) Extending the Search for Neutrino Point Sources with IceCube above the Horizon. *Physical Review Letters*, **103, 22**, 221102. 0911.2338. (Cited on page 170.)

Abdo, A. A. and et al. (2013a) in preparation. (Cited on page 167.)

— (2013b) in preparation. (Cited on page 194.)

Abdo, A. A. and et al. (2013) in preparation. (Cited on page 153.)

Abdo, A. A., et al. (2009a) Bright Active Galactic Nuclei Source List from the First Three Months of the Fermi Large Area Telescope All-Sky Survey. *Astrophys. J.*, **700**, 597. 0902.1559. (Cited on pages 24, 81, 95, 104, 108, 177, 186, 187, 203, and 204.)

— (2009b) Fermi Large Area Telescope Measurements of the Diffuse Gamma-Ray Emission at Intermediate Galactic Latitudes. *Physical Review Letters*, **103, 25**, 251101. 0912.0973. (Cited on page 71.)

— (2009c) Fermi/Large Area Telescope Discovery of Gamma-Ray Emission from a Relativistic Jet in the Narrow-Line Quasar PMN J0948+0022. *Astrophys. J.*, **699**, 976. 0905.4558. (Cited on page 201.)

— (2009d) Radio-Loud Narrow-Line Seyfert 1 as a New Class of Gamma-Ray Active Galactic Nuclei. *Astrophys. J. Lett.*, **707**, L142. 0911.3485. (Cited on page 201.)

— (2009e) The on-orbit calibration of the Fermi Large Area Telescope. *Astroparticle Physics*, **32**, 193. 0904.2226. (Cited on pages 49, 50, 51, 58, 59, and 62.)

— (2010a) A change in the optical polarization associated with a γ-ray flare in the blazar 3C279. *Nature*, **463**, 919. 1004.3828. (Cited on page 186.)

— (2010b) Fermi Large Area Telescope and Multi-wavelength Observations of the Flaring Activity of PKS 1510-089 between 2008 September and 2009 June. *Astrophys. J.*, **721**, 1425. 1007.1237. (Cited on pages 142, 176, and 203.)

— (2010c) Fermi Large Area Telescope First Source Catalog. *Astrophys. J. Suppl. S.*, **188**, 405. 1002.2280. (Cited on pages 59, 63, 84, 117, 133, 170, and 203.)

— (2010d) Fermi Large Area Telescope Observations of Misaligned Active Galactic Nuclei. *Astrophys. J.*, **720**, 912. (Cited on page 201.)

— (2010e) Fermi Observations of the Very Hard Gamma-ray Blazar PG 1553+113. *Astrophys. J.*, **708**, 1310. 0911.4252. (Cited on pages 80, 81, 83, 85, 87, 90, 91, 94, and 192.)

— (2010f) Gamma-Ray Emission Concurrent with the Nova in the Symbiotic Binary V407 Cygni. *Science*, **329**, 817. 1008.3912. (Cited on pages 154 and 155.)

— (2010g) Gamma-ray Light Curves and Variability of Bright Fermi-detected Blazars. *Astrophys. J.*, **722**, 520. 1004.0348. (Cited on pages 88, 95, and 158.)

— (2010h) PKS 1502+106: A New and Distant Gamma-ray Blazar in Outburst Discovered by the Fermi Large Area Telescope. *Astrophys. J.*, **710**, 810. 0912.4029. (Cited on page 186.)

— (2010i) Spectral Properties of Bright Fermi-Detected Blazars in the Gamma-Ray Band. *Astrophys. J.*, **710**, 1271. 1001.4097. (Cited on page 187.)

— (2010j) Spectrum of the Isotropic Diffuse Gamma-Ray Emission Derived from First-Year Fermi Large Area Telescope Data. *Physical Review Letters*, **104, 10**, 101101. 1002.3603. (Cited on page 55.)

— (2010k) The First Catalog of Active Galactic Nuclei Detected by the Fermi Large Area Telescope. *Astrophys. J.*, **715**, 429. 1002.0150. (Cited on page 185.)

— (2010l) The First Fermi Large Area Telescope Catalog of Gamma-ray Pulsars. *Astrophys. J. Suppl. S.*, **187**, 460. 0910.1608. (Cited on page 171.)

— (2010m) The Spectral Energy Distribution of Fermi Bright Blazars. *Astrophys. J.*, **716**, 30. 0912.2040. (Cited on pages 10 and 187.)

— (2011) Fermi Gamma-ray Space Telescope Observations of the Gamma-ray Outburst from 3C454.3 in November 2010. *Astrophys. J. Lett.*, **733**, L26. (Cited on pages 162, 185, and 186.)

— (2013) Determination of the Point-Spread Function for the Fermi Large Area Telescope from On-orbit Data and Limits on Pair Halos. (Cited on page 63.)

Abramowicz, M. A., Bjornsson, G., and Pringle, J. E. (Editors) (1998) *Theory of Black Hole Accretion Disks*. (Cited on page 20.)

Acciari, V., et al. (2009) Discovery of Very High Energy Gamma-ray Radiation from the BL Lac 1ES 0806+524. *Astrophys. J. Lett.*, **690**, L126. 0812.0978. (Cited on pages 121, 124, 128, and 130.)

Acciari, V. A., et al. (2010) Discovery of Variability in the Very High Energy γ-Ray Emission of 1ES 1218+304 with VERITAS. *Astrophys. J. Lett.*, **709**, L163. 1001.2590. (Cited on page 96.)

Ackermann, M., et al. (2010a) Fermi Gamma-ray Space Telescope Observations of Gamma-ray Outbursts from 3C 454.3 in 2009 December and 2010 April. *Astrophys. J.*, **721**, 1383. 1007.0483. (Cited on page 185.)

— (2010b) Fermi LAT observations of cosmic-ray electrons from 7 GeV to 1 TeV. *Phys. Rev. D*, **82, 9**, 092004. 1008.3999. (Cited on page 51.)

— (2011) The Second Catalog of Active Galactic Nuclei Detected by the Fermi Large Area Telescope. *Astrophys. J.*, **743**, 171. 1108.1420. (Cited on pages 25, 30, 40, 112, and 158.)

— (2012) The Imprint of the Extragalactic Background Light in the Gamma-Ray Spectra of Blazars. *Science*, **338**, 1190. 1211.1671. (Cited on page 194.)

Aharonian, F., et al. (2004) Observations of 54 Active Galactic Nuclei with the HEGRA system of Cherenkov telescopes. *Astron. Astrophys.*, **421**, 529. (Cited on page 121.)

— (2006) Evidence for VHE γ-ray emission from the distant BL Lac PG 1553+113. *Astron. Astrophys.*, **448**, L19. arXiv:astro-ph/0601545. (Cited on page 82.)

— (2007) An Exceptional Very High Energy Gamma-Ray Flare of PKS 2155-304. *Astrophys. J. Lett.*, **664**, L71. 0706.0797. (Cited on page 14.)

— (2009a) Simultaneous multiwavelength observations of the second exceptional γ-ray flare of PKS 2155-304 in July 2006. *Astron. Astrophys.*, **502**, 749. 0906.2002. (Cited on pages vii and ix.)

— (2009b) Simultaneous Observations of PKS 2155-304 with HESS, Fermi, RXTE, and Atom: Spectral Energy Distributions and Variability in a Low State. *Astrophys. J. Lett.*, **696**, L150. 0903.2924. (Cited on page 90.)

Aharonian, F. A. (2000) TeV gamma rays from BL Lac objects due to synchrotron radiation of extremely high energy protons. *New Astron.*, **5**, 377. arXiv:astro-ph/0003159. (Cited on page 38.)

Akiyama, M., et al. (2003) Optical Identification of the ASCA Medium Sensitivity Survey in the Northern Sky: Nature of Hard X-Ray-Selected Luminous Active Galactic Nuclei. *Astrophys. J. Suppl. S.*, **148**, 275. arXiv:astro-ph/0307164. (Cited on page 95.)

Albert, J., et al. (2007a) Detection of Very High Energy Radiation from the BL Lacertae Object PG 1553+113 with the MAGIC Telescope. *Astrophys. J. Lett.*, **654**, L119. arXiv:astro-ph/0606161. (Cited on pages 82, 84, and 88.)

— (2007b) Variable Very High Energy γ-Ray Emission from Markarian 501. *Astrophys. J.*, **669**, 862. arXiv:astro-ph/0702008. (Cited on page 14.)

— (2008a) Implementation of the Random Forest method for the Imaging Atmospheric Cherenkov Telescope MAGIC. *Nuclear Instruments and Methods in Physics Research A*, **588**, 424. 0709.3719. (Cited on page 121.)

— (2008b) VHE γ-Ray Observation of the Crab Nebula and its Pulsar with the MAGIC Telescope. *Astrophys. J.*, **674**, 1037. 0705.3244. (Cited on pages 3, 128, 133, and 138.)

— (2009a) MAGIC observations of PG 1553+113 during a multi-wavelength campaign in July 2006. *Astron. Astrophys.*, **493**, 467. 0812.3037. (Cited on page 84.)

— (2009b) MAGIC observations of PG 1553+113 during a multi-wavelength campaign in July 2006. *Astron. Astrophys.*, **493**, 467. 0812.3037. (Cited on page 88.)

Aleksić, J., et al., (MAGIC Collaboration), and Buson, S. (2013a) in preparation. (Cited on pages 121, 124, and 131.)

— (2013b) in preparation. (Cited on page 133.)

— (2013c) in preparation. (Cited on page 141.)

Aleksić, J., et al. (2010) Simultaneous multi-frequency observation of the unknown redshift blazar PG 1553+113 in March-April 2008. *Astron. Astrophys.*, **515**, A76. 0911.1088. (Cited on page 93.)

— (2011a) Gamma-ray Excess from a Stacked Sample of High- and Intermediate-frequency Peaked Blazars Observed with the MAGIC Telescope. *Astrophys. J.*, **729**, 115. 1002.2951. (Cited on pages 95, 112, 121, 133, and 139.)

— (2011b) MAGIC Discovery of Very High Energy Emission from the FSRQ PKS 1222+21. *Astrophys. J. Lett.*, **730**, L8. 1101.4645. (Cited on page 141.)

— (2011c) MAGIC Observations and multiwavelength properties of the quasar 3C 279 in 2007 and 2009. *Astron. Astrophys.*, **530**, A4. 1101.2522. (Cited on page 141.)

— (2012a) Discovery of VHE γ-ray emission from the BL Lacertae object B3 2247+381 with the MAGIC telescopes. *Astron. Astrophys.*, **539**, A118. 1201.2634. (Cited on pages 78 and 112.)

— (2012b) Discovery of VHE γ-rays from the blazar 1ES 1215+303 with the MAGIC telescopes and simultaneous multi-wavelength observations. *Astron. Astrophys.*, **544**, A142. 1203.0490. (Cited on pages 78 and 95.)

— (2012c) Performance of the MAGIC stereo system obtained with Crab Nebula data. *Astroparticle Physics*, **35**, 435. 1108.1477. (Cited on page 77.)

— (2012d) PG 1553+113: Five Years of Observations with MAGIC. *Astrophys. J.*, **748**, 46. 1101.2764. (Cited on page 80.)

Aliu, E., et al. (2009) Improving the performance of the single-dish Cherenkov telescope MAGIC through the use of signal timing. *Astroparticle Physics*, **30**, 293. 0810.3568. (Cited on page 77.)

Allison, J., et al. (2006) Geant4 developments and applications. *IEEE Transactions on Nuclear Science*, **53**, 270. (Cited on page 51.)

Atwood, W. B., et al. (2007) Design and initial tests of the Tracker-converter of the Gamma-ray Large Area Space Telescope. *Astroparticle Physics*, **28**, 422. (Cited on page 46.)

— (2009) The Large Area Telescope on the Fermi Gamma-Ray Space Telescope Mission. *Astrophys. J.*, **697**, 1071. 0902.1089. (Cited on pages 46, 47, 48, 50, and 58.)

Baldini, L., et al. (2006) The Silicon Tracker Readout Electronics of the Gamma-Ray Large Area Space Telescope. *IEEE Transactions on Nuclear Science*, **53**, 466. (Cited on page 47.)

— (2007) Preliminary results of the LAT Calibration Unit beam tests. In Ritz, S., Michelson, P., and Meegan, C. A. (Editors), *The First GLAST Symposium*, volume 921 of *American Institute of Physics Conference Series*, pp. 190–204. (Cited on page 51.)

Barnacka, A., Glicenstein, J.-F., and Moudden, Y. (2011) First evidence of a gravitational lensing-induced echo in gamma rays with Fermi LAT. *Astron. Astrophys.*, **528**, L3. 1011.4498. (Cited on pages 168, 171, 181, 182, and 187.)

Barthelmy, S. D., et al. (2005) The Burst Alert Telescope (BAT) on the SWIFT Midex Mission. *Space Sci. Rev.*, **120**, 143. arXiv:astro-ph/0507410. (Cited on page 78.)

Bassani, L., et al. (2006) INTEGRAL IBIS Extragalactic Survey: Active Galactic Nuclei Selected at 20-100 keV. *Astrophys. J. Lett.*, **636**, L65. arXiv:astro-ph/0512015. (Cited on page 169.)

Beckmann, V., et al. (2002) BeppoSAX spectral survey of BL Lacs - New spectra and results. *Astron. Astrophys.*, **383**, 410. arXiv:astro-ph/0112311. (Cited on page 80.)

Bednarek, W. (1993) On the gamma-ray emission from 3C 279. *Astrophys. J. Lett.*, **402**, L29. (Cited on page 39.)

Bennett, C. L., et al. (1986) The MIT-Green Bank (MG) 5 GHz survey. *Astrophys. J. Suppl. S.*, **61**, 1. (Cited on page 80.)

Bertsch, D. L., et al. (1993) Detection of gamma-ray emission from the quasar PKS 0208-512. *Astrophys. J. Lett.*, **405**, L21. (Cited on page 201.)

Bessell, M. S. (1979) UBVRI photometry. II - The Cousins VRI system, its temperature and absolute flux calibration, and relevance for two-dimensional photometry. *PASP*, **91**, 589. (Cited on page 78.)

Birkinshaw, M., Worrall, D. M., and Hardcastle, M. J. (2002) The X-ray jet and halo of PKS 0521-365. *Mon. Not. R. Astron. Soc.*, **335**, 142. arXiv:astro-ph/0204509. (Cited on page 202.)

Bisnovatyi-Kogan, G. S. and Tsupko, O. Y. (2010) Gravitational lensing in a non-uniform plasma. *Mon. Not. R. Astron. Soc.*, **404**, 1790. 1006.2321. (Cited on page 188.)

— (2012) Gravitational lens . *Mem. Soc. Astron. Italiana*, **83**, 54. (Cited on page 185.)

Blackburne, J. A., Pooley, D., and Rappaport, S. (2006) X-Ray and Optical Flux Anomalies in the Quadruply Lensed QSO 1RXS J1131-1231. *Astrophys. J.*, **640**, 569. arXiv:astro-ph/0509027. (Cited on page 188.)

Blandford, R. and Eichler, D. (1987) Particle acceleration at astrophysical shocks: A theory of cosmic ray origin. *Phys. Rep.*, **154**, 1. (Cited on pages 29 and 31.)

Blandford, R. D. and Payne, D. G. (1982) Hydromagnetic flows from accretion discs and the production of radio jets. *Mon. Not. R. Astron. Soc.*, **199**, 883. (Cited on page 18.)

Blandford, R. D. and Rees, M. J. (1978) Extended and compact extragalactic radio sources - Interpretation and theory. *Phys. Scr*, **17**, 265. (Cited on page 12.)

Blandford, R. D. and Znajek, R. L. (1977) Electromagnetic extraction of energy from Kerr black holes. *Mon. Not. R. Astron. Soc.*, **179**, 433. (Cited on pages 18 and 20.)

Błażejowski, M., et al. (2000) Comptonization of Infrared Radiation from Hot Dust by Relativistic Jets in Quasars. *Astrophys. J.*, **545**, 107. arXiv:astro-ph/0008154. (Cited on page 41.)

Blumenthal, G. R. and Gould, R. J. (1970) Bremsstrahlung, Synchrotron Radiation, and Compton Scattering of High-Energy Electrons Traversing Dilute Gases. *Reviews of Modern Physics*, **42**, 237. (Cited on pages 33 and 37.)

Boettcher, M. (2010) Models for the Spectral Energy Distributions and Variability of Blazars. *ArXiv e-prints*. 1006.5048. (Cited on page 41.)

Boinee, P., et al. (2003) Gleam: the GLAST Large Area Telescope Simulation Framework. In Ciprini, S., et al. (Editors), *Science with the New Generation of High Energy Gamma-Ray Experiments : Between Astrophysics and Astroparticle Physics*, p. 141. arXiv:astro-ph/0308120. (Cited on page 51.)

Bolton, J. G., Clarke, M. E., and Ekers, R. D. (1965) Identification of extragalactic radio sources between declinations -20deg and -44deg. *Australian Journal of Physics*, **18**, 627. (Cited on page 202.)

Böttcher, M., Mukherjee, R., and Reimer, A. (2002) Predictions of the High-Energy Emission from BL Lacertae Objects: The Case of W Comae. *Astrophys. J.*, **581**, 143. arXiv:astro-ph/0208171. (Cited on page 38.)

Breiman, e. a. (1984) *Classification and Regression Trees*. (Cited on page 53.)

Browne, I. W. A., et al. (2003) The Cosmic Lens All-Sky Survey - II. Gravitational lens candidate selection and follow-up. *Mon. Not. R. Astron. Soc.*, **341**, 13. arXiv:astro-ph/0211069. (Cited on page 194.)

Buehler, R. (2009) Fermi LAT detection of a GeV flare from the high redshift blazar B3 1343+451. *The Astronomer's Telegram*, **2217**, 1. (Cited on page 185.)

Burbidge, G. and Hewitt, A. (1987) An updated list of BL Lac objects, and their relation to galaxies and quasistellar objects. *Astronom. J.*, **93**, 1. (Cited on page 202.)

— (1990) The redshift peak at Z = 0.06. *Astrophys. J. Lett.*, **359**, L33. (Cited on page 202.)

Burnett, T. H. (2007) Localization of Gamma-ray Point Sources with the GLAST LAT. In Ritz, S., Michelson, P., and Meegan, C. A. (Editors), *The First GLAST Symposium*, volume 921 of *American Institute of Physics Conference Series*, pp. 530–531. (Cited on page 170.)

Burrows, D. N., et al. (2005) The Swift X-Ray Telescope. *Space Sci. Rev.*, **120**, 165. arXiv:astro-ph/0508071. (Cited on page 78.)

Buson, S., et al. (2012) FERMI LAT view of a sample of flaring gamma-ray AGN. In Aharonian, F. A., Hofmann, W., and Rieger, F. M. (Editors), *American Institute of Physics Conference Series*, volume 1505 of *American Institute of Physics Conference Series*, pp. 510–513. (Cited on page 153.)

Cameron, R. A. (2007) The GLAST LAT Instrument Science Operations Center. In Ritz, S., Michelson, P., and Meegan, C. A. (Editors), *The First GLAST Symposium*, volume 921 of *American Institute of Physics Conference Series*, pp. 534–535. (Cited on page 156.)

Carmona, E., et al. (2011) Performance of the MAGIC Stereo System. *ArXiv e-prints*. 1110.0947. (Cited on page 77.)

Carrasco, L., et al. (2010) NIR flaring of the blazar B2 0619+33. *The Astronomer's Telegram*, **2849**, 1. (Cited on page 202.)

Cash, W. (1979) Parameter estimation in astronomy through application of the likelihood ratio. *Astrophys. J.*, **228**, 939. (Cited on page 65.)

Celotti, A. and Fabian, A. C. (1993) The Kinetic Power and Luminosity of Parsecscale Radio Jets - an Argument for Heavy Jets. *Mon. Not. R. Astron. Soc.*, **264**, 228. (Cited on page 18.)

Celotti, A. and Ghisellini, G. (2008) The power of blazar jets. *Mon. Not. R. Astron. Soc.*, **385**, 283. 0711.4112. (Cited on pages 93 and 170.)

Chen, B., et al. (2011) Discovery of Energy-dependent X-Ray Microlensing in Q2237+0305. *Astrophys. J. Lett.*, **740**, L34. 1106.6052. (Cited on pages 24 and 188.)

Chiang, J. (2007) LAT Automated Science Processing for Gamma-Ray Bursts. In Axelsson, M. and Ryde, F. (Editors), *Gamma-Ray Bursts: Prospects for GLAST*, volume 906 of *American Institute of Physics Conference Series*, pp. 11–17. (Cited on page 156.)

Ciprini, S. (2010) Fermi LAT detection of an intense GeV flare from the high-redshift and gravitationally lensed blazar PKS 1830-211. *The Astronomer's Telegram*, **2943**, 1. (Cited on page 170.)

— (2012) Fermi LAT detection of a GeV flare from the gravitationally lensed blazar S3 0218+35. *The Astronomer's Telegram*, **4343**, 1. (Cited on page 194.)

Ciprini, S. and Fermi-LAT Collaboration (2012) Four years of Fermi LAT flare advocate activity. In Aharonian, F. A., Hofmann, W., and Rieger, F. M. (Editors), *American Institute of Physics Conference Series*, volume 1505 of *American Institute of Physics Conference Series*, pp. 697–700. 1111.6803. (Cited on pages 154 and 155.)

Ciprini, S. et al. (2007) 1D, 2D, 3D wavelet methods for gamma-ray source analysis. In Ritz, S., Michelson, P., and Meegan, C. A. (Editors), *The First GLAST Symposium*, volume 921 of *American Institute of Physics Conference Series*, pp. 546–547. (Cited on page 156.)

Cortina, J. (2012) MAGIC detects very high energy gamma-ray emission from the FSRQ PKS 1510-089. *The Astronomer's Telegram*, **3965**, 1. (Cited on pages 141 and 143.)

Costamante, L. (2008) Simultaneous X-RAY/TeV Observations of AN Exceptional Flare of PKS 2155-304. *International Journal of Modern Physics D*, **17**, 1449. (Cited on page 90.)

Costamante, L. and Ghisellini, G. (2002) TeV candidate BL Lac objects. *Astron. Astrophys.*, **384**, 56. arXiv:astro-ph/0112201. (Cited on pages 78, 82, 95, 121, 133, 138, and 139.)

Costamante, L., et al. (2001) Extreme synchrotron BL Lac objects. Stretching the blazar sequence. *Astron. Astrophys.*, **371**, 512. arXiv:astro-ph/0103343. (Cited on page 24.)

Courbin, F., et al. (1998) Image Deconvolution of the Radio Ring PKS 1830-211. *Astrophys. J. Lett.*, **499**, L119. arXiv:astro-ph/9802156. (Cited on page 168.)

— (2002) Cosmic Alignment toward the Radio Einstein Ring PKS 1830-211? *Astrophys. J.*, **575**, 95. arXiv:astro-ph/0202026. (Cited on page 168.)

Cramer, H. (1946) Book Reviews: Mathematical Methods of Statistics. *Science*, **104**, 450. (Cited on page 66.)

Cusumano, G., et al. (2010) The Palermo Swift-BAT hard X-ray catalogue. III. Results after 54 months of sky survey. *Astron. Astrophys.*, **524**, A64. 1009.0522. (Cited on page 91.)

D'Ammando, F. (2011) Fermi LAT detection of a GeV flare from the high-redshift blazar PKS 0528+134. *The Astronomer's Telegram*, **3412**, 1. (Cited on page 161.)

D'Ammando, F. and Gasparrini, D. (2011) Fermi LAT detection of a very intense and rapid gamma-ray flare from the blazar PKS 1510-089. *The Astronomer's Telegram*, **3473**, 1. (Cited on page 141.)

D'Ammando, F., et al. (2009) AGILE detection of the flaring gamma-ray blazar PKS 1510-089. *The Astronomer's Telegram*, **1957**, 1. (Cited on page 203.)

— (2011) AGILE detection of extreme γ-ray activity from the blazar PKS 1510-089 during March 2009. Multifrequency analysis. *Astron. Astrophys.*, **529**, A145. 1103.3647. (Cited on pages 142 and 147.)

— (2012a) PKS 2123-463: a confirmed γ-ray blazar at high redshift. *Mon. Not. R. Astron. Soc.*, **427**, 893. 1209.0479. (Cited on page 203.)

— (2012b) SBS 0846+513: a new gamma-ray emitting Narrow-Line Seyfert 1 galaxy. *ArXiv e-prints*. 1207.3092. (Cited on page 201.)

Danforth, C. W., et al. (2010) Hubble/COS Observations of the Lyα Forest Toward the BL Lac Object 1ES 1553+113. *Astrophys. J.*, **720**, 976. (Cited on page 80.)

Dar, A. and Laor, A. (1997) Hadronic Production of TeV Gamma-Ray Flares from Blazars. *Astrophys. J. Lett.*, **478**, L5. arXiv:astro-ph/9610252. (Cited on page 39.)

Davis, J. E. (2001) The Formal Underpinnings of the Response Functions Used in X-Ray Spectral Analysis. *Astrophys. J.*, **548**, 1010. arXiv:astro-ph/0011068. (Cited on page 56.)

De Caneva, G., et al. (2012) MAGIC discovery of the BL Lac 1ES 1727+502: Multiwavelength observations, spectral behavior and variability. In Aharonian, F. A., Hofmann, W., and Rieger, F. M. (Editors), *American Institute of Physics Conference Series*, volume 1505 of *American Institute of Physics Conference Series*, pp. 526–529. (Cited on page 133.)

de la Calle Pérez, I., et al. (2003) Search for High-Energy Gamma Rays from an X-Ray-selected Blazar Sample. *Astrophys. J.*, **599**, 909. arXiv:astro-ph/0309063. (Cited on page 121.)

de Rosa, A., et al. (2005) The broad-band X-ray spectrum of the blazar PKS B1830-211 by Chandra and INTEGRAL. *Astron. Astrophys.*, **438**, 121. arXiv:astro-ph/0504137. (Cited on pages 169, 170, 174, 182, 183, and 184.)

de Vaucouleurs, G., et al. (1991) *Third Reference Catalogue of Bright Galaxies. Volume I: Explanations and references. Volume II: Data for galaxies between 0^h and 12^h. Volume III: Data for galaxies between 12^h and 24^h.* (Cited on page 133.)

Dermer, C. D. and Schlickeiser, R. (1993) Model for the High-Energy Emission from Blazars. *Astrophys. J.*, **416**, 458. (Cited on pages 38 and 41.)

— (2002) Transformation Properties of External Radiation Fields, Energy-Loss Rates and Scattered Spectra, and a Model for Blazar Variability. *Astrophys. J.*, **575**, 667. arXiv:astro-ph/0202280. (Cited on page 42.)

Dermer, C. D., et al. (2009) Gamma-Ray Studies of Blazars: Synchro-Compton Analysis of Flat Spectrum Radio Quasars. *Astrophys. J.*, **692**, 32. 0808.3185. (Cited on page 183.)

Djorgovski, S., et al. (1992) A search for the optical/IR counterpart of the probable Einstein ring source 1830-211. *Mon. Not. R. Astron. Soc.*, **257**, 240. (Cited on page 168.)

Dobler, G. and Keeton, C. R. (2006) Finite source effects in strong lensing: implications for the substructure mass scale. *Mon. Not. R. Astron. Soc.*, **365**, 1243. arXiv:astro-ph/0502436. (Cited on page 188.)

Domínguez, A., et al. (2011) Extragalactic background light inferred from AEGIS galaxy-SED-type fractions. *Mon. Not. R. Astron. Soc.*, **410**, 2556. 1007.1459. (Cited on pages 91, 104, 107, 115, and 136.)

Donato, D. (2010) Fermi LAT observed another strong GeV flare from 4C 21.35 (PKS 1222+21). *The Astronomer's Telegram*, **2584**, 1. (Cited on page 203.)

Donato, D., Wood, D., and Cheung, C. C. (2010a) Fermi LAT detection of gamma-ray flaring activity from the radio galaxy NGC 1275. *The Astronomer's Telegram*, **2737**, 1. (Cited on page 201.)

Donato, D., et al. (2001) Hard X-ray properties of blazars (Donato+, 2001). *VizieR Online Data Catalog*, **337**, 50739. (Cited on pages 112 and 139.)

— (2010b) Flaring blazar B2 0619+33: Swift X-ray and UV/optical observations. *The Astronomer's Telegram*, **2848**, 1. (Cited on page 202.)

Dondi, L. and Ghisellini, G. (1995) Gamma-ray-loud blazars and beaming. *Mon. Not. R. Astron. Soc.*, **273**, 583. (Cited on page 201.)

Donnarumma, I., et al. (2010) AGILE detection of prolonged gamma-ray activity from the blazar PKS 1830-211. *The Astronomer's Telegram*, **2950**, 1. (Cited on page 170.)

— (2011) The Remarkable γ-Ray Activity in the Gravitationally Lensed Blazar PKS 1830-211. *Astrophys. J. Lett.*, **736**, L30. 1106.4224. (Cited on pages 170, 173, and 186.)

Elliot, J. L. and Shapiro, S. L. (1974) On the Variability of the Compact Nonthermal Sources. *Astrophys. J. Lett.*, **192**, L3. (Cited on page 186.)

Errando, M., et al. (2008) Discovery of very high energy gamma-rays from the flat spectrum radio quasar 3C 279 with the MAGIC telescope. In Aharonian, F. A., Hofmann, W., and Rieger, F. (Editors), *American Institute of Physics Conference Series*, volume 1085 of *American Institute of Physics Conference Series*, pp. 423–426. 0901.3275. (Cited on page 141.)

Esposito, J. A., et al. (1999) In-Flight Calibration of EGRET on the Compton Gamma-Ray Observatory. *Astrophys. J. Suppl. S.*, **123**, 203. (Cited on page 48.)

Fabian, A. C., et al. (2001a) PMN J0525-3343: soft X-ray spectral flattening in a blazar at z=4.4. *Mon. Not. R. Astron. Soc.*, **323**, 373. arXiv:astro-ph/0011566. (Cited on page 24.)

— (2001b) The blazar GB 1428+4217: a warm absorber at z=4.72? *Mon. Not. R. Astron. Soc.*, **324**, 628. arXiv:astro-ph/0101288. (Cited on pages 24 and 174.)

Falco, E. E., Kochanek, C. S., and Munoz, J. A. (1998) Limits on Cosmological Models from Radio-selected Gravitational Lenses. *Astrophys. J.*, **494**, 47. arXiv:astro-ph/9707032. (Cited on page 112.)

Falomo, R., Scarpa, R., and Bersanelli, M. (1994) Optical spectrophotometry of blazars. *Astrophys. J. Suppl. S.*, **93**, 125. (Cited on page 81.)

Falomo, R. and Treves, A. (1990) PG 1553 + 11 - A bright optically selected BL Lacertae object. *PASP*, **102**, 1120. (Cited on pages 80 and 81.)

Fermi, E. (1949) On the Origin of the Cosmic Radiation. *Physical Review*, **75**, 1169. (Cited on pages 29 and 32.)

Ficarra, A., Grueff, G., and Tomassetti, G. (1985) A new Bologna sky survey at 408 MHz. *Astron. Astrophys. Sup.*, **59**, 255. (Cited on page 112.)

Fiorucci, M. and Tosti, G. (1996) VRI photometry of stars in the fields of 12 BL Lacertae objects. *Astron. Astrophys. Sup.*, **116**, 403. (Cited on page 78.)

Fiorucci, M., Tosti, G., and Rizzi, N. (1998) VRI Photometry of Stars in the Fields of 16 Blazars. *PASP*, **110**, 105. (Cited on page 78.)

Fitzpatrick, E. L. (1999) Correcting for the Effects of Interstellar Extinction. *PASP*, **111**, 63. arXiv:astro-ph/9809387. (Cited on page 123.)

Fomin, V. P., et al. (1994) New methods of atmospheric Cherenkov imaging for gamma-ray astronomy. II. The differential position method. *Astroparticle Physics*, **2**, 151. (Cited on page 77.)

Foschini, L., et al. (2006) XMM-Newton observations of a sample of γ-ray loud active galactic nuclei. *Astron. Astrophys.*, **453**, 829. arXiv:astro-ph/0603268. (Cited on pages 169, 170, 174, 183, 184, and 186.)

Fossati, G., et al. (1998) A unifying view of the spectral energy distributions of blazars. *Mon. Not. R. Astron. Soc.*, **299**, 433. arXiv:astro-ph/9804103. (Cited on pages 23, 24, 25, and 26.)

— (2008) Multiwavelength Observations of Markarian 421 in 2001 March: An Unprecedented View on the X-Ray/TeV Correlated Variability. *Astrophys. J.*, **677**, 906. 0710.4138. (Cited on page 89.)

Franceschini, A., Rodighiero, G., and Vaccari, M. (2008) Extragalactic optical-infrared background radiation, its time evolution and the cosmic photon-photon opacity. *Astron. Astrophys.*, **487**, 837. 0805.1841. (Cited on page 104.)

Frank, J., King, A., and Raine, D. (1992) *Accretion power in astrophysics.* (Cited on page 19.)

Frü'hwirth, R., et al. (2000) *Data Analysis Techniques for High-Energy Physics*. (Cited on page 52.)

Frye, B. L., et al. (1999) BIMA and Keck Imaging of the Radio Ring PKS 1830-211. In Carilli, C. L., et al. (Editors), *Highly Redshifted Radio Lines*, volume 156 of *Astronomical Society of the Pacific Conference Series*, p. 240. arXiv:astro-ph/9802347. (Cited on page 168.)

Fuhrmeister, B., Liefke, C., and Schmitt, J. H. M. M. (2007) Simultaneous XMM-Newton and VLT/UVES observations of the flare star CN Leonis. *Astron. Astrophys.*, **468**, 221. (Cited on page 204.)

Fukugita, M., Shimasaku, K., and Ichikawa, T. (1995) Galaxy Colors in Various Photometric Band Systems. *PASP*, **107**, 945. (Cited on page 107.)

Gehrels, N., et al. (2004) The Swift Gamma-Ray Burst Mission. *Astrophys. J.*, **611**, 1005. (Cited on page 78.)

Georganopoulos, M. and Kazanas, D. (2003) Decelerating Flows in TeV Blazars: A Resolution to the BL Lacertae-FR I Unification Problem. *Astrophys. J. Lett.*, **594**, L27. arXiv:astro-ph/0307404. (Cited on pages 94 and 108.)

Ghisellini, G., Maraschi, L., and Tavecchio, F. (2009) The Fermi blazars' divide. *Mon. Not. R. Astron. Soc.*, **396**, L105. 0903.2043. (Cited on pages 14 and 24.)

Ghisellini, G. and Tavecchio, F. (2008) The blazar sequence: a new perspective. *Mon. Not. R. Astron. Soc.*, **387**, 1669. 0802.1918. (Cited on page 26.)

Ghisellini, G., Tavecchio, F., and Chiaberge, M. (2005) Structured jets in TeV BL Lac objects and radiogalaxies. Implications for the observed properties. *Astron. Astrophys.*, **432**, 401. arXiv:astro-ph/0406093. (Cited on pages 94 and 111.)

Ghisellini, G., et al. (1998) A theoretical unifying scheme for gamma-ray bright blazars. *Mon. Not. R. Astron. Soc.*, **301**, 451. arXiv:astro-ph/9807317. (Cited on page 24.)

— (2011a) High-redshift Fermi blazars. *Mon. Not. R. Astron. Soc.*, **411**, 901. 1009.3275. (Cited on page 185.)

— (2011b) The transition between BL Lac objects and flat spectrum radio quasars. *Mon. Not. R. Astron. Soc.*, **414**, 2674. 1012.0308. (Cited on pages 93 and 130.)

— (2012) Blue Fermi flat spectrum radio quasars. *Mon. Not. R. Astron. Soc.*, **425**, 1371. 1205.0808. (Cited on page 27.)

Giommi, P., et al. (2012a) A simplified view of blazars: clearing the fog around long-standing selection effects. *Mon. Not. R. Astron. Soc.*, **420**, 2899. 1110.4706. (Cited on pages 25, 26, and 27.)

— (2012b) Simultaneous Planck, Swift, and Fermi observations of X-ray and γ-ray selected blazars. *Astron. Astrophys.*, **541**, A160. 1108.1114. (Cited on pages 22, 26, 27, and 108.)

Giroletti, M., Orienti, M., and Cheung, C. C. (2012a) Fermi LAT detection of a potential echo gamma-ray flare from gravitational lens S3 0218+35. *The Astronomer's Telegram*, **4371**, 1. (Cited on page 194.)

— (2012b) M. Giroletti (INAF-IRA Bologna), M. Orienti (Univ. Bologna, INAF-IRA Bologna), C. C. Cheung (NRL/NRL) on behalf of the Fermi Large Area Telescope Collaboration. *The Astronomer's Telegram*, **4361**, 1. (Cited on page 194.)

Giroletti, M., et al. (2004) Parsec-Scale Properties of Markarian 501. *Astrophys. J.*, **600**, 127. arXiv:astro-ph/0309285. (Cited on pages 15 and 202.)

González, J. B., Raue, M., and Wagner, R. (2012) Synoptics study of blazars detected at very high energy gamma-rays. In Aharonian, F. A., Hofmann, W., and Rieger, F. M. (Editors), *American Institute of Physics Conference Series*, volume 1505 of *American Institute of Physics Conference Series*, pp. 550–553. (Cited on page 139.)

Graff, P. B., et al. (2008) A Multizone Model for Simulating the High-Energy Variability of TeV Blazars. *Astrophys. J.*, **689**, 68. 0808.2135. (Cited on page 41.)

Grazian, A., et al. (2000) The Asiago-ESO/RASS QSO Survey. I. The Catalog and the Local QSO Luminosity Function. *Astronom. J.*, **119**, 2540. arXiv:astro-ph/0002183. (Cited on page 95.)

Green, R. F., Schmidt, M., and Liebert, J. (1986) The Palomar-Green catalog of ultraviolet-excess stellar objects. *Astrophys. J. Suppl. S.*, **61**, 305. (Cited on page 80.)

Gregg, M. D., et al. (2002) The Reddest Quasars. *Astrophys. J.*, **564**, 133. arXiv:astro-ph/0107441. (Cited on page 168.)

Gregory, P. C. and Condon, J. J. (1991) The 87GB catalog of radio sources covering delta between O and + 75 deg at 4.85 GHz. *Astrophys. J. Suppl. S.*, **75**, 1011. (Cited on page 80.)

Grieger, B., Kayser, R., and Schramm, T. (1991) The deconvolution of the quasar structure from microlensing light curves. *Astron. Astrophys.*, **252**, 508. (Cited on page 188.)

Hartman, R. C., et al. (1999) The Third EGRET Catalog of High-Energy Gamma-Ray Sources. *Astrophys. J. Suppl. S.*, **123**, 79. (Cited on pages 142, 160, 161, and 201.)

— (2001) Multiepoch Multiwavelength Spectra and Models for Blazar 3C 279. *Astrophys. J.*, **553**, 683. arXiv:astro-ph/0102127. (Cited on page 160.)

Hayashida, M., et al. (2012) The Structure and Emission Model of the Relativistic Jet in the Quasar 3C 279 Inferred from Radio to High-energy γ-Ray Observations in 2008-2010. *Astrophys. J.*, **754**, 114. 1206.0745. (Cited on page 186.)

Healey, S. E., et al. (2007) CRATES: An All-Sky Survey of Flat-Spectrum Radio Sources. *Astrophys. J. Suppl. S.*, **171**, 61. arXiv:astro-ph/0702346. (Cited on pages 194 and 202.)

— (2008) CGRaBS: An All-Sky Survey of Gamma-Ray Blazar Candidates. *Astrophys. J. Suppl. S.*, **175**, 97. 0709.1735. (Cited on page 204.)

Hillas, A. M. (1985) Cerenkov light images of EAS produced by primary gamma. In Jones, F. C. (Editor), *International Cosmic Ray Conference*, volume 3 of *International Cosmic Ray Conference*, pp. 445–448. (Cited on page 77.)

Hinton, J. A. (2004) The status of the HESS project. *New Astron. Rev.*, **48**, 331. arXiv:astro-ph/0403052. (Cited on page 3.)

Holder, J., et al. (2006) The first VERITAS telescope. *Astroparticle Physics*, **25**, 391. arXiv:astro-ph/0604119. (Cited on page 3.)

Horan, D., et al. (2004) Constraints on the Very High Energy Emission from BL Lacertae Objects. *Astrophys. J.*, **603**, 51. arXiv:astro-ph/0311397. (Cited on pages 95, 121, and 133.)

Hoyle, F. and Fowler, W. A. (1963) Nature of Strong Radio Sources. *Nature*, **197**, 533. (Cited on page 7.)

Hungwe, F., Dutka, M., and Ojha, R. (2011) Record gamma-ray flux level detected from PKS 1510-089 by Fermi/LAT. *The Astronomer's Telegram*, **3694**, 1. (Cited on page 161.)

Hunter, S. D., et al. (1997) EGRET Observations of the Diffuse Gamma-Ray Emission from the Galactic Plane. *Astrophys. J.*, **481**, 205. (Cited on page 71.)

Ikejiri, Y., et al. (2011) Photopolarimetric Monitoring of Blazars in the Optical and Near-Infrared Bands with the Kanata Telescope. I. Correlations between Flux, Color, and Polarization. *Publ. Astron. Soc. Jpn.*, **63**, 639. 1105.0255. (Cited on page 106.)

Impey, C. D. and Tapia, S. (1988) New blazars discovered by polarimetry. *Astrophys. J.*, **333**, 666. (Cited on page 201.)

— (1990) The optical polarization properties of quasars. *Astrophys. J.*, **354**, 124. (Cited on page 201.)

Jannuzi, B. T., Smith, P. S., and Elston, R. (1994) The optical polarization properties of X-ray-selected BL Lacertae objects. *Astrophys. J.*, **428**, 130. (Cited on page 107.)

Jauncey, D. L., et al. (1991) An unusually strong Einstein ring in the radio source PKS1830 - 211. *Nature*, **352**, 132. (Cited on pages 167 and 168.)

Jones, D. L. and SHEVE Team (1993) Northern hemisphere VLBI observations of PKS 1830-211. In Davis, R. J. and Booth, R. S. (Editors), *Sub-arcsecond Radio Astronomy*, p. 150. (Cited on page 168.)

Jones, F. C. (1968) Calculated Spectrum of Inverse-Compton-Scattered Photons. *Physical Review*, **167**, 1159. (Cited on page 37.)

— (1994) A theoretical review of diffusive shock acceleration. *Astrophys. J. Suppl. S.*, **90**, 561. (Cited on page 30.)

Jorstad, S. G., et al. (2005) Polarimetric Observations of 15 Active Galactic Nuclei at High Frequencies: Jet Kinematics from Bimonthly Monitoring with the Very Long Baseline Array. *Astronom. J.*, **130**, 1418. arXiv:astro-ph/0502501. (Cited on page 141.)

Jovanović, P., et al. (2008) Microlensing of the X-ray, UV and optical emission regions of quasars: simulations of the time-scales and amplitude variations of microlensing events. *Mon. Not. R. Astron. Soc.*, **386**, 397. 0801.4473. (Cited on page 188.)

Kalberla, P. M. W., et al. (2005) The Leiden/Argentine/Bonn (LAB) Survey of Galactic HI. Final data release of the combined LDS and IAR surveys with improved stray-radiation corrections. *Astron. Astrophys.*, **440**, 775. arXiv:astro-ph/0504140. (Cited on pages 79, 84, 97, 123, 174, and 176.)

Katarzyński, K., et al. (2005) Correlation between the TeV and X-ray emission in high-energy peaked BL Lac objects. *Astron. Astrophys.*, **433**, 479. arXiv:astro-ph/0412405. (Cited on page 109.)

Kaufmann, S., et al. (2011) 1ES 0229+200: an extreme blazar with a very high minimum Lorentz factor. *Astron. Astrophys.*, **534**, A130. 1109.3628. (Cited on page 109.)

Kellermann, K. I., et al. (1989) VLA observations of objects in the Palomar Bright Quasar Survey. *Astronom. J.*, **98**, 1195. (Cited on page 11.)

Kida, S., et al. (2010) Radio Variability of a Fermi Large Area Telescope Bright Source 0FGL J1847.8+3223. *Astrophys. J. Lett.*, **714**, L36. (Cited on page 203.)

Kneiske, T. M. and Dole, H. (2010) A lower-limit flux for the extragalactic background light. *Astron. Astrophys.*, **515**, A19. 1001.2132. (Cited on pages 104 and 115.)

Kochanek, C. S. and Narayan, R. (1992) LensClean - an algorithm for inverting extended, gravitationally lensed images with application to the radio ring lens PKS 1830-211. *Astrophys. J.*, **401**, 461. (Cited on page 168.)

Komatsu, E., et al. (2009) Five-Year Wilkinson Microwave Anisotropy Probe Observations: Cosmological Interpretation. *Astrophys. J. Suppl. S.*, **180**, 330. 0803.0547. (Cited on pages 168 and 169.)

Lehár, J., et al. (2000) Hubble Space Telescope Observations of 10 Two-Image Gravitational Lenses. *Astrophys. J.*, **536**, 584. arXiv:astro-ph/9909072. (Cited on pages 168 and 169.)

— (2002) Erratum: "Hubble Space Telescope Observations of 10 Two-Image Gravitational Lenses". *Astrophys. J.*, **571**, 1021. (Cited on page 168.)

Li, T.-P. and Ma, Y.-Q. (1983) Analysis methods for results in gamma-ray astronomy. *Astrophys. J.*, **272**, 317. (Cited on pages 84, 113, 124, and 136.)

Liang, E. W. and Liu, H. T. (2003) The masses of central supermassive black holes and the variability time-scales in gamma-ray loud blazars. *Mon. Not. R. Astron. Soc.*, **340**, 632. (Cited on page 186.)

Lidman, C., et al. (1999) The Redshift of the Gravitationally Lensed Radio Source PKS 1830-211. *Astrophys. J. Lett.*, **514**, L57. arXiv:astro-ph/9902317. (Cited on page 168.)

Lin, Y. C., et al. (1995) EGRET observations of the BL Lacertae objects 0716+714 and 0521-365. *Astrophys. J.*, **442**, 96. (Cited on page 202.)

Lindfors, E. J., et al. (2006) Synchrotron flaring in the jet of 3C 279. *Astron. Astrophys.*, **456**, 895. arXiv:astro-ph/0606646. (Cited on page 40.)

Lobanov, A. P. and Zensus, J. A. (1999) Spectral Evolution of the Parsec-Scale Jet in the Quasar 3C 345. *Astrophys. J.*, **521**, 509. arXiv:astro-ph/9903318. (Cited on page 203.)

Lombardi, S. (2011) Advanced stereoscopic gamma-ray shower analysis with the MAGIC telescopes. In *International Cosmic Ray Conference*, volume 3 of *International Cosmic Ray Conference*, p. 262. 1109.6195. (Cited on page 77.)

Longair, M. S. (2010) *High Energy Astrophysics*. (Cited on page 33.)

Lovell, J. E. J., et al. (1996) PKS 1830-211: A Possible Compound Gravitational Lens. *Astrophys. J. Lett.*, **472**, L5. arXiv:astro-ph/9609117. (Cited on pages 167, 168, and 194.)

— (1998) The Time Delay in the Gravitational Lens PKS 1830-211. *Astrophys. J. Lett.*, **508**, L51. arXiv:astro-ph/9809301. (Cited on pages 168, 169, 181, 187, and 188.)

Lucarelli, F., et al. (2012) AGILE detection of increasing gamma-ray emission from the FSRQ PKS1510-089. *The Astronomer's Telegram*, **3934**, 1. (Cited on page 141.)

MacDonald, D. and Thorne, K. S. (1982) Black-hole electrodynamics - an absolute-space/universal-time formulation. *Mon. Not. R. Astron. Soc.*, **198**, 345. (Cited on page 20.)

MAGIC Collaboration, et al. (2008) Very-High-Energy gamma rays from a Distant Quasar: How Transparent Is the Universe? *Science*, **320**, 1752. 0807.2822. (Cited on page 104.)

Mahony, E. K., et al. (2010) High-frequency Radio Properties of Sources in the Fermi-LAT 1 year Point Source Catalog. *Astrophys. J.*, **718**, 587. 1003.4580. (Cited on page 202.)

Mankuzhiyil, N., et al. (2011) The Environment and Distribution of Emitting Electrons as a Function of Source Activity in Markarian 421. *Astrophys. J.*, **733**, 14. 1103.0909. (Cited on page 110.)

Mannheim, K. (1993) The proton blazar. *Astron. Astrophys.*, **269**, 67. arXiv:astro-ph/9302006. (Cited on pages 22 and 39.)

Mannheim, K. and Biermann, P. L. (1992) Gamma-ray flaring of 3C 279 - A proton-initiated cascade in the jet? *Astron. Astrophys.*, **253**, L21. (Cited on page 38.)

Mannucci, F., et al. (2001) Near-infrared template spectra of normal galaxies: k-corrections, galaxy models and stellar populations. *Mon. Not. R. Astron. Soc.*, **326**, 745. arXiv:astro-ph/0104427. (Cited on page 22.)

Maraschi, L. and Tavecchio, F. (2003) The Jet-Disk Connection and Blazar Unification. *Astrophys. J.*, **593**, 667. arXiv:astro-ph/0205252. (Cited on pages 13, 21, 42, 91, 108, 129, and 138.)

Mariotti, M. (2011a) Discovery of Very High Energy Gamma-Ray Emission from 1ES 1215+303 by MAGIC. *The Astronomer's Telegram*, **3100**, 1. (Cited on page 96.)

— (2011b) MAGIC discovers VHE gamma-ray emission from the blazar 1ES 1727+502. *The Astronomer's Telegram*, **3774**, 1. (Cited on page 133.)

— (2011c) MAGIC observes a very high energy gamma-ray flare from 1ES0806+524. *The Astronomer's Telegram*, **3192**, 1. (Cited on pages 122 and 124.)

Mariotti, M. and MAGIC Collaboration (2010) Discovery of Very High Energy Gamma-Ray Emission from NGC1275 by MAGIC. *The Astronomer's Telegram*, **2916**, 1. (Cited on page 201.)

Marscher, A. P. (2011) Simulations Of Millimeter-wave To Gamma-ray Flares Of Blazars In A Turbulent Jet. In *American Astronomical Society Meeting Abstracts #218*, p. 327.07. (Cited on pages 111 and 192.)

Marscher, A. P. and Jorstad, S. G. (2010) Rapid Variability of Gamma-ray Emission from Sites near the 43 GHz Cores of Blazar Jets. *ArXiv e-prints*. 1005.5551. (Cited on pages 40, 182, 186, and 193.)

Marscher, A. P., et al. (2008) The inner jet of an active galactic nucleus as revealed by a radio-to-γ-ray outburst. *Nature*, **452**, 966. (Cited on pages 15, 16, and 106.)

— (2010) Probing the Inner Jet of the Quasar PKS 1510-089 with Multi-Waveband Monitoring During Strong Gamma-Ray Activity. *Astrophys. J. Lett.*, **710**, L126. 1001.2574. (Cited on pages 142 and 149.)

Marshall, H. L., et al. (2005) A Chandra Survey of Quasar Jets: First Results. *Astrophys. J. Suppl. S.*, **156**, 13. arXiv:astro-ph/0409566. (Cited on page 201.)

Massaro, E., et al. (2004) Log-parabolic spectra and particle acceleration in the BL Lac object Mkn 421: Spectral analysis of the complete BeppoSAX wide band X-ray data set. *Astron. Astrophys.*, **413**, 489. arXiv:astro-ph/0312260. (Cited on pages 29, 114, and 122.)

— (2009) Roma-BZCAT: a multifrequency catalogue of blazars. *Astron. Astrophys.*, **495**, 691. 0810.2206. (Cited on page 13.)

Mathur, S. and Nair, S. (1997) X-Ray Absorption toward the Einstein Ring Source PKS 1830-211. *Astrophys. J.*, **484**, 140. arXiv:astro-ph/9703015. (Cited on pages 174 and 182.)

Mattox, J. R., et al. (1996) The Likelihood Analysis of EGRET Data. *Astrophys. J.*, **461**, 396. (Cited on pages 65, 68, 135, 143, and 159.)

— (1997) An Intense Gamma-Ray Flare of PKS 1622-297. *Astrophys. J.*, **476**, 692. arXiv:astro-ph/9610007. (Cited on page 185.)

Menten, K. M., et al. (2008) Submillimeter water and ammonia absorption by the peculiar interstellar medium in the gravitational lens of the PKS 1830-211 system. *Astron. Astrophys.*, **492**, 725. 0810.2782. (Cited on page 168.)

Meyer, E. T., et al. (2011) From the Blazar Sequence to the Blazar Envelope: Revisiting the Relativistic Jet Dichotomy in Radio-loud Active Galactic Nuclei. *Astrophys. J.*, **740**, 98. 1107.5105. (Cited on page 26.)

— (2012) Collective Evidence for Inverse Compton Emission from External Photons in High-power Blazars. *Astrophys. J. Lett.*, **752**, L4. 1203.4991. (Cited on page 27.)

Moiseev, A. A., et al. (2007) The anti-coincidence detector for the GLAST large area telescope. *Astroparticle Physics*, **27**, 339. arXiv:astro-ph/0702581. (Cited on page 48.)

Moralejo, R. A., et al. (2010) MARS: The MAGIC Analysis and Reconstruction Software. *Astrophysics Source Code Library*, p. 11004. (Cited on page 77.)

Mose Mariotti, M. (2010) MAGIC detects a VHE flare from 4C +21.35 (PKS 1222+21). *The Astronomer's Telegram*, **2684**, 1. (Cited on page 203.)

Mukherjee, R. (2001) EGRET (GeV) Blazars. In Aharonian, F. A. and Völk, H. J. (Editors), *American Institute of Physics Conference Series*, volume 558 of *American Institute of Physics Conference Series*, pp. 324–337. arXiv:astro-ph/0101301. (Cited on page 161.)

Mukherjee, R., et al. (1999) Broadband Spectral Analysis of PKS 0528+134: A Report on Six Years of EGRET Observations. *Astrophys. J.*, **527**, 132. arXiv:astro-ph/9901106. (Cited on page 161.)

Myers, S. T., et al. (2003) The Cosmic Lens All-Sky Survey - I. Source selection and observations. *Mon. Not. R. Astron. Soc.*, **341**, 1. arXiv:astro-ph/0211073. (Cited on page 194.)

Nair, S., Narasimha, D., and Rao, A. P. (1993) PKS 1830-211 as a gravitationally lensed system. *Astrophys. J.*, **407**, 46. (Cited on pages 168 and 182.)

Nalewajko, K. (2012) The brightest gamma-ray flares of blazars. *ArXiv e-prints*. 1211.0274. (Cited on pages 148 and 163.)

Neronov, A., Semikoz, D., and Vovk, I. (2011) High Galactic latitude Fermi sources of γ-rays with energies above 100 GeV. *Astron. Astrophys.*, **529**, A59. 1004.3767. (Cited on page 112.)

Nieppola, E., Tornikoski, M., and Valtaoja, E. (2006a) Spectral energy distributions of a large sample of BL Lacertae objects. *Astron. Astrophys.*, **445**, 441. arXiv:astro-ph/0509045. (Cited on pages 24 and 82.)

— (2006b) Spectral energy distributions of a large sample of BL Lacertae objects. *Astron. Astrophys.*, **445**, 441. arXiv:astro-ph/0509045. (Cited on pages 81 and 112.)

Nilsson, K., et al. (2003) R-band imaging of the host galaxies of RGB BL Lacertae objects. *Astron. Astrophys.*, **400**, 95. (Cited on pages 22, 78, and 112.)

— (2007) Host galaxy subtraction of TeV candidate BL Lacertae objects. *Astron. Astrophys.*, **475**, 199. 0709.2533. (Cited on pages 105, 117, 123, and 134.)

Nodes, C., et al. (2004) Radio emission and particle acceleration in plerionic supernova remnants. *Astron. Astrophys.*, **423**, 13. arXiv:astro-ph/0405251. (Cited on page 30.)

Nolan, P. L., et al. (2012) Fermi LAT second source catalog (2FGL) (Nolan+, 2012). *VizieR Online Data Catalog*, **219**, 90031. (Cited on pages 12, 56, 75, 97, 112, 114, 115, 123, 135, 143, 157, 158, 159, 160, and 170.)

Ojha, R., Dutka, M., and Torresi, E. (2011) Highest gamma-ray flux level detected from very high redshift blazar B3 1343+451. *The Astronomer's Telegram*, **3793**, 1. (Cited on page 185.)

Orienti, M. and D'Ammando, F. (2012) Fermi LAT detection of a New Gamma-ray Source in the Vicinity of TXS 0536+145. *The Astronomer's Telegram*, **3999**, 1. (Cited on page 185.)

Orienti, M., et al. (2013) Radio and γ-ray follow-up of the exceptionally high-activity state of PKS 1510-089 in 2011. *Mon. Not. R. Astron. Soc.*, **428**, 2418. 1210.4319. (Cited on page 193.)

Ormes, J. F., et al. (2007) The GLAST Background Model. In Ritz, S., Michelson, P., and Meegan, C. A. (Editors), *The First GLAST Symposium*, volume 921 of *American Institute of Physics Conference Series*, pp. 560–561. (Cited on page 51.)

Oshima, T., et al. (2001) ASCA Observation of the Lensed Blazar PKS 1830-211: An Implication of X-Ray Microlensing. *Astrophys. J.*, **551**, 929. (Cited on pages 174 and 188.)

Osterman, M. A., et al. (2006) Multiwavelength Observations of the Extreme X-Ray-selected BL Lacertae Object PG 1553+11 (1ES 1553+113). *Astronom. J.*, **132**, 873. arXiv:astro-ph/0605076. (Cited on pages 80 and 81.)

Ostrowski, M. and Schlickeiser, R. (1993) Diffusive first and second order Fermi acceleration at parallel shock waves. *Astron. Astrophys.*, **268**, 812. (Cited on pages 31 and 32.)

Padovani, P. (2007) The blazar sequence: validity and predictions. *Astrophys. Space Sci.*, **309**, 63. arXiv:astro-ph/0610545. (Cited on page 25.)

Padovani, P. and Giommi, P. (1995) The connection between x-ray- and radio-selected BL Lacertae objects. *Astrophys. J.*, **444**, 567. arXiv:astro-ph/9412073. (Cited on page 23.)

Padovani, P., Giommi, P., and Rau, A. (2012) The discovery of high-power high synchrotron peak blazars. *Mon. Not. R. Astron. Soc.*, **422**, L48. 1202.2236. (Cited on pages 26 and 27.)

Padovani, P., et al. (2003) A New Population of Radio Quasars. *Chinese Journal of Astronomy and Astrophysics Supplement*, **3**, 147. (Cited on pages 24 and 25.)

Pei, Y. C. (1992) Interstellar dust from the Milky Way to the Magellanic Clouds. *Astrophys. J.*, **395**, 130. (Cited on pages 79 and 97.)

Perlman, E. S., et al. (2005) Intrinsic Curvature in the X-Ray Spectra of BL Lacertae Objects. *Astrophys. J.*, **625**, 727. arXiv:astro-ph/0502298. (Cited on pages 80 and 81.)

Perna, R. and Keeton, C. R. (2009) Gravitational lensing of anisotropic sources. *Mon. Not. R. Astron. Soc.*, **397**, 1084. 0904.3935. (Cited on page 188.)

Pian, E., et al. (1996) The Broadband Energy Distribution of the Misaligned Gamma-Ray Blazar PKS 0521-365. *Astrophys. J.*, **459**, 169. (Cited on page 202.)

Piirola, V., et al. (2005) Polarimetric Study of the Massive Interacting Binary W Serpentis: Discovery of High-Latitude Scattering Spot/-Jet. *Astrophys. J.*, **632**, 576. (Cited on page 78.)

Pindor, B. (2005) Discovering Gravitational Lenses through Measurements of Their Time Delays. *Astrophys. J.*, **626**, 649. arXiv:astro-ph/0501518. (Cited on page 194.)

Piner, B. G., Pant, N., and Edwards, P. G. (2010) The Jets of TeV Blazars at Higher Resolution: 43 GHz and Polarimetric VLBA Observations from 2005 to 2009. *Astrophys. J.*, **723**, 1150. 1009.2269. (Cited on page 94.)

Pogge, R. W. (2000) Narrow-line Seyfert 1s: 15 years later. *New Astron. Rev.*, **44**, 381. arXiv:astro-ph/0005125. (Cited on page 201.)

Poole, T. S., et al. (2008) Photometric calibration of the Swift ultraviolet/optical telescope. *Mon. Not. R. Astron. Soc.*, **383**, 627. 0708.2259. (Cited on pages 79, 97, and 176.)

Pramesh Rao, A. and Subrahmanyan, R. (1988) 1830-211 - A flat-spectrum radio source with double structure. *Mon. Not. R. Astron. Soc.*, **231**, 229. (Cited on page 167.)

Prandini, E., et al. (2010) Constraining blazar distances with combined Fermi and TeV data: an empirical approach. *Mon. Not. R. Astron. Soc.*, **405**, L76. 1003.1674. (Cited on page 80.)

Primack, J. R., Bullock, J. S., and Somerville, R. S. (2005) Observational Gamma-ray Cosmology. In Aharonian, F. A., Völk, H. J., and Horns, D. (Editors), *High Energy Gamma-Ray Astronomy*, volume 745 of *American Institute of Physics Conference Series*, pp. 23–33. arXiv:astro-ph/0502177. (Cited on page 104.)

Protassov, R., et al. (2002) Statistics, Handle with Care: Detecting Multiple Model Components with the Likelihood Ratio Test. *Astrophys. J.*, **571**, 545. arXiv:astro-ph/0201547. (Cited on page 68.)

Raiteri, C. M., et al. (2011) The long-lasting activity of <ASTROBJ>3C 454.3</ASTROBJ>. GASP-WEBT and satellite observations in 2008-2010. *Astron. Astrophys.*, **534**, A87. 1107.1093. (Cited on page 186.)

Rando, R., for the Fermi LAT Collaboration, and , a. . a. ., and (2009) Post-launch performance of the Fermi Large Area Telescope. *ArXiv e-prints*. 0907.0626. (Cited on pages 59 and 61.)

Rao, R. C. (1945) Information and the accuracy attainable in the estimation of statistical parameters. *Bull. Calcutta Math. Soc.* (Cited on page 66.)

Rau, A., et al. (2012) BL Lacertae objects beyond redshift 1.3 - UV-to-NIR photometry and photometric redshift for Fermi/LAT blazars. *Astron. Astrophys.*, **538**, A26. 1112.0025. (Cited on page 26.)

Readhead, A. C. S., et al. (1989) A limit of the anisotropy of the microwave background radiation on arc minute scales. *Astrophys. J.*, **346**, 566. (Cited on page 122.)

Rector, T. A., Gabuzda, D. C., and Stocke, J. T. (2003) The Radio Structure of High-Energy-Peaked BL Lacertae Objects. *Astronom. J.*, **125**, 1060. arXiv:astro-ph/0302397. (Cited on pages 80 and 81.)

Rees, M. J. (1966) Appearance of Relativistically Expanding Radio Sources. *Nature*, **211**, 468. (Cited on pages 11 and 15.)

Reimer, A., et al. (2008) A hard X-ray view on two distant TeV-blazars. In Aharonian, F. A., Hofmann, W., and Rieger, F. (Editors), *American Institute of Physics Conference Series*, volume 1085 of *American Institute of Physics Conference Series*, pp. 518–521. (Cited on pages 81, 83, and 91.)

Richards, J. L., et al. (2011) Blazars in the Fermi Era: The OVRO 40 m Telescope Monitoring Program. *Astrophys. J. Suppl. S.*, **194**, 29. 1011.3111. (Cited on page 122.)

Roming, P. W. A., et al. (2005) The Swift Ultra-Violet/Optical Telescope. *Space Sci. Rev.*, **120**, 95. arXiv:astro-ph/0507413. (Cited on page 78.)

Rybicki, G. B. and Lightman, A. P. (1979) *Radiative processes in astrophysics*. (Cited on pages 32, 33, and 36.)

Sadler, E. M., et al. (2006) The properties of extragalactic radio sources selected at 20GHz. *Mon. Not. R. Astron. Soc.*, **371**, 898. arXiv:astro-ph/0603437. (Cited on page 194.)

Sanchez, D. and Escande, L. (2010) Fermi LAT detection of a rapid and extraordinary GeV outburst from 3C 454.3. *The Astronomer's Telegram*, **3041**, 1. (Cited on page 161.)

Scarpa, R., Falomo, R., and Pian, E. (1995) A study of emission lines variability of the active galaxy PKS 0521-365. *Astron. Astrophys.*, **303**, 730. (Cited on page 202.)

Scarpa, R., et al. (1999) Hubble Space Telescope Observations of the Optical Jets of PKS 0521-365, 3C 371, and PKS 2201+044. *Astrophys. J.*, **526**, 643. arXiv:astro-ph/9906462. (Cited on page 202.)

Schachter, J. F., et al. (1993) Ten new BL Lacertae objects discovered by an efficient X-ray/radio/optical technique. *Astrophys. J.*, **412**, 541. (Cited on page 121.)

Schinzel, F. K., et al. (2011) Identification of γ-ray emission from 3C 345 and NRAO 512. *Astron. Astrophys.*, **532**, A150. 1107.2926. (Cited on page 203.)

Schlegel, D. J., Finkbeiner, D. P., and Davis, M. (1998) Maps of Dust Infrared Emission for Use in Estimation of Reddening and Cosmic Microwave Background Radiation Foregrounds. *Astrophys. J.*, **500**, 525. arXiv:astro-ph/9710327. (Cited on pages 78, 79, 97, and 114.)

Schlickeiser, R., Campeanu, A., and Lerche, L. (1993) Stochastic particle acceleration at parallel astrophysical shock waves. *Astron. Astrophys.*, **276**, 614. (Cited on page 30.)

Schneider, P., Ehlers, J., and Falco, E. E. (1992) *Gravitational Lenses*. (Cited on pages 167 and 187.)

Schultz, C., et al. (2012) Spectral variability and multiwavelength studies of the high-frequency-peaked BL Lacertae object 1ES 0806+524 with the MAGIC telescopes. In Aharonian, F. A., Hofmann, W., and Rieger, F. M. (Editors), *American Institute of Physics Conference Series*, volume 1505 of *American Institute of Physics Conference Series*, pp. 534–537. (Cited on page 121.)

Shen, Z.-Q., et al. (1998) A 5 GHz Southern Hemisphere VLBI Survey of Compact Radio Sources. II. *Astronom. J.*, **115**, 1357. arXiv:astro-ph/9803104. (Cited on page 201.)

Shimmins, A. J., Manchester, R. N., and Harris, B. J. (1969) Accurate Flux Densities at 5009 MHz of 753 Radio Sources. *Australian Journal of Physics Astrophysical Supplement*, **8**, 3. (Cited on page 167.)

Sikora, M., Begelman, M. C., and Rees, M. J. (1994) Comptonization of diffuse ambient radiation by a relativistic jet: The source of gamma rays from blazars? *Astrophys. J.*, **421**, 153. (Cited on page 41.)

Sikora, M., et al. (2001) Modeling the Production of Flares in Gamma-Ray Quasars. *Astrophys. J.*, **554**, 1. arXiv:astro-ph/0102091. (Cited on page 186.)

— (2009) Constraining Emission Models of Luminous Blazar Sources. *Astrophys. J.*, **704**, 38. 0904.1414. (Cited on page 186.)

Sironi, L. and Spitkovsky, A. (2011) Particle Acceleration in Relativistic Magnetized Collisionless Electron-Ion Shocks. *Astrophys. J.*, **726**, 75. 1009.0024. (Cited on page 109.)

Sluse, D., et al. (2007) Multi-wavelength study of the gravitational lens system RXS J1131-1231. III. Long slit spectroscopy: microlensing probes the QSO structure. *Astron. Astrophys.*, **468**, 885. arXiv:astro-ph/0703030. (Cited on page 188.)

Smith, P. S. (2010) Detection of optical activity in the radio source B2 0619+33. *The Astronomer's Telegram*, **2831**, 1. (Cited on page 202.)

Sokolov, A. and Marscher, A. P. (2005) External Compton Radiation from Rapid Nonthermal Flares in Blazars. *Astrophys. J.*, **629**, 52. arXiv:astro-ph/0504639. (Cited on page 186.)

Sowards-Emmerd, D., et al. (2005) A Northern Survey of Gamma-Ray Blazar Candidates. *Astrophys. J.*, **626**, 95. arXiv:astro-ph/0503115. (Cited on page 204.)

Stamerra, A., et al. (2011) Swift follow-up of the flaring BL Lac 1ES0806+524. *The Astronomer's Telegram*, **3208**, 1. (Cited on pages 122 and 126.)

Stecker, F. W., de Jager, O. C., and Salamon, M. H. (1992) TeV gamma rays from 3C 279 - A possible probe of origin and intergalactic infrared radiation fields. *Astrophys. J. Lett.*, **390**, L49. (Cited on page 83.)

Striani, E., et al. (2009) AGILE detection of the gamma-ray blazar PKS 1830-211. *The Astronomer's Telegram*, **2242**, 1. (Cited on pages 170 and 177.)

Strong, A. W., Moskalenko, I. V., and Reimer, O. (2004) Diffuse Galactic Continuum Gamma Rays: A Model Compatible with EGRET Data and Cosmic-Ray Measurements. *Astrophys. J.*, **613**, 962. arXiv:astro-ph/0406254. (Cited on page 71.)

Subrahmanyan, R., et al. (1990) 1830-211 - Gravitational Lensed Images of a Flat-Spectrum Radio Core. *Mon. Not. R. Astron. Soc.*, **246**, 263. (Cited on page 168.)

Takalo, L. O., et al. (2007) Optical Monitoring of Candidate TeV Blazars. In Ho, L. C. and Wang, J.-W. (Editors), *The Central Engine of Active Galactic Nuclei*, volume 373 of *Astronomical Society of the Pacific Conference Series*, p. 249. (Cited on pages 81 and 83.)

Tanaka, Y. T., et al. (2011) Fermi Large Area Telescope Detection of Bright γ-Ray Outbursts from the Peculiar Quasar 4C +21.35. *Astrophys. J.*, **733**, 19. 1101.5339. (Cited on pages 149 and 176.)

Tavecchio, F. and Ghisellini, G. (2008) Spine-sheath layer radiative interplay in subparsec-scale jets and the TeV emission from M87. *Mon. Not. R. Astron. Soc.*, **385**, L98. 0801.0593. (Cited on page 108.)

— (2012) "Flat" broad line region and gamma-ray absorption in blazars. *ArXiv e-prints*. 1209.2291. (Cited on page 149.)

Tavecchio, F., Maraschi, L., and Ghisellini, G. (1998) Constraints on the Physical Parameters of TeV Blazars. *Astrophys. J.*, **509**, 608. arXiv:astro-ph/9809051. (Cited on pages 41, 42, and 118.)

Tavecchio, F., et al. (2009) The hard TeV spectrum of 1ES 0229+200: new clues from Swift. *Mon. Not. R. Astron. Soc.*, **399**, L59. 0905.0899. (Cited on page 109.)

— (2010) TeV BL Lac objects at the dawn of the Fermi era. *Mon. Not. R. Astron. Soc.*, **401**, 1570. 0909.0651. (Cited on pages 91, 94, 95, 108, 118, and 129.)

Teraesranta, H., et al. (1998) Fifteen years monitoring of extragalactic radio sources at 22, 37 and 87 GHz. *Astron. Astrophys. Sup.*, **132**, 305. (Cited on page 79.)

Tingay, S. J. and Edwards, P. G. (2002) The Parsec-Scale Structure and Evolution of PKS 0521-365. *Astronom. J.*, **124**, 652. (Cited on page 202.)

Torniainen, I., et al. (2008) Cluster analyses of gigahertz-peaked spectrum sources with self-organising maps. *Astron. Astrophys.*, **482**, 483. (Cited on page 202.)

Torres, D. F., et al. (2003) Gravitational microlensing of γ-ray blazars. *Mon. Not. R. Astron. Soc.*, **339**, 335. arXiv:astro-ph/0205441. (Cited on page 195.)

Tramacere, A., et al. (2007) SWIFT observations of TeV BL Lacertae objects. *Astron. Astrophys.*, **467**, 501. arXiv:astro-ph/0611276. (Cited on page 84.)

Treves, A., Falomo, R., and Uslenghi, M. (2007) On the distance of <ASTROBJ>PG 1553+11</ASTROBJ>. A lineless BL Lacertae object active in the TeV band. *Astron. Astrophys.*, **473**, L17. 0709.1271. (Cited on page 82.)

Ulrich, M. H. (1981) The appearance of broad emission lines in the spectrum of the BL Lac object PKS 0521-36. *Astron. Astrophys.*, **103**, L1. (Cited on page 202.)

Urry, C. M. and Padovani, P. (1995) Unified Schemes for Radio-Loud Active Galactic Nuclei. *PASP*, **107**, 803. arXiv:astro-ph/9506063. (Cited on pages 7, 8, 10, 11, 12, and 108.)

van Ommen, T. D., et al. (1995) Time delay in the Einstein ring PKS 1830-211. *Astrophys. J.*, **444**, 561. (Cited on pages 169 and 181.)

Vanden Berk, D. E., et al. (2001) Composite Quasar Spectra from the Sloan Digital Sky Survey. *Astronom. J.*, **122**, 549. arXiv:astro-ph/0105231. (Cited on page 22.)

Véron-Cetty, M.-P. and Véron, P. (2006) A catalogue of quasars and active nuclei: 12th edition. *Astron. Astrophys.*, **455**, 773. (Cited on page 112.)

Villforth, C., et al. (2010) Variability and stability in blazar jets on time-scales of years: optical polarization monitoring of OJ 287 in 2005-2009. *Mon. Not. R. Astron. Soc.*, **402**, 2087. 0912.0005. (Cited on page 107.)

Virbhadra, K. S. and Ellis, G. F. R. (2000) Schwarzschild black hole lensing. *Phys. Rev. D*, **62, 8**, 084003. arXiv:astro-ph/9904193. (Cited on page 167.)

Virtanen, J. and Vainio, R. (2003) Simulations on the Effect of Internal Structure of Shock Fronts on Particle Acceleration (Poster). In

Takalo, L. O. and Valtaoja, E. (Editors), *High Energy Blazar Astronomy, ASP Conference Proceedings, Vol. 299, held 17-21 June 2002 at Tuorla Observatory, Piikkio, Finland. Edited by Leo O. Takalo and Esko Valtaoja. ISBN: 1-58381-146-X. San Francisco: Astronomical Society of the Pacific, 2003, p.157.*, p. 157. (Cited on page 109.)

Virtanen, J. J. P. and Vainio, R. (2005) Stochastic particle acceleration in parallel relativistic shocks. In Bulik, T., Rudak, B., and Madejski, G. (Editors), *Astrophysical Sources of High Energy Particles and Radiation*, volume 801 of *American Institute of Physics Conference Series*, pp. 410–411. (Cited on page 30.)

Voges, W., et al. (1999) The ROSAT all-sky survey bright source catalogue. *Astron. Astrophys.*, **349**, 389. arXiv:astro-ph/9909315. (Cited on page 201.)

Wagner, S. J. (2010) Detection of VHE Gamma-ray Emission from a Type 1 Quasar. In *AAS/High Energy Astrophysics Division 11*, volume 11 of *AAS/High Energy Astrophysics Division*, p. 27.06. (Cited on pages 141 and 203.)

Weekes, T. C., et al. (1989) Observation of TeV gamma rays from the Crab nebula using the atmospheric Cerenkov imaging technique. *Astrophys. J.*, **342**, 379. (Cited on page 3.)

Weidinger, M., Rüger, M., and Spanier, F. (2010) Modelling the steady state spectral energy distribution of the BL-Lac Object PKS 2155-30.4 using a selfconsistent SSC model. *Astrophysics and Space Sciences Transactions*, **6**, 1. 1001.2145. (Cited on pages 111, 118, and 119.)

Wiklind, T. and Combes, F. (1996) The redshift of the gravitational lens of PKS1830-211 determined from molecular absorption lines. *Nature*, **379**, 139. (Cited on page 168.)

— (1998) The Complex Molecular Absorption Line System at Z = 0.886 toward PKS 1830-211. *Astrophys. J.*, **500**, 129. arXiv:astro-ph/9709141. (Cited on pages 168 and 181.)

— (2001) Time Delay of PKS 1830-211 Using Molecular Absorption Lines. In Brainerd, T. G. and Kochanek, C. S. (Editors), *Gravitational Lensing: Recent Progress and Future Go*, volume 237 of *Astronomical Society of the Pacific Conference Series*, p. 155. (Cited on pages 169, 181, and 188.)

Wilk, S. S. (1945) The large-sample distribution of the likelihood ratio for testing composite hypotheses. *Ann. Math. Stat.* (Cited on page 67.)

Wills, B. J., Wills, D., and Breger, M. (2011) McDonald Observatory Archive of Optical Linear Polarization Measurements. *Astrophys. J. Suppl. S.*, **194**, 19. (Cited on page 107.)

Wisotzki, L., et al. (1993) The new double QSO HE 1104-1805: Gravitational lens with microlensing or binary quasar? *Astron. Astrophys.*, **278**, L15. (Cited on page 188.)

Witt, H. J., Mao, S., and Keeton, C. R. (2000) Analytic Time Delays and H_0 Estimates for Gravitational Lenses. *Astrophys. J.*, **544**, 98. arXiv:astro-ph/0004069. (Cited on page 169.)

Yonehara, A., et al. (1998) An X-Ray Microlensing Test of AU-Scale Accretion Disk Structure in Q2237+0305. *Astrophys. J. Lett.*, **501**, L41. arXiv:astro-ph/9804251. (Cited on page 188.)

Zhang, S., et al. (2008a) High Energy Properties of PKS 1830-211. In *Proceedings of the 7th INTEGRAL Workshop*. (Cited on page 169.)

— (2008b) High-Energy Properties of PKS 1830-211. *Astrophys. J.*, **683**, 400. 0803.1900. (Cited on pages 169, 170, 174, 183, and 184.)